

ABSTRACT

Title of Document: THERMOACOUSTIC-PIEZOELECTRIC
SYSTEMS WITH DYNAMIC MAGNIFIERS

Mostafa Nouh, Doctor of Philosophy, 2013

Directed By: Professor Amr Baz
Department of Mechanical Engineering

Thermoacoustic energy conversion is an emergent technology with considerable potential for research, development, and innovation. In thermoacoustic resonators, self-excited acoustic oscillations are induced in a working gas by means of a temperature gradient across a porous body and vice versa with no need of moving parts. In the first part of this dissertation, thermoacoustic resonators are integrated with piezoelectric membranes to create a new class of energy harvesters. The incident acoustic waves impinge on a piezo-diaphragm located at one end of the thermoacoustic-piezoelectric (*TAP*) resonator to generate an electrical power output. The *TAP* design is enhanced by appending the resonator with an elastic structure aimed at enhancing the strain experienced by the piezo-element to magnify the electric energy produced for the same input acoustic power. An analytical approach to model the thermal, acoustical, mechanical and electrical domains of the developed harvester is introduced and optimized. The performance of the harvesters is compared with experimental data obtained from an in-house built prototype with similar dimensions. In an attempt to further understand the dynamics and transient behavior of the excited waves in the presence of piezoelectric coupling, a novel approach to compute and accurately predict critical temperature gradients that onset the acoustic waves is discussed. The developed model encompasses tools from electric circuit

analogy of the lumped acoustical and mechanical components to unify the modeling domain. In the second part of the dissertation, piezo-driven thermoacoustic refrigerators (*PDTARs*) are presented. The *PDTARs* rely on the inverse thermoacoustic effect for their operation. A high amplitude pressure wave in a working medium is used to create a temperature gradient across the ends of a porous body located in an acoustic resonator. Finally, *PDTARs* with dynamic magnifiers are introduced. The developed design is shown, theoretically and experimentally, as capable of potentially enhancing the cooling effect of *PDTARs* by increasing the temperature gradient created across the porous body.

THERMOACOUSTIC-PIEZOELECTRIC SYSTEMS
WITH DYNAMIC MAGNIFIERS

By

Mostafa Nouh

Dissertation submitted to the Faculty of the Graduate School of the
University of Maryland, College Park, in partial fulfillment
of the requirements for the degree of
Doctor of Philosophy
2013

Advisory Committee:
Professor Amr Baz, Chair
Professor Balakumar Balachandran
Professor Don DeVoe
Professor Nikhil Chopra
Professor Norman Wereley (Dean Representative)

© Copyright by
Mostafa Nouh
2013

DEDICATION

To ...

my parents, *Amal* and *Akram*

and my wife, *Ingy*

... for their everlasting patience and support.

and my daughter *Yasmeen*

... for the never-ending joy she brings to my life.

Acknowledgements

I would like to thank my advisor, Prof. Baz for all the support he has given me during my graduate career. As nerve-wrecking an experience a PhD can be, Dr. Baz has been an excellent mentor to have. His dedication, perseverance and unwavering integrity are simply infectious. Because of his guidance, I am a better researcher now than four years ago.

I am also indebted to all my friends and lab mates who have given me much support and so many smiles and laughs. I would like to thank Jason, for taking the time to teach me about all those lab instruments and for helping me with my experimentation. Andrew, for being a good friend and teaching me about American sports and good places to eat. Mohamed, for making the office such an enjoyable place to work. Abdulaziz and Yaser, for their help with classes during our first years. And Saeed and Hajid, for always taking interest in my progress.

Thanks are due to Professor Osama Aldraihem of King Saud University for his invaluable technical inputs and for the support from the National Plan for Science and Technology, and King Abdulaziz City for Science and Technology (KACST), Saudi Arabia, Project Number 30-380.

Thanks are also due to my friends at College Park, Ahmed, Hossam, Walaa, Hatem and Omar, for all the good times they've given me over the years. And all my friends from the water polo team at Maryland for all the fun we had playing together.

Last but not least, I would like to express my gratitude to my wife Ingy for keeping me sane. Her sacrifices are most appreciated. And my parents whose prayers, kindness, guidance and never-ending love have been a lifetime blessing.

Always, it is impossible to remember all, and I apologize to those I have inadvertently left out.

Table of Contents

Table of Contents	iv
List of Tables	vii
List of Figures	viii
Nomenclature	xiv
Chapter 1	1
1. Introduction	1
1.1. Literature Survey	1
1.1.1. Historical Development	1
1.1.2. Integration with Piezo-transducers	6
1.2. Background	9
1.2.1. Standing Wave Thermoacoustic Engines	9
1.2.2. Thermoacoustic Refrigerators	12
1.3. Objective and Scope of Thesis	14
Chapter 2	18
2. Thermoacoustic-piezoelectric Harvesters: Modeling and Theoretical Analysis	18
2.1. Introduction	18
2.2. Waveforms in Acoustic Resonators	19
2.3. Boundary Conditions	21
2.4. Integration with Piezo-element	22
2.5. Implementing a Dynamic Magnifier	27
2.6. Piezo displacement and Energy flow	34
2.6.1. Energy, Power and Efficiency	34
2.6.2. Magnification Ratio	35
2.6.3. TAP and DMTAP Performance Comparisons	39
2.7. Temperature Effect and Stack Region Equations	45
2.7.1. Critical temperature gradients	45
2.7.2. Energy balance and onset temperature difference	47
2.8. Graphical User Interface: Development and Applications	52
2.9. Summary	56
Chapter 3	58
3. Design Optimization of Thermoacoustic-Piezoelectric Harvesters with Dynamic Magnifiers	58
3.1. Introduction	58
3.2. Single Objective Optimization	59
3.2.1. Efficiency Oriented Design	60
3.2.2. Power Oriented Design	67
3.2.3. Temperature Oriented Design	73
3.3. Multi-Objective Optimization	75
3.4. Summary	81
Chapter 4	82
4. Experimental Investigation of Thermoacoustic-Piezoelectric Harvesters with Dynamic Magnifiers	82
4.1. Introduction	82

4.2.	Standing wave thermoacoustic-piezoelectric harvester (TAP).....	83
4.2.1.	Experimental Setup.....	83
4.2.2.	Temperature Distribution.....	85
4.2.3.	Pressure Propagation.....	87
4.2.4.	Velocity Flow Field	89
4.2.5.	Modal and Deflection Characteristics of the Piezo Diaphragm.....	97
4.2.6.	Output Voltage, Power and Efficiency	99
4.3.	Speaker-driven Resonator with a Dynamic Magnifier (No Stack).....	103
4.3.1.	Introduction.....	103
4.3.2.	Voltage output from Piezo-elements	105
4.3.3.	Vibrometer Scanning of Piezo Surface.....	111
4.4.	Experimental Prototype of DMTAP Harvester (with Stack).....	113
4.5.	Summary	122
Chapter 5.....		124
5.	Transient Characteristics and Stability Analysis of Standing Wave Thermoacoustic-Piezoelectric Harvesters.....	124
5.1.	Introduction.....	124
5.2.	Temperature Gradient	125
5.3.	Electric Circuit Analog of a Standing Wave TAP Harvester	126
5.3.1.	Hot Duct and Helmholtz Resonator.....	126
5.3.2.	Stack.....	126
5.3.3.	Piezo Diaphragm.....	129
5.4.	Electric Circuit Analog of a Standing Wave TAP Harvester	131
5.5.	Transient Response of TAP Harvester.....	134
5.5.1.	SPICE Modeling	134
5.5.2.	Root Locus Technique	136
5.5.3.	Performance of open-ended standing wave resonator (no piezo).....	137
5.5.4.	Performance of TAP with piezo-diaphragm	141
5.6.	Comparison with Experimental Prototype.....	144
5.6.1.	Frequency of oscillations	144
5.6.2.	Temperature Gradient	145
5.7.	Summary	148
Chapter 6.....		150
6.	Piezo-driven Thermoacoustic Refrigerators: Modeling and Theoretical Analysis 150	
6.1.	Introduction.....	150
6.2.	Piezoelectric Speakers	151
6.3.	Constant Area PDTAR	153
6.3.1.	Pressure and Velocity Waveforms.....	153
6.3.2.	Boundary Conditions	156
6.3.3.	Acoustic Power	158
6.4.	Variable Area PDTAR.....	160
6.5.	Performance of the PDTAR.....	162
6.5.1.	Speaker Deflection Characteristics.....	163
6.5.2.	Stack Effect.....	166
6.5.3.	Stack Location	167

6.5.4.	Attenuation Effect.....	169
6.5.5.	DeltaEC Model	171
6.6.	PDTAR with a dynamic magnifier	173
6.7.	Summary.....	176
Chapter 7.....		177
7.	Experimental Investigation of Piezo-driven Thermoacoustic Refrigerators	177
7.1.	Introduction.....	177
7.2.	PDTAR Experimental Prototype	177
7.3.	Experimental Setup.....	179
7.4.	Performance of the PDTAR.....	181
7.4.1.	Pressure P(L).....	181
7.4.2.	Temperature Difference (ΔT)	184
7.5.	PDTAR with a dynamic magnifier	184
7.5.1.	Experimental Prototype	184
7.5.2.	Performance of the PDTAR with a dynamic magnifier.....	188
7.5.3.	Comparison with the mathematical model	194
7.6.	Possible improvements to the PDTAR experimental setup.....	196
7.6.1.	Resonator matching	196
7.6.2.	Air tight Resonators	196
7.7.	Summary	198
Chapter 8.....		199
8.	Conclusions and Future Work	199
8.1.	Conclusions.....	199
8.2.	Future Work	200
8.2.1.	Miniature Thermoacoustic-Piezoelectric Harvesters	200
8.2.2.	Solar and Waste-heat Driven Thermoacoustic-Piezoelectric Energy Harvesting.....	201
8.2.3.	Effect of Varying Area Resonators.....	202
8.3.	Original Contributions	203
Appendices.....		206
Appendix A: Numerical Modeling of Thermoacoustic-Piezoelectric Systems using <i>DeltaEC</i>		206
A.1.	Introduction.....	206
A.2.	DeltaEC.....	207
A.3.	Piezo-elements in DeltaEC	209
A.4.	Transfer Functions for the Piezo-diaphragm Coupling Matrix.....	210
A.5.	Numerical Modeling of Piezo-driven Thermoacoustic Refrigerators.....	226
Bibliography		230

List of Tables

Table 2.1 <i>TAP</i> and <i>DMTAP</i> Design Parameters	31
Table 3.1 Design Parameters for 2 different prototype thermoacoustic-piezoelectric harvesters	60
Table 3.2 Maximum feasible efficiency and minimum temperature difference for the <i>DMTAP</i> harvesters for different objective weights using a multi-objective optimization algorithm.....	79
Table 4.1 Main geometrical parameters of the <i>TAP</i>	84
Table 4.2 Thermo-physical properties of the working gas and operating parameters of the <i>TAP</i>	85
Table 4.3 Springs and mass ratios used in the <i>DMTAP</i> experiments	116
Table 4.4 <i>DMTAP</i> to <i>TAP</i> voltage ratio: Experimental results and theoretical predictions.....	119
Table 5.1 Comparison between theoretical and experimental oscillation frequencies	145
Table 6.1 Dimensions of a variable area <i>PDTAR</i>	163
Table 7.1 Experiments done with a <i>PDTAR</i> with a dynamic magnifier	189
Table A.1.0.1 Values of the transfer functions coefficients governing the <i>PZT-5A</i> diaphragm	222
Table A.1.0.2 Impedance values inputted to <i>DeltaEC</i> for the thermoacoustic refrigerator speaker	228

List of Figures

Figure 1.1 Schematic and photo of a powerful standing wave thermoacoustic engine (background) at Cryenco in Denver, CO to supply acoustic power to an orifice pulse tube refrigerator (foreground).	3
Figure 1.2 A traveling wave thermoacoustic-stirling hybrid engine, producing 1 kW of power at an efficiency of ~30% with no moving parts [16].....	4
Figure 1.3 An ice cream cabinet powered by a thermoacoustic refrigerator	6
Figure 1.4 Standing wave thermoacoustic engine in operation	10
Figure 1.5 Stack spacing magnitude relative to the thermal and viscous boundary layers [33]	11
Figure 1.6 Schematic of a typical half-wavelength standing wave thermoacoustic refrigerator [33].....	13
Figure 2.1 Schematic of a standing wave thermoacoustic-piezoelectric harvester (<i>TAP</i>).....	19
Figure 2.2 (a) First [<i>desired</i>] and (b) Second [<i>undesired</i>] vibration modes of a piezoelectric diaphragm anchored at the circumference.....	23
Figure 2.3 Force balance diagram for the simplified piezo-element in a <i>TAP</i> harvester (excluding piezo-element internal stiffness s and damping b).....	24
Figure 2.4 Schematic of a standing wave thermoacoustic-piezoelectric harvester integrated with	28
Figure 2.5 Force balance diagram for the magnifier mass and piezo-element in the <i>DMTAP</i> harvester (excluding piezo-element internal stiffness s and damping b and internal stiffness k_m and damping c_m of the magnifier mass).....	29
Figure 2.6 Dimensionless frequency of self-sustained oscillations for different resonator lengths for <i>TAP</i> , <i>DMTAP</i> , closed-closed and closed-open tubes.....	32
Figure 2.7 Pressure and velocity waveforms for <i>TAP</i> and <i>DMTAP</i> harvesters in comparison with closed-closed and closed-open tubes for resonator lengths of (a) 1.5 cm and (b) 4 cm	33
Figure 2.8 Frequency response of conversion efficiency η_e and corresponding magnification ratio x_{2m} / x_1 for a <i>TAP</i> and a <i>DMTAP</i> at $m_m = 0$, $k_c = \infty$	37
Figure 2.9 Frequency response of conversion efficiency η_e and corresponding magnification ratio x_{2m} / x_1 for a <i>TAP</i> and a <i>DMTAP</i> at $m_m = m$, $k_c = 0.75 s$	38
Figure 2.10 Frequency response of conversion efficiency η_e and corresponding magnification ratio x_{2m} / x_1 for a <i>TAP</i> and a <i>DMTAP</i> at $m_m = m$, $k_c = 0.11 s$	39
Figure 2.11 (a) Dimensionless harvested electric power output and (b) corresponding acoustic to electric energy conversion efficiency for an electric load of 10 Ω	41
Figure 2.12 (a) Dimensionless harvested electric power output and (b) corresponding acoustic to electric energy conversion efficiency for an electric load of 100 Ω	42
Figure 2.13 (a) Dimensionless harvested electric power output and (b) corresponding acoustic to electric energy conversion efficiency for an electric load of 1000 Ω	43
Figure 2.14 (a) Dimensionless harvested electric power output and (b) corresponding acoustic to electric energy conversion efficiency for an electric load of 10000 Ω	44

Figure 2.15 Geometric parameters of resonator and stack	48
Figure 2.16 Temperature difference required to onset acoustic oscillations for <i>TAP</i> and <i>DMTAP</i> of resonator lengths 1.5 and 4 cm	50
Figure 2.17 Screen Capture of the developed <i>GUI</i> utility	53
Figure 2.18 <i>GUI</i> screenshots: Effect of varying k_c on the normalized electric output and the acoustic-to-electric energy conversion efficiency resulting in (a) magnification and (b) demagnification [solid line: <i>TAP</i> , dashed line: <i>DMTAP</i>].....	54
Figure 2.19 <i>GUI</i> screenshots: Effect of varying m_m on the normalized electric output and the acoustic-to-electric energy conversion efficiency resulting in (a) magnification and (b) demagnification.....	54
Figure 2.20 <i>GUI</i> screenshots: Effect of varying the working gas on the onset temperature difference expected in the stack for different stack locations. (a) Atmospheric Air. (b) Hydrogen.....	56
Figure 3.1 Optimization of η_e in a <i>DMTAP</i> : Objective function, variables and constraints	61
Figure 3.2 Maximum η_e for <i>DMTAP</i> harvester prototype 1 (a) and 2 (b) achieved using 3 different minimization based algorithms. Horizontal dotted line shows maximum <i>TAP</i> efficiency for comparison.....	63
Figure 3.3 Variation of η_e with different combinations of $q_1 = m_m/m$, $q_2 = k_c / s$ and $q_3 = Z_L$ for <i>DMTAP</i> prototype 1 (a) and 2 (b)	65
Figure 3.4 Variation of <i>TAP</i> and <i>DMTAP</i> efficiency η_e with the electric load Z_L for prototype 1	66
Figure 3.5 Optimization of electric power output E_L in a <i>DMTAP</i> : Objective function, variables and constraints.....	67
Figure 3.6 Maximum normalized electric power $E_{L, norm}$ for <i>DMTAP</i> harvester prototype 1 (a) and 2 (b) achieved using 3 different minimization based algorithms. Dotted line shows maximum power for the <i>TAP</i> harvester for comparison.....	69
Figure 3.7 Variation of <i>TAP</i> and <i>DMTAP</i> normalized Power $E_{L, norm}$ and Voltage V_{norm} with the electric load Z_L for prototype 1 (a, c) and prototype 2 (b, d)	70
Figure 3.8 Maximum magnification ratio x_{2m} / x_2 for <i>DMTAP</i> harvester prototype 1 (a) and 2 (b) achieved using 3 different minimization based algorithms.	72
Figure 3.9 Optimization of ΔT at $x_s / L = 0.2$ in a <i>DMTAP</i> : Objective function, variables and constraints	73
Figure 3.10 Minimum temperature difference required across a stack placed at 1/5 the resonator length to onset oscillations for <i>DMTAP</i> harvester prototype 1 (a) and 2 (b) achieved using 3 different minimization based. Horizontal line shows minimum temperature difference required for the <i>TAP</i> harvester for comparison.	75
Figure 3.11 Multi-objective optimization for a case with $W_i = 0.25$, $W_j = 0.75$ for <i>DMTAP</i> harvester prototype 1 (a) and 2 (b) achieved using 3 different minimization algorithms. Point with maximum η_e and lowest ΔT to satisfy the optimization weights is located at $f_{MO} = 1$	77
Figure 3.12 Pareto map for a <i>DMTAP</i> harvester prototype 1 (a) and 2 (b). Line starts at optimum point for objective 1: minimum ΔT and ends with optimum point for objective 2: maximum η_e . Points above the line are feasible and underneath it are not.	80

Figure 4.1 Schematic drawing of the standing wave thermoacoustic-piezoelectric harvester (<i>TAP</i>)	83
Figure 4.2 <i>TAP</i> harvester used in experiments	84
Figure 4.3 Temperature contours inside a section of the <i>TAP</i> resonator	86
Figure 4.4 Temperature distribution along the <i>TAP</i> resonator (<i>DeltaEC</i>).....	87
Figure 4.5 Theoretical prediction for pressure and volume velocity distribution inside the <i>TAP</i>	88
Figure 4.6 Experimental versus <i>DeltaEC</i> data for the pressure level across the resonator.....	89
Figure 4.7 Measurement of velocity distribution inside the <i>TAP</i> using 3D Stereoscopic Particle Image Velocimetry (PIV).....	90
Figure 4.8 Particle Image Velocimetry Correlation Maps.....	91
Figure 4.9 Flow distribution of the <i>TAP</i> at a section (a) adjacent to the piezo diaphragm and (b) at the end of the Helmholtz resonator	92
Figure 4.10 Flow distribution of the <i>TAP</i> at (a) the Helmholtz tube entrance and (b) inside the resonator	93
Figure 4.11 Distinct correlation peaks for different resonator locations	94
Figure 4.12 Schematic showing the numerical integration scheme used to obtain the volume velocity from the PIV data points	95
Figure 4.13 Comparison between experimental and theoretical values for the gas volume velocity along the <i>TAP</i> resonator	96
Figure 4.14 <i>PZT-5A</i> Piezo diaphragm (63 mm, .191 mm thick) from Piezo Systems, Inc.	97
Figure 4.15 Modal characteristics of the <i>PZT-5A</i> piezo diaphragm before and after tuning	98
Figure 4.16 Contours of transverse velocity of the tuned piezo diaphragm operating at its first natural mode (388 Hz)	99
Figure 4.17 Output voltage of the <i>TAP</i> harvester for different values of Z_L	100
Figure 4.18 (a) Output electric power density and (b) acoustic to electric energy conversion efficiency of the <i>TAP</i> harvester for different values of the load resistance (Z_L)	102
Figure 4.19 Digi-key 41 mm Buzzer Piezo-element	103
Figure 4.20 Schematic diagram of the experimental setup when used as (a) <i>DMTAP</i> -like system and (b) <i>TAP</i> -like system	104
Figure 4.21 Sine swept frequency response of voltage outputs V_1 and V_{2m} of the two piezo-elements ($k_c = 17,800 N/m$).....	106
Figure 4.22 Sine swept frequency response of voltage outputs V_1 , V_2 and V_{2m} of the two piezo-elements compared with the theoretical predictions ($k_c = 29,180 N/m$) ..	108
Figure 4.23 Sine swept frequency response of voltage outputs V_1 , V_2 and V_{2m} of the two piezo-elements ($k_c = 29,180 N/m$).....	110
Figure 4.24 Experimental Setup of the laser vibrometer used to scan the surface of the piezo-elements to obtain values for the transverse deflection	112
Figure 4.25 Contours of transverse velocity of <i>DMTAP</i> and <i>TAP</i> showing the first and second deflection modes	113
Figure 4.26 Schematic of the experimental <i>DMTAP</i> harvester prototype	114
Figure 4.27 Experimental prototype of a <i>DMTAP</i> harvester	114

Figure 4.28 Piezo-element on aluminum backing with tuning masses at symmetric locations	115
Figure 4.29 Piezo-element peak-to-peak voltages V_1 , V_2 and V_{2m} for different configurations of springs and mass ratios given in Table 4.3.....	118
Figure 4.30 Surface deflections of the piezo-membrane in the <i>TAP</i> experiments and the <i>DMTAP</i> experiments having a positive magnification ratio $V_{2m}/V_2 > 1$ (values in <i>mm/s</i>).....	120
Figure 4.31 Surface deflections of the piezo-membrane in the <i>TAP</i> experiments and the <i>DMTAP</i> experiments having a negative magnification ratio $V_{2m}/V_2 < 1$ (values in <i>mm/s</i>).....	121
Figure 4.32 Deflection against voltage of the piezo-membranes for all the performed <i>TAP</i> and <i>DMTAP</i> experiments.....	122
Figure 5.1 Electric circuit equivalent of a standing wave <i>TAP</i> harvester.....	129
Figure 5.2 Simplified electric circuit equivalent of a <i>TAP</i> harvester.....	131
Figure 5.3 Electric circuit equivalent of an open-ended standing wave thermoacoustic resonator.....	133
Figure 5.4 <i>LTSPICE</i> schematic of a <i>TAP</i> energy harvester	135
Figure 5.5 Close up on root locus plot for open-ended standing wave resonator.....	137
Figure 5.6 Stable, marginally stable and unstable pressure pulsations v_c in the open-ended standing wave resonator obtained by (a) <i>MATLAB</i> and (b) <i>LTSPICE</i> model	139
Figure 5.7 Frequency response of open-ended standing wave resonator at $\Delta T/T_a = 1.62$ (resonant frequency ~ 165 Hz).....	140
Figure 5.8 Comparison of v_c and I_l in an open-ended standing wave resonator obtained via <i>LTSPICE</i>	140
Figure 5.9 Close up on (a) positive and (b) negative sections of the imaginary axis in the root locus plot for <i>TAP</i> harvester	142
Figure 5.10 Stable, marginally stable and unstable pressure pulsations v_c in the <i>TAP</i> harvester obtained by (a) Root locus analysis and (b) <i>LTSPICE</i> model.....	143
Figure 5.11 Frequency response of the <i>TAP</i> system at $\Delta T/T_a = 1.71$ (resonant frequency ~ 453 Hz).....	143
Figure 5.12 Comparison of v_c and I_l in the <i>TAP</i> harvester obtained via <i>LTSPICE</i> ..	144
Figure 5.13 Temperature gradient in the stack of the <i>TAP</i> harvester at different power inputs. Horizontal lines show the predicted and the actual gradient required to onset oscillations.	147
Figure 5.14 (a) Temperature evolution inside the stack of the <i>TAP</i> harvester at 40 W of power input, and (b) temperature distribution along the resonator at steady state	148
Figure 6.1 (a) PZ-94 Piezo-speaker from ISL Products, (b) Schematic diagram of speaker's operation, and (c) Dimensions of the speaker (units in mm ± 0.5).....	153
Figure 6.2 Schematic drawing of a constant area <i>PDTAR</i>	154
Figure 6.3 Propagation of acoustic power inside a thermoacoustic refrigerator	159
Figure 6.4 Schematic of a variable area <i>PDTAR</i>	161
Figure 6.5 Deflection Characteristics for the PZ-94 Piezo-Speaker.....	164
Figure 6.6 Variation of (a) Pressure, (b) velocity and (c) acoustic power with time and frequency for the given <i>PDTAR</i>	165
Figure 6.7 (a) Acoustic power in the vicinity of the stack location at resonant freq. of 387 Hz, and (b) frequency response of acoustic power with and without the stack.	166

Figure 6.8 Optimal stack locations in a typical <i>PDTAR</i>	168
Figure 6.9 (a) Pressure and (b) velocity waveforms at 387 Hz in the <i>PDTAR</i> resonator for different wave attenuation factors	169
Figure 6.10 Frequency response of (a) Pressure and (b) velocity in the <i>PDTAR</i> resonator for different wave attenuation factors	170
Figure 6.11 <i>DeltaEC</i> schematic diagram for the <i>PDTAR</i>	171
Figure 6.12 Stack Section in the <i>DeltaEC</i> model of the <i>PDTAR</i>	172
Figure 6.13 <i>DeltaEC</i> 's temperature variation along the resonator of the <i>PDTAR</i>	172
Figure 6.14 Schematic of a <i>PDTAR</i> with a dynamic magnifier (<i>DMPDTAR</i>)	174
Figure 7.1 Experimental prototype of a <i>PDTAR</i>	178
Figure 7.2 (a) View of the stack before it is rolled up, and (b) top cross sectional view of the assembled stack	179
Figure 7.3 Experimental setup used to analyze the <i>PDTAR</i> performance	180
Figure 7.4 Comparison between theoretical and experimental data of the pressure at the end of the resonator $P(L)$ for the given <i>PDTAR</i> prototype	181
Figure 7.5 Evolution of the temperature difference across the stack ends during the <i>PDTAR</i> operation (ΔT at 7 minutes is almost 7 K)	183
Figure 7.6 PZ-94 Piezo-speaker with and without the plastic-diaphragm	185
Figure 7.7 End pressure $P(L)$ for a <i>PDTAR</i> with a PZ-94 speaker and a <i>PDTAR</i> with the speaker without the plastic diaphragm	186
Figure 7.8 End pressure $P(L)$ for a <i>PDTAR</i> with a PZ-94 speaker and a <i>PDTAR</i> with a PZ-94 speaker with an aluminum plate on top	187
Figure 7.9 End pressure $P(L)$ for a <i>PDTAR</i> with a PZ-94 speaker and a <i>PDTAR</i> with a PZ-94 speaker with an aluminum plate on top with glue in the center to attach the magnifier spring to it	187
Figure 7.10 Experimental prototype of a <i>PDTAR</i> with a dynamic magnifier	188
Figure 7.11 End pressure $P(L)$ for the conventional <i>PDTAR</i> and a <i>PDTAR</i> with Magnifier #1	190
Figure 7.12 End pressure $P(L)$ for the conventional <i>PDTAR</i> and a <i>PDTAR</i> with Magnifier #1	190
Figure 7.13 Steady-state temperature difference of <i>PDTAR</i> with Magnifier#1 (ΔT is about 10 K)	191
Figure 7.14 Temperature development of hot and cold stack ends for the <i>PDTAR</i> and a <i>PDTAR</i> with Magnifier #1	192
Figure 7.15 Steady state temperature difference of a <i>PDTRAR</i> with (a) no stack (0 K), (b) Magnifier#2 (4 K), (c) no magnifier (7 K) and (d) Magnifier #1 (10 K)	193
Figure 7.16 Volume velocity at the beginning of the resonator ($x = 0$) for the <i>PDTAR</i> and a <i>PDTAR</i> with Magnifier #1 as computed by the mathematical model	194
Figure 7.17 End pressure $P(L)$ for the conventional <i>PDTAR</i> and a <i>PDTAR</i> with Magnifier #1 as computed by the mathematical model	195
Figure 7.18 Comparison between experimental and theoretical data for the end pressure $P(L)$ for the conventional <i>PDTAR</i> and a <i>PDTAR</i> with Magnifier #1	195
Figure 8.1 Open-ended small-scale experimental thermoacoustic engine without an energy harvesting element [54]	201

Figure 8.2 (a) A solar-driven standing wave thermoacoustic engine courtesy of Penn State University [55] and (b) a schematic of a solar-powered traveling wave thermoacoustic engine courtesy of the Chinese Academy of Science [56]	202
Figure 8.3 (a) A Schematic of a diaphragm driven resonator excited by a piezoelectric bimorph and (b) a photo of the experimental prototype of the resonator in a study of gas-filled axisymmetric acoustic area-varying resonators by El-Sabbagh [57].....	203
Figure A.1.0.1 Screenshot of <i>DeltaEC</i> interface of the beginning segment of a <i>TAP</i> model.....	207
Figure A.1.0.2 Screenshot of <i>DeltaEC</i> interface of the stack and hot heat exchanger of a <i>TAP</i> model.....	208
Figure A.1.0.3 Schematic of the developed <i>DeltaEC</i> model for a <i>TAP</i>	209
Figure A.1.0.4 <i>PZT-5A</i> Piezo diaphragm (63 mm, .191 mm thick) from Piezo Systems, Inc.	211
Figure A.1.0.5 Schematic of the <i>PZT-5A</i> Piezo diaphragm supported on aluminum backing.....	211
Figure A.1.0.6 <i>ANSYS</i> Finite element model of the piezo diaphragm tuning configuration.....	212
Figure A.1.0.7 <i>ANSYS</i> FEM model: First mode of Piezo diaphragm before tuning – 313.8 <i>Hz</i>	212
Figure A.1.0.8 <i>ANSYS</i> FEM model: First mode of Piezo diaphragm after tuning (supported on aluminum backing with added center weight) – 390.4 <i>Hz</i>	213
Figure A.1.0.9 Flow chart of the ERA procedure.....	216
Figure A.1.0.10 Using ERA to solve the Inverse Problem.....	217
Figure A.1.0.11 Unit impulse inputs applied to the piezo diaphragm in the FEM to obtain the transfer functions (a) $T_{12}(i\omega)$, $T_{22}(i\omega)$ and (b) $T_{11}(i\omega)$, $T_{21}(i\omega)$	218
Figure A.1.0.12 Time response of the diaphragm center point deflection $u_{center}(t)$ and charge $q(t)$ to a unit voltage impulse while maintaining a zero differential pressure.....	220
Figure A.1.0.13 Time response of the diaphragm center point deflection $u_{center}(t)$ and charge $q(t)$ to a unit pressure impulse while maintaining a zero voltage.....	221
Figure A.1.0.14 Frequency response of the magnitude of the transfer functions $T_{11}(i\omega)$, $T_{12}(i\omega)$, $T_{21}(i\omega)$ and $T_{22}(i\omega)$	223
Figure A.1.0.15 Schematic of the DUCER segment used to model the piezo-element in <i>DeltaEC</i>	225
Figure A.1.0.16 Modeling a thermoacoustic-piezoelectric harvester (<i>TAP</i>) using <i>DeltaEC</i>	225
Figure A.1.0.17 Piezo-speaker (ISL Products PZ-94 Harsh Environment Speaker) [44].....	227
Figure A.1.0.18 Setup used to measure Z_m and τ of the piezo speaker	228
Figure A.1.0.19 Schematic of the developed <i>DeltaEC</i> model for a piezo-driven thermoacoustic refrigerator.....	229

Nomenclature

A_p	Cross sectional area of piezo diaphragm
A_x	Cross sectional area of resonator at distance x from nose
A_1, A_2	Wave amplitude constants
B_ω	Bandwidth of frequencies
b	Damping coefficient of piezo diaphragm
C_{st}	Stack Compliance
C_p	Piezoelectric blocked (clamped) capacitance
\overline{C}	Controllability matrix
c	Speed of sound in working gas
c_k	Stack compliance per unit length
c_m	Damping coefficient of magnifier mass
c_p	Isobaric specific heat of working gas
c_{33}^E	Short circuit Young's Modulus in poling direction
D_3	Electrical displacement (charge per unit area or electric flux density)
d_{33}	Piezoelectric strain coefficient measured in poling direction due to an electric field applied in poling direction
E_3	Electric field intensity (voltage across element per unit voltage)
\dot{E}_{res}	Acoustic power losses along resonator walls
\dot{E}_L	Electric power dissipated in electric load
\dot{E}_T	Acoustic power radiated to resonator end
f_k	Rott function of gas thermal penetration depth
$f_{res,1}$	First resonance mode frequency
f_v	Rott function of gas viscous penetration depth
G	Velocity gain in stack/regenerator
H_{ab}	Hankel matrix
I	Electric current

k	Wave number
k_c	Stiffness of coupling spring
k_m	Stiffness of magnifier mass
k_s	Ratio of tube to piezo-element cross sectional area
k_{33}	Piezo electromechanical coupling factor
K_c	Thermal conductivity
L	Resonator length
l	Half the plate thickness
m	Effective vibrating mass of piezo diaphragm
m_m	Magnifier mass
\bar{O}	Observability matrix
P	Spatial component of working gas pressure
P_{ac}	Acoustic power supplied by speaker to resonator
ΔP_p	Pressure difference across piezo diaphragm/speaker
p	Pressure of working gas
Q	Volume velocity of working gas
Q_o	Volume flow rate supplied by speaker
Q_x	Volume velocity of gas particles at distance x from resonator nose
\dot{Q}_{in}	Heat input rate to hot heat exchanger
q	Electric charge
R	Resonator radius
R_{st}	Stack Resistance
R_1, R_2, R_3	Wave amplitude constants
r_1, r_3	Radii of beginning and end segments of thermoacoustic refrigerators
r_2	Half of stack grid length of the thermoacoustic refrigerator
r_k	Stack thermal relaxation per unit length
S_1, S_2, S_3	Cross sectional area of thermoacoustic refrigerator segments
s	Stiffness of piezo diaphragm
s_g	Entropy of working gas
S_3	Piezoelectric strain

T	Temperature of working gas
T_3	Piezoelectric stress
$T(i\omega)$	Electro-acoustic coupling 2x2 matrix of piezo-element
$T'(i\omega)$	Modified electro-acoustic coupling 2x2 matrix of piezo-element
$T_{DE}(i\omega)$	Electro-acoustic coupling 2x2 matrix of piezo-element used by <i>DeltaEC</i>
ΔT	Temperature difference across stack
∇T	Temperature gradient across stack
t	Time
t_p	Thickness of piezo diaphragm
U	Spatial component of working gas x -component of velocity
u	x -component of velocity of working gas
V	Electric Voltage
V_{rms}	Root mean square voltage
ΔVol	Volumetric displacement of working gas adjacent to piezo diaphragm
v	Total velocity of working gas
\dot{W}_{st}	Acoustic energy produced/absorbed in stack
x	Distance from resonator nose in direction of wave propagation
x_s	Stack center position
x_1	Displacement of magnifier mass of a <i>DMTAP</i>
x_2	Displacement of piezo diaphragm of a <i>TAP</i>
x_{2m}	Displacement of piezo diaphragm of a <i>DMTAP</i>
Δx	Stack length
y	Direction perpendicular to wave propagation
y_o	Half the plate spacing
Z_e	Electric impedance of piezo diaphragm
Z_L	Impedance of electric load
Z_m	Mechanical impedance of piezo diaphragm
Z_R	Acoustic impedance at right end of resonator

Greek Symbols

α	Wave number loss/attenuation factor
β	Gas expansion coefficient
Γ	Normalized temperature gradient across stack
γ	Ratio of isobaric to isochoric specific heats of the working gas
ε_s	Plate heat capacity ratio
ε_{33}^T	Permittivity (dielectric constant) in poling direction at constant stress
η_e	Efficiency of energy conversion from acoustic to electric energy
η_o	Overall efficiency of thermoacoustic device
δ_k	Thermal penetration depth (boundary layer thickness)
δ_v	Viscous Penetration depth (boundary layer thickness)
κ	Function of working gas thermo-physical properties
Λ_n	Diagonal matrix of the system's n singular values
λ	Wavelength
μ	Viscosity of working gas
Π	Effective circumference of plate perpendicular to heat flow in stack
ρ	Density of working gas
σ	Prandtl number
τ, τ'	Cross correlation (coupling) variables of piezo diaphragm
τ_{TAP}	Periodic time of oscillation
Ψ	Reciprocal coupling factor of piezo
ω	Angular oscillation frequency

Subscripts

<i>center</i>	center
<i>crit</i>	critical
<i>exp</i>	experimental
<i>m</i>	mean
<i>max</i>	maximum
<i>norm</i>	normalized

<i>P</i>	Piezo
<i>reg</i>	Regenerator
<i>R</i>	Resonator
<i>st</i>	Stack

Acronyms

<i>BTL</i>	Bell Telephone Laboratories
<i>CCCC</i>	Current Dependent Current Source
<i>COP</i>	Coefficient of Performance
<i>DeltaEC</i>	Design Environment for Low Amplitude thermoacoustic Energy Conversion
<i>DMTAP</i>	Dynamically Magnified Thermoacoustic-Piezoelectric ‘engine’
<i>DOF</i>	Degree of Freedom
<i>ERA</i>	Element Realization Algorithm
<i>LANL</i>	Los Alamos National Laboratory
<i>PDTAR</i>	Piezo-driven Thermoacoustic Refrigerator
<i>PIV</i>	Particle Image Velocimetry
<i>SETAC</i>	Shipboard Electronics Thermoacoustic Chiller
<i>STAR</i>	Space Thermoacoustic Refrigerator
<i>TADTAR</i>	Thermoacoustically Driven Thermoacoustic Refrigerator
<i>TAP</i>	Thermoacoustic-Piezoelectric ‘engine’

Chapter 1

1. Introduction

1.1. Literature Survey

1.1.1. Historical Development

Thermoacoustics is an emerging technology that uses the phenomenon of interaction of acoustic fields with adjacent solid boundaries to develop engines and refrigerators. In its current state, thermoacoustic systems generally take the form of acoustic cavities, referred to as resonators, with a solid porous body, referred to as the stack, located between a heat source and sink, referred to as heat exchangers.

There exists two main opposite thermoacoustic effects. The first is called “*the direct effect*”, and involves the development of self-sustained pressure oscillations from an input temperature gradient generated across the two ends of a solid boundary. Feeding off this effect, are the thermoacoustic engines, where energy is converted from a thermal input into an acoustic energy output. Engines of this type can be thermally driven by any source of heat, appealingly waste heat energy from combustion [1, 2] or concentrated solar power [3, 4]. The induced acoustic energy can be converted to electricity by means of conventional electromagnetic transducers or

by smart piezo-elements [5, 6], thus presenting a more compact, reliable, and efficient class of energy harvesters.

The second thermoacoustic effect, known as the “*reverse effect*”, is observed when an acoustic input energy from a driver source (e.g. speaker) is used to generate a temperature gradient across the two ends of the stack. Devices based on the reverse effect are called thermoacoustic refrigerators and work by converting acoustic energy into a thermal output that can be used to create a cooling effect.

The development of the first concepts of thermoacoustic engines can be credited to the Bell Telephone Laboratories (BTL) whereby heat energy was converted into acoustic pressure waves and then into electricity by using reversed acoustical speakers (Hartley [7] and Marrison [8]). Although the BTL concepts were attractive because of their simplicity and reliability, their conversion efficiency was relatively low ($<10\%$). Furthermore, as reported by Ceperley [9], the pressure oscillations were relatively weak. These critical performance metrics were enhanced considerably by the introduction of porous solid media into the resonator tubes by Feldman in 1966 [10]. The porous media enabled the existence of large temperature gradients which in turn resulted in the generation of pressure oscillations that are capable of performing useful work. Such a breakthrough concept by Feldman is considered the major milestone in the development of working prototypes of a class of thermoacoustic engines which are commonly known as *standing wave thermoacoustic engines*. An example of this class of engines is shown in Figure 1.1.

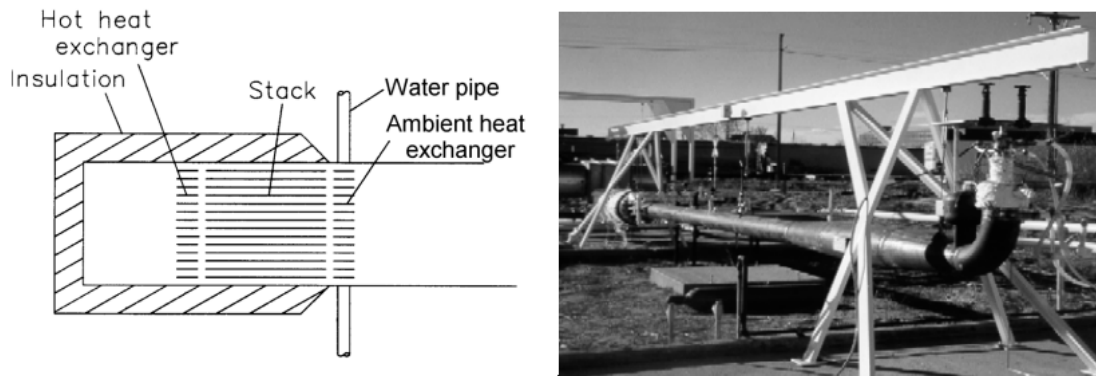


Figure 1.1 Schematic and photo of a powerful standing wave thermoacoustic engine (background) at Cryenco in Denver, CO to supply acoustic power to an orifice pulse tube refrigerator (foreground).

A radically different concept for achieving higher efficiencies is introduced by Ceperley in 1979 [9] and 1982 [11] whereby the produced acoustic waves were forced to undergo phasing similar to the inherently reversible and thus highly efficient Stirling engine. The resulting class of thermoacoustic engines is called the *traveling wave thermoacoustic engines*. Despite of their potential, the development of this class of engines has always been hampered by the need for seals which are capable of withstanding high pressure and many cycles of operation without failure. Recent advances in the Stirling technology have included free-piston machines and the use of linear alternators. Unfortunately, these advances did not completely eliminate the unreliability and high cost of sliding seals. The Fluidyne engine by West [12] in 1983 was the first attempt to totally eliminate sliding seals, by using U-tube liquid pistons. Unfortunately, this solution has limited the operation to low frequencies by virtue of the high mass of the liquid pistons. Ceperley [9, 11] has repeatedly attempted to totally eliminate the sliding seals but his experimental engines were not able to

amplify the acoustic power. Much later, Yazaki *et al.* [13] first demonstrated such an engine, however low efficiencies were observed because of unanticipated heat and viscous losses. However, Backhaus and Swift [14] accounted for these heat losses and devised an acoustical method to counteract the viscous losses. This resulted in a high efficiency hybrid engine with efficiency of conversion of the heat input into acoustic power reaching about 30%. A smaller version of that engine was provided with a pair of linear alternators in order to produce 57 watts of electricity at up to 17.8% thermal to electric efficiency (Petach *et al.*, [15]). An example of this class of engines is shown in Figure 1.2.

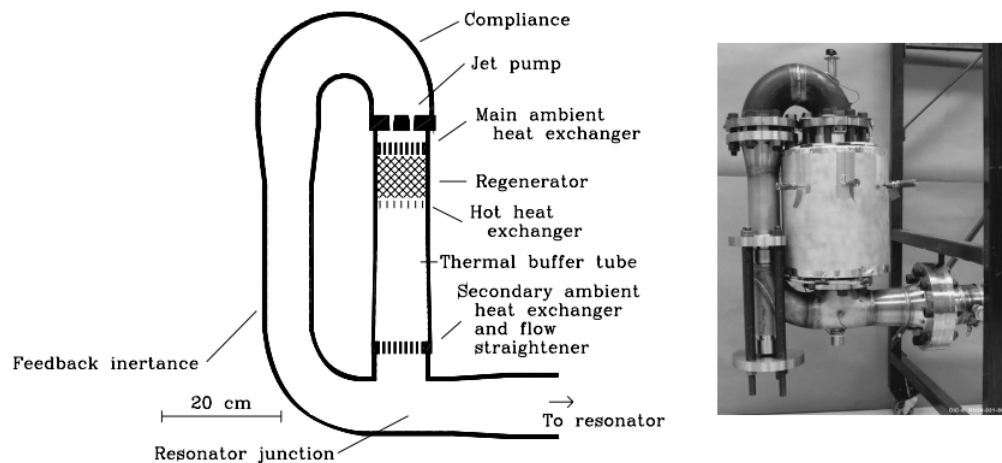


Figure 1.2 A traveling wave thermoacoustic-stirling hybrid engine, producing 1 kW of power at an efficiency of ~30% with no moving parts [16]

As for the development of the thermoacoustic refrigerators, the first known working prototype was built by Hofler [17] who was a member of Wheatley's group. Soon afterward, a thermoacoustic refrigerator known as the beer cooler was also built at LANL [18]. This refrigerator used a heat driven prime mover instead of a speaker to

drive it. At the Naval Postgraduate School, an extension of Hofler's refrigerator design was built to be launched on the Space Shuttle Discovery. This refrigerator is known as the Space Thermoacoustic Refrigerator (*STAR*) [19]. A thermoacoustically driven thermoacoustic refrigerator (*TADTAR*) was also built at the Naval Postgraduate School by Adeff and Hofler [3]. This refrigerator used a lens to focus light from the sun to create heat for running a thermoacoustic engine. The output from this engine was used, in turn, to drive the thermoacoustic refrigerator, completely eliminating all moving parts. With 100 Watts of input energy from the sun, 2.5 Watts of cooling power was obtained. The Shipboard Electronics Thermoacoustic Chiller (*SETAC*) was built to cool electronics aboard the U.S.S. Deyo [20]. *SETAC* was able to operate at a maximum coefficient of performance (*COP*) of 21% relative to Carnot. However, when operated at the power necessary to cool the racks of electronics it was designed for, *SETAC* was only able to obtain a *COP* of 8% relative to Carnot. One of the biggest thermoacoustic refrigerators ever built is the *TRITON*. It is named because it was designed to have the cooling power of a three-ton air conditioner. Though the performance characteristics of the *TRITON* are not well documented, information about it can be found on Penn State's website [21]. Tijani performed a number of studies on the effects of varying individual components of thermoacoustic refrigerators [22, 23]. He built a refrigerator based on the results of his research with a *COP* of 11% when helium was used as the working fluid. A qualitative thermoacoustic refrigerator designed to be a demonstration unit was built by Russel [24]. This refrigerator is low cost and easy to make. However, it was very

inefficient because it was designed to demonstrate the concept rather than to operate as a practical and efficient unit.

Ben and Jerry's ice cream funded a project at Penn State to make a clean thermoacoustic refrigerator that would cool their ice cream freezers [21]. This refrigerator has a cooling capacity of 119 W and an overall *COP* of 19 % of Carnot's. Prototypes of this refrigerator, as shown in Figure 1.3, are currently being used by Ben and Jerry's in the Boston and Washington, D.C. areas, and if the prototypes are successful this may become the first commercially produced line of thermoacoustic refrigerators as Ben and Jerry's would like to switch all their stores over to the clean technology.

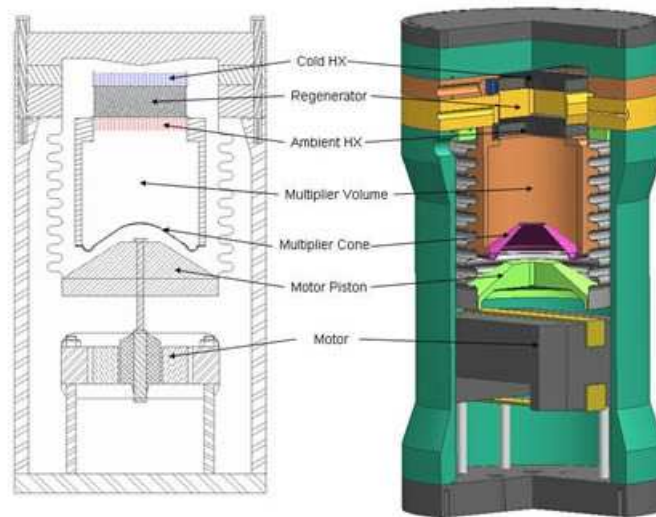


Figure 1.3 An ice cream cabinet powered by a thermoacoustic refrigerator
(The Ben & Jerry's Project, 2005) [21]

1.1.2. Integration with Piezo-transducers

Using piezo-elements to harvest energy from thermoacoustic engines is promising for numerous reasons. Piezo transducers are light weight devices that are

particularly suitable for operating efficiently at high oscillation frequencies which, in turn, will result in compact acoustic resonators and engines. On the contrary, the conventionally used electromagnetic alternators are not only heavy but are also limited to low frequency operations.

The technology of using piezoelectric alternators dates back to 1974, when Martini *et al.* [25] utilized a piezoelectric stack to convert the acoustic oscillations of a Stirling engine into electric energy. The high mechanical impedance of the stack has limited its suitability for practical thermoacoustic engines. Since then, extensive amount of efforts have been exerted to employ various configurations of either piezoelectric alternators or actuators in thermoacoustic engines or refrigerators. Examples of these efforts include the work of Keolian and Bastyr in 2006 [26], Symko *et al.* in 2004 [27], and 2007 [28], and Matveev *et al.* in 2007 [5], whose work in particular is used in many areas of this study for comparative purposes. In the work of Keolian and Bastyr, the emphasis was placed on the development of large scale thermoacoustic engines and the proposed system included heavy moving masses communicating with arrays of piezoelectric alternators. This is contrast of the work of Symko *et al.* and Matveev *et al.*, where focus was on the development of small engines for thermal management in microelectronics. Note that the work of Symko *et al.* was primarily experimental in nature whereas the work of Matveev *et al.* was limited to the theoretical analysis.

In the present work, focus is placed on developing a comprehensive theoretical and experimental study of thermoacoustic-piezoelectric harvesters with Helmholtz-like resonators. Such a class of harvesters is originally proposed by Anderson and Symko in 2009 [29] for standing wave engines and Sun *et al.* in 2009 [30] for traveling wave engines because of its attractive attributes. Namely, these engines were shown to generate higher pressures than conventional engines with straight resonators due to the positive feedback action produced from the Helmholtz cavities. This action results in lowering the threshold for generating sustained acoustic oscillations. Furthermore, the large diameter cavity enables the use of a large piezoelectric alternator which, in turn, is capable of harnessing more of the acoustic power. Note that neither of the theoretical work of Anderson and Symko or the theoretical and experimental work of Sun *et al.* 2009 has considered the use of piezoelectric alternators with the proposed resonator geometry.

As for the refrigerators, nearly all of the thermoacoustic refrigerators in existence are driven by electromagnetic loud speakers. However, the performance of electromagnetic loudspeakers is greatly diminished at high frequencies. For this reason, piezoelectric drivers have been used for high frequency applications of thermoacoustic refrigeration [31]. Avoiding electromagnetic drivers may also be required for applications involving magnetic sensitive equipment. Unlike their electromagnetically driven counterparts, numerical and experimental models for piezo-driven thermoacoustic refrigerators are lacking.

1.2. Background

1.2.1. Standing Wave Thermoacoustic Engines

The simplest class of thermoacoustic prime movers is the *standing wave engine*. Modeling, operation and optimization of this class of engines constitutes a dominant portion of this dissertation. Known by its simple design, lack of moving parts and its reliability on environmentally benign fluids, a standing wave thermoacoustic engine stands as a promising candidate in the field of heat engines and energy harvesting. Being in the research and development phase, the development and operation of standing wave thermoacoustic engines have not yet reached technical maturity. Energy conversion efficiencies obtained to date remain relatively lower than their conventional counterparts [32].

The operation of standing wave thermoacoustic engines is based on acoustically excited parcels of working fluid carrying out an approximated thermodynamic cycle that lacks a piston and hardly has any moving parts. This is achieved by exciting the working fluid in the presence of a temperature gradient. As suggested by Figure 1.4, an acoustic wave travels up the gradient while the working fluid, usually gas, particles are in intimate thermal contact with the adjacent solid surfaces. While a parcel of gas is at its mean position but moving to higher temperatures, it is being relatively compressed, with a consequent rise in temperature. If the temperature rise is not sufficient to counteract the temperature increase in the adjacent surfaces, as the particle is displaced, heat is transferred to the gas during this

compression phase. Conversely, heat is lost during the rarefaction process and energy is thus consecutively being added to the acoustic wave.

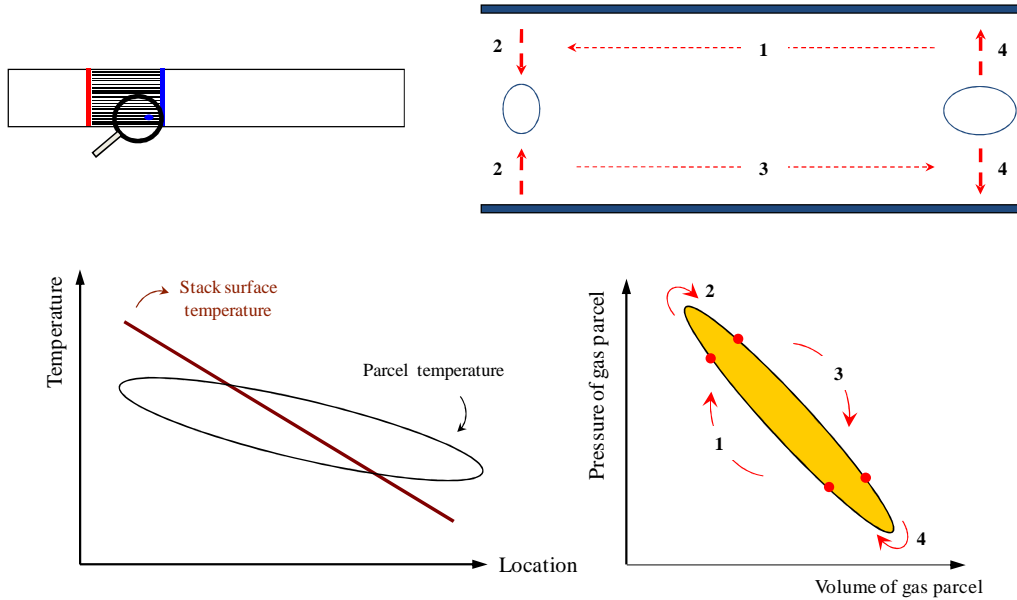


Figure 1.4 Standing wave thermoacoustic engine in operation

Resonators of standing wave engines are usually of a $\lambda/4$ (open end) to $\lambda/2$ (rigid end) length, where λ is the wavelength of the self-sustained oscillations. In its simplest forms, the stack located inside the engine resonator is a porous body as shown in Figure 1.5. The stack spacing is of the order of the thermal boundary layer thickness δ_k , through which acoustic oscillations with standing wave time phasing occur. This explains the name of this class of engines. δ_k , sometimes also referred to as the thermal penetration depth, is given by,

$$\delta_k = \sqrt{\frac{2K_c}{\omega\rho_m c_p}} \quad (1.1)$$

where K_c , ω , ρ_m and c_p are the thermal conductivity, oscillation frequency, mean density and the isobaric specific heat of the working gas respectively. The stack spacing gaps are thus required to be small to ensure adequate thermal contact and heat transfer between the gas and the solid boundary. However, the smaller this gap gets, the thicker the corresponding viscous penetration depth δ_v becomes, raising the possibility of more energy dissipation due to viscous losses, slower gas particles and less acoustic power outcome eventually. The viscous penetration depth δ_v is given by,

$$\delta_v = \sqrt{\frac{2\mu}{\rho_m \omega}} \quad (1.2)$$

with μ being the gas viscosity. This is typically being avoided by careful selection of working fluids that have an adequate ratio of thermal to viscous boundary layer thicknesses. The square of this ratio, is referred to as the Prandtl number σ , which is given by $\sigma = c_p \mu / K_c$. Most gases have a Prandtl number in the vicinity of unity, thus making them more suitable for these applications. Working gases such as atmospheric air, helium, helium-neon and helium-argon mixtures are common in thermoacoustic systems.

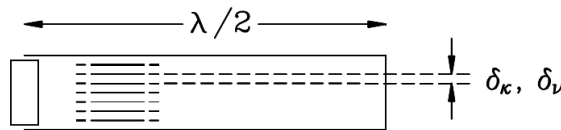


Figure 1.5 Stack spacing magnitude relative to the thermal and viscous boundary layers [33]

For the gas in the stack to produce work, the heat exchangers must maintain a sufficiently large temperature gradient across the stack ends, above a specific critical value, referred to as the critical temperature gradient ∇T_{crit} given by [18],

$$\nabla T_{crit} = \frac{T_m \beta \omega P(x_s)}{\rho_m c_p U(x_s)} \quad (1.3)$$

where T_m and β are the gas mean temperature and expansion coefficient. $P(x_s)$ and $U(x_s)$ are the pressure and velocity magnitudes at the stack center location where the velocity of the gas along the stack's temperature gradient is 90° out of phase with the oscillating pressure.

1.2.2. Thermoacoustic Refrigerators

The main purpose of thermoacoustic refrigerators is to remove heat from a low temperature and reject it to a higher temperature, while necessarily consuming work. With the help of a source (e.g. a speaker) to drive an acoustic wave in the resonator, heat is pumped and acoustic power is being absorbed in the stack. Emphasis is placed here on simple standing wave thermoacoustic refrigerators. One other class of refrigerators is called the Orifice pulse-tube refrigerator and is more similar in terms of operation to traveling wave engines but is, however, beyond the scope of this work.

When a working gas parcel is at one of the stack ends, its pressure is high, and when it approaches the other end, its pressure becomes low as shown in Figure 1.6. Adiabatic temperature oscillations accompany the pressure oscillations, so the parcel's temperature tends to rise adiabatically as it moves towards the high pressure region and vice versa. However, the plate's temperature gradient is relatively small, so when the parcel is at the low pressure/temperature region, it is cooler than the surrounding plates and can absorb heat from the plates. At the opposite end, the parcel becomes warmer than the solid boundary surrounding it, thus it rejects heat to the plates. Hence, heat is pumped up the temperature gradient. The combined action of all the gas parcels in the stack in effect removes heat from the cold end of the stack and rejects it at the other.

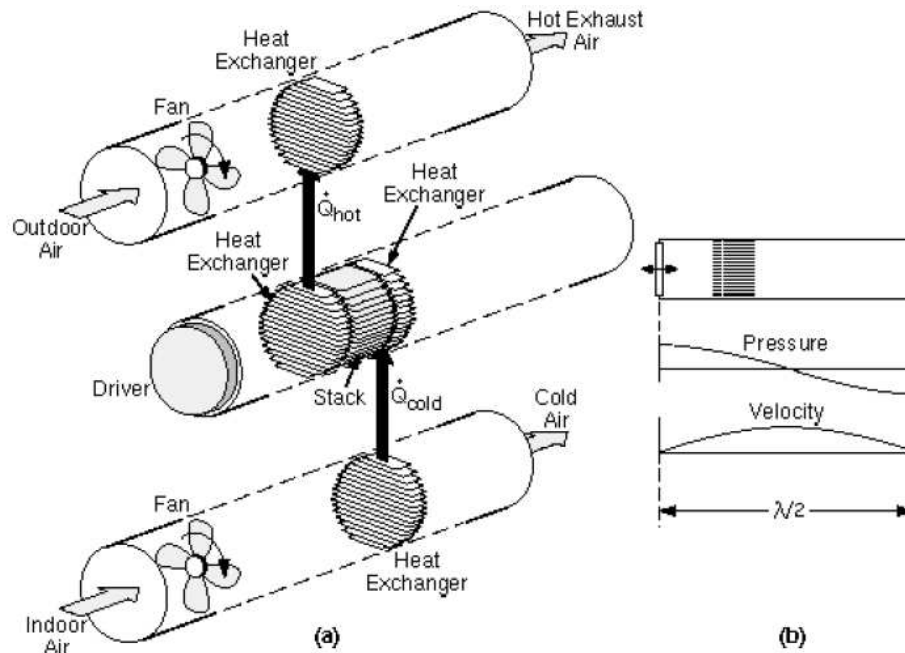


Figure 1.6 Schematic of a typical half-wavelength standing wave thermoacoustic refrigerator [33]

It should be noted here that a thermal contact between the parcel and the adjacent plates must be neither too weak nor too strong. If the thermal contact is too weak, no heat would be transferred between the parcel and the plates and no heat pumping would take place. For a too strong contact, the parcel's temperature would trace an oscillating line exactly on top of the solid's local temperature, which would shift the time phasing of the heat transfer by roughly 90° . With such phasing, the net heat transfer from the parcel to any particular location on the stack would be zero, and again no heat pumping would occur. Successful operation is therefore dependent upon the proper design of the stack spacing to be roughly a few δ_k .

1.3. Objective and Scope of Thesis

The present thesis aims at presenting a complete analysis of thermoacoustic engines and refrigerators integrated with piezoelectric elements. Design, modeling, construction and operation of prototypes of these thermoacoustic-piezoelectric energy harvesters as well as the piezo-driven thermoacoustic refrigerators will be carried out. Though attempts of modeling these classes of systems is available in literature with brief experimentation in some, very little, if any, has been suggested as means of optimizing these systems and enhancing their performance. In terms of numerical modeling, this work also intends to present methods of integrating the developed mathematical models with the commonly used thermoacoustic modeling software *DeltaEC* [34], while incorporating the characteristics of the piezo-elements in the resonators of thermoacoustic harvesters and the characteristics of piezo-speakers in thermoacoustic refrigerators.

The performance of prototypes of thermoacoustic-piezoelectric energy harvesters and refrigerators will be presented in the experimental section of this work. Measurements of key performance characteristics including but not limited to acoustic pressure and velocity waveforms, power flux and temperature distributions are carried out. Comparisons with numerical predictions are shown validating the findings of the developed theoretical models.

The major contribution of this thesis lies in introducing a novel approach for enhancing the performance of thermoacoustic systems integrated with piezoelectricity, using the concept of dynamic magnification. Literature lacks a solid proposal of methods to improve performance of engines as energy harvesters, and of refrigerators as cooling devices, specifically in terms of the energy conversion efficiencies.

The overall efficiency of the thermoacoustic-piezoelectric energy is the product of the thermal to acoustic and acoustic to electric energy conversion efficiencies. In that sense, techniques adapted to enhance the induced acoustic energy or the power output of the piezo-transducer should both reflect a better overall efficiency in order to improve the performance of such a class of systems. Efforts attempted to achieve better acoustic power from the stack are mainly concerned with optimizing the stack parameters such as the material, porosity and spacing, and using different stack

geometry such as parallel plates, pin arrays and circular pores and/or changing the tube geometry and aspect ratio.

In previous efforts, impedance matching between the transducer and the acoustic tube is seen as a way to maximize the output power from the engine [5]. This, however, results in a system that optimally performs at specific frequencies, exclusively governed by the tube dimensions and the transducer parameters in order to satisfy the impedance matching condition. For thermoacoustic-piezoelectric harvesters, the innovation introduced here is to couple the piezo-element with a mechanical system, as simple as a spring-mass system. This coupling can produce considerable improvement of the performance of these devices if adequately tuned.

The concept of dynamic magnification of output energy through coupling of elastic structures is motivated by earlier investigations such as Cornwell *et al.* [35], Ma *et al.* [36] and Aldraihem and Baz [37]. Proper tailoring of the parameters of such a system can help increase the strain experienced by the piezo-element. This in turn will enhance the harnessed piezoelectric power from the input acoustic energy. Variation of the parameters of the magnifier can also help maximize the harvested energy over a broader frequency range and hence improve the operating bandwidth of the overall system.

In this study, the use of such technique is extended and employed in thermoacoustic devices with proper account of the coupling between the thermal,

acoustical, mechanical, and electrical fields. The proposed idea can be extended to optimize more performance metrics other than the peak power output such as the total integrated power over specific frequency ranges. The idea could also be extended to piezo-driven thermoacoustic refrigerators to amplify the source flow provided to the resonator tubes from the speaker, as is seen in the later chapters of this thesis.

Therefore, this dissertation is presented in eight chapters. In Chapter 1, a brief introduction of thermoacoustic engines and refrigerators was presented. In Chapter 2, the mathematical modeling is presented for standing wave thermoacoustic systems coupled directly with piezoelectric elements or via a dynamic magnification system. Chapter 3 introduces a detailed optimization scheme of the proposed class of harvesters that can be tailored to satisfy different design objectives. Chapter 4 presents the experimental portion of the study related to thermoacoustic-piezoelectric energy harvesters, with and without dynamic magnifiers. Chapter 5 provides a stability analysis of this class of harvesters and a look into the transient operation characteristics that lead up to the onset of sound oscillations. Chapter 6 presents the mathematical modeling of standing wave thermoacoustic refrigerators which are driven directly by piezoelectric transducers or via a dynamic magnification system. In Chapter 7, experimental validations of the models developed in Chapters 6 are presented. Finally, possible directions and future extensions of the present work as well as some concluding remarks are outlined in Chapter 8.

Chapter 2

2. Thermoacoustic-piezoelectric Harvesters: Modeling and Theoretical Analysis

2.1. Introduction

In this chapter, the main equations governing the pressure and velocity propagation of a working gas inside thermoacoustic resonators are presented. Using the appropriate boundary conditions and impedance matching, the resonator is integrated with a piezo-element for energy harvesting purposes. With a porous stack placed inside the resonator, the system at hand is referred to as a standing wave thermoacoustic-piezoelectric (*TAP*) harvester.

The model is extended to implement the *TAP* with a dynamic magnifier. The adopted system is referred to as a **dynamically magnified** standing wave thermoacoustic-piezoelectric (*DMTAP*) harvester. A comprehensive analysis of the *DMTAP* is presented and a thorough comparison is made between the performance of both devices in terms of waveforms, power output and energy conversion efficiency.

At the end of this chapter, a simplified thermal analysis is carried out to show the effect of both the *TAP* and the *DMTAP* on the critical temperature gradient required to onset self-sustained oscillations. Equations governing the heat transfer between the

working gas particles and adjacent boundaries are given as a function of the different geometrical and thermo-physical parameters of the stack and gas respectively. Comments are made with reference to areas of design interest such as optimal stack placement in these types of energy harvesters.

2.2. Waveforms in Acoustic Resonators

A schematic of a constant cross section standing wave thermoacoustic-piezoelectric harvester (TAP) is shown in Figure 2.1.

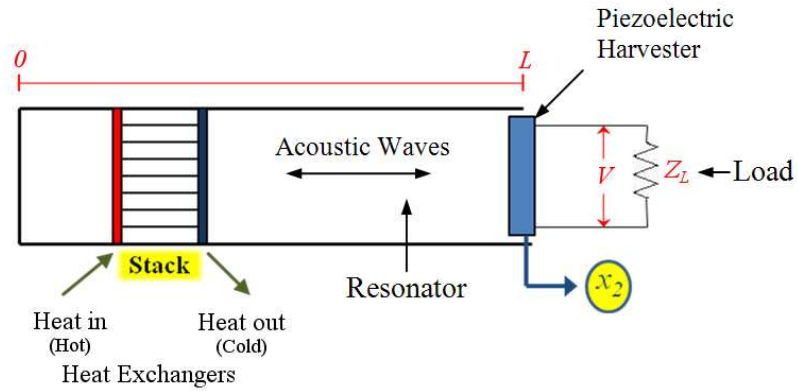


Figure 2.1 Schematic of a standing wave thermoacoustic-piezoelectric harvester (TAP)

The propagation of pressure and velocity in the harvester's resonator is both time- and space-dependent. Neglecting the effect of the stack on the waveforms and assuming negligible thermal and viscous losses, plane linear acoustic waves in the propagation direction x are considered. The pressure $p(x,t)$ and the x -component of velocity $u(x,t)$ of the working gas can be written as,

$$p(x,t) = [A_1 e^{-ikx} + A_2 e^{ikx}] e^{i\omega t} \quad (2.1)$$

and,

$$u(x,t) = \frac{1}{\rho c} [A_1 e^{-ikx} - A_2 e^{ikx}] e^{i\omega t} \quad (2.2)$$

where A_1 and A_2 are amplitude constants that can be determined from the boundary conditions, ρ and c are the density and speed of sound in the working gas respectively, ω represents the angular frequency and k is the complex wave number given by,

$$k = \left(\frac{\omega}{c} \right) + \alpha i \quad (2.3)$$

with the imaginary component α denoting a loss factor. The pressure and velocity expressions in equations (2.1) and (2.2) are the products of separable spatial and time dependent components. Assuming sinusoidal time dependence, the spatial components of pressure $P(x)$ and velocity $U(x)$ can be separated and written as,

$$P(x) = A_1 e^{-ikx} + A_2 e^{ikx} \quad (2.4)$$

and,

$$U(x) = \frac{1}{\rho c} [A_1 e^{-ikx} - A_2 e^{ikx}] \quad (2.5)$$

2.3. Boundary Conditions

For a resonator of length L , a closed rigid end at $x = 0$ implies a zero working gas velocity at this section, *i.e.* $U(0) = 0$. Substituting in equation (2.5) suggests that $A_1 = A_2 = A$.

At the other end of the resonator ($x = L$), there exists 3 different scenarios. This can be another rigid end, at which case imposes another zero velocity boundary (*i.e.* $U(L) = 0$). The resonator can also be open ended forcing the oscillating amplitude of the gas pressure to vanish upon interfacing with the atmosphere outside (*i.e.* $P(L) = 0$). Defining the acoustic impedance at any section of the resonator tube as the pressure to velocity ratio at this section, the acoustic impedance at the right end of the tube Z_R then becomes,

$$Z_R = \frac{P(L)}{U(L)} \quad (2.6)$$

Given the above definition of Z_R , the boundary conditions in the rigid and open ended cases can now be generally expressed as,

$$Z_R = \begin{cases} \infty & \rightarrow \text{rigid end} \\ 0 & \rightarrow \text{open end} \end{cases} \quad (2.7)$$

It is intuitive now that the third possible scenario is to have a lumped-element connected to that end of the tube that has a finite Z_R value between 0 and ∞ . In the case of the *TAP* system under consideration here, the right end of the resonator is equipped with a piezo-element aimed at harnessing the incoming acoustic energy. Thus, the piezo impedance defines the second boundary condition governing the waveform equations.

2.4. Integration with Piezo-element

The piezo-element attached to the end of the acoustic resonator is ideally a circular diaphragm anchored at all circumferential points. The first mode resonance is the preferred operating mode as the diaphragm works against itself in the second mode as shown in Figure 2.2. While a finite element model of the diaphragm is carried out in Appendix (A), the piezo-element in the subsequent sections of this chapter is modeled as a rigid piston moving back and forth in the x -direction with a single degree of freedom (*DOF*). This simplified treatment is used to derive simplified equations of motion and obtain approximate estimates of the system performance characteristics and onset frequencies.

The constitutive equations of the piezo-element in this case are given by,

$$\begin{Bmatrix} S_3 \\ D_3 \end{Bmatrix} = \begin{pmatrix} \frac{1}{c_{33}^E} & d_{33} \\ d_{33} & \epsilon_{33}^T \end{pmatrix} \begin{Bmatrix} T_3 \\ E_3 \end{Bmatrix} \quad (2.8)$$

where S_3 and D_3 are the piezo strain and electrical displacement, T_3 and E_3 are the stress and electrical field intensity, c_{33}^E and d_{33} represent Young's modulus and the piezoelectric strain coefficient in the poling x -direction and ϵ_{33}^T is the permittivity at constant stress.

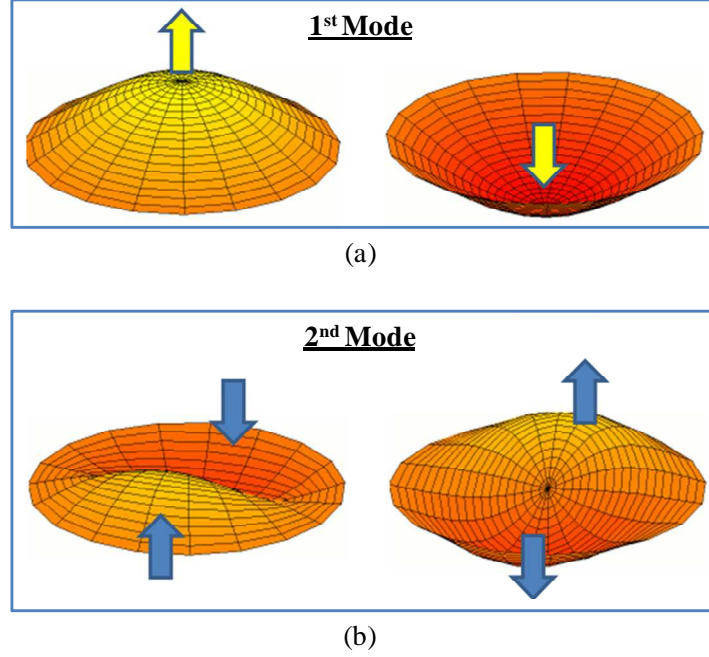


Figure 2.2 (a) First [*desired*] and (b) Second [*undesired*] vibration modes of a piezoelectric diaphragm anchored at the circumference

A force balance of the piezo-element yields the following equation for the x_2 degree of freedom,

$$m\ddot{x}_2 + b\dot{x}_2 - A_p P(L) + T_3 A_p = 0 \quad (2.9)$$

where m , b and A_p are the effective vibrating mass, damping coefficient and the cross sectional area of the piezo-element respectively. Substituting the first row from equation (2.8) into equation (2.9) yields,

$$m\ddot{x}_2 + b\dot{x}_2 - A_p P(L) + c_{33}^E (S_3 - d_{33} E_3) A_p = 0 \quad (2.10)$$

Substituting for the piezo-element strain by x_2 / t_p and the electric field by V / t_p where t_p and V are piezo-element thickness and the voltage across the load Z_L , then equation (2.10) becomes,

$$m\ddot{x}_2 + b\dot{x}_2 - A_p P(L) + c_{33}^E \left(\frac{x_2}{t_p} - d_{33} \frac{V}{t_p} \right) A_p = 0 \quad (2.11)$$

which can be rewritten as,

$$m\ddot{x}_2 + b\dot{x}_2 + s x_2 - d_{33} s V - \frac{SP(L)}{k_s} = 0 \quad (2.12)$$

where s is the piezo-element stiffness coefficient given by $c_{33}^E A_p / t_p$ and k_s is the ratio of the tube to the piezo-element cross sectional areas.

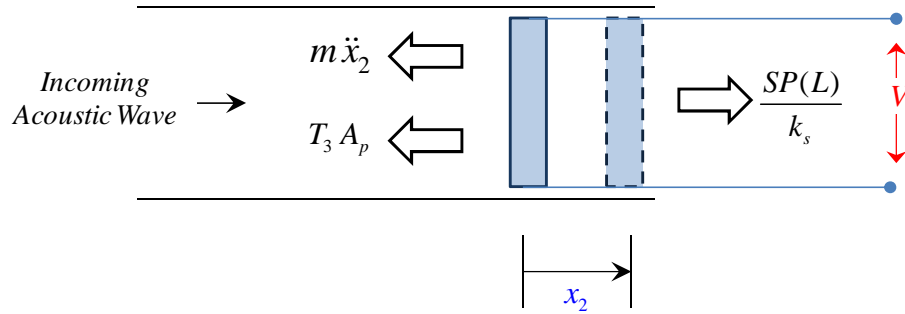


Figure 2.3 Force balance diagram for the simplified piezo-element in a TAP harvester (excluding piezo-element internal stiffness s and damping b)

The second row of equation (2.8) yields another equation which governs the electrical degree of freedom V and is given by,

$$D_3 = d_{33} T_3 + \epsilon_{33}^T E_3 \quad (2.13)$$

The electrical displacement D_3 is equal to q / A_p where q is the electric charge. Equation (2.13) can thus be written as,

$$q = d_{33} c_{33}^E A_p \left(\frac{x_2}{t_p} - d_{33} \frac{V}{t_p} \right) + \epsilon_{33}^T A_p \frac{V}{t_p} \quad (2.14)$$

Regrouping the x_2 and V terms and differentiating equation (2.14) once with respect to time gives,

$$\frac{A_p c_{33}^E}{t_p} d_{33} \dot{x}_2 + \left(1 - \frac{d_{33}^2 c_{33}^E}{\epsilon_{33}^T} \right) \frac{\epsilon_{33}^T A_p}{t_p} \dot{V} - \dot{q} = 0 \quad (2.15)$$

Using Ohm's law to relate electric current and voltage by the load impedance (i.e. $\dot{q} = -V / Z_L$) gives,

$$\frac{A_p c_{33}^E}{t_p} d_{33} \dot{x}_2 + \left(1 - \frac{d_{33}^2 c_{33}^E}{\epsilon_{33}^T} \right) \frac{\epsilon_{33}^T A_p}{t_p} \dot{V} + \frac{V}{Z_L} = 0 \quad (2.16)$$

Introducing the electromechanical coupling factor k_{33} ,

$$k_{33}^2 = \frac{d_{33}^2 c_{33}^E}{\epsilon_{33}^T} \quad (2.17)$$

and the piezoelectric clamped capacitance C_p ,

$$C_p = \left(1 - k_{33}^2 \right) \frac{A_p \epsilon_{33}^T}{t_p} \quad (2.18)$$

Equation (2.16) can now be simplified to,

$$sd_{33}\dot{x}_2 + C_p\dot{V} + \frac{V}{Z_L} = 0 \quad (2.19)$$

For sinusoidal oscillations and by eliminating V from equations (2.12) and (2.19), the following equation is obtained,

$$\frac{P(L)}{\dot{x}_2} = \frac{k_s}{S} \left[i\omega m + b + \frac{s}{i\omega} + \frac{\psi^2 Z_L}{1 + i\omega Z_L C_p} \right] \quad (2.20)$$

where $\psi = d_{33}s$ is the reciprocal coupling factor. The above equation agrees with those developed by [5] and [38] in similar studies. The expression at the right hand side of equation (2.20) is a pressure to velocity ratio of the piezo element and thus is equated to Z_R from equation (2.6) which represents the pressure to velocity ratio of the working gas at $x = L$. Equating (2.6) and (2.20) yields,

$$f_{TAP}(\omega, \alpha) = 0 \quad (2.21)$$

where f_{TAP} is given by,

$$f_{TAP} = i(\rho c) \cot(kL) - \frac{k_s}{S} \left[i\omega m + b + \frac{s}{i\omega} + \frac{\psi^2 Z_L}{1 + i\omega Z_L C_p} \right] \quad (2.22)$$

Solving (2.21) for both real and imaginary parts yields the frequency of self-sustained oscillations for different values of L for a *TAP* harvester.

2.5. Implementing a Dynamic Magnifier

Consider the *DMTAP* harvester shown in Figure 2.4 which consists, in its simplest form, of a spring-mass system which is placed between the piezo-element and the acoustic resonator. To formulate more general equations for the system, the magnifier body is assumed to have a mass m_m , stiffness k_m and a damping coefficient c_m and a stiffness k_c of the spring coupling the mass m_m with the piezo-element. The system now has 3 *DOFs*, namely the displacement x_1 of m_m , displacement x_{2m} of the piezo-element and the electrical *DOF* V across the load Z_L . Applying the same technique used with the *TAP* and using the force balance diagram shown in Figure 2.5, the governing equations of the *DMTAP* can be derived as follows,

x_1 – DOF:

$$m_m \ddot{x}_1 + c_m \dot{x}_1 + k_m x_1 + k_c (x_1 - x_{2m}) - \frac{SP(L)}{k_s} = 0 \quad (2.23)$$

x_{2m} – DOF:

$$m \ddot{x}_{2m} + b \dot{x}_{2m} + s x_{2m} + k_c (x_{2m} - x_1) - d_{33} s V = 0 \quad (2.24)$$

V – DOF:

$$s d_{33} \dot{x}_{2m} + C_p \dot{V} + \frac{V}{Z_L} = 0 \quad (2.25)$$

For sinusoidal oscillations, and by eliminating V and x_{2m} from equations (2.23), (2.24) and (2.25), the ratio of the end pressure $P(L)$ to the velocity of the magnifier

mass m_m can be expressed in terms of the parameters of the dynamic magnifier and the piezo-element as follows,

$$\frac{P(L)}{\dot{x}_1} = \frac{k_s}{S} \frac{\left[i\omega m_m + c_m + \frac{k_c}{i\omega} + \frac{k_m}{i\omega} \right] \left[i\omega m + b + \frac{s}{i\omega} + \frac{k_c}{i\omega} + \frac{\psi^2 Z_L}{1 + i\omega Z_L C_p} \right] + \frac{k_c^2}{\omega^2}}{\left[i\omega m + b + \frac{s}{i\omega} + \frac{k_c}{i\omega} + \frac{\psi^2 Z_L}{1 + i\omega Z_L C_p} \right]} \quad (2.26)$$

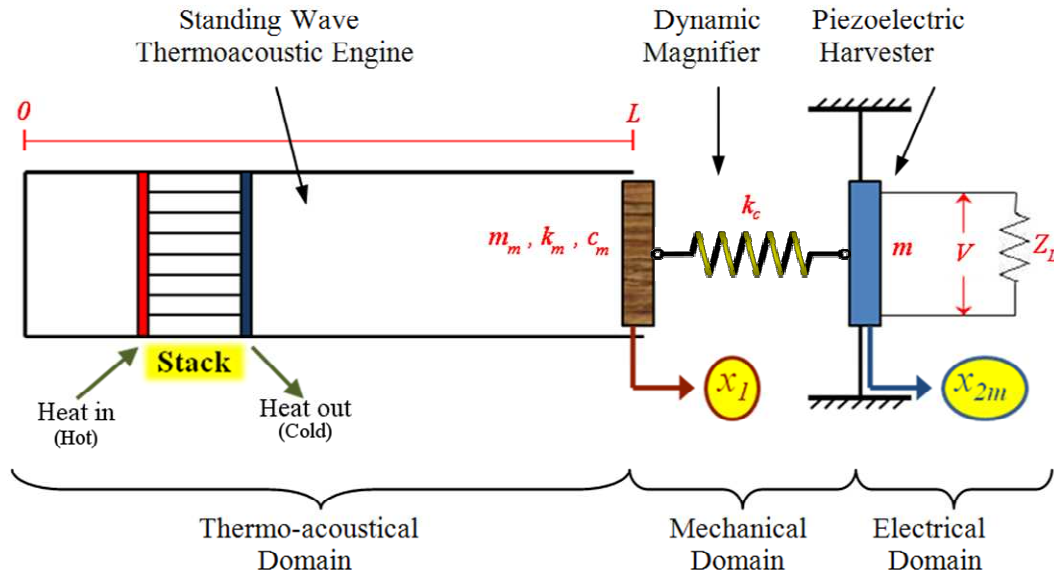


Figure 2.4 Schematic of a standing wave thermoacoustic-piezoelectric harvester integrated with a dynamic magnifier (DMTAP)

The expression at the right hand side of equation (2.26) represents the impedance value that should be equated to Z_R from equation (2.6) which represents the pressure to velocity ratio of the working gas at $x = L$. Equating (2.6) and (2.26) yields,

$$f_{DMTAP}(\omega, \alpha) = 0 \quad (2.27)$$

where f_{DMTAP} is given by,

$$f_{DMTAP} = i(\rho c) \cot(kL) - \frac{k_s}{S} \frac{\left[i\omega m_m + c_m + \frac{k_c}{i\omega} + \frac{k_m}{i\omega} \right] \left[i\omega m + b + \frac{s}{i\omega} + \frac{k_c}{i\omega} + \frac{\psi^2 Z_L}{1 + i\omega Z_L C_p} \right] + \frac{k_c^2}{\omega^2}}{\left[i\omega m + b + \frac{s}{i\omega} + \frac{k_c}{i\omega} + \frac{\psi^2 Z_L}{1 + i\omega Z_L C_p} \right]} \quad (2.28)$$

Solving equation (2.27) for both real and imaginary parts yields the frequency of self-sustained oscillations for different values of L of a *DMTAP* harvester.

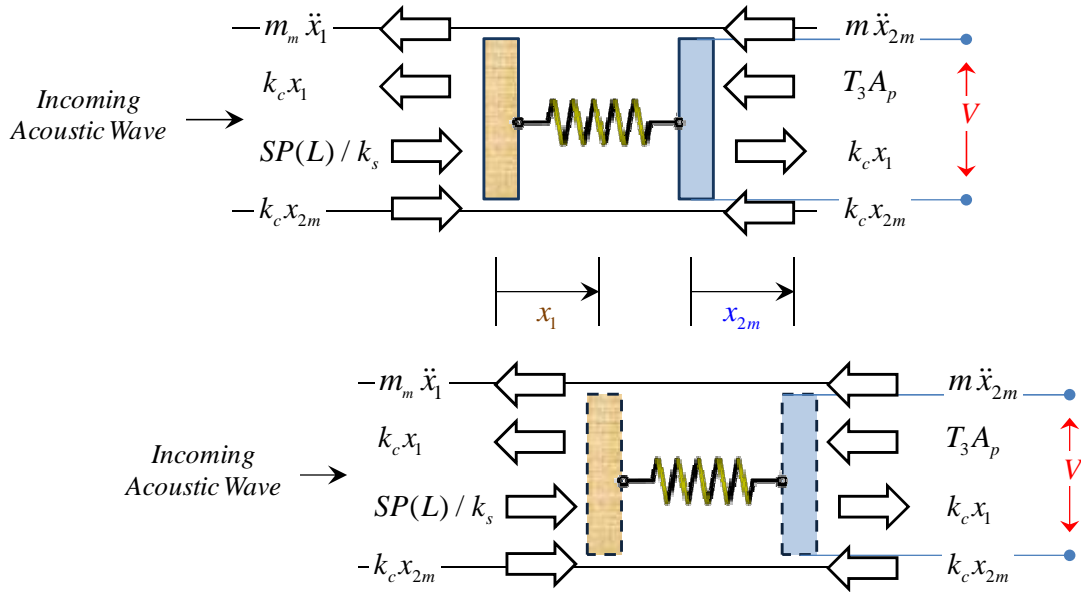


Figure 2.5 Force balance diagram for the magnifier mass and piezo-element in the *DMTAP* harvester (excluding piezo-element internal stiffness s and damping b and internal stiffness k_m and damping c_m of the magnifier mass)

Table 2.1 lists values of some design parameters of a *TAP* harvester [5] and a *DMTAP* harvester used in the analysis carried over in the subsequent section with a dynamic magnifier that has a mass and stiffness m_m and k_c , respectively. Also, air is considered to be the working gas with mean pressure P_m and temperature T_m which

are set equal to 10^5 Pa and 400 K respectively. An electric load Z_L of 100Ω is attached to the piezo-element in both a *TAP* and a *DMTAP*.

The frequencies of self-sustained oscillations ω for both the *TAP* and the *DMTAP* are obtained using equations (2.21) and (2.27). These frequencies are plotted against the resonator length as shown in Figure 2.6. The vertical axis represents a normalized frequency which is equal to $\omega L / c$, the solid line represents the natural frequency of the piezo-element alone while the dashed and the dash-dotted lines represent the closed-open and closed-closed tube frequencies for comparative purposes. Closed-open resonator tubes are ideally quarter wavelength resonators (*i.e.* $\lambda = 4L$) with a resonant frequency given by $\omega = 2\pi c / \lambda$. From these facts, the normalized frequency of closed-open resonator tubes would be a constant ($\omega L / c = \pi / 2$). In the case of closed-closed tubes, the resonator tubes are half wavelength resonators yielding a normalized frequency of $\omega L / c = \pi$.

Table 2.1 *TAP* and *DMTAP* Design Parameters

Parameter	Value	
	<i>TAP</i>	<i>DMTAP</i>
S	$7.85e-5 \text{ m}^2$	$7.85e-5 \text{ m}^2$
k_s	4	4
m	$3.46e-7 \text{ kg}$	$3.46e-7 \text{ kg}$
m_m	<i>N/A</i>	$3.46e-7 \text{ kg}$
b	$3.88e-5 \text{ kg / s}$	$3.88e-5 \text{ kg / s}$
s	574 N / m	574 N / m
ψ^2	$9.44e-9 \text{ kg (s}\Omega)^{-1}$	$9.44e-9 \text{ kg (s}\Omega)^{-1}$
C_p	$2.76e-8 \text{ F}$	$2.76e-8 \text{ F}$
k_c	<i>N/A</i>	229.6 N / m

The results shown in Figure 2.6 suggest that the addition of the dynamic magnifier to the thermoacoustic harvester under study results in reducing the frequency of the self-sustained oscillations. More interestingly, it can be noticed that the behavior of the resonator approaches that of a half wavelength resonator at increasing lengths for the *TAP* harvester. In the case of the *DMTAP*, the behavior of the resonator tends to fall somewhere in between the quarter and the half wavelength tubes at increasing lengths.

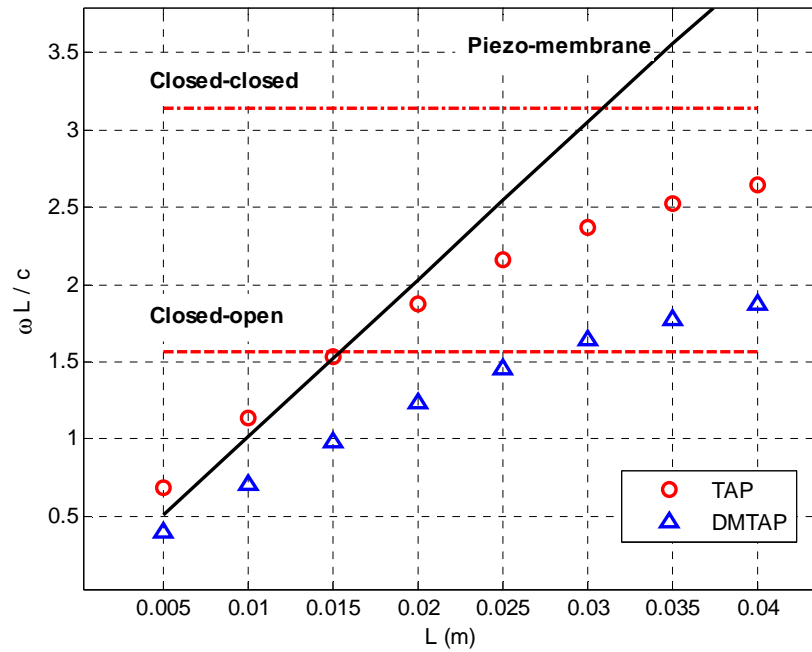


Figure 2.6 Dimensionless frequency of self-sustained oscillations for different resonator lengths for *TAP*, *DMTAP*, closed-closed and closed-open tubes

Figure 2.7 provides displays of the acoustic waveforms along the resonator for a length of 1.5 cm and 4 cm respectively. These patterns are obtained from equations (2.4) and (2.5). The figure shows the variation of the real component of pressure and the imaginary component of velocity along the length of the resonator. These are the dominating components of both pressure and velocity expressions in their complex form and are typically utilized by thermoacoustic codes such as *DeltaEC* to give a good approximation of their absolute values.

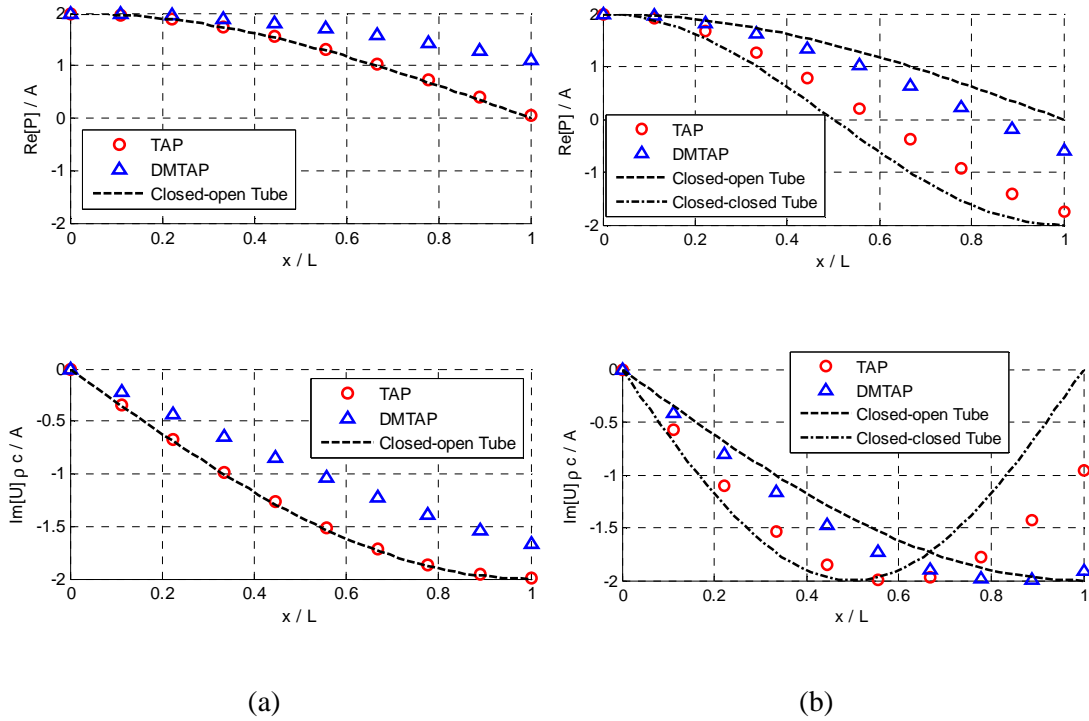


Figure 2.7 Pressure and velocity waveforms for *TAP* and *DMTAP* harvesters in comparison with closed-closed and closed-open tubes for resonator lengths of (a) 1.5 cm and (b) 4 cm

It is evident here, as suggested by Figure 2.7, that the behavior of the *TAP* with a length of 1.5 cm resembles that of a closed-open tube in which case the pressure amplitude eventually decays to zero to match the outside atmospheric pressure at the open end of the resonator. In this case also, the velocity of the working gas reaches its anti-node (peak) value at the open end to satisfy a standing wave pattern as confirmed by the plots.

At the same length of the resonator (1.5 cm), the *DMTAP* is relatively closer to a closed-open tube behavior but is expected to fully imitate it around 3 cm of tube length as suggested by Figure 2.6. On the other hand, both the *TAP* and the *DMTAP*

resonators of 4 cm long are expected to have a behavior that falls somewhere in between the half and quarter wavelength resonators as implied by Figure 2.7.

2.6. Piezo displacement and Energy flow

2.6.1. Energy, Power and Efficiency

The acoustic energy produced in the stack \dot{W}_{st} is only a fraction of the heat input \dot{Q}_{in} to the hot heat exchanger. This acoustic power generated in the stack due to the thermoacoustic phenomenon incurs some losses before being radiated to the end of the tube where the piezo-element is located. These losses are mathematically mainly attributed to losses along the resonator walls \dot{E}_{res} , *i.e.*

$$\dot{W}_{st} = \dot{E}_T + \dot{E}_{res} \quad (2.29)$$

where \dot{E}_T is the amount of acoustic power left after those losses given by,

$$\dot{E}_T = \frac{1}{2} S \operatorname{Re} \{ P(L) \operatorname{conj}[U(L)] \} \quad (2.30)$$

and the useful electric power dissipated in the electric load is given by,

$$\dot{E}_L = \frac{1}{2} \operatorname{Re} \left\{ \frac{V \operatorname{conj}(V)}{Z_L} \right\} \quad (2.31)$$

The efficiency η_e of the conversion of acoustic to electric energy can then be expressed using equation (2.31) as a ratio of equation (2.30), *i.e.*,

$$\eta_e = \frac{\dot{E}_L}{\dot{E}_T} \quad (2.32)$$

Finally, the overall efficiency of the thermoacoustic device η_o can be estimated as a product of all the above energy conversions,

$$\eta_o = \left(\frac{\dot{E}_L}{\dot{E}_T} \right) \left(\frac{\dot{E}_T}{\dot{W}_{st}} \right) \left(\frac{\dot{W}_{st}}{\dot{Q}_{in}} \right) = \dot{E}_L / \dot{Q}_{in} \quad (2.33)$$

Expressions governing \dot{W}_{st} and \dot{E}_{res} are governed mainly by thermo-physical, geometrical and variable stack parameters. These are derived separately in the coming sections.

2.6.2. Magnification Ratio

To examine the effect of using the dynamic magnification concept, it is useful to investigate the displacement x_2 of the piezo-element in the *TAP* case in relation to the displacement x_{2m} of piezo-element in the *DMTAP* case. If the magnification ratio x_{2m} / x_2 exceeds unity, this indicates that more strain is experienced by the piezo-element upon dynamic magnification and hence more power output is expected. The mass m_m is taken to be the same as m , as listed in Table 2.1, while c_m and k_m are neglected for simplicity. The ratio x_{2m} / x_1 in the *DMTAP* can be an acceptable approximation of the magnification ratio under these assumptions. Appropriate selection of k_c that would ensure the ratio exceeds 1 makes the use of *DMTAP* advantageous over the *TAP*.

Figure 2.8 through Figure 2.10 show three possible scenarios when using a *DMTAP* under the above simplified conditions. The plots show the effect of frequency on the efficiency η_e of conversion from acoustic to electric energy at a load Z_L of 1000Ω . In these plots, the tube lengths of the *TAP* and the *DMTAP* are set such that they resonate at the same frequency.

In Figure 2.8, a control test is carried out, whereby k_c is set equal to ∞ and m_m equal to 0. This represents a situation where the mass and the piezo-element are in contact (no coupling spring) and the first mass is negligible, *i.e.* the *DMTAP* becomes a *TAP* harvester. It is shown that the x_{2m} / x_1 is equal to 1 and η_e of the *DMTAP* coincides with that of the *TAP*, thus validating the use of x_{2m} / x_1 as an approximate magnification ratio.

In Figure 2.9 and Figure 2.10, the masses m_m and m are set to be equal. Also, the stiffness of the coupling spring is set to be 3/4 that of the piezo-element stiffness for the results of Figure 2.9 and 0.11 of the piezo-element stiffness for the behavior shown in Figure 2.10. The rest of the parameters are maintained as given in Table 2.1.

It is interesting to note that previous two plots show that the efficiency of the *DMTAP* starts exceeding that of the *TAP* when the ratio x_{2m} / x_1 starts exceeding 1.

This is indicated by the double headed black arrows. Even though there is a bandwidth of lower frequencies in both cases where the *DMTAP* shows better efficiency than the *TAP*, it is of greater interest to have η_e of the *DMTAP* higher than that of the *TAP* at the resonant frequency as evident in Figure 2.10. This is more important to look for since the energy conversion efficiency only becomes significantly high around resonance.

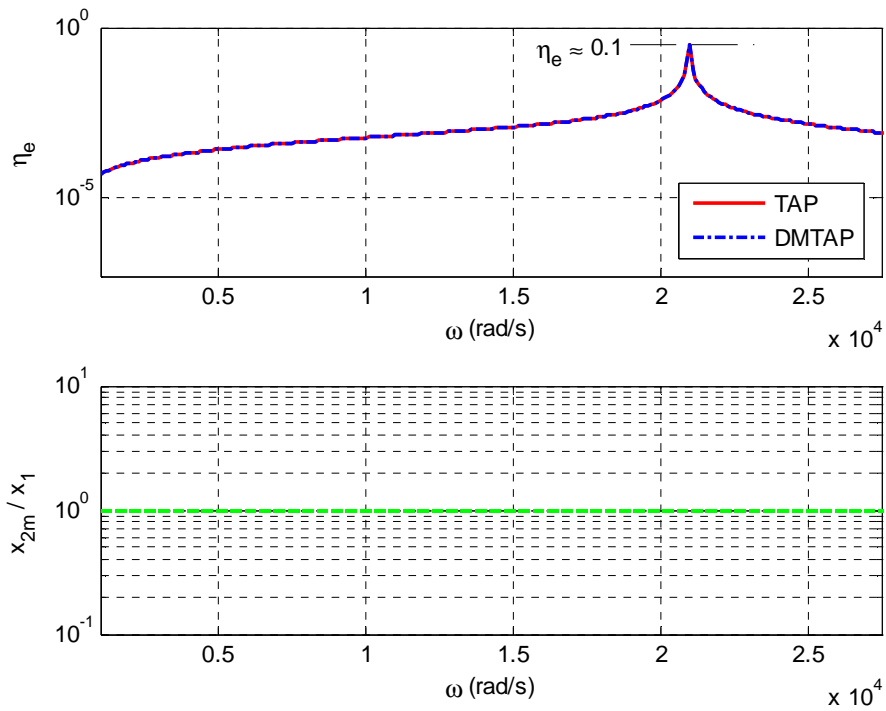


Figure 2.8 Frequency response of conversion efficiency η_e and corresponding magnification ratio

$$x_{2m} / x_1 \text{ for a TAP and a DMTAP at } m_m = 0, k_c = \infty$$

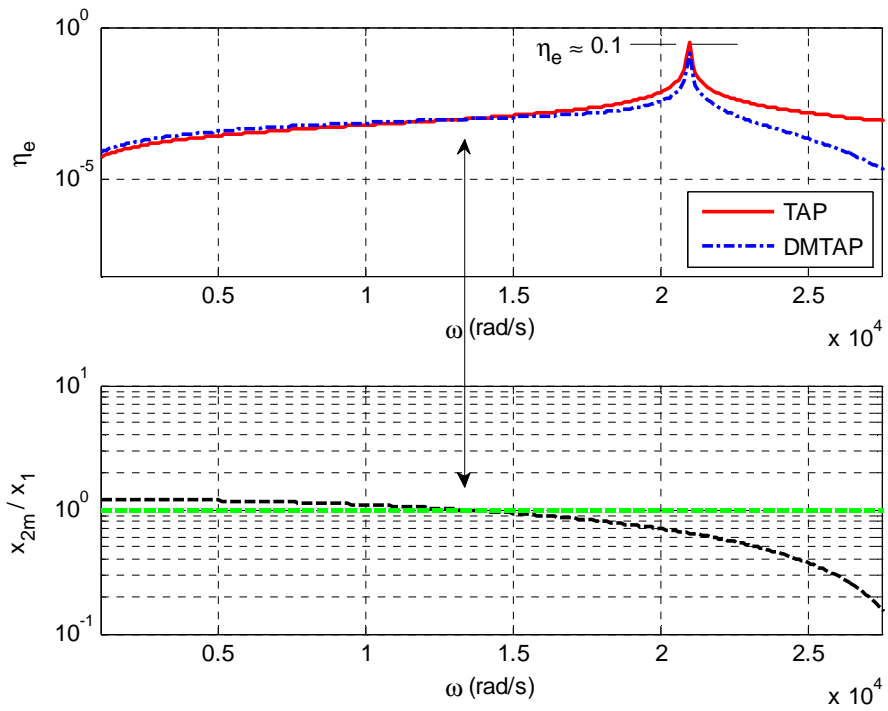


Figure 2.9 Frequency response of conversion efficiency η_e and corresponding magnification ratio

$$x_{2m} / x_1 \text{ for a TAP and a DMTAP at } m_m = m, k_c = 0.75 s$$

(Double headed arrows indicate frequencies at which magnification ratio is equal to 1)

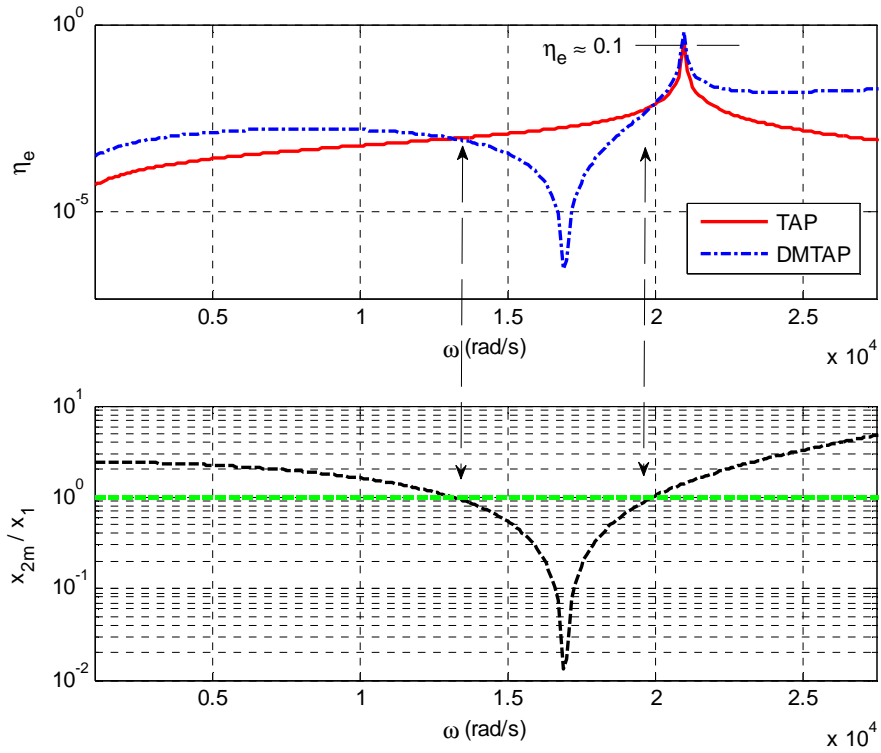


Figure 2.10 Frequency response of conversion efficiency η_e and corresponding magnification ratio

$$x_{2m} / x_1 \text{ for a TAP and a DMTAP at } m_m = m, k_c = 0.11 s$$

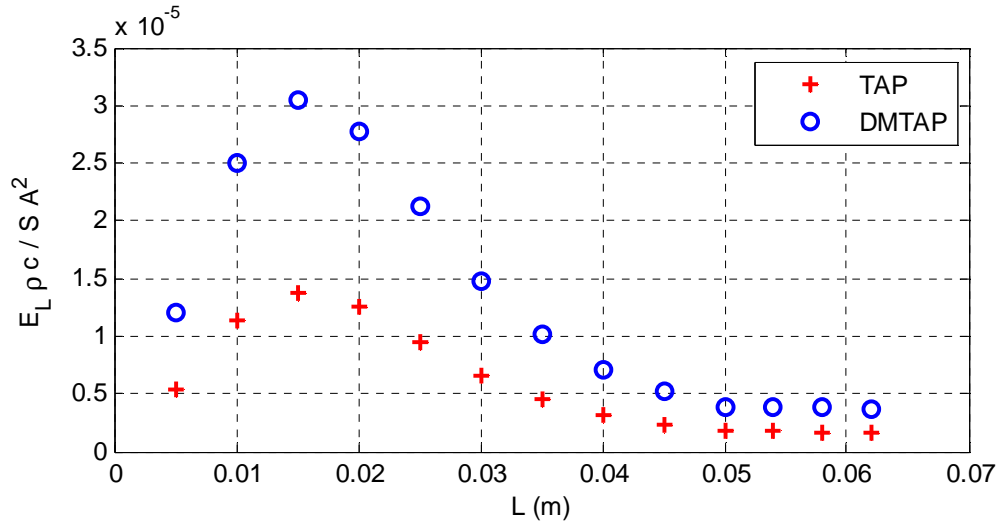
(Double headed arrows indicate frequencies ω at which magnification ratio is equal to 1)

2.6.3. TAP and DMTAP Performance Comparisons

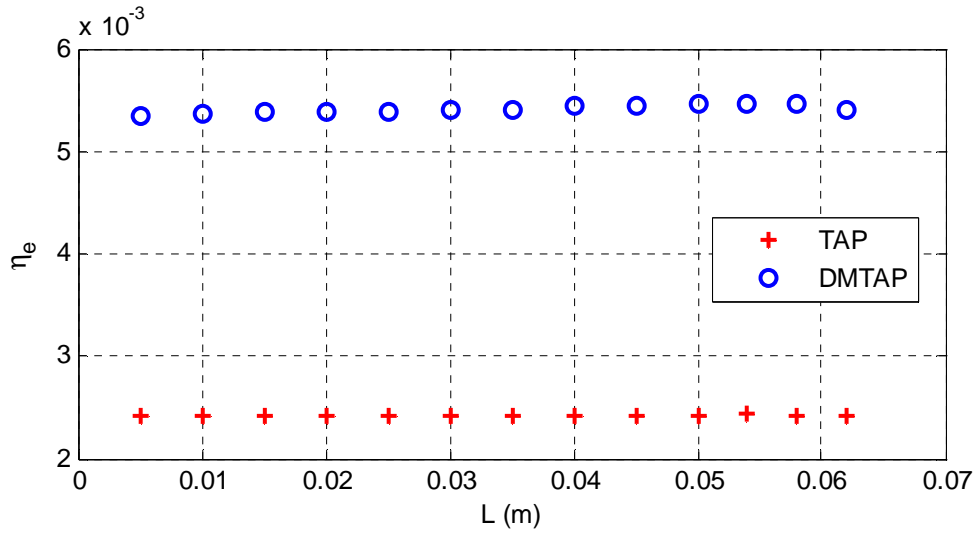
In Figure 2.11 through Figure 2.14, comparisons are made between a TAP and a DMTAP in terms of the harvested piezoelectric power and conversion efficiency. Output power used here is normalized using system parameters, namely gas density ρ , speed of sound c , resonator cross section S and the wave amplitude squared A^2 . This quantity is convenient for comparing useful amounts of electricity generated by the piezo-element for given values of sound pressure amplitude. The

comparison is made for electric loads of 10, 100, 1000 and 10000 Ω , and is based on the parameters provided in Table 2.1.

From the obtained results, it is noticed first that the strain amplification that takes place in the piezo-element due to the addition of the magnifier significantly increases the amount of useful electric energy harvested and enhances the efficiency as well. The second observation is that the performance of both the *TAP* and the *DMTAP* is sensitive to the value of the impedance Z_L of the electric load. Generally speaking, the values of the normalized electric output and efficiency are fairly low at low resistances. It is not before the load resistance becomes 1000 Ω that values of the efficiency η_e start to exceed 10 % peaking at around 34 % for the *DMTAP* system with a resonator length of 5.5 cm. At 10000 Ω however, the output power and efficiency begin deteriorating again. In conclusion, it can be shown that with appropriate selection of the added mass and spring stiffness, a *DMTAP* can contribute to raising the overall efficiency η_o of a thermoacoustic standing wave harvester by improving the efficiency of its energy harvester component η_e .

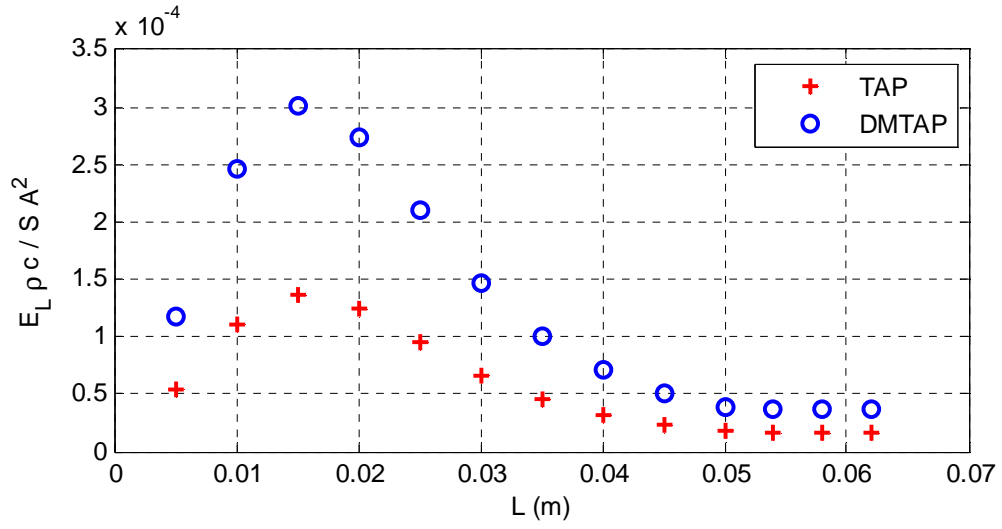


(a)

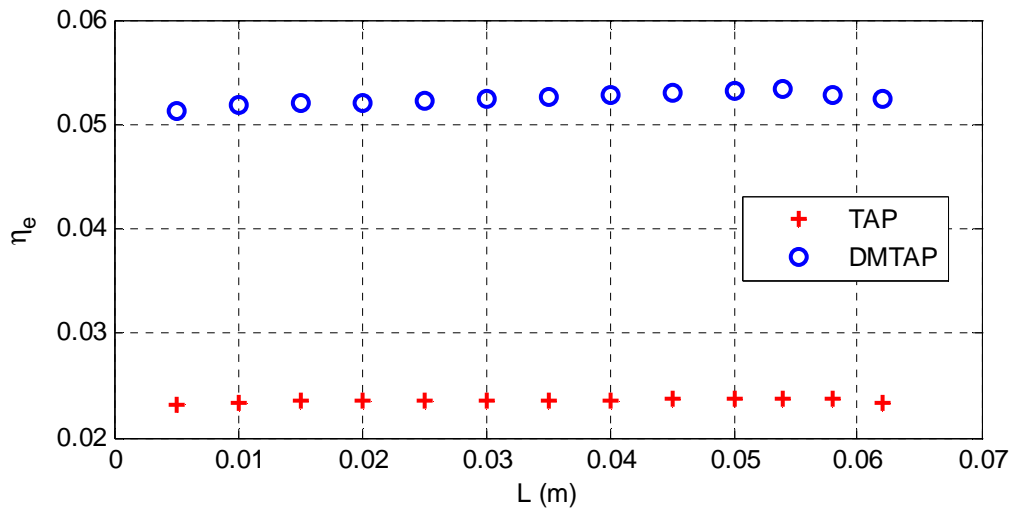


(b)

Figure 2.11 (a) Dimensionless harvested electric power output and (b) corresponding acoustic to electric energy conversion efficiency for an electric load of 10Ω

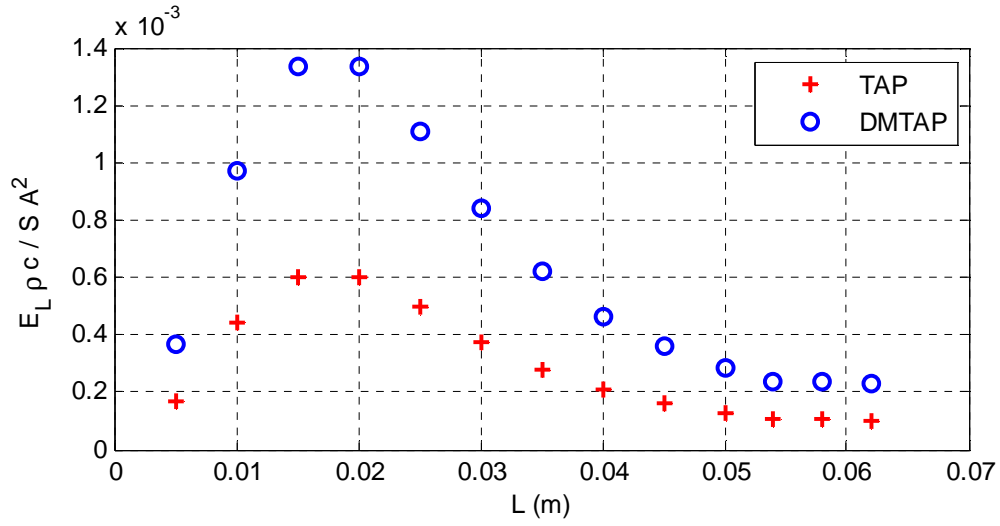


(a)

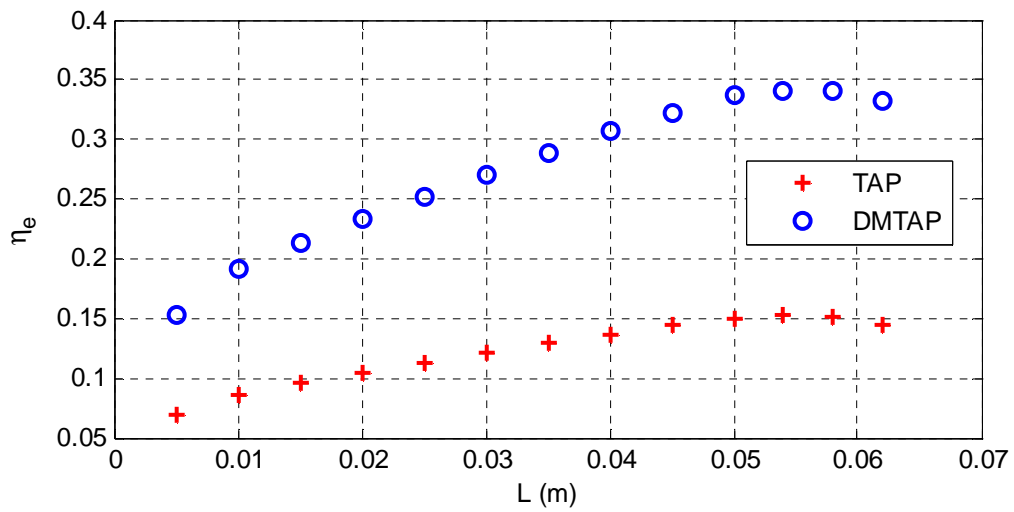


(b)

Figure 2.12 (a) Dimensionless harvested electric power output and (b) corresponding acoustic to electric energy conversion efficiency for an electric load of 100Ω

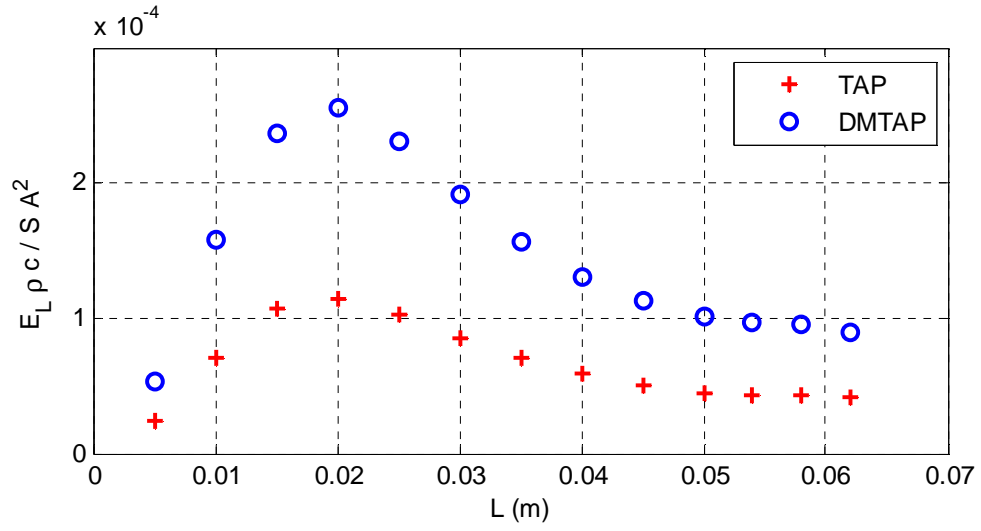


(a)

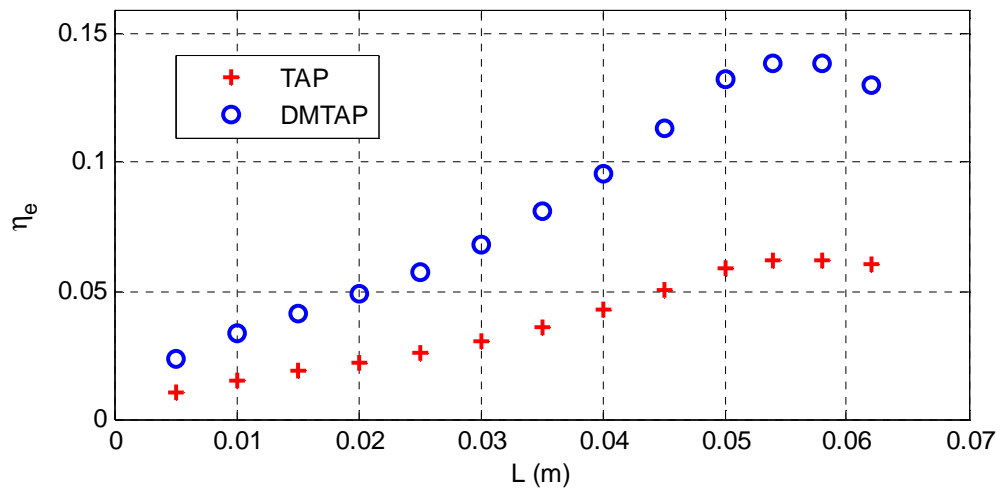


(b)

Figure 2.13 (a) Dimensionless harvested electric power output and (b) corresponding acoustic to electric energy conversion efficiency for an electric load of 1000Ω



(a)



(b)

Figure 2.14 (a) Dimensionless harvested electric power output and (b) corresponding acoustic to electric energy conversion efficiency for an electric load of 10000Ω

2.7. Temperature Effect and Stack Region Equations

2.7.1. Critical temperature gradients

Thermal energy flow around a stack of parallel plates is governed by the general equation of heat transfer [18],

$$\rho T \left(\frac{\partial s_g}{\partial t} + v \cdot \nabla s_g \right) = \nabla \cdot (K_c \nabla T) \quad (2.34)$$

+ higher order terms in velocity

where T , s_g , v and K_c are the temperature, entropy, total working gas velocity and its thermal conductivity respectively. Keeping the first order terms only and neglecting thermal conduction in the x -direction, equation (2.34) can be simplified to,

$$\rho_m T_m \left(i\omega s_g + U \frac{\partial s_g}{\partial x} \right) = K_c \frac{\partial^2 T}{\partial y^2} \quad (2.35)$$

where T_m and ρ_m denote the mean gas temperature and density. U , as defined earlier, is the x -component of the gas velocity. For an oscillatory temperature profile, in a manner similar to that of the pressure and velocity,

$$T = T_m + T(x) e^{i\omega t} \quad (2.36)$$

The gas entropy s_g can be expressed in terms of P and T , as follows,

$$s_g = \left(\frac{c_p}{T_m} \right) T - \left(\frac{\beta}{\rho_m} \right) P \quad (2.37)$$

where c_p is the isobaric specific heat and β is the thermal expansion coefficient.

Combining equations (2.35) through (2.37) yields,

$$i\omega\rho_m c_p T - K_c \frac{d^2 T}{dy^2} = i\omega T_m \beta P - \rho_m c_p \nabla T_m U \quad (2.38)$$

which can be solved using specified boundary conditions [18] to give,

$$T = \left(\frac{T_m \beta}{\rho_m c_p} P - \frac{\nabla T_m U}{\omega} \right) \left(1 - e^{-(1+i)y/\delta_k} \right) \quad (2.39)$$

where δ_k is the thermal penetration depth indicating the thickness of air above and beneath one plate beyond which thermal conduction is negligible, and is expressed as,

$$\delta_k = \sqrt{\frac{2K_c}{\omega\rho_m c_p}} \quad (2.40)$$

Assuming that the working gas far from the plate ($y \gg \delta_k$) makes negligible thermal contact with the plate, T can be simplified to,

$$T = \left(\frac{T_m \beta}{\rho_m c_p} P - \frac{\nabla T_m U}{\omega} \right) \quad (2.41)$$

The first term of equation (2.41) represents temperature oscillations due to adiabatic compression and expansion in fluid, while the second represents oscillations resulting from a temperature gradient in the gas due to oscillations in x -direction. The critical temperature gradient required for onset of self-sustained oscillations can be estimated by equating equation (2.41) to zero giving,

$$\nabla T_{crit} = \frac{T_m \beta \omega P(x_s)}{\rho_m c_p U(x_s)} \quad (2.42)$$

The terms $P(x_s)$ and $U(x_s)$ are the pressure and velocity at the stack center position. The temperature gradient along the stack normalized with respect to the critical value ∇T_{crit} is referred to as the normalized gradient Γ [33].

2.7.2. Energy balance and onset temperature difference

Figure 2.15 shows a schematic illustrating some of the geometric parameters of the resonator and stack. Note that R and L denote the resonator radius and length. Also, Δx and x_s define the stack length and center position respectively, while y_o and l denote half the plate spacing and half its thickness.

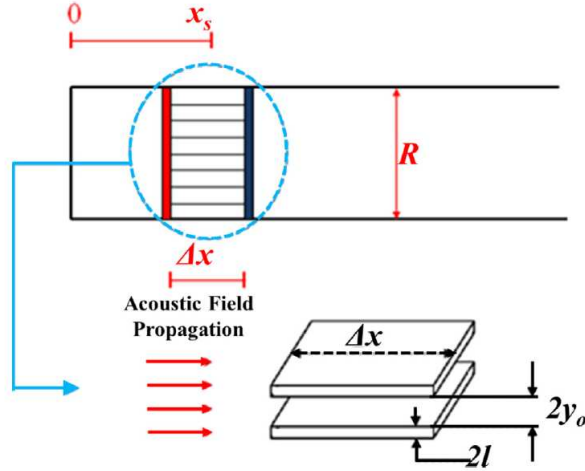


Figure 2.15 Geometric parameters of resonator and stack

The plate perimeter inside the tube Π is given by,

$$\Pi = \frac{\pi R^2}{l + y_o} \quad (2.43)$$

The acoustic work produced in the stack \dot{W}_{st} given by equation (2.29) can be equivalently given by [33],

$$\dot{W}_{st} = \frac{1}{4} \Pi \delta_k \Delta x \frac{(\gamma - 1) \omega P(x_s)^2}{\rho_m c^2 (1 + \varepsilon_s)} \left(\frac{\Gamma}{(1 + \sqrt{\sigma})(1 - \delta_v/y_o + \delta_v^2/2y_o^2)} - 1 \right) - \frac{1}{4} \Pi \delta_v \Delta x \frac{\omega \rho_m U(x_s)^2}{(1 - \delta_v/y_o + \delta_v^2/2y_o^2)} \quad (2.44)$$

with γ being the ratio of isobaric to isochoric specific heats of the working gas and ε_s being the plate heat capacity ratio. Finally, σ is the gas Prandtl number and δ_v is the viscous penetration depth given as a function of the gas viscosity μ by,

$$\delta_v = \sqrt{\frac{2\mu}{\rho\omega}} \quad (2.45)$$

The acoustic power dissipated in the resonator walls can be roughly approximated by [18],

$$\dot{E}_{res} = \frac{1}{4} \frac{P_{max}^2}{\rho_m c^2} \omega \pi R L \left[\delta_k \frac{\gamma-1}{1+\epsilon_s} \left(1 + \frac{2R}{L} \right) + \delta_v \right] \quad (2.46)$$

where P_{max} is the maximum pressure amplitude along the resonator. Combining equations (2.29), (2.30), (2.44) and (2.46) gives,

$$\Gamma = \left[\frac{\left\{ \left[\left(\frac{1}{4} \frac{P_{max}^2}{\rho_m c^2} \omega \pi R L \left[\delta_k \frac{\gamma-1}{1+\epsilon_s} \left(1 + \frac{2R}{L} \right) + \delta_v \right] \right) + \left(\frac{S}{2} \text{Re} \{ P(L) \text{conj}[U(L)] \} \right) \right] \right\} + \frac{1}{4} \Pi \delta_v \Delta x \frac{\omega \rho_m U(x_s)^2}{(1 - \delta_v/y_o + \delta_v^2/2y_o^2)}}{\frac{1}{4} \Pi \delta_k \Delta x \frac{(\gamma-1) \omega P(x_s)^2}{\rho_m c^2 (1+\epsilon_s)}} + 1 \right] \times (1 + \sqrt{\sigma}) (1 - \delta_v/y_o + \delta_v^2/2y_o^2) \quad (2.47)$$

Using the definition of Γ , the temperature difference can then be obtained from equations (2.42) and (2.47) as follows,

$$\Delta T = \nabla T_{crit} \Gamma \Delta x \quad (2.48)$$

The temperature difference required to produce self-sustained oscillations is a key performance characteristic of the standing wave thermoacoustic harvester. As expected from the governing equations, that difference strongly depends on the position of the stack in the tube.

This relationship is plotted in Figure 2.16 for resonator lengths of 1.5 and 4 cm, for both the *TAP* and the *DMTAP*. For these calculations, it is assumed that the stack is 1/10 of the resonator length in both cases. The spacing between the stack plates is chosen to be twice the thermal penetration depth (i.e. $y_o = \delta_k$), and the plates are considered infinitely thin. The mean temperature is still maintained at 400 K and the electric load Z_L is 1000 Ω . All the thermo-physical properties are obtained for air at 400 K and atmospheric pressure.

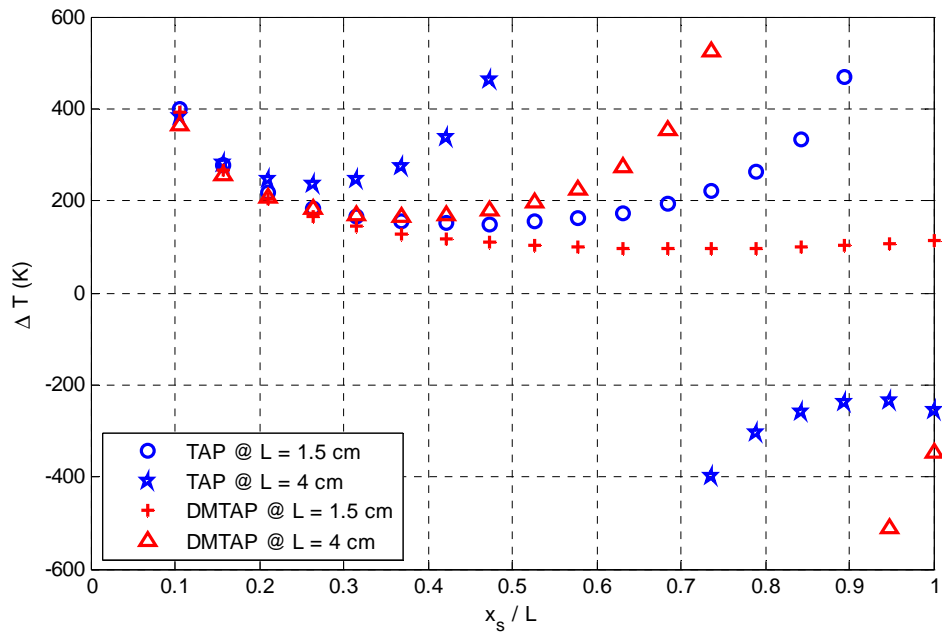


Figure 2.16 Temperature difference required to onset acoustic oscillations for *TAP* and *DMTAP* of resonator lengths 1.5 and 4 cm

Several conclusions can be drawn from the results in Figure 2.16. For the shorter resonator length of 1.5 cm, the *DMTAP* requires a lower temperature difference for almost any position of the stack along the tube length when compared with the *TAP*. Such temperature difference may reach values as low as 200 K at $x_s / L = 0.425$. This feature is indicative of an important performance enhancement resulting from the addition of the dynamic magnifier. With this small temperature difference across the stack, lower thermal input is needed to initiate the self-sustained oscillations.

For longer resonators, the comparison is more critical and is sensitive to the placement of the stack. Note that these resonators have pressure waves with a node close to the middle of the tube as shown in Figure 2.7. Consequently, there exists a point where the temperature difference required becomes negative. In physical terms, that requires a heat input to the right end of the stack instead of its left end as considered in Figure 2.1 and Figure 2.4. In turn, this means switching the locations of the hot and cold heat exchangers. In that domain, the *TAP* seems to require a less temperature difference than the *DMTAP* as shown in Figure 2.16. For example, for a 4 cm long resonator the temperature difference becomes almost 200 K for the *TAP* and 500 K for the *DMTAP* when the stack is placed at $x_s / L = 0.95$.

Accordingly, it should be emphasized here that the optimal stack placement in standing wave harvesters should be in the left quarter of the resonator, to compromise

between better acoustic power output and better efficiency. Stacks should be typically located whereas the magnitude of gas velocity is relatively small to reduce any viscous dissipation losses that might affect the conversion efficiency, yet simultaneously at a location where the pressure-velocity product is reasonably high to generate more acoustic power [33]. Taking the above factors into consideration, it stands that *DMTAP* systems would be potentially more useful to use given the optimal stack location.

2.8. Graphical User Interface: Development and Applications

To ease calculations and analysis of various configurations of thermoacoustic-piezoelectric harvesters equipped with an auxiliary elastic structure, a graphical user interface (*GUI*) is hereby presented. The developed program aims at giving the user indications of the presence or lack of dynamic magnification of the output piezo power upon plugging in different mass and spring stiffness for the magnifier system. The *GUI* also allows for varying the operating conditions of the *TAP* and the *DMTAP* under investigation, including but not limited to user-specified mean pressure and temperature, stack porosity and hydraulic radius, resonator length and diameter as well as piezo parameters such the clamped capacitance, reciprocal coupling factor and electric load resistance. Moreover, the interface provides a library of different working gases typically available for thermoacoustic operation such as: air, helium, nitrogen, hydrogen, neon, and equally divided gas mixtures of helium-argon, helium-xenon, and neon-xenon.

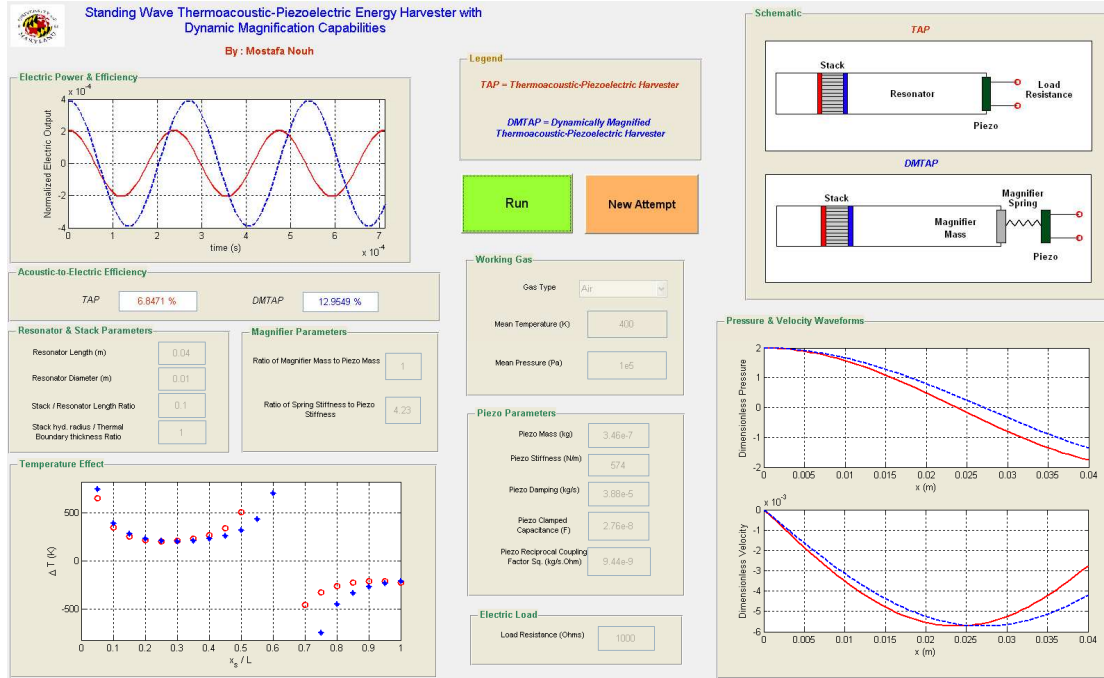


Figure 2.17 Screen Capture of the developed GUI utility

The proposed utility can be used to rapidly optimize the magnifier parameters that give the best operation and peak efficiency for different resonator configurations. The variation of the magnifier mass m_m and the coupling spring k_c imposes a change of the piezo deflection and the right hand side impedance Z_R at the resonator end. The acoustic waveforms, amount of electric power extracted by the piezo and energy conversion efficiency change correspondingly. Figure 2.18 shows examples of two different k_c values having opposing effects on the normalized power output and the acoustic-to-electric efficiency, while keeping m_m equal to the piezo mass m in both cases. Figure 2.19 shows examples of two different m_m values having opposing

effects on the normalized power output and the acoustic-to-electric efficiency, while keeping k_c equal to the piezo stiffness s in both cases.

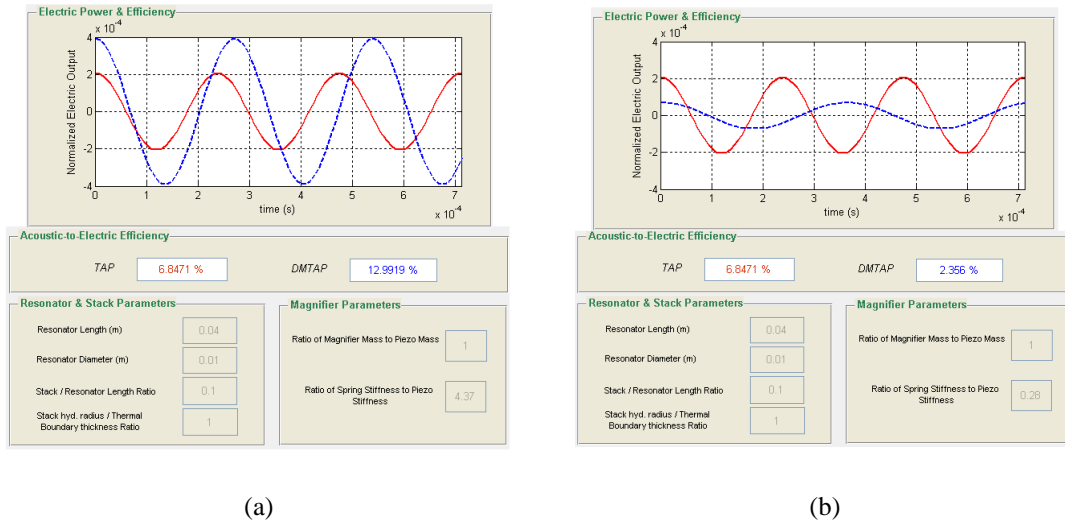


Figure 2.18 GUI screenshots: Effect of varying k_c on the normalized electric output and the acoustic-to-electric energy conversion efficiency resulting in (a) magnification and (b) demagnification [solid line: TAP , dashed line: $DMTAP$]

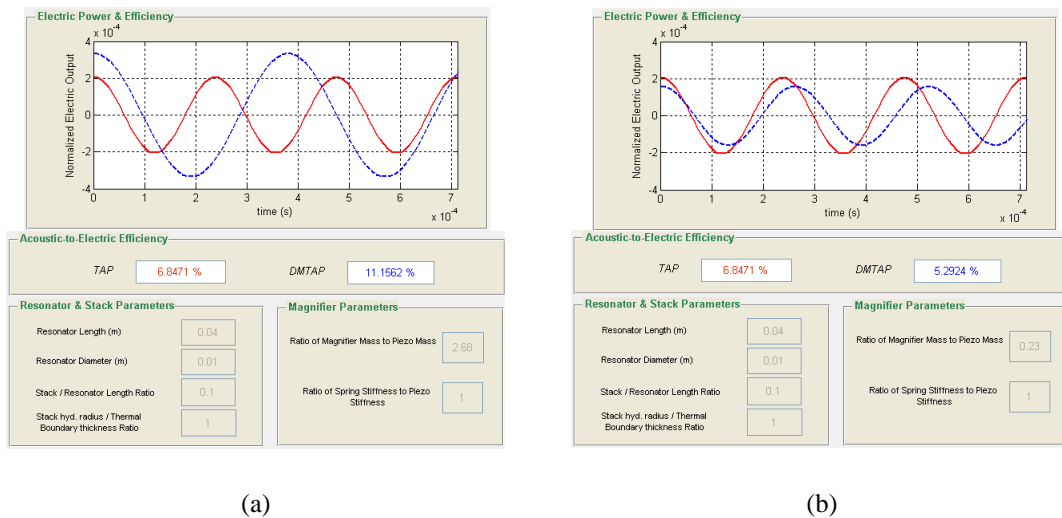


Figure 2.19 GUI screenshots: Effect of varying m_m on the normalized electric output and the acoustic-to-electric energy conversion efficiency resulting in (a) magnification and (b) demagnification [solid line: TAP , dashed line: $DMTAP$]

DMTAPs with carefully selected magnifier parameters can achieve as good as double the normalized piezo electric output ($\dot{E}_L \rho c / SA^2$) and acoustic-to-electric energy conversion efficiency (η_e) as shown in Figure 2.11 through Figure 2.14.

The *GUI* can be also deployed to examine the temperature effect of the *DMTAP* versus the *TAP* for different stack locations as discussed thoroughly in the previous section. Due to the nature of the equations governing the temperature gradients in the stack, and the dominant thermo-physical terms in these expressions, the type of the working gas used in the device makes a crucial difference in the expected temperatures. While the comparison shown in Figure 2.16 is carried out for an air filled resonator, the *GUI* allows for different options.

Figure 2.20 shows examples of two different working gases, namely air and hydrogen, and otherwise equal resonator, stack and piezo parameters. It can be seen that when using hydrogen, the *TAP* is deemed advantageous in terms of temperature difference as the onset difference required is less than the *DMTAP* for almost all stack locations. It's also shown that a generally lower temperature difference (200 *K* as opposed to 500 *K*) is required when using hydrogen instead of atmospheric air.

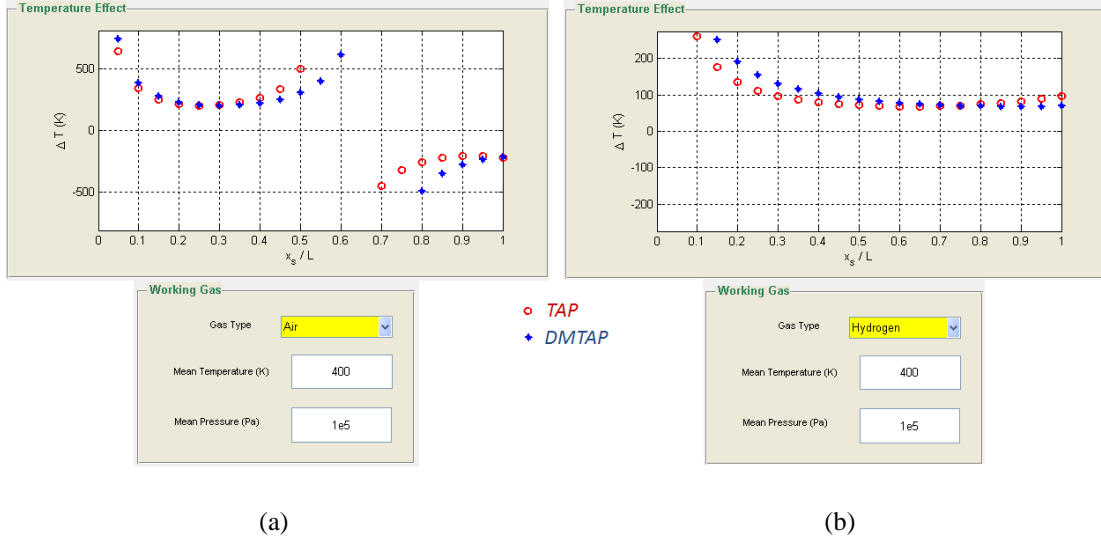


Figure 2.20 GUI screenshots: Effect of varying the working gas on the onset temperature difference expected in the stack for different stack locations. (a) Atmospheric Air. (b) Hydrogen.

2.9. Summary

This chapter has presented an in-depth analysis of standing wave thermoacoustic resonators integrated with piezoelectric elements. A comprehensive modeling approach has been discussed starting from the basic governing equations of plane waves in an acoustic cavity. A novel approach has been introduced aiming at enhancing the performance of this class of energy harvesters, namely the addition of dynamic magnifiers. Theory and comparative results have been provided that show the potential of the proposed design and its superiority over the conventional thermoacoustic piezo-electric harvesters.

A thermal analysis was used to discuss the governing equations in the stack region and comparisons again were made between both systems with reference to

areas of design interest such as the optimal stack placement and the required temperature gradient to onset the oscillations.

Finally, a *GUI* was presented that can ease the optimization and selection processes when designing an efficient dynamically magnified thermoacoustic-piezoelectric energy harvester.

Chapter 3

3. Design Optimization of Thermoacoustic-Piezoelectric Harvesters with Dynamic Magnifiers

3.1. Introduction

Dynamically magnified thermoacoustic-piezoelectric systems (*DMTAP*) can be advantageous when the appropriate properties of the magnifier are chosen. The *DMTAP* can be designed to achieve a higher efficiency than a conventional *TAP* of the same size, and/or a lower temperature gradient across the stack ends. While shown to be promising, no methodology has yet been discussed to aid the selection of the optimal parameters of the dynamic magnifier in order to improve the performance of the thermoacoustic-piezoelectric harvester.

This chapter attempts to devise rational design strategies to optimally select the magnifier parameters while satisfying a particular set of design constraints. First, single objective optimization is carried out based on three different design requirements: efficiency, power output and critical temperature difference to onset oscillations. Section 4 illustrates multi-objective optimization and discusses design tradeoffs and Pareto maps for different *DMTAP* prototypes.

3.2. Single Objective Optimization

A couple of prototypes are considered for performance analysis and optimization. Prototype 1 is a small scale harvester with a resonator length of 0.015 m, and a stack 10% of the resonator length. The properties of prototype 1 are chosen similar to the harvester presented in Chapter 2 for comparative purposes. The second design is a larger scale thermoacoustic-piezoelectric system that is 0.51 m long and has a stack that is 6% of the resonator length. The properties of prototype 2 are similar to those used in the experimental harvester presented in details in Chapter 4 but with a uniform resonator cross section area for simplicity. Table 3.1 lists dimensions and parameters of both designs.

We are concerned here with the optimization of two specific design goals: the acoustic to electric energy conversion efficiency η_e and the temperature difference ΔT required to onset oscillations. The computation cycle begins by matching the acoustic and structural impedances at the end of the tube is used to solve for the frequency of self-sustained oscillations and the wave number as per equation (2.28). Consequently, the oscillation pressure and velocity waveforms can be obtained from equations (2.1) and (2.2). Finally, equations (2.29) through (2.48) provide the energy balance needed to obtain the efficiency and the temperature difference.

Table 3.1 Design Parameters for 2 different prototype thermoacoustic-piezoelectric harvesters

	Symbol	Prototype 1	Prototype 2	Units
Resonator				
Length	L	0.015	0.51	m
Area	S	$7.85e-5$	$3.96e-3$	m^2
Stack				
Length (fraction of tube length)	$\Delta x / L$	0.1	0.06	
Spacing (fraction of thermal penetration depth)	y_o / δ_k	1	1	
Gas				
Type		Air	Air	
Mean Temp.	T_m	400	400	K
Mean Pressure	P_m	$1e5$	$1e5$	Pa
Piezo				
Area (fraction of tube area)	$1 / k_s$	1 / 4	1 / 4	
Mass	m	$3.46e-7$	$4.28e-3$	kg
Damping	b	$3.77e-5$	0.0021	kg / s
Stiffness	s	574	21300	N / m
Clamped Capacitance	C_p	$2.76e-8$	$1.8e-8$	F
Reciprocal Coupling Factor	ψ^2	$9.44e-9$	$19.5e-9$	$kg / s.\Omega$

3.2.1. Efficiency Oriented Design

Efficiency oriented optimization targets the magnifier parameters which will give the highest feasible η_e . The resulting optimum efficiency is compared with that of a conventional thermoacoustic-piezoelectric harvester. The optimization scheme is carried out using *MATLAB* minimization routines with an objective function denoted by $f_{obj} = 1 / \eta_e$ to ensure maximization of the efficiency. Assuming that both the *TAP* and *DMTAP*, under consideration, use the same piezo-element, same size resonator and stack and the same working gas, then the optimization variables are simply the

magnifier parameters and the electric load. For simplicity, k_m and c_m are ignored in this analysis, and the magnifier is modeled as a rigid mass with a spring connecting it to the piezo-element. The magnifier mass and spring stiffness are forced to lie within 1/10 to 10 times the piezo mass and stiffness respectively for practical considerations. The electric load is allowed to vary between 1Ω to $1 \text{M}\Omega$. Finally, the global search *MATLAB* toolbox is used to minimize f_{obj} starting at different initial points to ensure that the optimum f_{obj} point is a global rather than a local minimum. Figure 3.1 summarizes the optimization process.

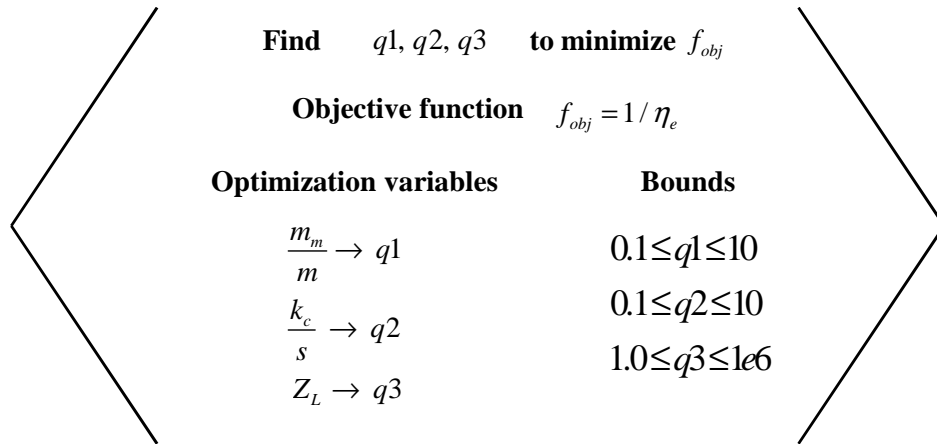
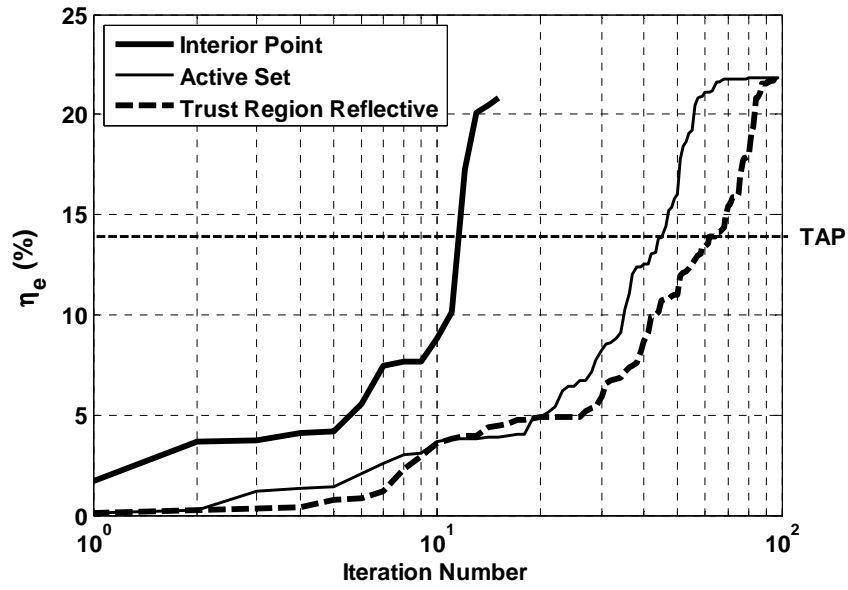


Figure 3.1 Optimization of η_e in a *DMTAP*: Objective function, variables and constraints

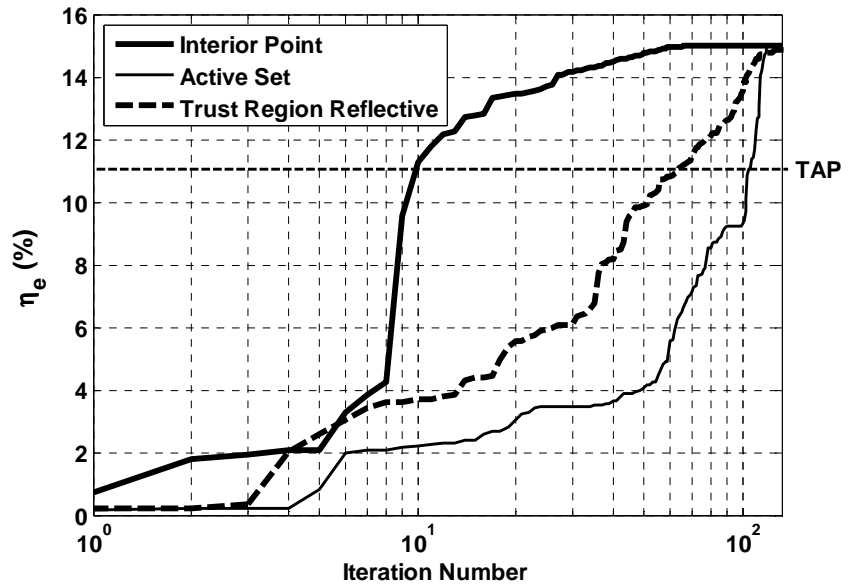
Changing the magnifier parameters continuously changes the dynamics of the acoustic wave in the resonator. Depending on the pressure and velocity patterns, it is determined how much acoustic power can be extracted at the end of the tube. The chosen values for m_m and k_c may result in a very stiff end, i.e. the behavior of the resonator approaches that of a rigid ended tube where $U(L) \approx 0$. This is undesirable

since small velocities at the resonator end will result in low acoustic power \dot{E}_T as per equation (2.30). Since η_e is the \dot{E}_L / \dot{E}_T ratio, a *DMTAP* having a higher efficiency than the *TAP* is not sufficient, because it may be the result of a low \dot{E}_T rather than an amplified \dot{E}_L . For this purpose, a post optimization filter is used to target the points having $\eta_{e,DMTAP} > \eta_{e,TAP}$ that also satisfy $\dot{E}_{L,DMTAP} > \dot{E}_{L,TAP}$, to ensure that electric energy harvested is amplified.

Figure 3.2 shows the highest feasible η_e that can be obtained for a *DMTAP* harvester for the two designs listed in Table 3.1 as obtained using three different *MATLAB* algorithms. These algorithms are namely: *Active Set*, *Interior Point*, and *Trust Region Reflective*. For prototype 1, it can be seen that a maximum η_e of 22.3 % is possible when a magnifier is attached to the prototype. This is achieved with a magnifier mass which is 5.23 times the piezo mass, and a spring of 8.29 the piezo stiffness. The piezo-element in this case is connected to an electric load of $2.3 \text{ k}\Omega$. This value is in very close agreement with that obtained in Chapter 2 for a device of the same geometry when connected to a load of $1 \text{ k}\Omega$. For the conventional *TAP* harvester working with the same load, η_e is 12.5 % only. The only room for efficiency improvement for a *TAP* harvester is through varying the electric load, and a maximum feasible η_e of 14.2% is found to take place at $Z_L = 1.36 \text{ k}\Omega$. This value is also in very close agreement with Chapter 2's result for a device of the same geometry when connected to a load of $1 \text{ k}\Omega$.



(a)



(b)

Figure 3.2 Maximum η_e for *DMTAP* harvester prototype 1 (a) and 2 (b) achieved using 3 different minimization based algorithms. Horizontal dotted line shows maximum *TAP* efficiency for comparison.

For prototype 2, a maximum *DMTAP* η_e of 15.1 % is possible. This is achieved with a magnifier mass 2.12 times the piezo mass, a spring of 9.7 the piezo stiffness, and an electric load of 46.3 k Ω , while the maximum *TAP* efficiency for this prototype is 10.9 % and takes place at a load of 26.5 k Ω . Note that three *MATLAB* optimization methods yield nearly the same optimum efficiency η_e but at different convergence rates with the *Interior Point* route exhibiting the fastest rate of convergence.

Figure 3.3 shows a contour of the $q_1 = m_m / m$, $q_2 = k_c / s$, and $q_3 = Z_L$ combinations and the corresponding efficiencies for the two *DMTAP* prototypes. Since the three design variables undergo optimization, it is not possible to look at their combined effect on a single 3-dimensional plot, but instead 2-D co-dependent plots are considered as shown. For the second prototype, it is observed here that the optimum selection occurs almost at k_c / s ratio of 9.7, which is close to the upper bound set for that variable. While this may suggest higher possible values of η_e if this ceiling is moved further, it has been confirmed that having k_c / s higher than 10 does not significantly improve the efficiency. In fact, η_e of 15.1 % can be also achieved with q_2 set equal to 4.7 which is shown in Figure 3.3 (b). From a practical point of view, working with a spring that is 20 times the piezo stiffness or a mass that is 20 times heavier than the piezo is less feasible.

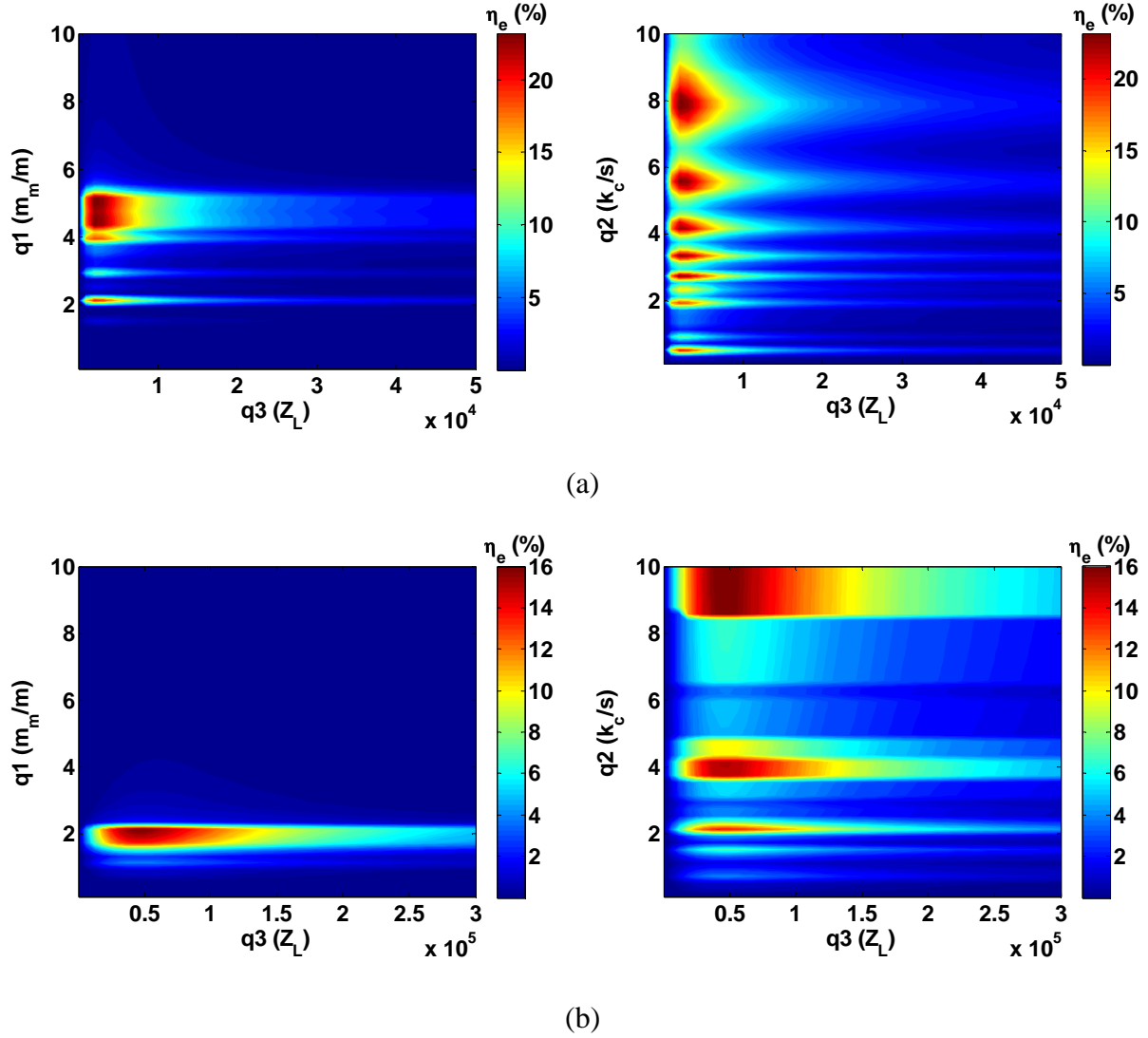
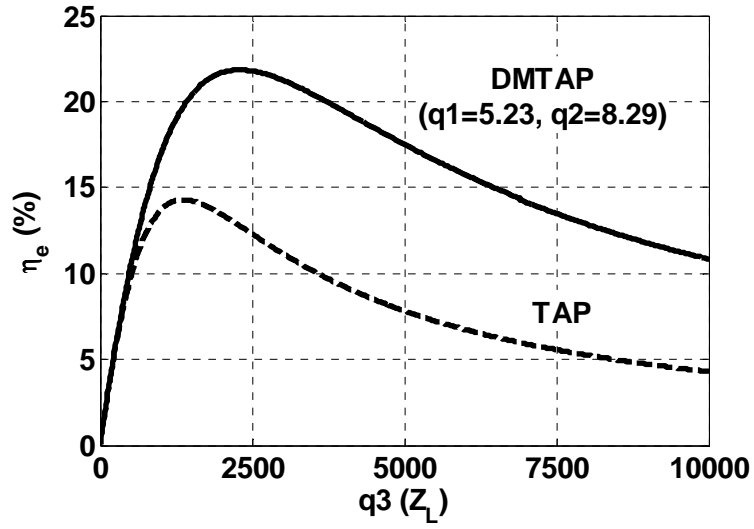


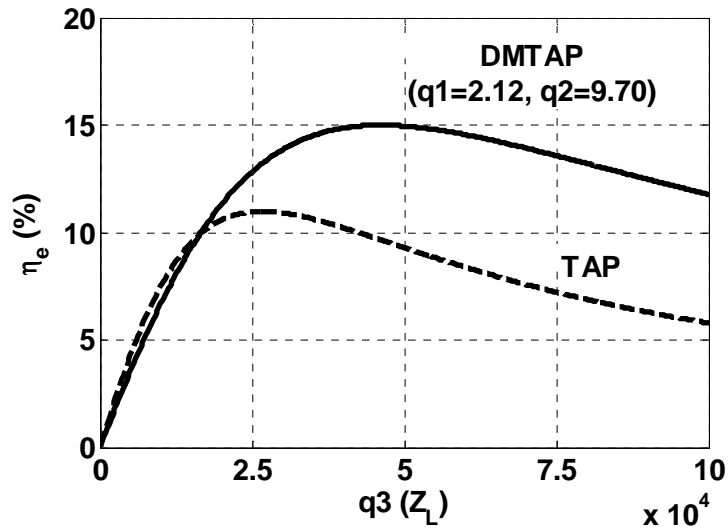
Figure 3.3 Variation of η_e with different combinations of $q_1 = m_m/m$, $q_2 = k_c / s$ and $q_3 = Z_L$ for DMTAP prototype 1 (a) and 2 (b)

Figure 3.4 shows a comparison between the harvesters with and without a magnifier, if the mass and stiffness ratios (q_1 and q_2) are fixed at the optimal values, while varying q_3 (electric load). This evidently shows that the DMTAP is superior in

terms of efficiency over the entire range of resistive loads and not only at the optimal point.



(a)



(b)

Figure 3.4 Variation of *TAP* and *DMTAP* efficiency η_e with the electric load Z_L for prototype 1 (a) and prototype 2 (b)

3.2.2. Power Oriented Design

Maximum efficiency points are not necessarily the points at which the piezo-transducer outputs maximum electric power. Instead these points are the points at which the maximum power \dot{E}_L is generated as a fraction of the available acoustic power \dot{E}_T at $x = L$. Therefore, another approach for optimizing the performance of a *DMTAP* is to target q_1 , q_2 and q_3 which will maximize \dot{E}_L irrespective of the magnitude of the incoming acoustic energy. The formulation of the optimization problem for this case is shown in Figure 3.5. Now, f_{obj} is set equal to $1/\dot{E}_{L,norm}$, where $\dot{E}_{L,norm}$ and V_{norm} are normalized forms of the electric power and voltage:

$$\dot{E}_{L,norm} = \frac{\rho c}{S} \dot{E}_L \quad (3.1)$$

$$V_{norm} = \frac{\rho c}{S} V \quad (3.2)$$

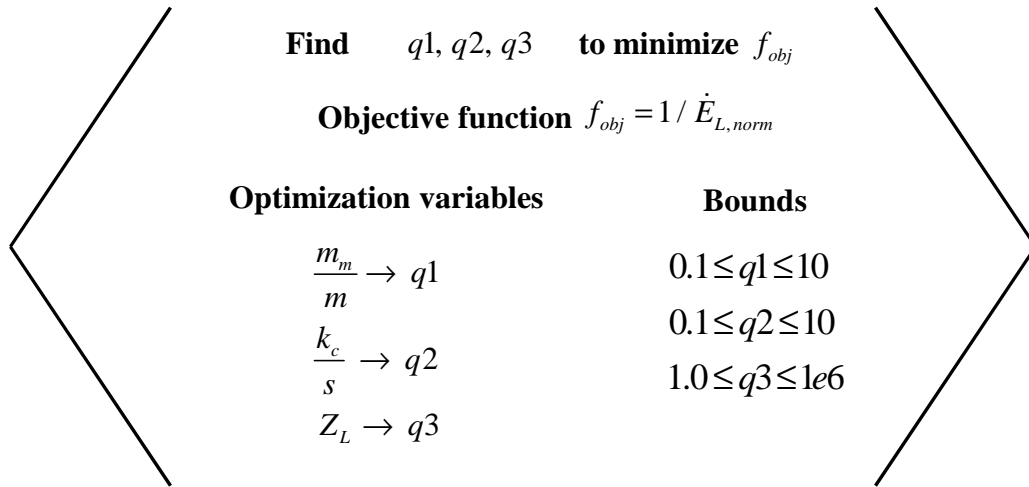
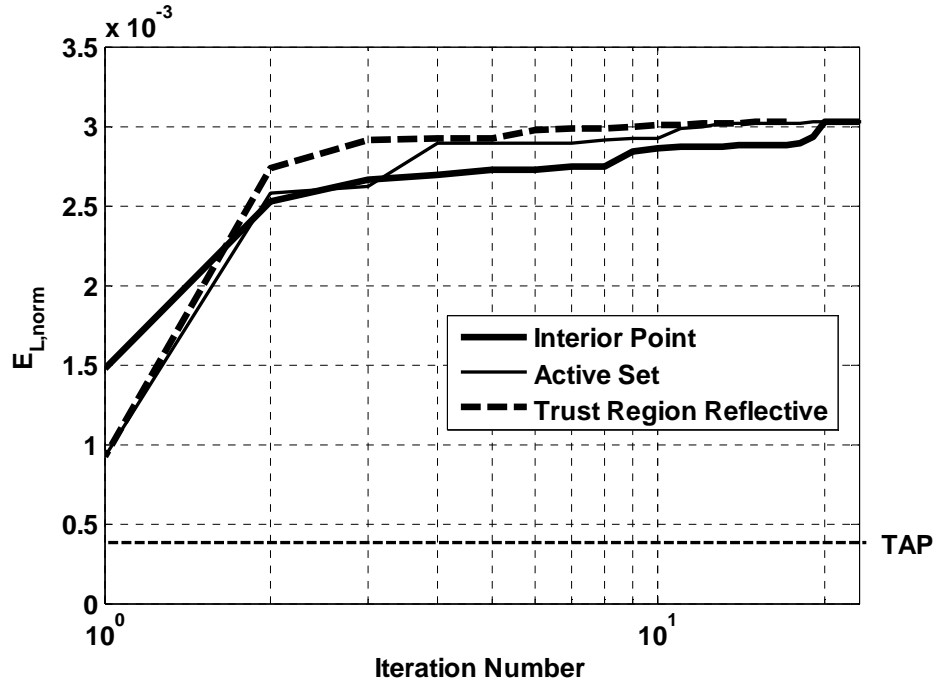


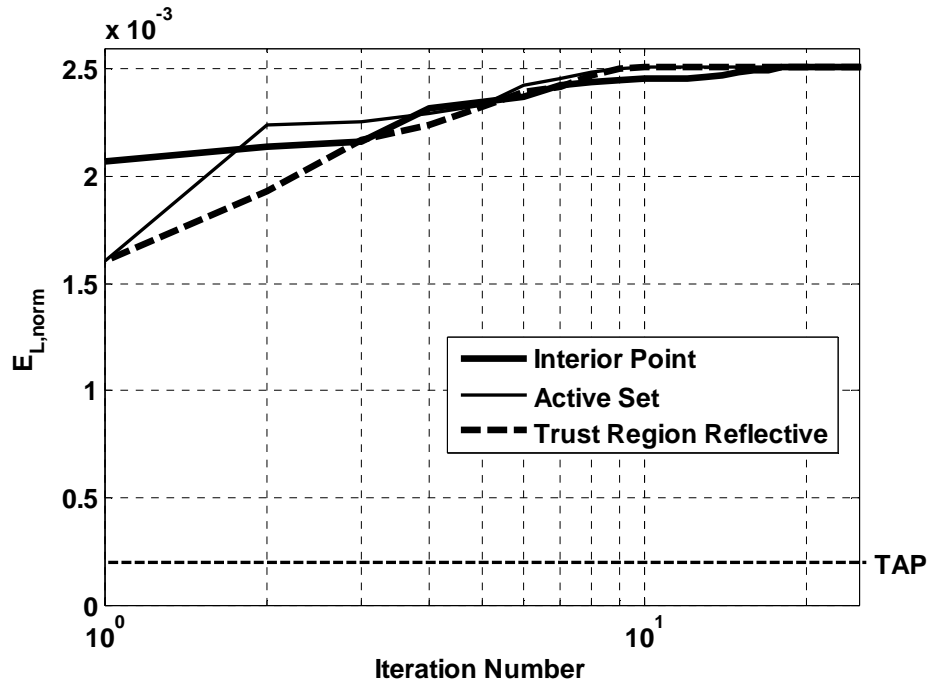
Figure 3.5 Optimization of electric power output E_L in a *DMTAP*: Objective function, variables and constraints

The Optimal values of $\dot{E}_{L, norm}$ for the small and the large prototypes are shown in Figure 3.6. With q_1 and q_2 fixed at the optimum values for power output determined from the iterations, Figure 3.7 shows how the normalized power output and voltage across the piezo-element vary with the change in q_3 (the electric load). It can be seen that the magnified prototypes 1 and 2 have the potential of generating respectively as much as 6 and 10 times the power generated by a conventional harvester of the same size if the magnifier parameters are optimally selected. The plot also shows that output voltage across the piezo-element can be tripled by using the magnifier. The maximum value of $\dot{E}_{L, norm}$ possible for the magnified prototypes 1 and 2 are 0.003 and 0.0025 compared to 0.00045 and 0.00025 for *TAP* harvesters of the same sizes.

It is helpful to note here that the $\dot{E}_{L, norm}$ values corresponding to the maximum efficiency points (Section 3.1) are 0.0026 and 0.0019 for the *DMTAP* harvesters confirming that maximum efficiency points are slightly different than maximum power output ones. Also, it is important to note that the three *MATLAB* optimization methods yield nearly the same energy norm $\dot{E}_{L, norm}$ at almost similar convergence rates.



(a)



(b)

Figure 3.6 Maximum normalized electric power $E_{L, norm}$ for DMTAP harvester prototype 1 (a) and 2 (b) achieved using 3 different minimization based algorithms. Dotted line shows maximum power for the TAP harvester for comparison.

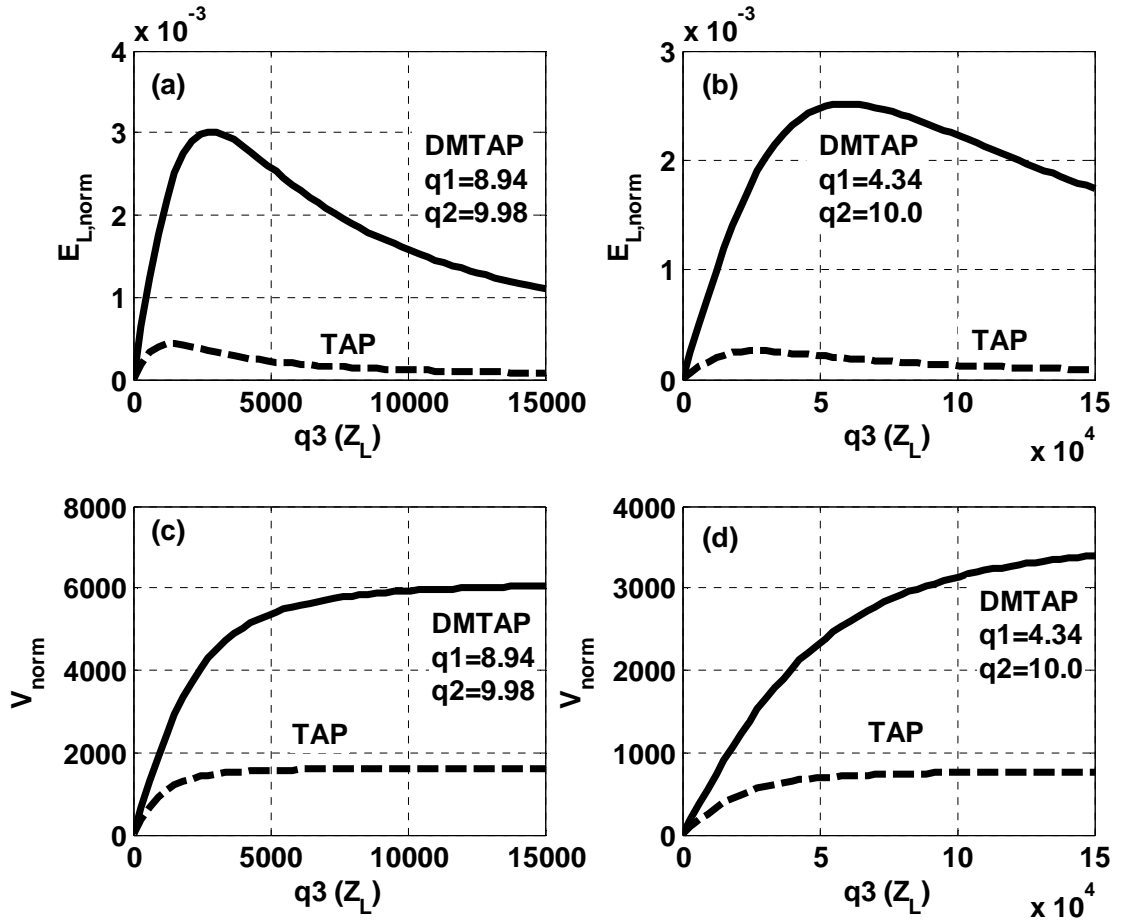


Figure 3.7 Variation of *TAP* and *DMTAP* normalized Power $E_{L, norm}$ and Voltage V_{norm} with the electric load Z_L for prototype 1 (a, c) and prototype 2 (b, d)

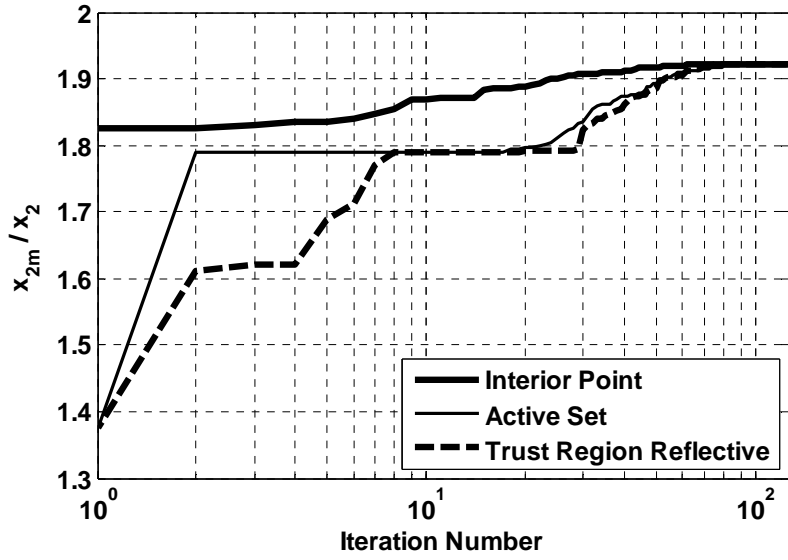
A magnification ratio is defined to be the ratio between the deflection x_{2m} of the piezo-element in the magnifier case and x_2 of the piezo-element in the conventional case. For two piezo-elements of the same material, characteristics and size, the ratio x_{2m} / x_2 that is greater than unity can be indicative of whether or not the piezo-element in the *DMTAP* harvester is generating more power than that of the *TAP*, since the voltage across the transducer and its deflection are linearly correlated.

Equation (3.3) which is derived from equations (2.16) and (2.24) shows the voltage - deflection relationship for the piezo-element,

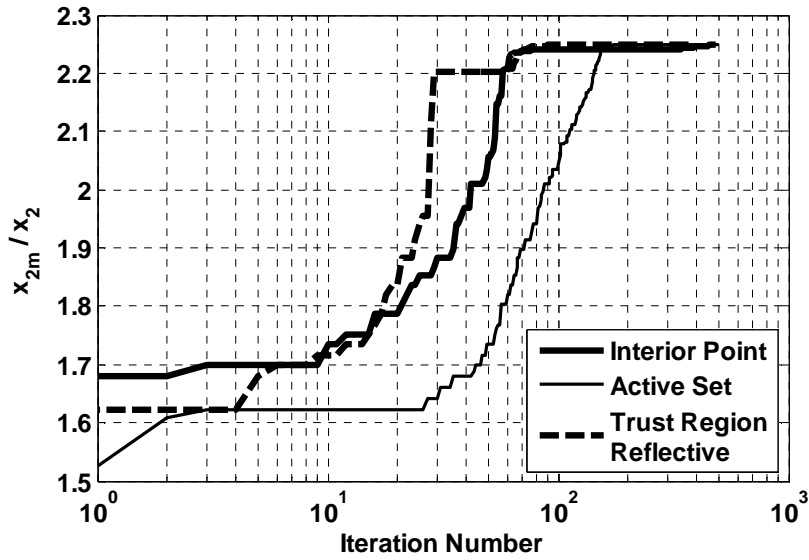
$$-\left(\frac{1+i\omega C_p Z_L}{i\omega s d_{33}}\right)V = \begin{cases} x_2 & \rightarrow TAP \\ x_{2m} & \rightarrow DMTAP \end{cases} \quad (3.3)$$

Hence, optimization of the ratio x_{2m} / x_2 could be also used as an alternative metric for selecting the operating points with maximum output power.

Figure 3.8 shows the optimization of the magnification ratio for both prototypes. It is observed that while voltage can be magnified up to 3 times by using dynamic magnification, the magnification ratio only goes up to 1.93 for the case of prototype 1 and 2.35 for prototype 2. This is attributed to the fact that the *TAP* and the *DMTAP* of the same size operate at slightly different frequencies as implied by equations (2.21) and (2.27). This is an inherent factor in equation (3.3) explaining why the voltage amplification ratio can be slightly different than the magnification ratio x_{2m} / x_2 .



(a)



(b)

Figure 3.8 Maximum magnification ratio x_{2m}/x_2 for DMTAP harvester prototype 1 (a) and 2 (b) achieved using 3 different minimization based algorithms.

3.2.3. Temperature Oriented Design

Minimizing the temperature gradient across the stack ends which is required to operate thermoacoustic harvesters will decrease the input thermal energy needed to drive the harvester, and thus will function as another way to improve the overall efficiency of a thermoacoustic-piezoelectric system. Adding the magnifier to the *TAP* system shifts the frequency of the self-sustained oscillations due to the associated changes of the impedance at $x = L$. This alters the pressure and velocity waveforms inside the resonator. The required temperature difference for a stack of a given length is a function of the acoustic pressure and velocity at the stack center location as well as the frequency among other parameters as discussed earlier in Equation (2.47). Therefore, it is possible to choose q_1 , q_2 and q_3 such that ΔT is minimized. A stack center location of 1/5 the tube length is chosen for comparison purposes as this location is known to be the optimal stack placement for standing wave harvesters [33]. In this case, f_{obj} is set to ΔT at $x_s / L = 0.2$.

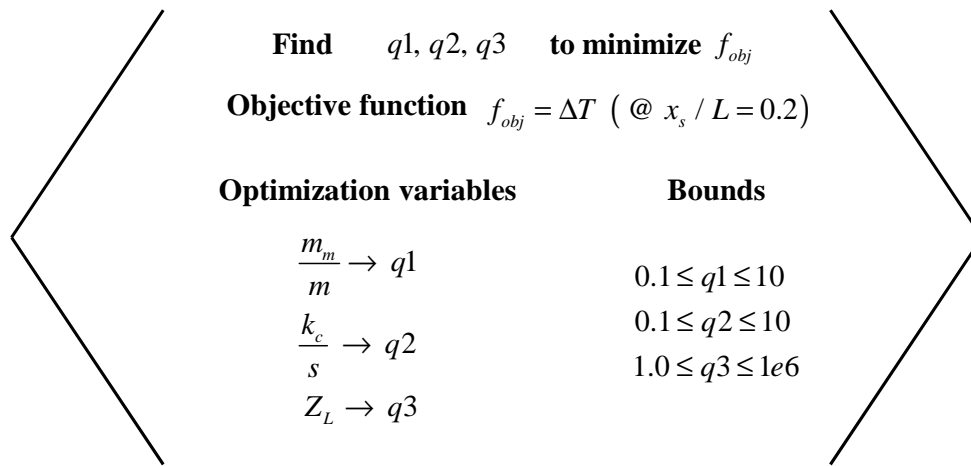
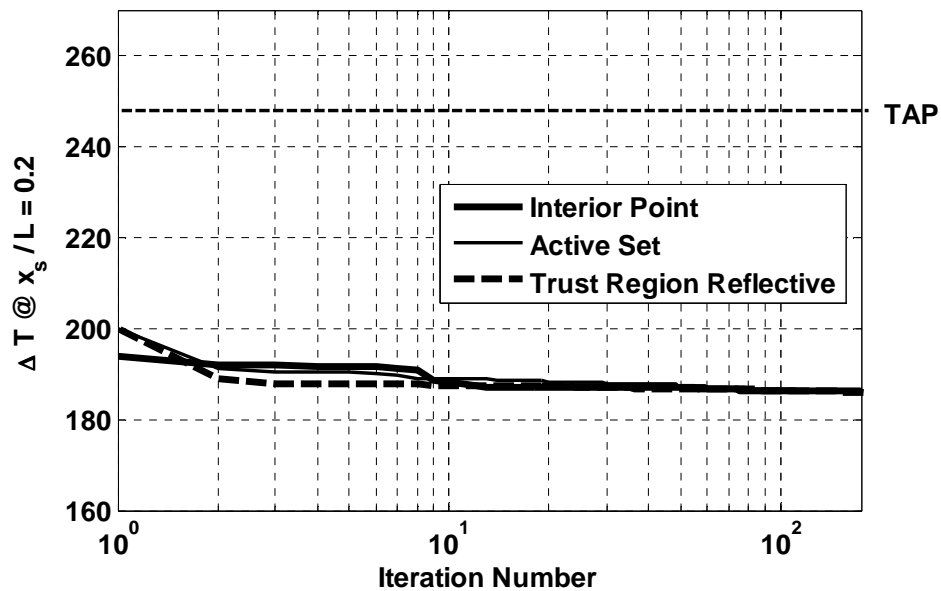
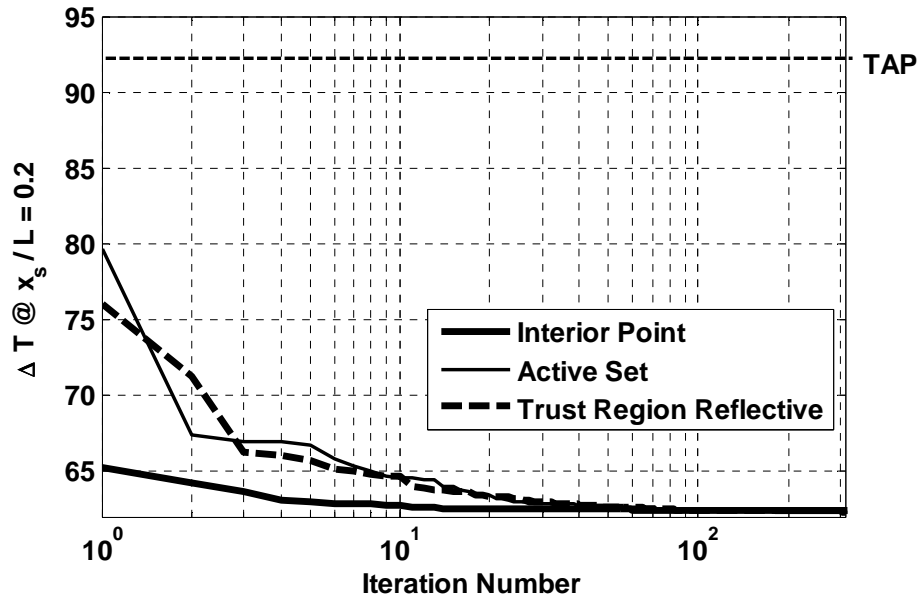


Figure 3.9 Optimization of ΔT at $x_s / L = 0.2$ in a *DMTAP*: Objective function, variables and constraints

Figure 3.10 shows that tuning the magnifier parameters can reduce the temperature difference required to sustain oscillations significantly, from around 247 K to 186 K for the small device, and from 92 K to 63 K for the large device. However, η_e associated with these settings is drastically lower. This calls for multi-objective optimization that balances between the need for a low temperature gradient for a lower thermal power input and a high acoustic to electric power conversion efficiency in the piezo-transducer.



(a)



(b)

Figure 3.10 Minimum temperature difference required across a stack placed at 1/5 the resonator length to onset oscillations for *DMTAP* harvester prototype 1 (a) and 2 (b) achieved using 3 different minimization based. Horizontal line shows minimum temperature difference required for the *TAP* harvester for comparison.

3.3. Multi-Objective Optimization

The goal behind multi-objective optimization of the *DMTAP* is to maximize the device efficiency while keeping the temperature difference across the stack ends within acceptable limits, or to minimize the temperature difference while preventing the efficiency from significantly deteriorating. This is achieved by giving weights to both design objectives to weigh the importance of each in the optimization process.

The three optimization variables q_1 , q_2 and q_3 are then chosen to minimize the new multi-objective function f_{MO} given by,

$$f_{MO} = \left(W_i \frac{\eta_{e, \max}}{\eta_e} \right) + \left(W_j \frac{\Delta T}{\Delta T_{\min}} \right) \quad (3.4)$$

where W_i and W_j are relative weights given to the efficiency and the temperature objectives respectively to indicate whether the optimization is more lenient towards maximizing η_e or towards lowering ΔT . W_i and W_j are structured such that,

$$0 \leq W_i \leq 1 \quad (3.5)$$

and,
$$W_j = 1 - W_i \quad (3.6)$$

at all times. Note that $\eta_{e, \max}$ and ΔT_{\min} represent the maximum feasible efficiency and minimum feasible temperature difference for each *DMTAP* prototype, previously estimated in section 3. For any given W_i and W_j , the minimum possible value for f_{MO} is 1, and occurs at $\eta_e = \eta_{e, \max}$ and $\Delta T = \Delta T_{\min}$. For any other combination of the optimization variables, η_e is expected to be less than $\eta_{e, \max}$ and ΔT greater than ΔT_{\min} giving f_{MO} that is greater than 1.

Figure 3.11 shows a multi-objective optimization for a case where the optimization weights are set to $W_i = 0.25$ and $W_j = 0.75$ for the two *DMTAP*

prototypes. The iterations converge to $f_{MO}=1$ which represents the point with maximum η_e and lowest ΔT satisfying those optimization weights.

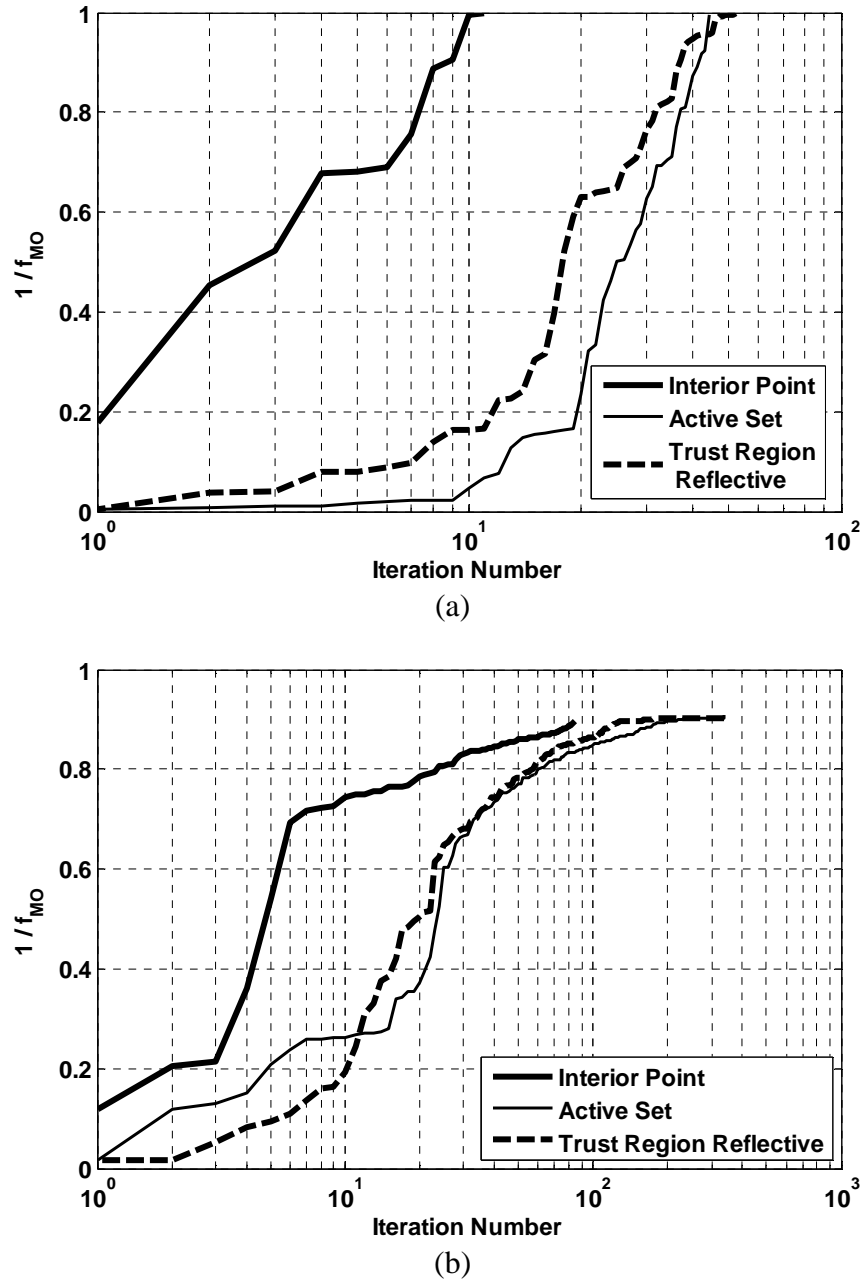


Figure 3.11 Multi-objective optimization for a case with $W_i = 0.25$, $W_j = 0.75$ for *DMTAP* harvester prototype 1 (a) and 2 (b) achieved using 3 different minimization algorithms. Point with maximum η_e and lowest ΔT to satisfy the optimization weights is located at $f_{MO} = 1$.

A set of multi-objective optimization runs can be carried out with W_i varied across the domain from 0 to 1 with considerably small increments while estimating the optimal efficiency and temperature difference each time that satisfy the corresponding weights. The outcome of such a procedure gives a combination of efficiencies and temperature differences that satisfy different design objectives, starting from an efficiency oriented design to a temperature oriented design. The line connecting those points is referred to as the Pareto front and represents a key design optimization map. Any combination of η_e and ΔT that lies above the Pareto line represent an operation point that can be further optimized, while any combination underneath the line should not be feasible.

Table 3.2 shows a sample of the weights W_i and W_j used to build up the Pareto map, while Figure 3.12 (a) and (b) shows the map for both *DMTAP* harvester prototypes. Both figures confirm the results obtained earlier using the single objective optimizations starting at the point of minimum feasible temperature difference across the stack ends (186 K for prototype 1 and 63 K for prototype 2) to the maximum possible acoustic to electric energy conversion efficiency for both sizes (22.3 % for prototype 1 and 15.1 % for prototype 2).

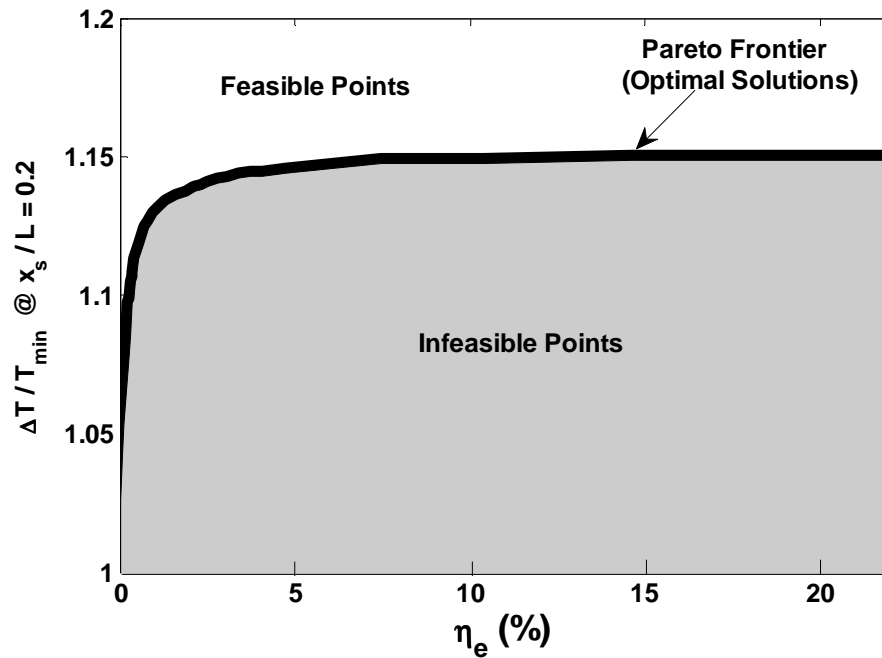
Firstly noted, is the fact that the highest temperature difference required for both *DMTAP* prototypes still remains lower than that incurred by *TAP* harvesters of the same size. The last row in Table 3.2 shows a temperature difference of 213.21 K and 81.31 K for prototypes 1 and 2 respectively, even when the weight given to the

temperature objective in the optimization process is zero. The temperature difference required for *TAP* harvesters of the same size was estimated to be 247 K and 92 K.

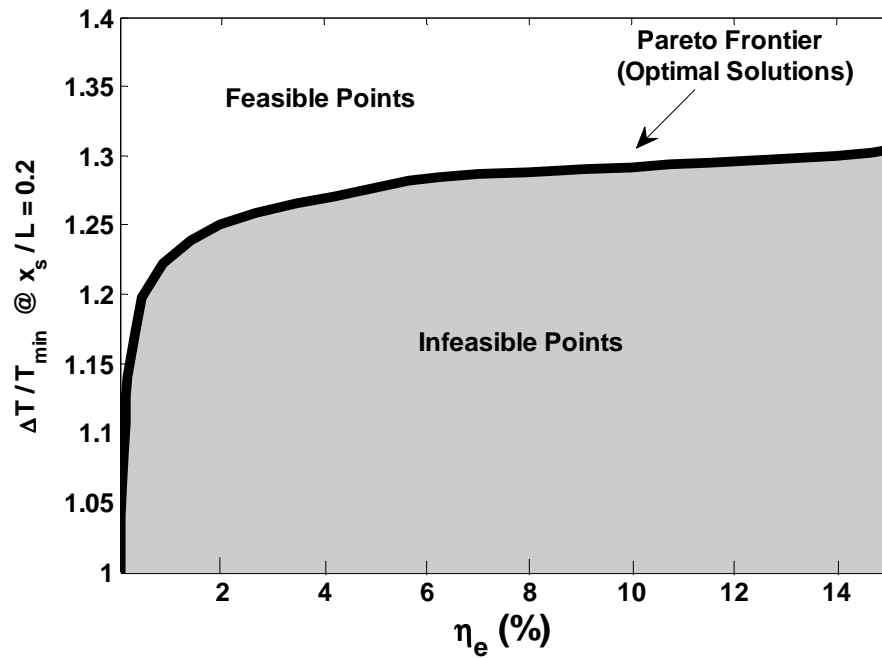
The second observation that can be drawn from Figure 3.12 is that for the 2 designs listed in Table 3.1, it is challenging to work out a good balance between a good efficiency and a low temperature difference. This is represented by the sharpness of the Pareto line curvature. For prototype 1 for example, to reduce the temperature difference from around 213 K to 212 K by varying the magnifier parameters, an efficiency drop from 22.3 % to about 3.5 % is inevitable. Looking into ways to enhance the Pareto pattern and hence find a good balance between different design objectives can be an area of further investigation.

Table 3.2 Maximum feasible efficiency and minimum temperature difference for the *DMTAP* harvesters for different objective weights using a multi-objective optimization algorithm

Weights		Prototype 1		Prototype 2		Comment
W_i	W_j	η_e (%)	$\Delta T_{(x_s/L=0.2)}$ (K)	η_e (%)	$\Delta T_{(x_s/L=0.2)}$ (K)	
0	1	~ 0	185.63	~ 0	62.31	Min. temp. difference
0.0139	0.9861	0.043	190.64	0.0186	64.14	
0.0268	0.9732	0.069	193.32	0.028	64.78	
0.0518	0.9482	0.118	195.71	0.056	66.31	
0.1	0.9	0.234	200.10	0.081	67.64	
0.1638	0.8362	0.553	206.80	0.142	71.01	
0.3162	0.6838	1.17	210.12	0.441	74.65	
0.6105	0.3895	3.429	212.23	0.835	76.17	
0.8483	0.1517	7.465	213.13	4.92	79.5	
1	0	22.3	213.21	15.1	81.31	Maximum efficiency



(a)



(b)

Figure 3.12 Pareto map for a *DMTAP* harvester prototype 1 (a) and 2 (b). Line starts at optimum point for objective 1: minimum ΔT and ends with optimum point for objective 2: maximum η_e . Points above the line are feasible and underneath it are not.

3.4. Summary

This chapter has presented different methods and approaches to optimize the performance of thermoacoustic-piezoelectric harvesters augmented with dynamic magnifiers. A detailed overview of the optimization schemes was discussed. It was shown that the outcome of the optimization process relies heavily on the design objective. Details were given on how to compute best efficiency, highest power and lower temperature difference settings, as well as multi-objective optimization. Two different sizes of prototypes of the energy harvesters were considered. An acoustic to electric energy conversion efficiency 1.6 times that obtained by conventional harvesters, as well as a temperature difference that is $3/4$ of that required for the conventional harvester was theoretically deemed feasible for both prototypes.

The obtained results demonstrate the potential of *DMTAP* systems as effective energy harvesters when the design parameters are adequately tuned. The presented techniques can serve as invaluable tools to aid the design, build up and further analysis of such prototypes. The next chapter experimentally validates the proposed theory and mechanisms in practical terms.

Chapter 4

4. Experimental Investigation of Thermoacoustic-Piezoelectric Harvesters with Dynamic Magnifiers

4.1. Introduction

This chapter presents the different experiments carried out in attempts to validate the theoretical predictions of chapters 2 and 3. It starts off by introducing the experimental prototype used for the standing wave thermoacoustic-piezoelectric harvester (*TAP*). Experimental data of the harvester's performance in terms of frequency, pressure, velocity, temperature, power output and efficiency is compared with those obtained previously from the theoretical analysis, finite element model and the numerical thermoacoustic modeling software *DeltaEC*.

Next, an attempt to examine the potential of the dynamic magnification concept is demonstrated. The experimental prototype of the *DMTAP* is presented. Results show obvious magnification in the strain experienced by the piezo-element, and expectedly the voltage output, upon proper choice of magnifier constants. Electric output is measured as well to confirm and calibrate the results obtained from measuring the piezo deflection. The experiments carried out through the chapter are used to validate the theory and modeling presented in Chapters 2 and 3.

4.2. Standing wave thermoacoustic-piezoelectric harvester (TAP)

4.2.1. Experimental Setup

A schematic drawing of the *TAP* used is shown in Figure 4.1. The resonator consists of five sections: a heat cavity, stack, resonator tube, Helmholtz resonator cavity, and a piezoelectric diaphragm. The heat source generates a temperature gradient along the stack which in turn produces standing acoustic waves in the resonator tube and cavity. The oscillation energy of the acoustic waves is amplified by the Helmholtz-like resonator and harnessed by the piezoelectric diaphragm which converts the incident pressure pulsations directly into electrical energy to power the load Z_L , eliminating the need for any moving parts. Figure 4.2 shows the *TAP* used in the experiments and modeled using *DeltaEC*.

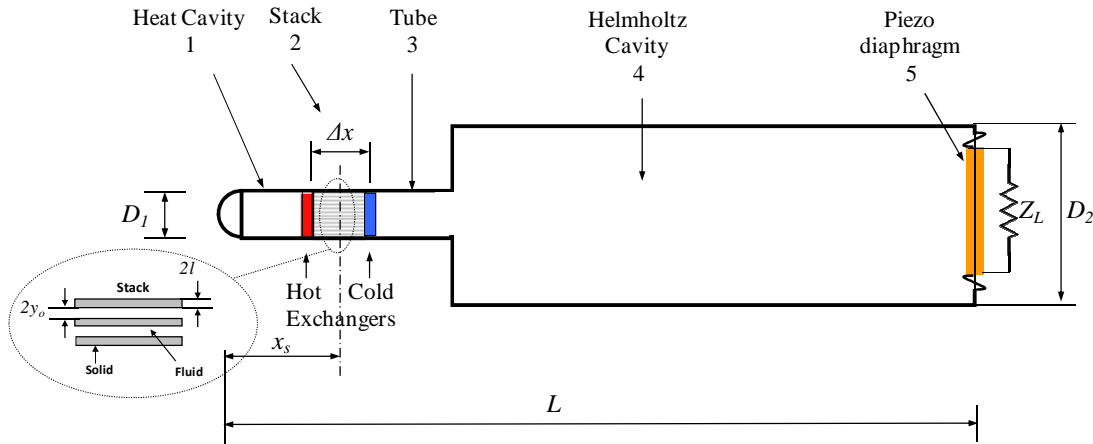


Figure 4.1 Schematic drawing of the standing wave thermoacoustic-piezoelectric harvester (*TAP*)

Modeling thermoacoustic-piezoelectric systems using *DeltaEC* is carried out by the help of finite element modeling of the piezo-diaphragm. Details on how to

incorporate piezo-elements in thermoacoustic modeling using *DeltaEC* is provided in Appendix A. Table 4.1 lists the main dimensions and geometrical parameters of the *TAP* used in the experiments, while Table 4.2 provides information about the thermo-physical parameters of the working gas as well as some other operating parameters such as the frequency of oscillations.

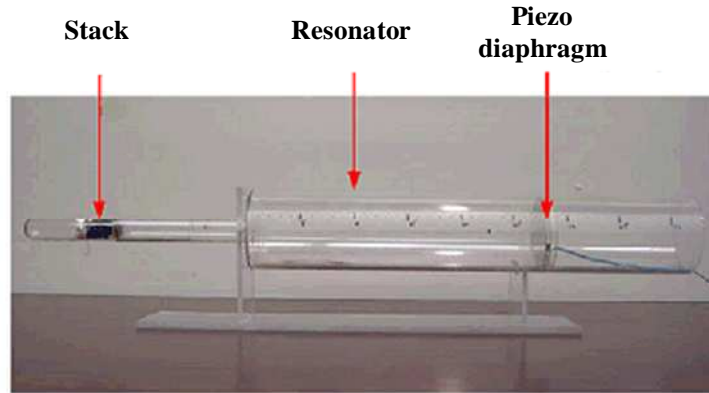


Figure 4.2 *TAP* harvester used in experiments

Table 4.1 Main geometrical parameters of the *TAP*

Resonator		Heat Exchangers (HX)		Stack	
Total Length L	51 cm (= $\lambda / 2$) [*]	HX ^{**} thickness t_{HX}	7.5 mm	Length Δx	33.75 mm
Tube Diameter D	$D_1 = 19.5$ mm $D_2 = 71$ mm	HX Blockage Ratio BR_{HX}	0.75	Hydraulic Radius y_o (i.e. half-plate spacing)	~ 0.34 mm
				Stack Blockage Ratio BR_s	0.75

* λ = wavelength, ** *HX* = Heat Exchangers

Table 4.2 Thermo-physical properties of the working gas and operating parameters of the *TAP*

Working Gas	
Gas type	Atmospheric Air
Isobaric to Isochoric Specific Heat Ratio γ	1.4
Speed of sound in gas at mean temperature T_m	469.03 m/s
Density ρ (at 790 K)	0.441 kg/m ³
Density ρ (at 305 K)	1.142 kg/m ³
Isobaric Specific Heat c_p	1004.7 J/kg K
Avg. Thermal Expansion Coefficient β	1.826e-3 K ⁻¹
Thermal Conductivity K_c	2.5694e-2 W/m K
Prandtl Number σ	~ 0.631
Viscosity μ	1.8127e-5 kg m/s
Mean Pressure P_m	10 ⁵ Pa
Other Parameters	
Frequency of Operation ω	359.44 Hz
Avg. Viscous Penetration Depth δ_v	2.6871E-04 m
Avg. Thermal Penetration Depth δ_k	3.3812E-04 m

4.2.2. Temperature Distribution

The performance of the *TAP* is determined experimentally for the prototype shown in Figure 4.2. An electrical heater in the form of a resistance wire is used to simulate the hot heat exchanger and hence the heat input. The heater provides the input thermal energy necessary to onset the self-sustained acoustic waves. For the *TAP* under consideration, such a condition is attained when the heater thermal power input \dot{Q}_{in} is equal to 44.82 watts.

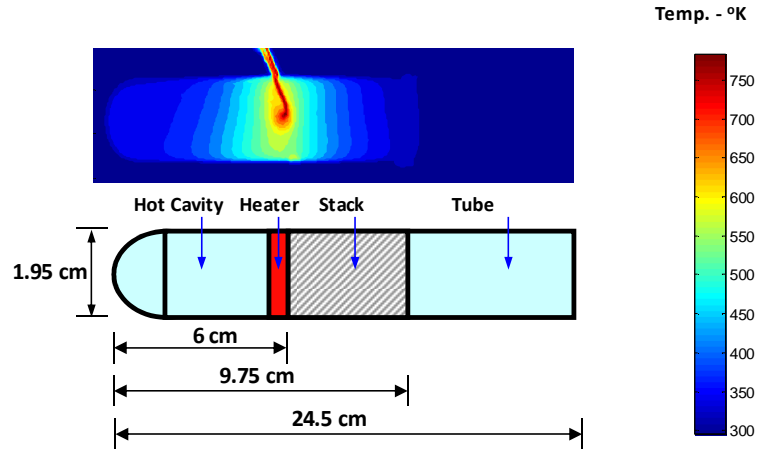


Figure 4.3 Temperature contours inside a section of the *TAP* resonator

The temperature distribution inside the resonator is measured using an infrared camera (ThermaCAM® SC3000, from FLIR Systems, Boston, MA). The camera has an image resolution of 320 x 240 pixels with a sensitivity of less than 20 m°C at a temperature of 30 °C. It can operate over the range of temperatures between -20 °C up to 2000 °C. Figure 4.3 shows the temperature distribution as measured for the *TAP* prototype indicating a maximum temperature of 790 K, and a temperature slope down to around 305 K across the stack length (33.75 mm) yielding an approximate linear gradient of about 1.29×10^{-4} K/m. Figure 4.4 shows the temperature distribution obtained from a *DeltaEC* model for the *TAP* based on the procedure described in Appendix (A). Close agreement is evident between the experiment and the predictions.

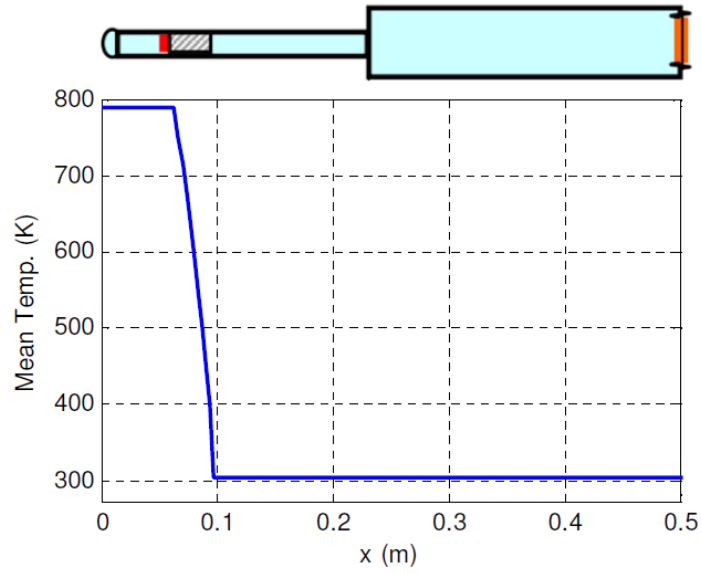


Figure 4.4 Temperature distribution along the *TAP* resonator (*DeltaEC*)

4.2.3. Pressure Propagation

Figure 4.5 shows the amplitudes of pressure P and volume velocity Q (also denoted as volumetric flow rate) as predicted by *DeltaEC* along the resonator. The plot shows that a pressure node and a corresponding velocity anti-node are expected to occur at about 30 cm from the nose end.

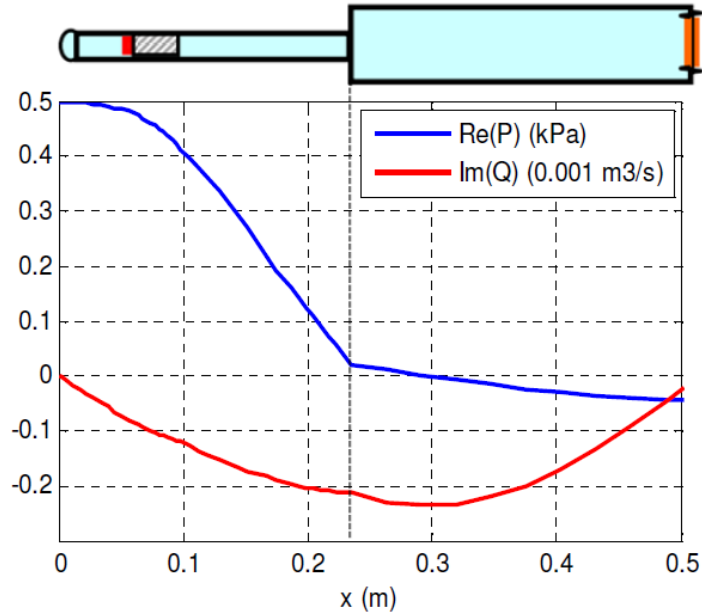


Figure 4.5 Theoretical prediction for pressure and volume velocity distribution inside the *TAP*

To verify the predicted pressure distribution experimentally, the pressure level along the Helmholtz-like resonator is measured using a microphone mounted at the end of a sliding arm. The measurements were taken as the microphone is moved, on discrete steps, along the resonator gradually and the pressure is recorded at these discrete locations. Figure 4.6 shows a comparison between the experimentally obtained values and the predictions of *DeltaEC*. The experiments are in good agreement with the predictions near the pressure node but some discrepancies are observed near the two ends of the resonator. These discrepancies can be attributed to the interference with the boundaries of the resonator and unaccounted for friction/viscous losses.

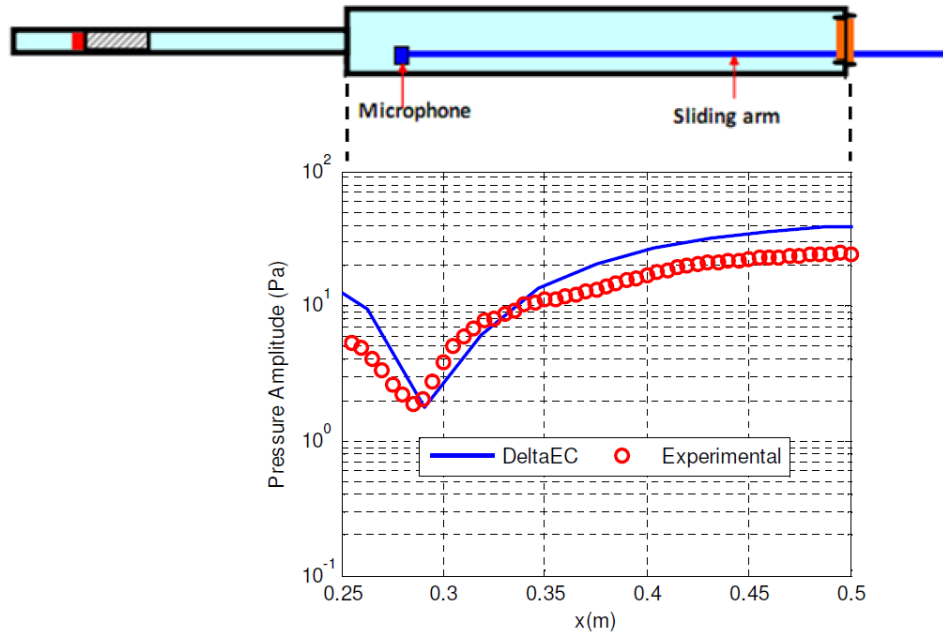


Figure 4.6 Experimental versus *DeltaEC* data for the pressure level across the resonator

4.2.4. Velocity Flow Field

The velocity distribution inside the resonator is measured using the 3D stereoscopic imaging Particle Image Velocimetry (PIV) system from LaVision, Inc. (Ypsilanti, MI). The system uses a high speed camera to image illuminated flow particles, injected inside the resonator. The combination of successive camera projections separated by a defined time increment allows the reconstruction of the real particle displacement inside the measurement area and the velocity components. The experimental assembly for this procedure is shown in Figure 4.7.

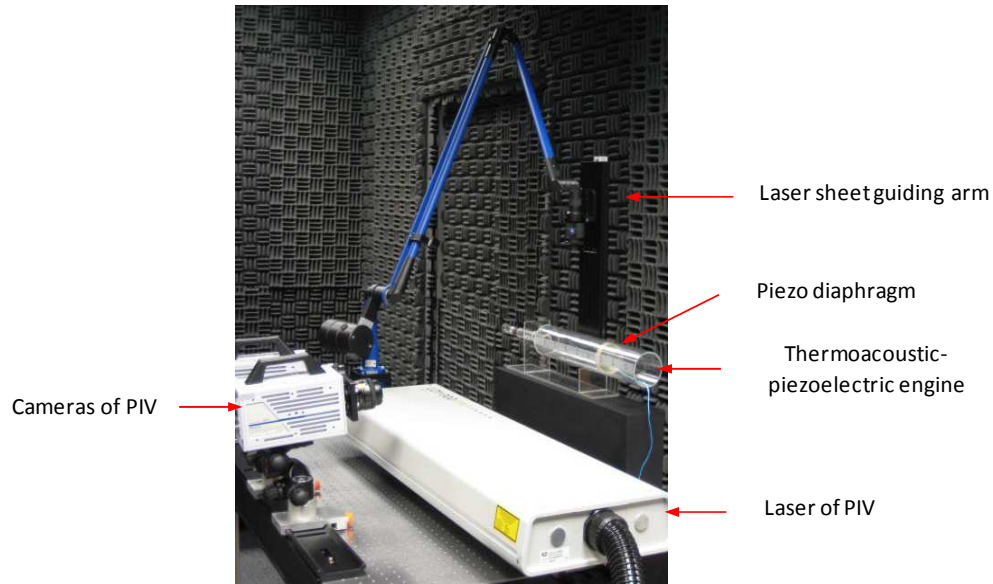


Figure 4.7 Measurement of velocity distribution inside the *TAP* using 3D Stereoscopic Particle Image Velocimetry (PIV)

The instantaneous velocity vectors of the oscillating laminated particles in the resonator are calculated upon processing of each two successive camera images using correlation schemes. Briefly explained, the particle images in the first camera exposure and the second camera exposure are placed on top of each other. For each particle image in the first exposure, all possible matches with particle images in the second exposure are considered, and those possibilities are represented as peaks in a map, referred to as the “*correlation map*” [45]. Each possible match receives a weight, indicated as the amplitude of the peaks in the map. Eventually, one peak prevails and becomes the highest revealing the most probable match and hence the most probable displacement of each particle. This process is repeated for a large number of successive images to capture the entire waveform.

The shape of such correlation maps are an indication of how good a set of PIV measurement data are. The more distinct a correlation map peak is, and the higher it is compared to other peaks on the map, the more likely the calculated velocity vectors are descriptive of the actual path of the gas particles. Figure 4.8 shows the contrast between acceptable and mediocre PIV correlation maps.

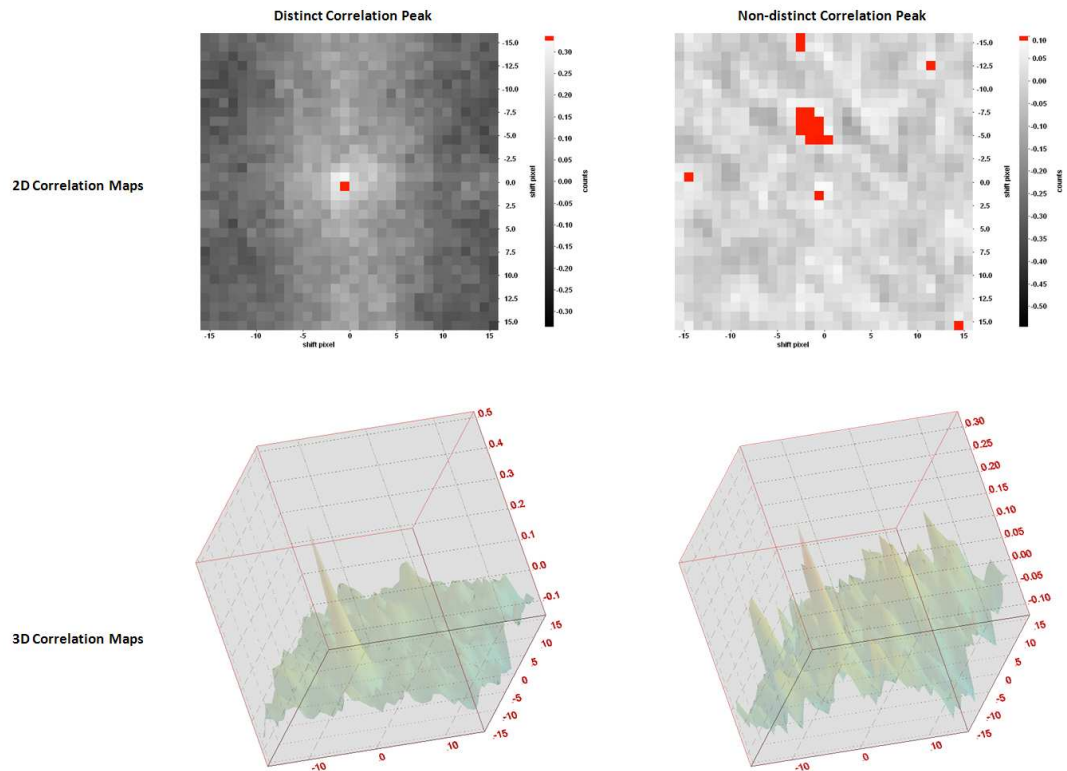


Figure 4.8 Particle Image Velocimetry Correlation Maps

Figure 4.9 and Figure 4.10 show velocity distributions of the working gas particles at four different locations inside the resonator tube, while Figure 4.11 shows the correlation maps taken at random points in the those four locations to validate the produced results. The displayed distributions are recorded at five time instances

during the acoustic wave oscillation cycle. The different instances are separated by one quarter of the oscillation periodic time τ_{TAP} .

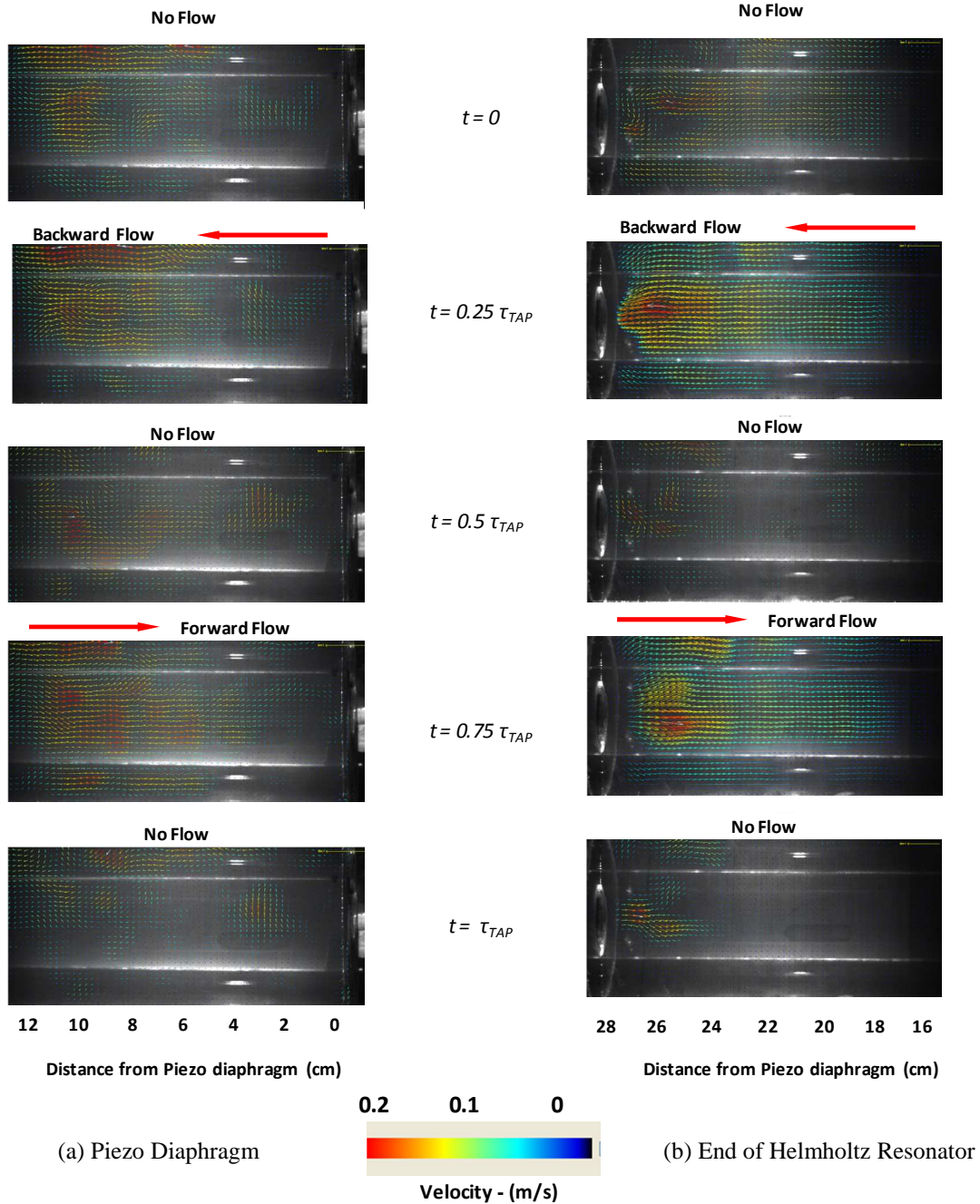


Figure 4.9 Flow distribution of the TAP at a section (a) adjacent to the piezo diaphragm and (b) at the end of the Helmholtz resonator

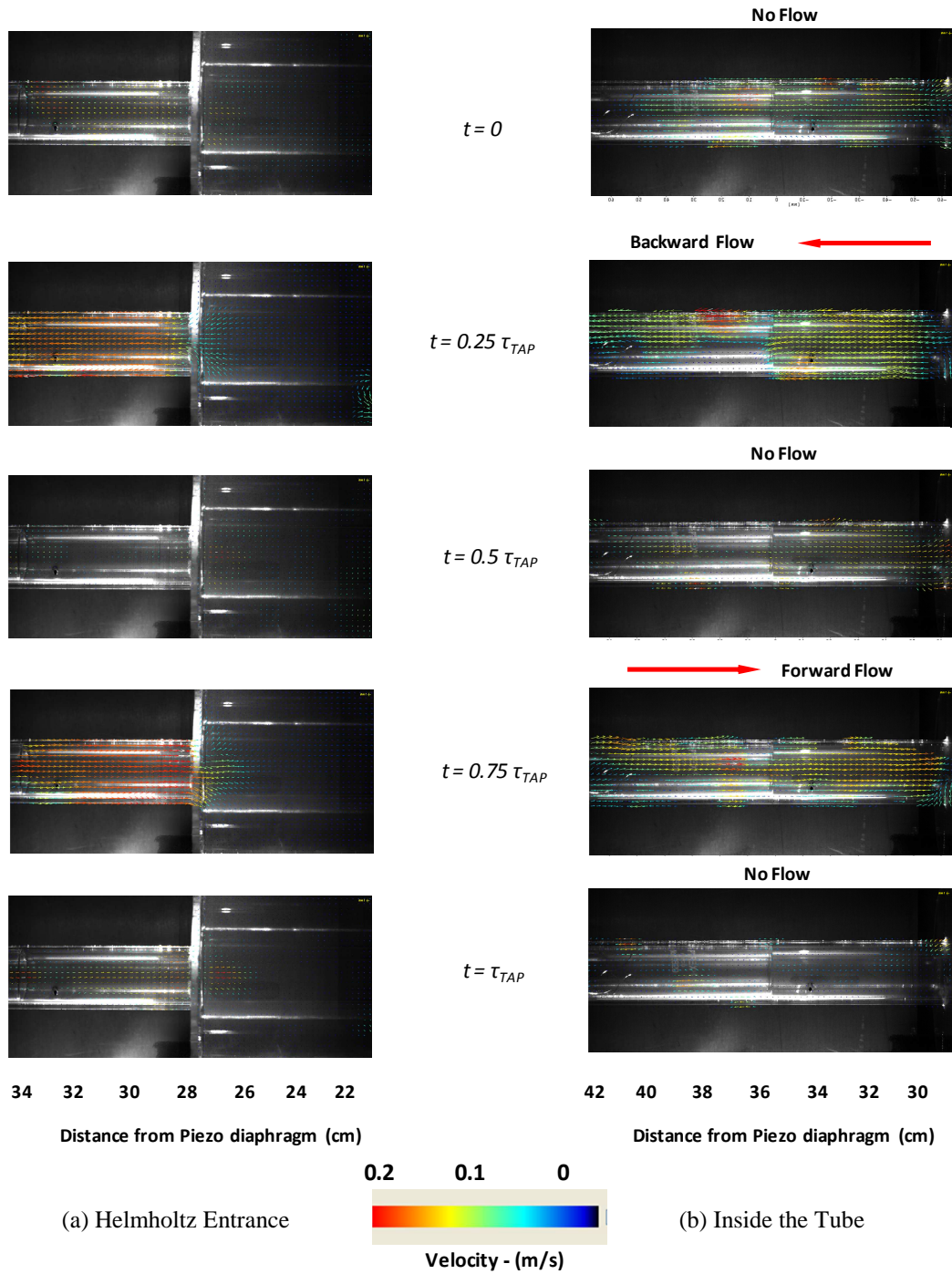


Figure 4.10 Flow distribution of the TAP at (a) the Helmholtz tube entrance and (b) inside the resonator

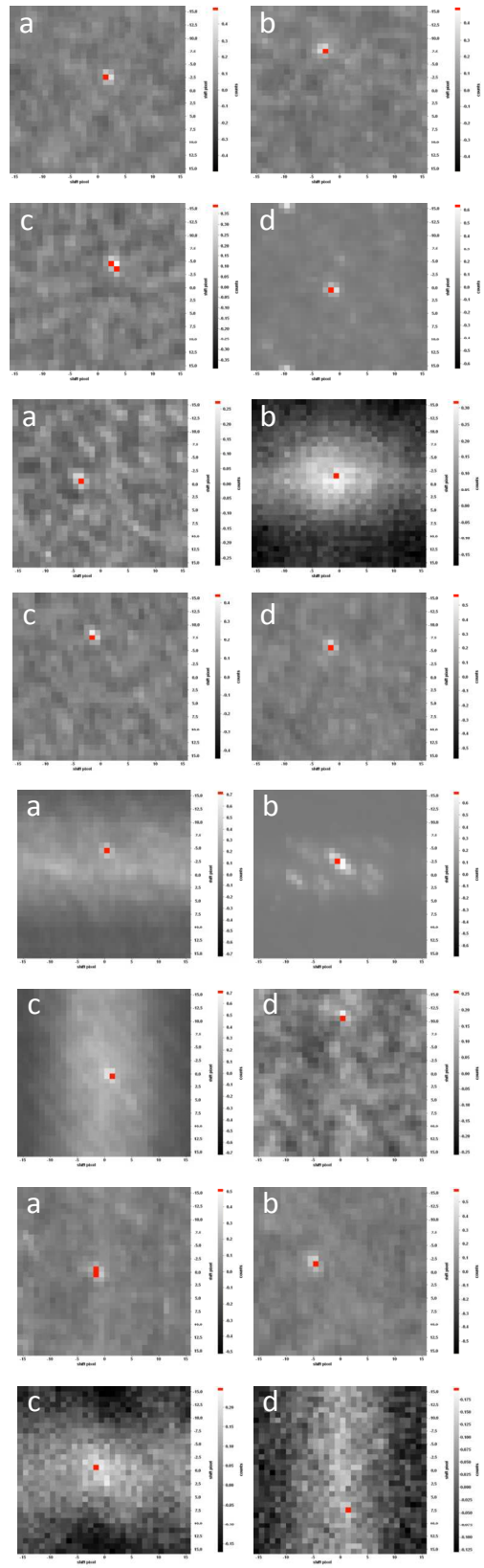
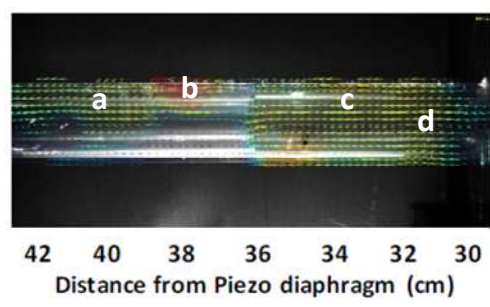
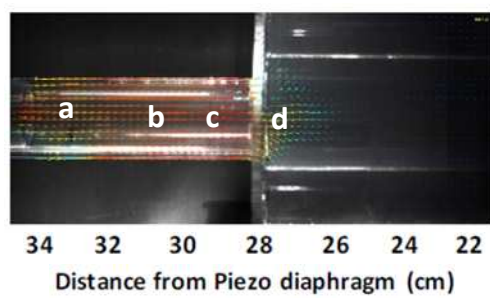
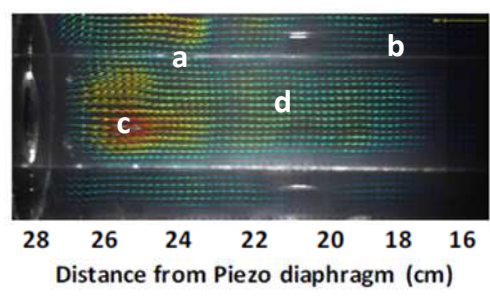
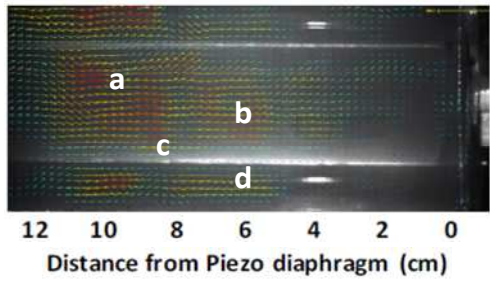


Figure 4.11 Distinct correlation peaks for different resonator locations

Upon processing of the particle velocity data from the PIV, a numerical integration can be carried out to obtain mean values for the volume velocity Q at these locations. Theoretically, if the cross section area of the resonator at an x distance from the nose end is denoted A_x , then the corresponding volume velocity Q_x is obtained by integrating the velocity profile of the working gas at that cross section U_x over A_x as follows,

$$Q_x = \int U_x dA_x \quad (4.1)$$

The experimental average volume velocity at any cross section of the resonator $Q_{x,exp}$ is obtained numerically by integrating the velocity over the cross sectional area of this particular location obtained from the PIV data points.

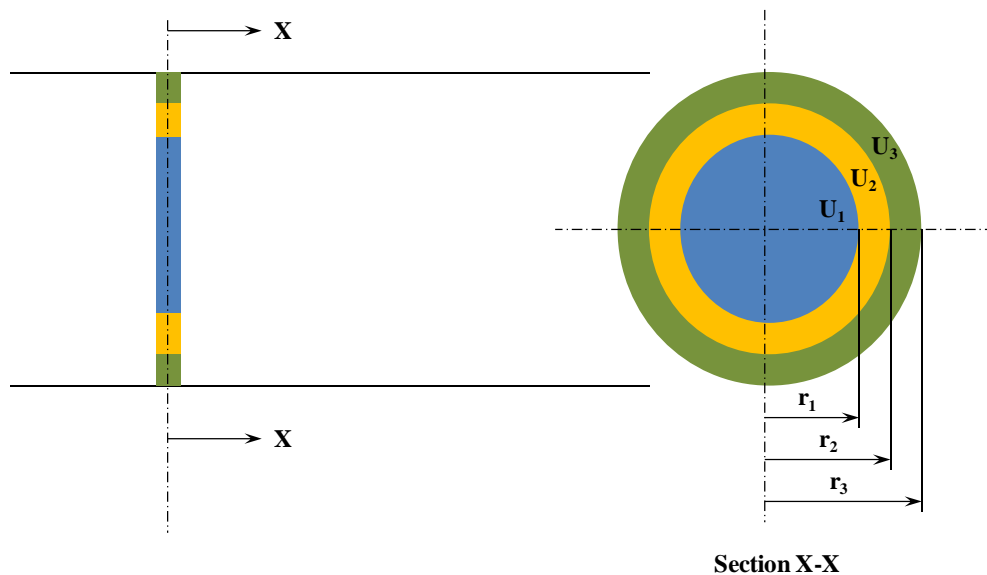


Figure 4.12 Schematic showing the numerical integration scheme used to obtain the volume velocity from the PIV data points

At any given cross section, the area is discretely divided into a finite number of smaller concentric areas, and then the average results from the data points of the gas particle velocity in those areas is used to obtain a good approximation for $Q_{x,\text{exp}}$. For the example shown in Figure 4.12 for illustration purposes, $Q_{x,\text{exp}}$ would be calculated as follows,

$$Q_{x,\text{exp}} = U_1(\pi r_1^2) + U_2(\pi[r_2^2 - r_1^2]) + U_3(\pi[r_3^2 - r_2^2]) \quad (4.2)$$

Applying the above procedure on a finer scale, Figure 4.13 is obtained which shows a comparison between the experimental and theoretical prediction results of the volume velocity inside the *TAP* resonator.

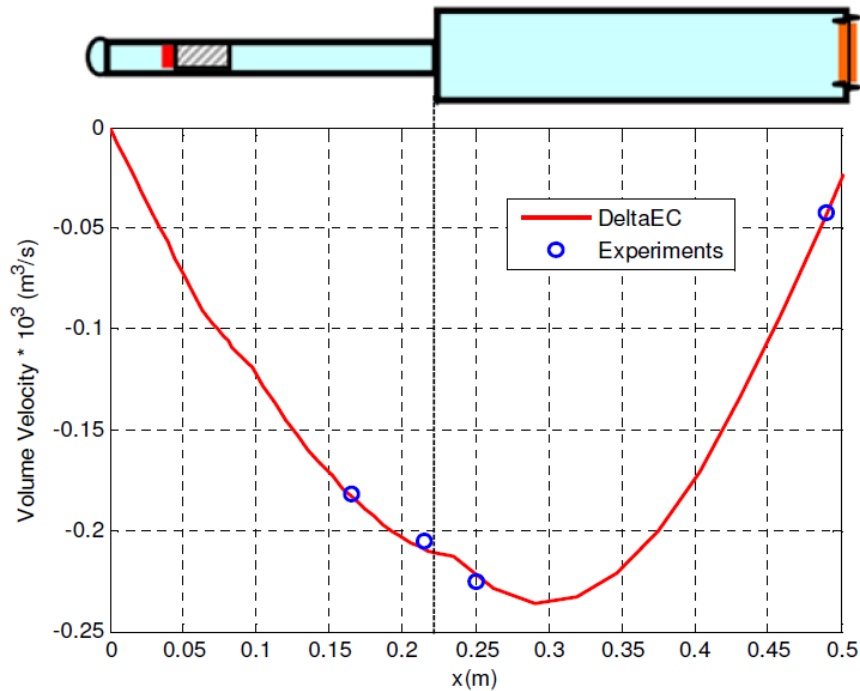


Figure 4.13 Comparison between experimental and theoretical values for the gas volume velocity along the *TAP* resonator

4.2.5. Modal and Deflection Characteristics of the Piezo Diaphragm

The experimental *TAP* prototype relies in its operation on a Lead-Zirconate-Titanate (*PZT-5A*) piezoelectric circular diaphragm. The diaphragm is supplied by Piezo Systems Inc., Woburn, MA (part no. T107-A4E-573). It has a diameter of 63.5 mm, a thickness of 1.905 mm and a capacitance of 112.5 nF at 388 *Hz*.

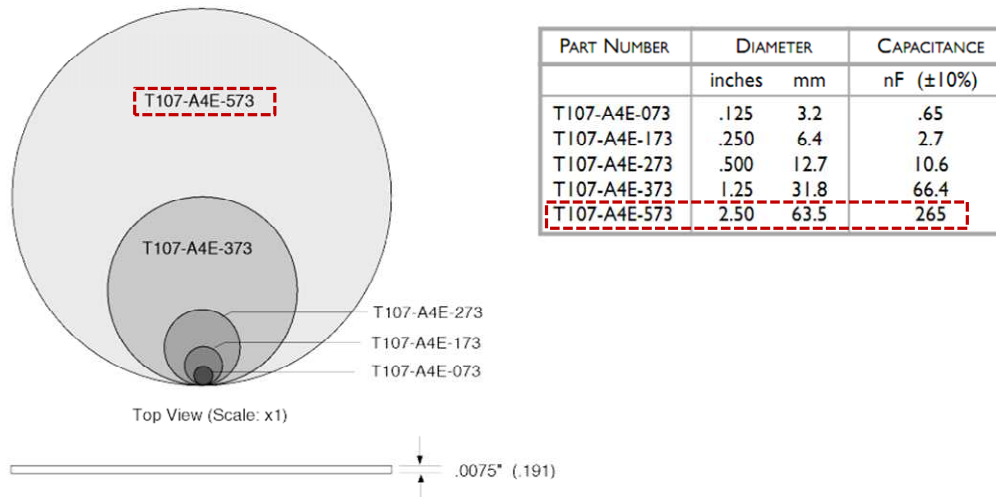


Figure 4.14 *PZT-5A* Piezo diaphragm (63 mm, .191 mm thick) from Piezo Systems, Inc.

Upon subjection to a broadband acoustic excitation, the frequency response of the diaphragm is obtained. Results show a first natural frequency of about 300 *Hz*. The diaphragm is then tuned to force a first natural frequency in resonance with the acoustic cavity at about 388 *Hz*. This is achieved by supporting the diaphragm on an aluminum substrate of 0.1 mm thickness and a 71 mm diameter. A weight of 2.81 g is also added at the center of the diaphragm in the form of 2 nuts attached to the back of the diaphragms at its center.

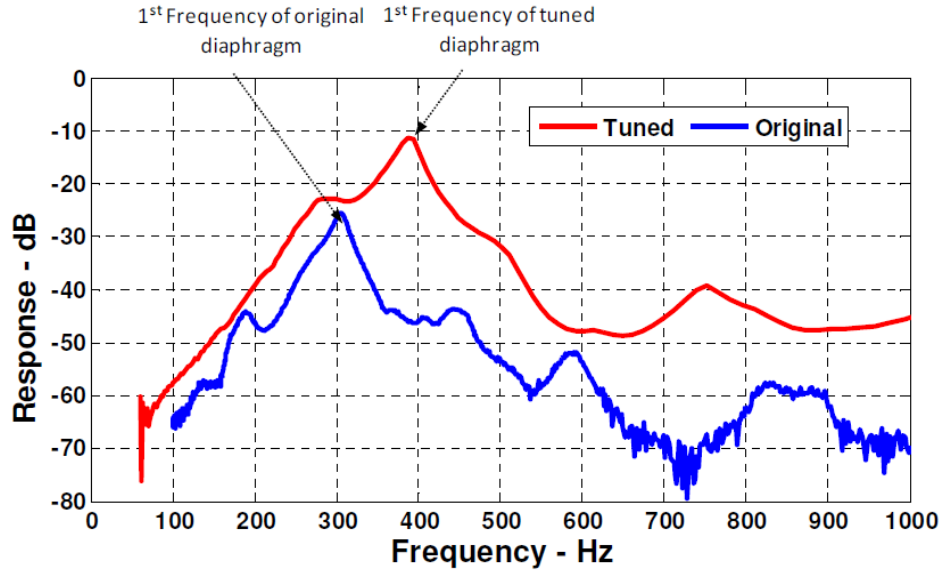


Figure 4.15 Modal characteristics of the *PZT-5A* piezo diaphragm before and after tuning

Figure 4.15 shows the modal characteristics of the piezo diaphragm before and after tuning. Both natural frequencies match those obtained from the FEM presented in Appendix (A). Figure 4.16 shows the contours of transverse velocity of the diaphragm when operating at its natural frequency of 388 *Hz*. The amplitude of transverse deflections is around 0.02 mm. The contours are obtained using the PSV200 scanning Laser Doppler Vibrometer from Polytec-PI, Hopkinson, MA.

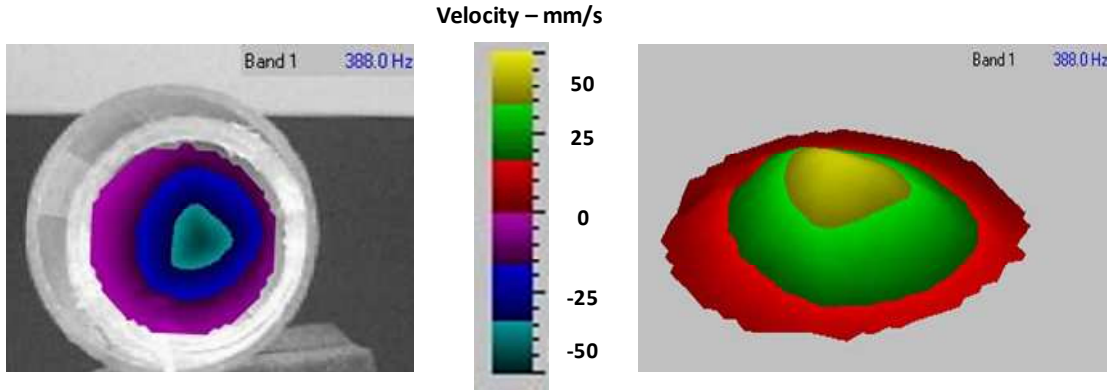


Figure 4.16 Contours of transverse velocity of the tuned piezo diaphragm operating at its first natural mode (388 Hz)

4.2.6. Output Voltage, Power and Efficiency

The experimental output voltage V of the harvester is displayed in Figure 4.17 for the harvester with the original and tuned piezo-diaphragms. It is evident that tuning the piezo-diaphragm to resonate with the acoustic cavity is essential to enhancing the harvester performance. Displayed also on the figure are the *DeltaEC* predictions when the tuned piezo-diaphragm is connected to different resistive loads Z_L . Close agreement is clear between the experiments and the predictions.

The electric output power of the harvester is displayed in Figure 4.18 (a) when the harvester is operating with the original and tuned piezo-diaphragms. The output power is normalized by the diaphragm's volume indicating the power density at different values of Z_L . The displayed results indicate that a maximum power of 0.21 mW/cm^3 (corresponding to 0.128 mW of total output power) is attained when the load

resistance Z_L is 3170Ω . Note that the electrical power output \dot{E}_L of the *TAP* is calculated using the root mean square voltage values V_{rms} using the relationship,

$$\dot{E}_L = V_{rms}^2 / Z_L \quad (4.3)$$

where,

$$V_{rms} = \frac{1}{\sqrt{2}} V \quad (4.4)$$

Figure 4.18 (b) shows the efficiency of conversion from acoustic to electric power in the piezo-diaphragm (η_e) peaking at about 9.7 % at a load resistance of 3170Ω . Note that η_e is the electric power output as a percentage of the acoustic power radiated to the end of the tube where the diaphragm is located, i.e. the pressure and volume velocity product at $x = L$.

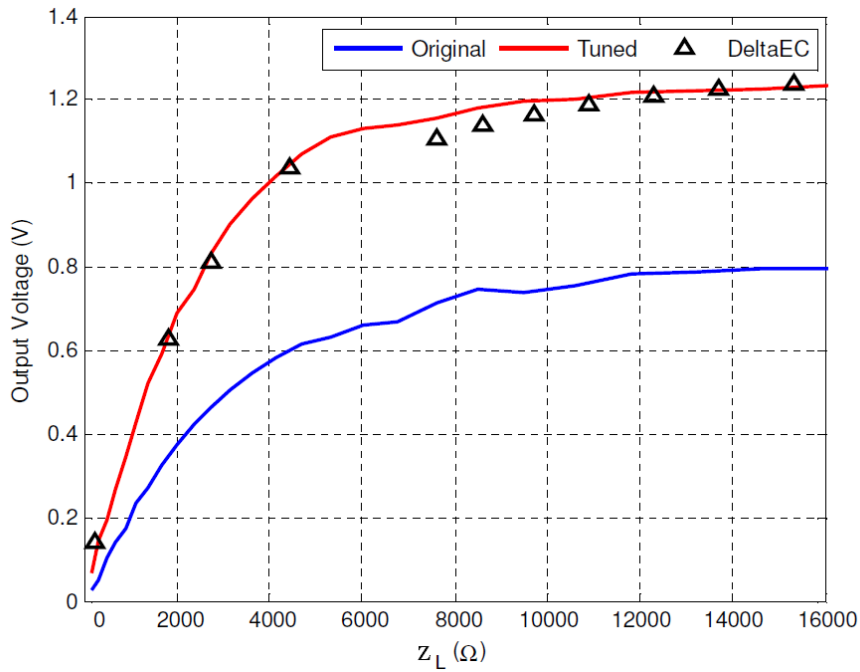


Figure 4.17 Output voltage of the *TAP* harvester for different values of Z_L

Values of η_e presented here are in good agreement with similar analyses in literature, which are mainly theoretical in nature. It is shown in a similar study that η_e is typically around 0.2% at a resistance of 10 Ω , in the range of 2-3% at a resistance of 100 Ω and ranges from 6 to a maximum of 15 % at a resistance of 1000 Ω , and then starts deteriorating [5]. In another investigation of thermoacoustic power generation using piezoelectric transducers [6], a maximum overall efficiency of the device (thermal to acoustic to electric) of 10% is achieved. In addition, the power harvested from the piezo-diaphragm presented here per unit volume reaches about 210 $\mu W/cm^3$. This is typical of energy harvesting techniques using *PZT* piezoelectric transducers ([46],[47] and [48]).

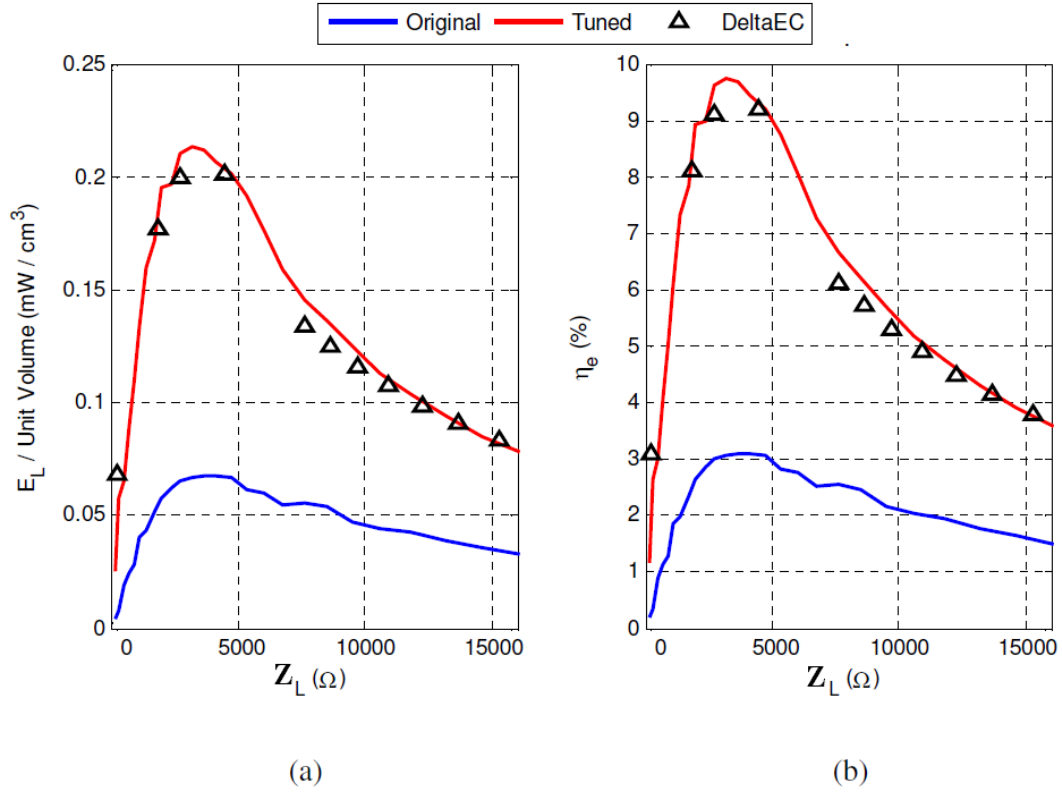


Figure 4.18 (a) Output electric power density and (b) acoustic to electric energy conversion efficiency of the TAP harvester for different values of the load resistance (Z_L)

It should be noted that the acoustic power reaching the piezo-diaphragm (at $x = L$) is only a percentage of the power initially produced in the stack. The power flow along the tube involves losses due to viscosity and friction with the resonator walls. These can be approximately estimated using expressions given as a function of the tube geometry, gas thermo-physical properties, viscous boundary layer thickness, frequency of oscillation and maximum pressure amplitude in the resonator such as equation (2.46).

4.3. Speaker-driven Resonator with a Dynamic Magnifier (No Stack)

4.3.1. Introduction

In this experiment, an investigation of the performance of the *DMTAP* discussed in details in Chapter 2 is attempted. The experimental setup used here is simpler than the design suggested by Figure 2.4. The acoustic oscillations produced by the stack are simulated by a speaker placed at the beginning of the resonator. The resonator is 2.75" (6.985 *cm*) in diameter. A circular buzzer *PZT-4* piezo-element placed on a 0.008" (0.203 *mm*) thick aluminum sheet of a diameter equal to that of the tube is attached to the other end of the resonator. The piezo-element is manufactured by Digi-Key Corp. (Figure 4.19). This piezo-element is then connected to a similar one through a mechanical spring of known stiffness.

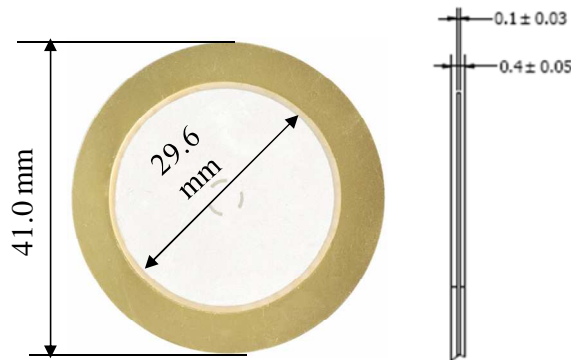
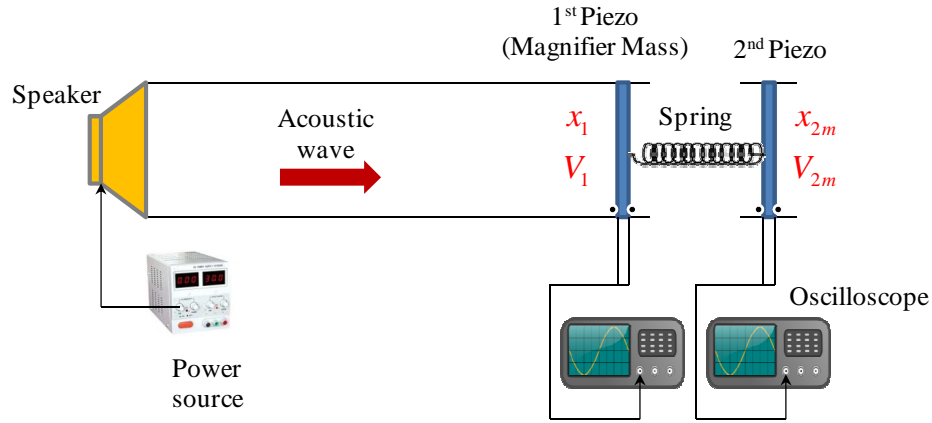


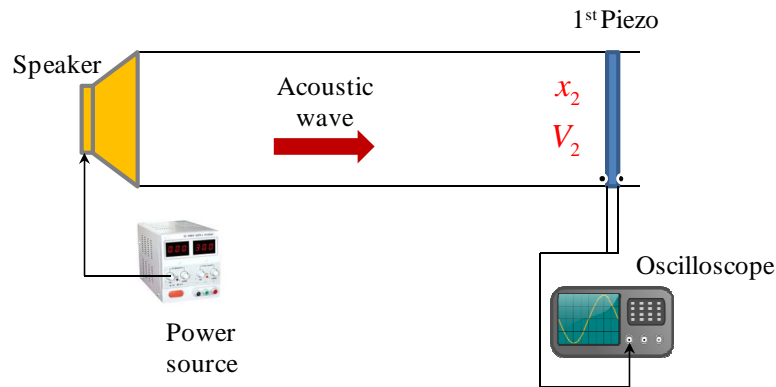
Figure 4.19 Digi-key 41 mm Buzzer Piezo-element

The second piezo-element is supported by a separate stand than the rest of the resonator. Furthermore, the section between the two piezo-elements is open to the air.

This way, by detaching the connecting spring and the second piezo-element, the system at hand is simply a speaker-driven cavity with one piezo-element at one end. The piezo-element converts the incoming acoustic energy from the speaker into an electrical output, thus simulating a *TAP*-like system. When the second piezo-element is reattached to the first one using the coupling spring, the system in effect acts like a *DMTAP*. The first piezo-element in this case acts as the dynamic magnifier mass. A schematic of the experimental setup is shown in Figure 4.20.



(a)



(b)

Figure 4.20 Schematic diagram of the experimental setup when used as (a) *DMTAP*-like system and (b) *TAP*-like system

4.3.2. Voltage output from Piezo-elements

For different values of the stiffness k_c of the spring connecting the two piezo-elements, the system is found to have a first natural frequency in the range starting 400 to 600 Hz when operating as a *TAP* or a *DMTAP* like system. Thus, using the speaker as the source of the acoustic energy and with no electrical loads used, a sine sweep over the domain 0 to 800 Hz is carried out while monitoring the voltage output from both piezo-elements (V_1 and V_{2m}) over this range of frequencies. Having values of V_{2m} less than V_1 would mean that the *TAP* still operates as a better energy harvester than the *DMTAP*. This would eliminate the need for having to compare V_{2m} with the voltage V_2 from the first piezo when no springs are attached (*i.e.* the *TAP* case). However, having values of V_{2m} higher than V_1 is an indication that the power output in the second piezo-element is more than that obtained from the first one. Even though this can be taken as a valid approximation for the magnification in most cases, the voltage output from the second piezo V_{2m} should still be compared with the voltage V_2 to confirm that the proposed system does serve as a magnifier of the power harvested.

The variable parameters in such an experiment are mainly the spring constant k_c and the masses of the 2 piezo-elements. Both piezo-elements are similar and have the same weight. Both elements are supported by an aluminum backing of the same thickness, thus their total masses are equal. Small masses in the order of 1 to 5 grams can still be attached to the piezo-elements as a way of varying the mass of the *DMTAP*. Several combinations of k_c and added weights are attempted while

monitoring the voltage output over the sine swept frequency range on a signal analyzer. Figure 4.21 shows an example of an undesirable case where the energy traveling from the first to the second piezo through the coupling spring is not magnified, hence V_1 values are higher than V_{2m} over the considered frequency range. The spring used here has a constant of k_c equals to $17,800 \text{ N/m}$. In this case, the added spring-mass structure serves as means of dissipating or absorbing the energy being conveyed to the second piezo-element instead of amplifying it. The figure displays also the nature of the dominant modes in the frequency spectrum. Notable are the two modes, at 490 and 580 Hz , resulting from combining the harvester with the dynamic magnifier. However, because of the weak nature of the coupling between the harvester and magnifier, the contribution of the second mode to the output voltage is also weak.

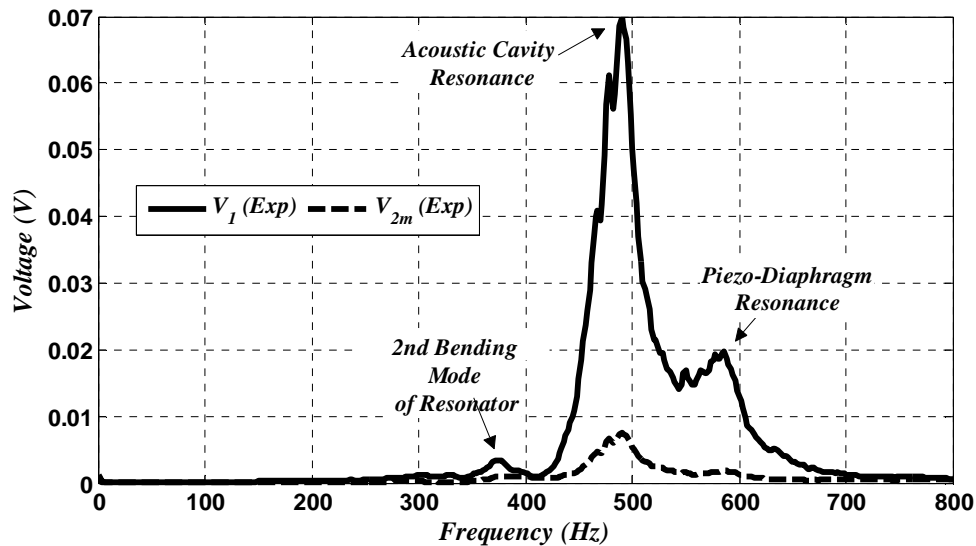


Figure 4.21 Sine swept frequency response of voltage outputs V_1 and V_{2m} of the two piezo-elements ($k_c = 17,800 \text{ N/m}$)

Upon the addition of small masses to the piezo-elements, the voltage obtained from the second piezo begins improving in comparison with the case with no masses added. However, it's the combination of the masses and the proper spring constant that decides the performance of the *DMTAP*. The best results are obtained using a spring of k_c equal to around 29,180 N/m with no added masses. In this case, a strong coupling exists between the piezo-element and the dynamic magnifier resulting in enhanced performance.

Figure 4.22 shows the response of the voltages: V_1 , V_2 and V_{2m} for this case. Note that V_1 in this case rises from its peak of 70 mV , in Figure 4.21, to about 160 mV , while V_{2m} dramatically jumps from a peak of 8 mV to almost 450 mV . It is evident here that the energy transferred through the spring to the second piezo-element is magnified. This is manifested clearly by comparing the performance with that of the case without a magnifier where the output voltage V_2 peak at about 290 mV and hence are much lower than the 450 mV achieved by the second piezo in the *DMTAP* case.

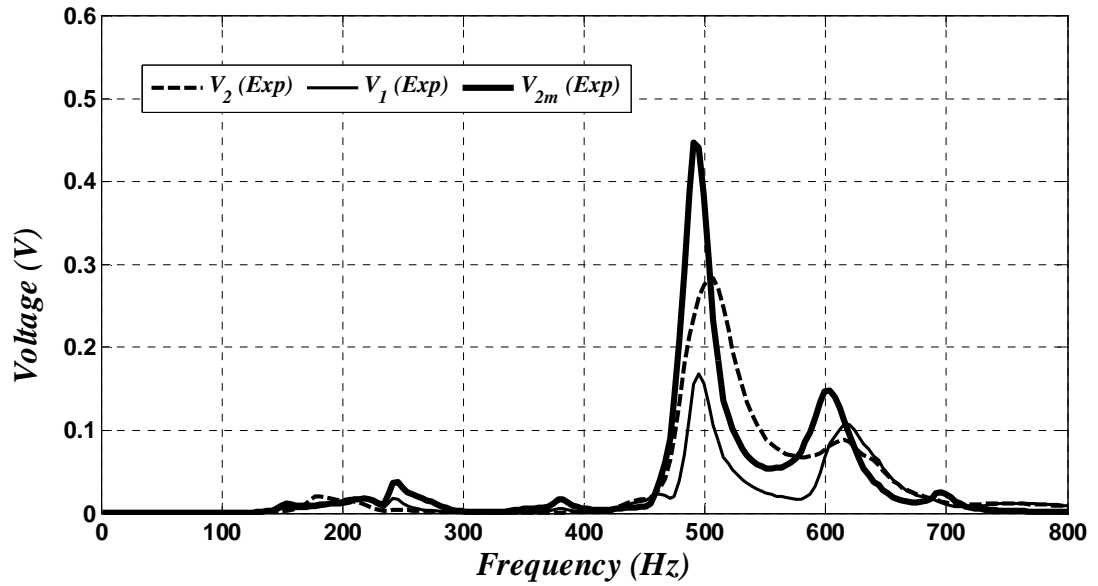
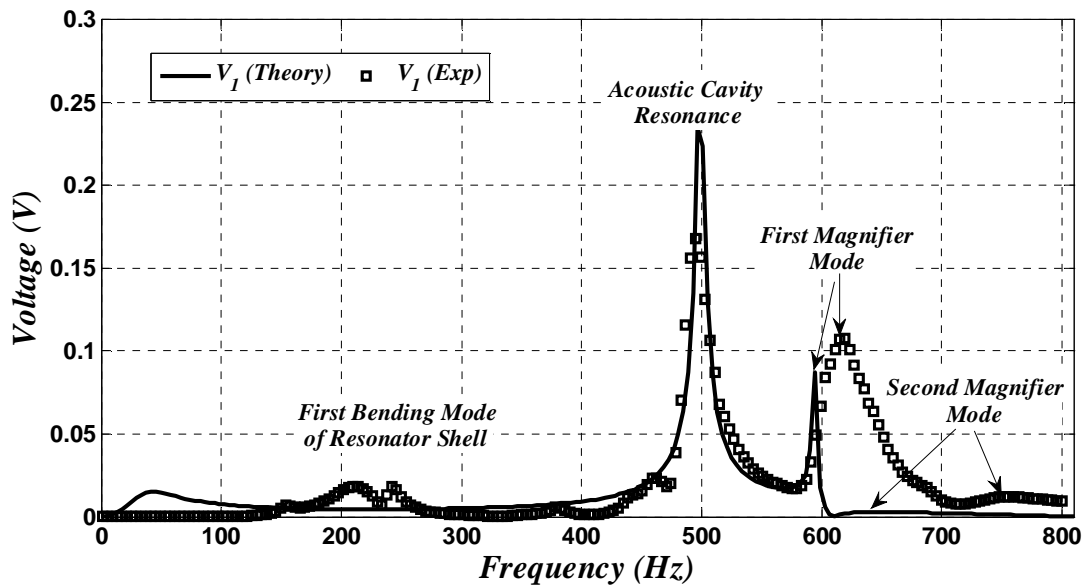


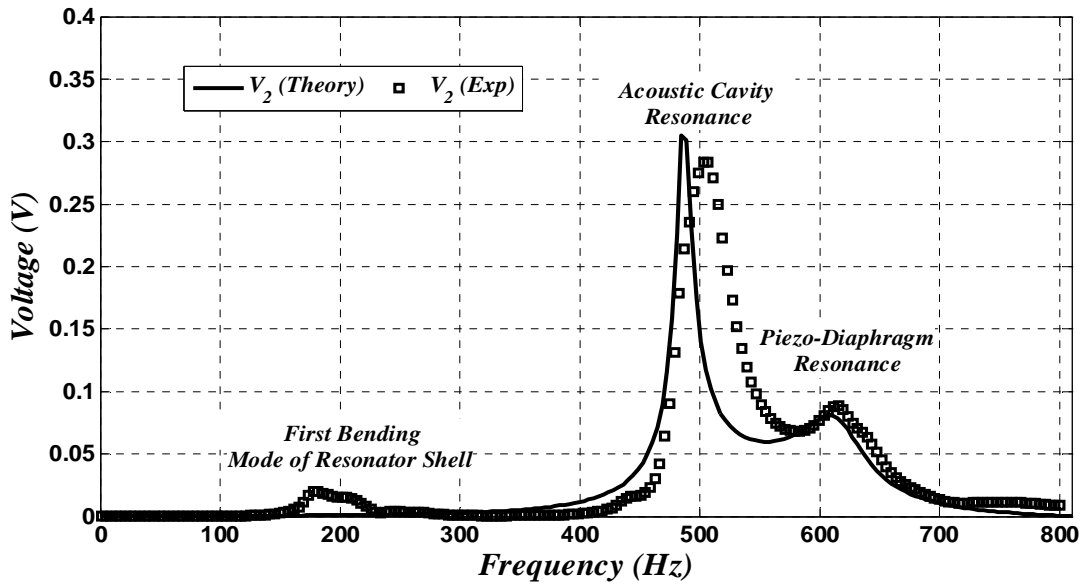
Figure 4.22 Sine swept frequency response of voltage outputs V_1 , V_2 and V_{2m} of the two piezo-elements compared with the theoretical predictions ($k_c = 29,180 \text{ N/m}$)

The equations presented in Chapter 2 are used to model the system at hand and compare with the experimental results. A *MATLAB* code is developed to simulate the experiment and predict values of V_1 , V_2 and V_{2m} over the frequency range 0 to 800 *Hz* for the cases presented in Figure 4.22. Equations (2.22) and (2.28) are obtained for a resonator with a rigid end at the hot side of the stack, and are thus slightly modified to reflect the speaker impedance at $x = 0$. The rest of the procedure, however, remains unchanged. The obtained theoretical characteristics and the corresponding experimental frequency responses are displayed in Figure 4.23. The figure shows, to a great extent, a good agreement between theoretical predictions and experimental results.

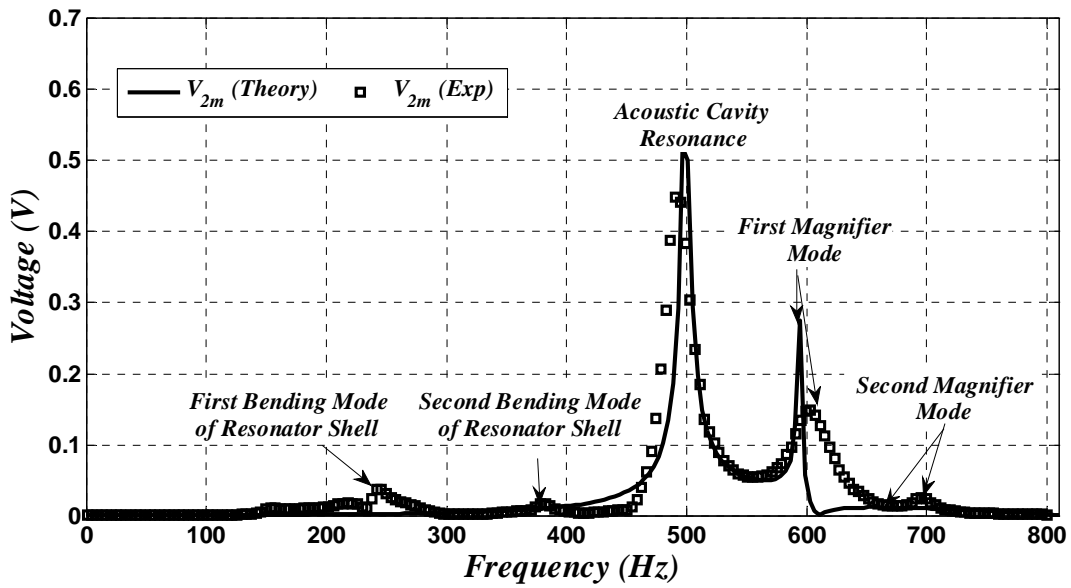
Displayed on the figures are the clearly identified structural and acoustic modes of the resonator as well as the structural modes of the piezo-diaphragm and magnifier system. Note that in the case of a harvester without a dynamic magnifier, the output voltage V_2 shows only on distinct peak at 480 Hz to indicate the acoustic resonance of the resonator cavity and another peak at 615 Hz to quantify the resonant frequency of the piezoelectric diaphragm. However, in the case of a harvester with a dynamic magnifier, the frequency spectrum of the output voltage V_{2m} shows two bending modes of the resonator shell at 230 and 380 Hz, acoustic resonance of the resonator cavity at 500 Hz, combined resonant frequencies of the piezoelectric diaphragm and the magnifier at 605 Hz and 700 Hz.



(a)



(b)



(c)

Figure 4.23 Sine swept frequency response of voltage outputs V_1 , V_2 and V_{2m} of the two piezo-elements ($k_c = 29,180$ N/m)

4.3.3. *Vibrometer Scanning of Piezo Surface*

To verify that the voltage measurements presented earlier reflect the corresponding piezo deflection and for the purpose of voltage-displacement calibration as well, the surface of the piezo-elements in the *TAP* and the *DMTAP* case are scanned using a laser vibrometer during operation. The contours are obtained using the PSV200 scanning Laser Doppler Vibrometer from Polytec-PI, Hopkinson, MA. The setup for this experiment is shown in Figure 4.24.

Figure 4.25 shows results from a vibrometer scanning of the first piezo-element when the spring and the second piezo are detached (the *TAP* case) and a scanning of the second piezo-element after placing it back and attaching it to the first piezo using the spring (the *DMTAP* case). The contours of transverse velocity show clearly the difference in the deflection pattern between first mode and the second mode. It is also evident that the measurements of the voltage output are confirmed as the *DMTAP* case shows to have a significantly higher transverse velocity than the *TAP* in both cases. It is also shown that operating at the first mode is not only favorable to avoid having the piezo-element work against itself, but also because the piezo-elements experience much higher strain compared to the secondary modes.

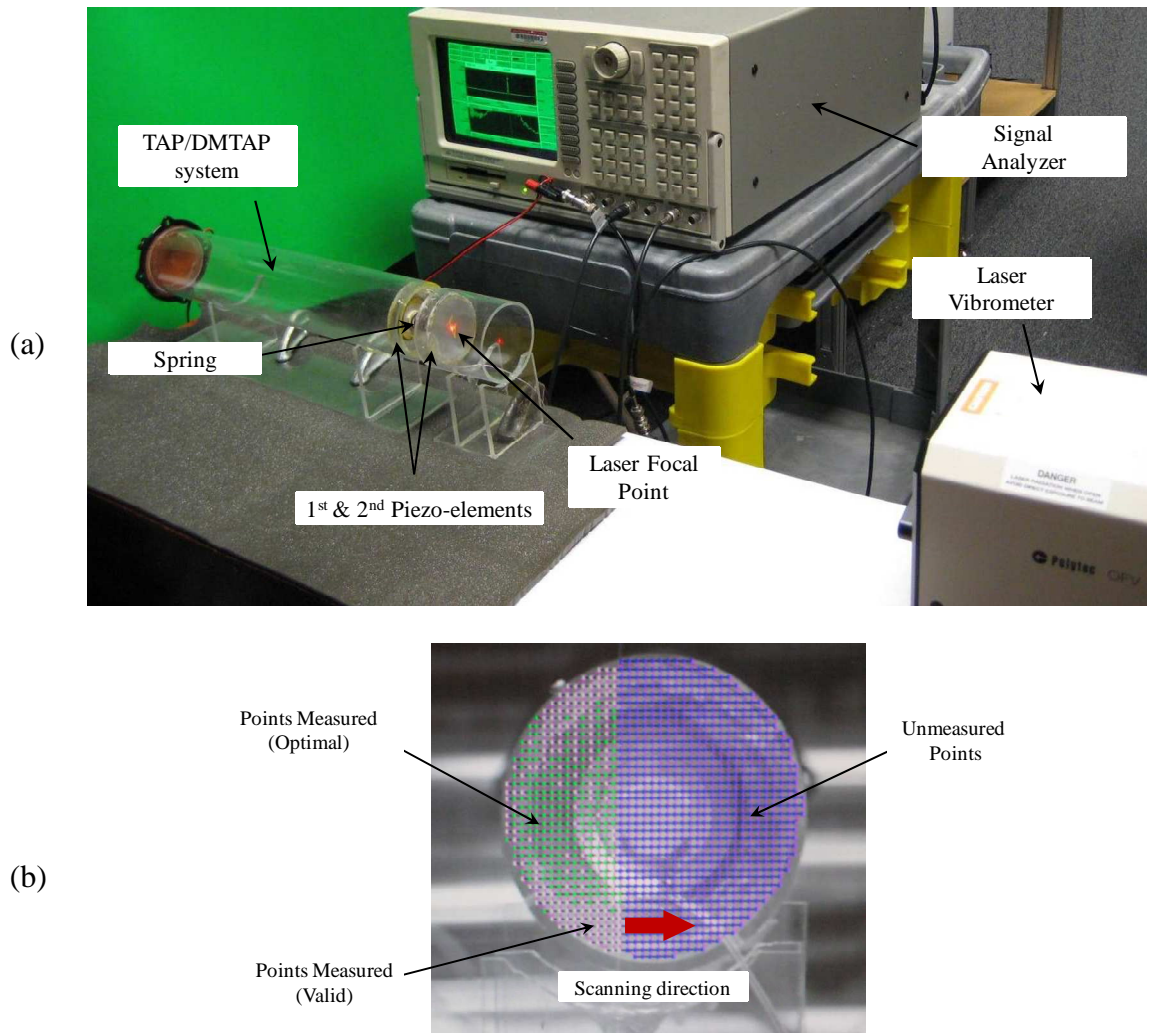


Figure 4.24 Experimental Setup of the laser vibrometer used to scan the surface of the piezo-elements to obtain values for the transverse deflection

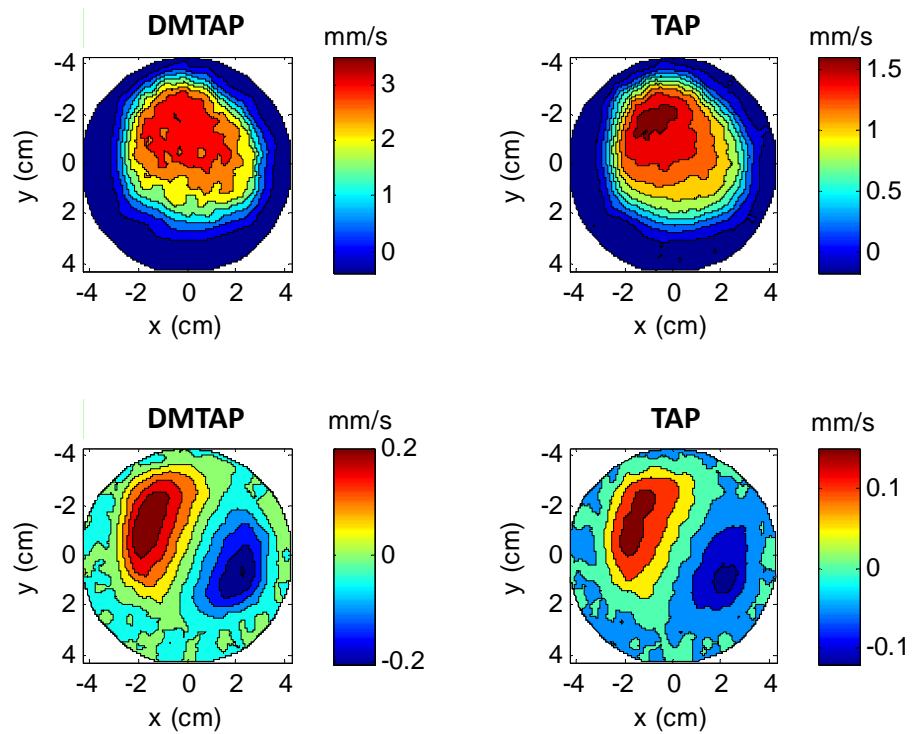


Figure 4.25 Contours of transverse velocity of *DMTAP* and *TAP* showing the first and second deflection modes

4.4. Experimental Prototype of *DMTAP* Harvester (with Stack)

In this section, the performance of an experimental prototype of an actual *DMTAP* harvester with a stack is investigated and compared with that of a conventional *TAP*. A schematic diagram of the *DMTAP* harvester is shown in Figure 4.26, and the experimental harvester is shown in Figure 4.27.

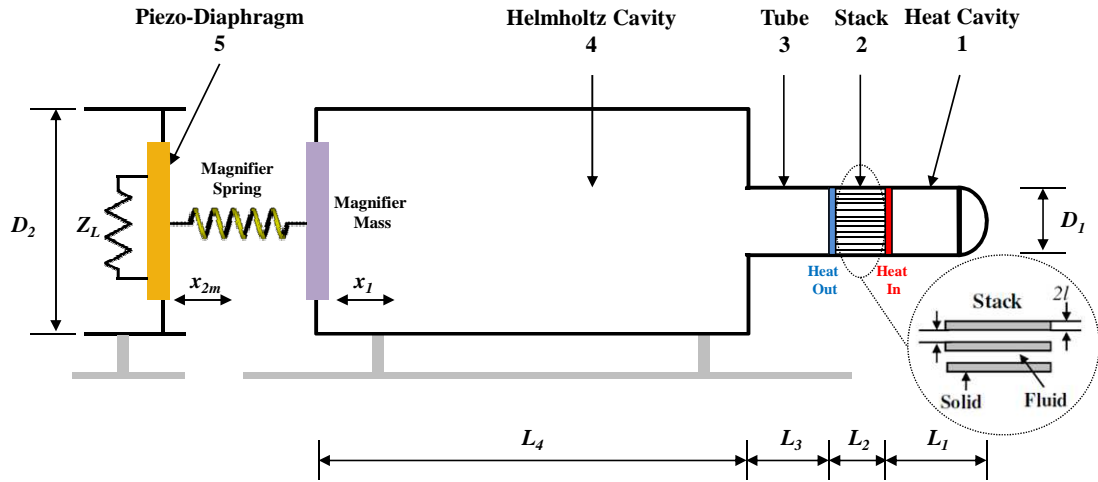


Figure 4.26 Schematic of the experimental *DMTAP* harvester prototype

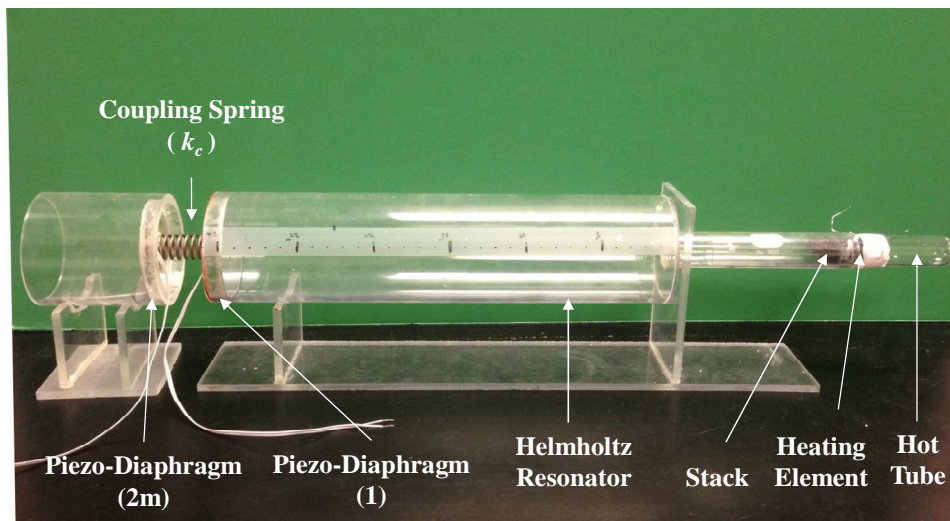


Figure 4.27 Experimental prototype of a *DMTAP* harvester

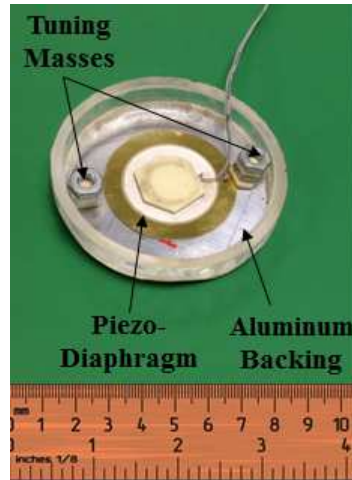


Figure 4.28 Piezo-element on aluminum backing with tuning masses at symmetric locations

The same concept is used whereby an identical piezo-element is used as the magnifier mass, such that by detaching the coupling spring, the *DMTAP* harvester shown in Figure 4.27 becomes a *TAP* for comparative purposes. Different springs with varying stiffness can be used to simulate different values of k_c , while small nuts with known masses can be placed at symmetric locations on the piezo-element to change the value of the magnifier mass m_m as shown in Figure 4.28.

The stack-less speaker driven resonator in the previous section simulated the operation of a system similar to a *DMTAP* harvester and showed possible and significant amplification of the harvested power from the piezo-element upon proper choice of the magnifier parameters. The speaker driven setup also enabled us to control the frequency of the acoustic oscillations and hence examine the harvested power over a swept range of frequencies. In an actual thermoacoustic-piezoelectric harvester with a stack and external heating, the self-excited oscillations should occur at the resonant frequency of the cavity coupled with the piezo-element or the dynamic

magnifier system. As presented earlier, this was estimated to be in the vicinity of 400 Hz.

Several experiments were carried out using different combinations of k_c and m_m , and for each the voltages across the two piezo elements V_1 and V_{2m} were measured, and eventually compared with the voltage V_2 from the piezo-element in the *TAP* case. Table 4.3 lists a selection of seven experiments (numbered ‘a’ to ‘g’) that were carried out with different stiffness ratios k_c/s varying from 0.01 to 3.90 and mass ratios m_m/m varying from 0.20 to 1.38.

Table 4.3 Springs and mass ratios used in the *DMTAP* experiments

Experiment no.	Spring Stiffness (k_c)		Piezo Stiffness (s)	k_c/s	m_m/m
	lb/in	N/m	N/m		
(a)	33.15	5805.45	38703.00	0.15	1.00
(b)	221.00	38703.02	38703.00	1.00	1.00
(c)	861.00	150784.16	38703.00	3.90	1.00
(d)	2.65	464.09	38703.00	0.01	1.38
(e)	221.00	38703.02	38703.00	1.00	1.38
(f)	2.65	464.09	38703.00	0.01	0.20
(g)	861.00	150784.16	38703.00	3.90	0.20

Figure 4.29 displays the peak to peak time oscillations of the voltages V_1 , V_2 and V_{2m} for each of the combinations listed in Table 4.3. The voltage magnification ratio V_{2m}/V_2 indicates how the voltage from the *DMTAP* harvester compares to that of the *TAP*, and is of greatest interest to us. It can be seen that dynamic magnification does

take place in plots (a), (b) and (e) with case (a) showing the maximum amplification, i.e. highest V_{2m}/V_2 ratio. Plots (c), (d), (f) and (g) however show undesirable attenuation of the voltage from V_2 to V_{2m} .

The *GUI* developed in section 2.8 can be used to predict the theoretical voltage magnification ratios corresponding to the shown experiments. The piezo-element properties have to be adjusted to reflect those of the *PZT-4* buzzer elements shown in Figure 4.19. The geometrical dimensions inputted to the *GUI* are those listed in Table 4.2. A comparison between the predicted and experimental values of V_{2m}/V_2 is presented in Table 4.4. The comparison reveals good agreement between the mathematical model and the experimental data. It should be noted here that the model presented earlier in Chapter 2 assumes a one-dimensional propagating wave in the x -direction and hence a piezo-element that is deflecting with one *DOF*: x_2 in the *TAP* case and x_{2m} in the *DMTAP* case, rather than a circular piezo-diaphragm fixed at the circumferential points. The developed *GUI* is also limited to a constant area resonator, while the experimental harvester includes a small tube and a Helmholtz resonator. These limitations may have contributed to the minor discrepancies between some of the predictions and the experimental findings.

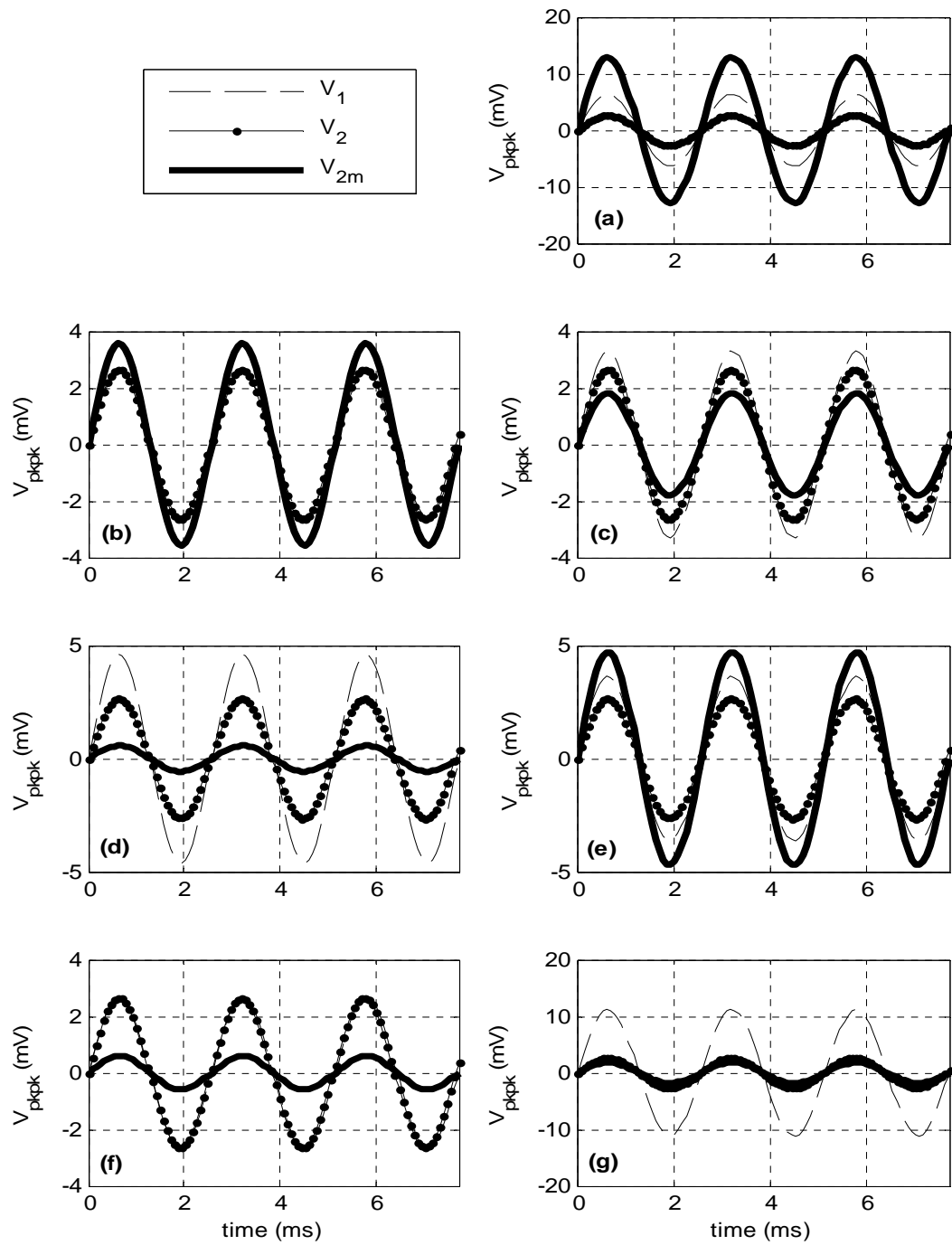
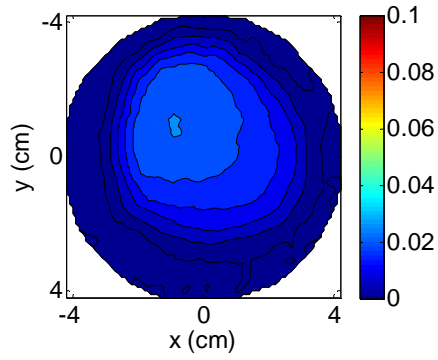


Figure 4.29 Piezo-element peak-to-peak voltages V_1 , V_2 and V_{2m} for different configurations of springs and mass ratios given in Table 4.3

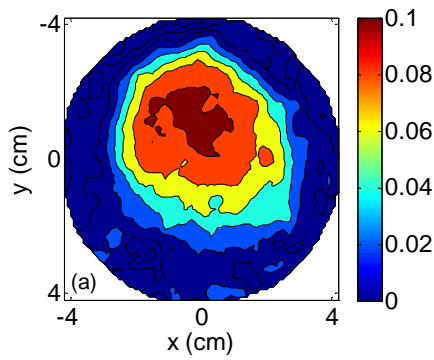
Table 4.4 *DMTAP* to *TAP* voltage ratio: Experimental results and theoretical predictions

Experiment no.	Parameters		Experiment			Theory
	k_c / s	m_m / m	$V_2 (mV)$	$V_{2m} (mV)$	V_{2m} / V_2	V_{2m} / V_2
(a)	0.15	1.00	3.18	12.85	4.05	3.85
(b)	1.00	1.00	3.18	3.57	1.12	1.27
(c)	3.90	1.00	3.18	1.82	0.57	0.66
(d)	0.01	1.38	3.18	0.56	0.18	0.25
(e)	1.00	1.38	3.18	4.71	1.48	1.28
(f)	0.01	0.20	3.18	0.60	0.19	0.27
(g)	3.90	0.20	3.18	1.81	0.57	0.66

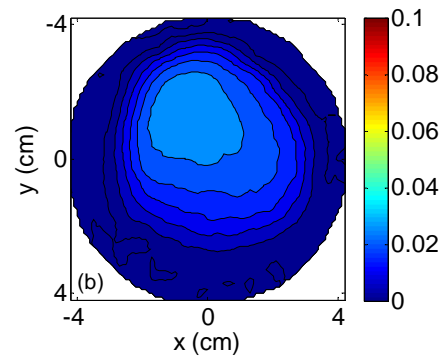
Figure 4.30 shows the scanned surface of the piezo-elements carried out using the laser vibrometer for the *TAP* case, as well as the *DMTAP* experiments listed in Table 4.4 having a positive voltage magnification ratio (i.e. $V_{2m} / V_2 > 1$). The scans show the deflection in mm/s and are set to a fixed color bar scale to illustrate the amount of amplification that happens in the deflection of the piezo-element when the *DMTAP* is adequately tuned. This is very clear in the vibrometer scan of the *DMTAP* used in experiment (a), where a deflection (and a voltage output) of about 4 times that of the conventional *TAP* is observed. Figure 4.31 shows the rest of the *DMTAP* experiments, namely the ones where the selected magnifier parameters did not result in output voltage improvement. The *TAP* case is again placed for comparison. Finally, Figure 4.32 shows the output voltage from the piezo-elements in relation to their deflection for all the carried out experiments.



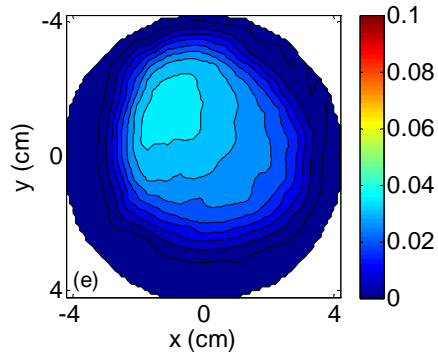
TAP



DMTAP # (a)

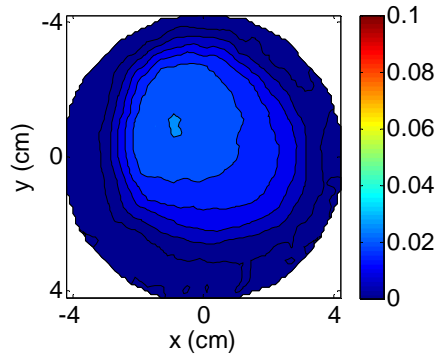


DMTAP # (b)

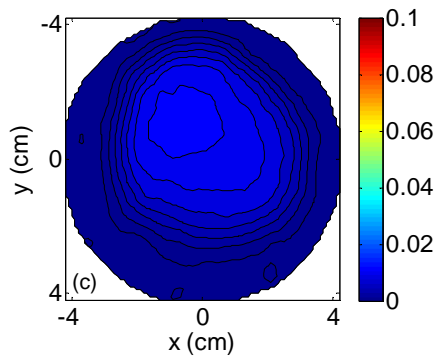


DMTAP # (e)

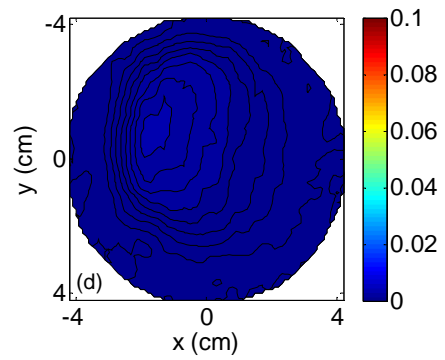
Figure 4.30 Surface deflections of the piezo-membrane in the *TAP* experiments and the *DMTAP* experiments having a positive magnification ratio $V_{2m} / V_2 > 1$ (values in *mm/s*)



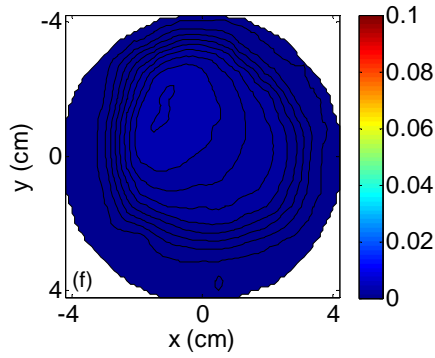
TAP



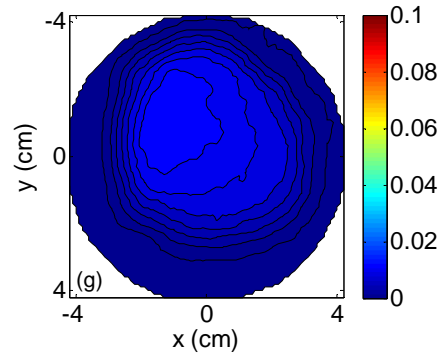
DMTAP # (c)



DMTAP # (d)



DMTAP # (f)



DMTAP # (g)

Figure 4.31 Surface deflections of the piezo-membrane in the *TAP* experiments and the *DMTAP* experiments having a negative magnification ratio $V_{2m}/V_2 < 1$ (values in *mm/s*)

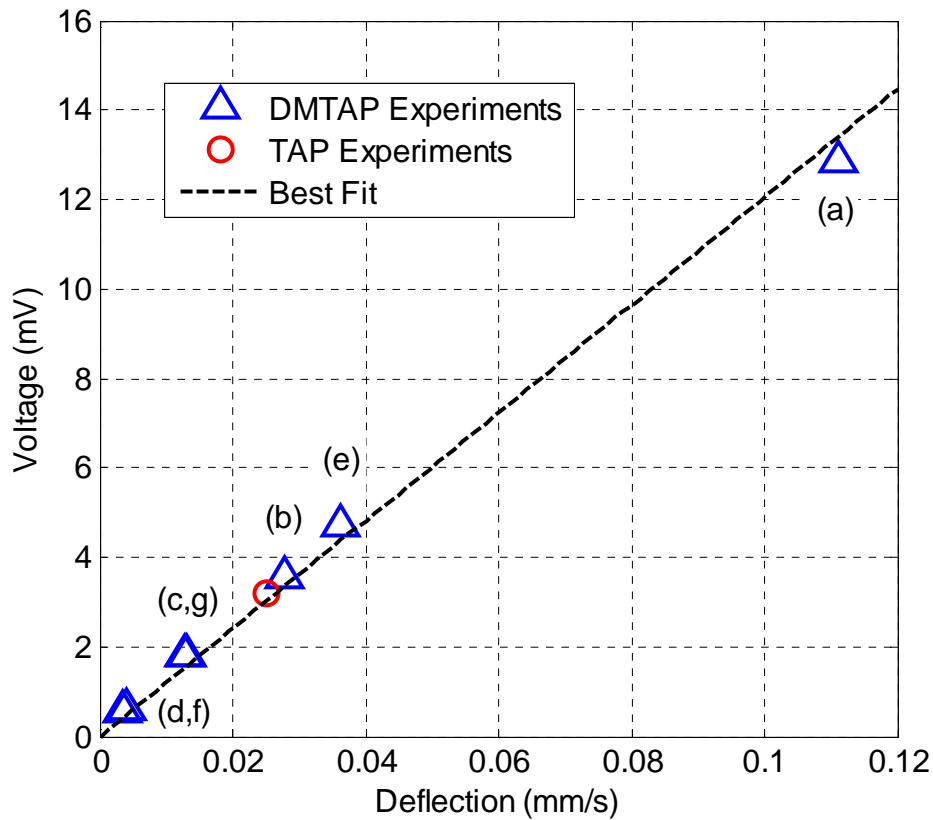


Figure 4.32 Deflection against voltage of the piezo-membranes for all the performed *TAP* and *DMTAP* experiments

4.5. Summary

This chapter illustrated the experimental testing carried out with thermoacoustic-piezoelectric energy harvesters, with and without dynamic magnifiers. The chapter presented a complete performance investigation of conventional *TAPs* that included measurements of temperature, pressure and velocity distributions, piezo-diaphragm modal characteristics, output power and efficiency. Comparisons have been made along the way between the theoretical predictions and the experimentally obtained data.

Furthermore, an experiment to show the potential of experimental *DMTAPs* has also been presented showing clearly the superiority of the magnified devices in terms of both voltage output and piezo movement. Equations developed for the *TAP* and the *DMTAP* in Chapter 2 have been employed to verify the results and close agreement was observable.

Chapter 5

5. Transient Characteristics and Stability Analysis of Standing Wave Thermoacoustic-Piezoelectric Harvesters

5.1. Introduction

In all the mathematical modeling and the experimental data presented in Chapters 2, 3 and 4, the focus so far has been on steady state operation of the thermoacoustic-piezoelectric harvester. In literature, no attempt has been reported on predicting mathematically the transient behavior of this class of harvesters leading up to the onset of self-excited oscillations. It is therefore the purpose of this chapter to develop a rigorous approach to predict the limits of self-excited oscillations.

Onset of acoustic oscillations in standing wave *TAP* harvesters is predicted using equations obtained from the equivalent electric network developed for the system. The developed model encompasses tools from electric circuit analogy of the lumped acoustic and mechanical components of the harvester to unify the modeling domain. This approach can become extremely attractive when integrated with electrical circuit simulation tools such as *SPICE* (Simulation Program with Integrated Circuit Emphasis), as will be shown, in order to efficiently design this type of thermoacoustic harvesting systems. The developed results are compared with those obtained from an alternative technique using root locus theory. Finally, all the theoretical data are

validated against the experimental prototype of the *TAP* harvester shown in Chapter 4.

5.2. Temperature Gradient

For a stack of length $L_2 = \Delta x$ with temperatures T_h at its hot end and T_a at its cold end, the temperature gradient across the stack (assumed to be linear) is given as,

$$\nabla T = \frac{T_h - T_a}{\Delta x} = \frac{\Delta T}{\Delta x} \quad (5.1)$$

Self-sustained oscillations are developed in the resonator once the temperature gradient crosses a certain threshold ∇T_{onset} setting the following condition for onset of oscillations in standing wave *TAPs*,

$$\nabla T \geq \nabla T_{onset} \quad (5.2)$$

For a constant stack length, it is evident that a certain temperature difference ΔT is required across the stack ends to excite the harvester, consequently known as ΔT_{onset} .

5.3. Electric Circuit Analog of a Standing Wave TAP Harvester

Analogies exist between acoustic and electric networks [49], mainly because acoustic equations regarding pressure and volume flow have the same format as electric equations regarding voltage and current flow respectively. The lumped elements representing the different components of the TAP shown in Figure 4.1 can be modeled in the electric domain using analogous electric circuit components giving the equivalent electric network shown in Figure 5.1.

5.3.1. Hot Duct and Helmholtz Resonator

The hot duct at the hot end of the stack is modeled by the compliance C_h while the ambient part of the resonator at the cold end of the stack is represented by the compliance C_R . These are given as functions of their respective lengths and cross sectional areas as:

$$C_h = \frac{\pi D_1^2 L_1}{4\rho c^2} \quad (5.3)$$

$$C_R = \frac{\pi(D_1^2 L_3 + D_2^2 L_4)}{4\rho c^2} \quad (5.4)$$

where ρ and c represent the mean density of the working gas and the speed of sound respectively.

5.3.2. Stack

In the stack, the thermal-relaxation resistance per unit length, r_k , is obtained from [33]:

$$r_k = \frac{1}{\text{Im}(-f_k)} \left(\frac{4\gamma P_m}{\pi\omega D_1^2 (\gamma-1)} \right) \quad (5.5)$$

while the compliance per unit length, c_k , is given by:

$$c_k = \frac{\pi D_1^2}{4\gamma P_m} [1 + (\gamma-1) \text{Re}(f_k)] \quad (5.6)$$

where f_k is the spatially averaged thermo-viscous function, also known as Rott's function, given for different geometries and several stack configurations in [33].

Hence, for a stack of length Δx , the stack components R_{st} and C_{st} are given by:

$$R_{st} = r_k \Delta x \quad (5.7)$$

$$C_{st} = c_k \Delta x \quad (5.8)$$

The mean temperature T_m changes axially through the stack, and hence the mean density ρ_o changes to satisfy ideal gas characteristics. To enforce conservation of mass flux through the stack, the volume velocity at the ambient end must grow as T_m . This suggests a volumetric velocity source to accompany the temperature profile. If the volume velocity at the hot end of the stack is modeled as the current I_1 , the volume velocity at the ambient end of the stack would then be τI_1 . This indicates that a gain $G = \tau - 1$ is supplied by the volume velocity source. In its general form, G is defined as [33]:

$$G = \frac{f_k - f_v}{(1 - f_v)(1 - \sigma)} \frac{\Delta T}{T_a} \quad (5.9)$$

In equation (5.9), σ is Prandtl number of the working gas. As suggested by equation (5.9), this term is equal to zero for sections with a zero temperature gradient such as the hot duct and the Helmholtz resonator. G is also almost zero for large-diameter ducts even the if they involve a temperature gradient because f_k and f_v become very small. For channels with a very small pore size ($r_h \ll \delta_k$) and a nonzero temperature gradient, such as regenerators in traveling wave engines, G takes the small channel limit of equation (5.9):

$$G_{reg} = \frac{\Delta T}{T_a} = \frac{T_h}{T_a} - 1 \quad (5.10)$$

For larger pore channels where $r_h / \delta_k \sim 1$, such as the case with stacks in standing wave engines, G takes the boundary-layer limit of equation (5.9):

$$G_{st} = \frac{1-i}{2} \frac{1}{1+\sqrt{\sigma}} \frac{\delta_k}{r_h} \frac{\Delta T}{T_a} \quad (5.11)$$

where δ_k is the thermal penetration depth and r_h is the hydraulic radius of the stack configuration.

Contrary to traveling wave engines where G_{reg} is entirely real, G_{st} in standing wave engines contains a nonzero imaginary part that reflects imperfect thermal contact in the stack pores and the resultant time delay between the gas's cyclic motion along the temperature gradient and it's expansion and contraction. τ is then given by:

$$\tau = \frac{1-i}{2} \frac{1}{1+\sqrt{\sigma}} \frac{\delta_k}{r_h} \frac{\Delta T}{T_a} + 1 \quad (5.12)$$

As a result, the time phasing between the pressure and velocity of the working gas approaches that of a typical standing wave. Note that if pressure and velocity were exactly out of phase, no acoustic power would be generated in the resonator, as the acoustic flux at any point x along the resonator is approximated as the real part of the pressure and velocity product. To reflect the previous in the equivalent circuit, the volume velocity source, is represented by the current-controlled current source (CCCC) set to $(\tau - 1)I_1$ in Figure 5.1.

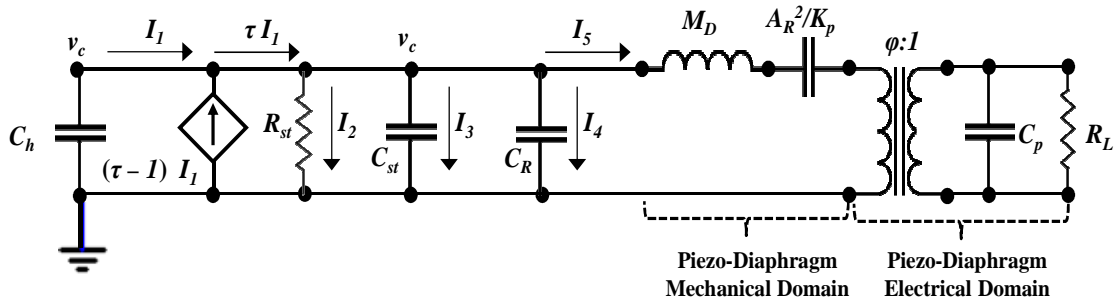


Figure 5.1 Electric circuit equivalent of a standing wave *TAP* harvester

5.3.3. Piezo Diaphragm

The capacitance of the piezo-diaphragm at the end of the resonator, C_p , is calculated as:

$$C_p = \frac{\varepsilon A_R}{t_p} (1 - k^2) \quad (5.13)$$

where k^2 is given as:

$$k^2 = \frac{dc^E}{\varepsilon} \quad (5.14)$$

where ε is the permittivity, t_p is the thickness of the piezo-diaphragm, c^E is the elastic modulus, d is the piezo strain constant, and A_R is the area of the diaphragm. The equivalent capacitance of the mechanical domain of the piezo-diaphragm can be expressed as A_R^2 / K_p where:

$$K_p = \frac{c^E A_R}{t_p} \quad (5.15)$$

Also the equivalent inductance due to the mass of the piezo-diaphragm, M_D is given as:

$$M_D = \frac{m_p}{A_R^2} \quad (5.16)$$

where, m_p in this expression is defined as the mass of the piezo-diaphragm. Finally the coupling between the mechanical and electrical domains of the piezo-element is modeled as a transformer with a turning ratio ϕ given by:

$$\phi = -\frac{dK_p}{A_R} \quad (5.17)$$

Further simplification of the circuit analog diagram can be performed, as shown in Figure 5.2. In Figure 5.2, Z is the equivalent impedance of the load resistor R_L in parallel with the piezo capacitance C_p . This is, in the Laplace domain (where $s = i\omega$ is the Laplace complex number, and ω is the system's resonance frequency), given as:

$$Z = \frac{R_L}{1 + R_L C_p s} \quad (5.18)$$

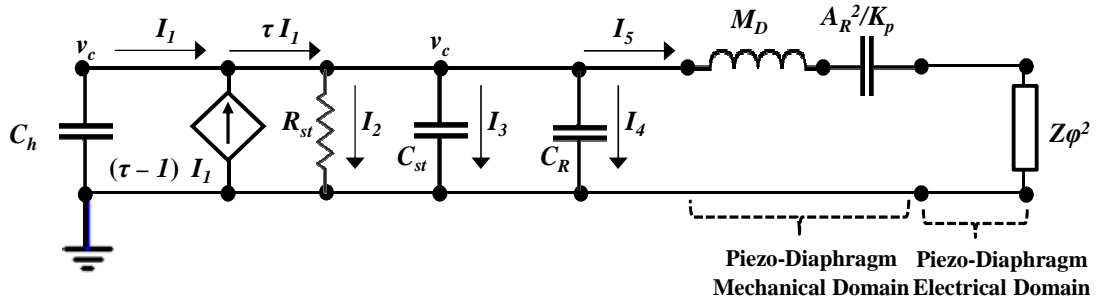


Figure 5.2 Simplified electric circuit equivalent of a TAP harvester

5.4. Electric Circuit Analog of a Standing Wave TAP Harvester

In the lumped-parameter model of the standing wave TAP represented by Figure 5.2, the single pressure v_c can be given by:

$$v_c = \frac{-I_1}{C_h s} \quad (5.19)$$

$$v_c = I_2 R_{st} \quad (5.20)$$

$$v_c = \frac{I_3}{C_{st}s} \quad (5.21)$$

$$v_c = \frac{I_4}{C_R s} \quad (5.22)$$

or,

$$v_c = \left(M_D s + \frac{K_p}{A_R^2 s} + Z\phi^2 \right) I_5 \quad (5.23)$$

while currents I_1 through I_5 are related by:

$$\tau I_1 = I_2 + I_3 + I_4 + I_5 \quad (5.24)$$

Solving equations (5.19) through (5.24) yields the following differential equation with respect to v_c :

$$\left([a_4 + \tau b_4]s^4 + [a_3 + \tau b_3]s^3 + [a_2 + \tau b_2]s^2 + [a_1 + \tau b_1]s + a_0 \right) v_c = 0 \quad (5.25)$$

where:

$$\begin{aligned} a_4 &= M_D A_R^2 C_p R_{st} R_L (C_{st} + C_R) \\ a_3 &= M_D A_R^2 (R_{st} (C_{st} + C_R) + C_p R_L) \\ a_2 &= R_{st} R_L (A_R^2 \phi^2 (C_{st} + C_R) + C_p (C_{st} K_p + C_R K_p + A_R^2)) + M_D A_R^2 \\ a_1 &= R_{st} (C_{st} K_p + C_R K_p + A_R^2) + R_L A_R^2 \phi^2 \\ a_0 &= K_p \end{aligned} \quad (5.26)$$

and:

$$\begin{aligned}
b_4 &= M_D A_R^2 C_h C_p R_{st} R_L \\
b_3 &= M_D A_R^2 C_h R_{st} \\
b_2 &= R_{st} R_L C_h (A_R^2 \phi^2 + C_R K_p) \\
b_1 &= R_{st} C_h K_p
\end{aligned}
\tag{5.27}$$

Equation (5.25) can be adjusted to reflect a standing wave thermoacoustic tube without a piezo-diaphragm at the end by setting $R_L = C_p = K_p = 0$ and replacing the inductance due to the mass of the piezo-element M_D by L_R representing the inductance of the open-ended Helmholtz resonator, as shown in Figure 5.3. Substituting the previous adjustments in equations (5.26) and (5.27), and dividing by A_R throughout, the new equation governing the system simplifies to:

$$\left[(L_R R_{st} (C_{st} + C_R) + \tau L_R C_h R_{st}) s^2 + L_R s + R_{st} \right] v_c = 0
\tag{5.28}$$

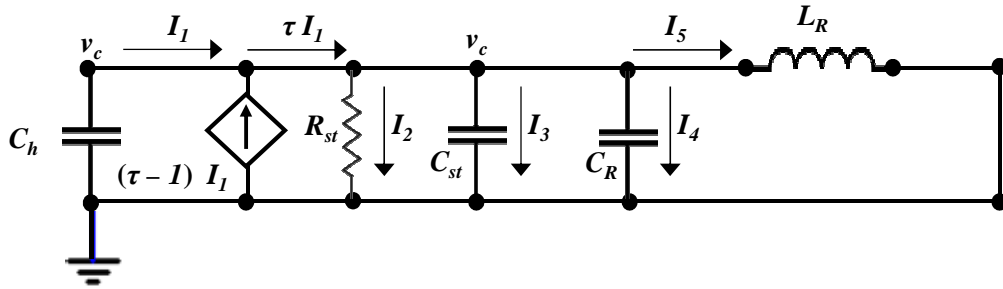


Figure 5.3 Electric circuit equivalent of an open-ended standing wave thermoacoustic resonator

As mentioned earlier, the gain τ is a complex value with real and imaginary parts. Replacing i by s/ω in equation (5.12), τ can be expressed as:

$$\tau = \alpha \frac{\Delta T}{T_a} \left(1 - \frac{s}{\omega} \right) + 1 \quad (5.29)$$

Where α is equal to:

$$\alpha = \frac{1}{2} \frac{1}{1 + \sqrt{\sigma}} \frac{\delta_k}{r_h} \quad (5.30)$$

Substituting (5.29) in (5.25) yields a higher order form of the equation governing the *TAP* system:

$$\left(\begin{aligned} & \left[-\alpha \frac{\Delta T}{T_a} \frac{b_4}{\omega} \right] s^5 + \left[a_4 + \alpha \frac{\Delta T}{T_a} \left(b_4 - \frac{b_3}{\omega} \right) + b_4 \right] s^4 + \left[a_3 + \alpha \frac{\Delta T}{T_a} \left(b_3 - \frac{b_2}{\omega} \right) + b_3 \right] s^3 \\ & + \left[a_2 + \alpha \frac{\Delta T}{T_a} \left(b_2 - \frac{b_1}{\omega} \right) + b_2 \right] s^2 + \left[a_1 + \left(\alpha \frac{\Delta T}{T_a} + 1 \right) b_1 \right] s + a_0 \end{aligned} \right) v_c = 0 \quad (5.31)$$

5.5. Transient Response of TAP Harvester

5.5.1. SPICE Modeling

The *RLC* electric circuits developed in the previous section are modeled on a commercial code in an attempt to obtain the harvester's transient performance characteristics in both cases, with and without the piezo cap. The software used is *LTSPICE*, a freeware high performance *SPICE* simulator software developed by Linear Technology. To account for the current controlled current source (representing the volumetric velocity source due to the external heating) in *LTSPICE*, a virtual zero value voltage source V_1 is connected in series with C_h . A current source I_{input} is set as

a multiplier of the current I_1 flowing in V_1 in the time domain. This is inputted as follows:

$$I_{input} = \alpha \frac{\Delta T}{T_a} I_1 - \frac{1}{\omega} \frac{d}{dt}(I_1) \quad (5.32)$$

Note that α is a function of δ_k which is a frequency dependent term. In addition, equations (5.31) and (5.32) contain ω in some of its coefficients. Consequently, the solution of equation (5.31) to obtain the system's critical ΔT and its frequency of oscillations ω is an iterative process, that requires an adequate initial guess of ω that needs to eventually match ω outputted in the final solution. Finally, the impedance $Z\phi^2$ in Figure 5.2 is achieved in *LTSPICE* using a parallel combination of a resistor $R_L\phi^2$ and a capacitance C_p / ϕ^2 . A schematic of the *SPICE* model of the *TAP* is displayed in Figure 5.4.

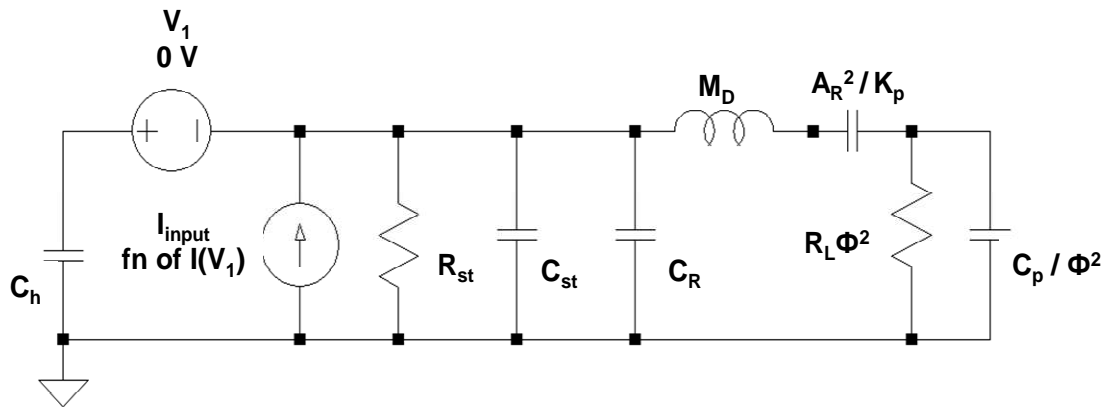


Figure 5.4 *LTSPICE* schematic of a *TAP* energy harvester

The values of the different circuit components are obtained from the expressions presented in the previous section, using the values given in Table 3.1 for prototype 2, which is the experimental *TAP* harvester discussed in Chapter 4.

5.5.2. *Root Locus Technique*

Pressure oscillations resulting in the traveling wave resonator, with and without the piezo cap, are governed by the differential equation given in equation (5.31) which can be solved using the *SPICE* model developed earlier for different values of $\Delta T / T_a$. When the temperature difference reaches the critical threshold for this resonator, pressure oscillations inside the tube should be self-sustained and should not die out. It can thus be deduced that the stability of the system's response will depend on values of $\Delta T / T_a$. A root locus approach can be introduced to determine the values of the temperature difference which will cause the poles of the system to cross the imaginary axis and hence define the stability of the oscillations [51]. This is done by regrouping the terms in equation (5.31) and casting it in the form,

$$1 + \frac{T_a}{\Delta T} \frac{N(s)}{D(s)} = 0 \quad (5.33)$$

where:

$$N(s) = (a_4 + b_4)s^4 + (a_3 + b_3)s^3 + (a_2 + b_2)s^2 + (a_1 + b_1)s + a_0 \quad (5.34)$$

and:

$$D(s) = \alpha \left[\left(-\frac{b_4}{\omega} \right) s^5 + \left(b_4 - \frac{b_3}{\omega} \right) s^4 + \left(b_3 - \frac{b_2}{\omega} \right) s^3 + \left(b_2 - \frac{b_1}{\omega} \right) s^2 + (b_1) s \right] \quad (5.35)$$

5.5.3. Performance of open-ended standing wave resonator (no piezo)

Figure 5.5 shows that a temperature ratio of $\Delta T / T_a = 1.62$ will cause the open-ended system to produce marginally stable pressure oscillations at a resonant frequency of about 165 Hz. Further increasing in the temperature ratio will force the system to an unstable state, represented by the self-sustained acoustic oscillations.

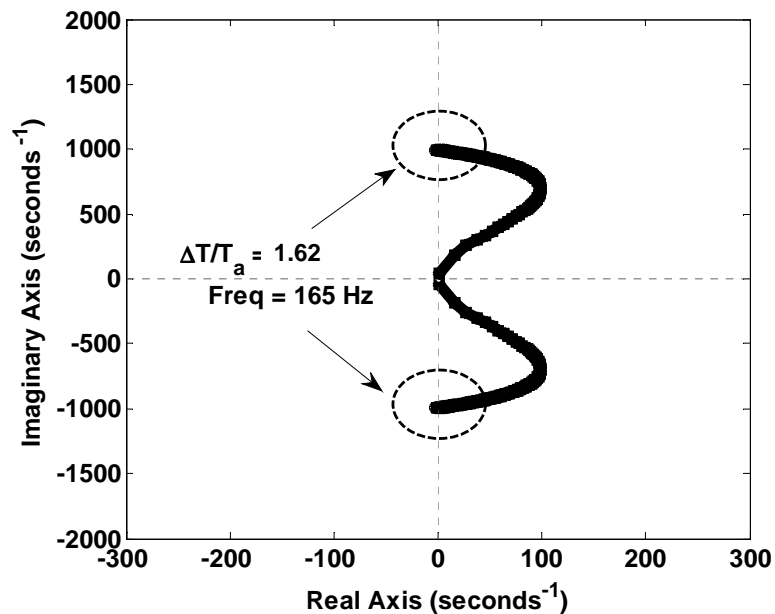


Figure 5.5 Close up on root locus plot for open-ended standing wave resonator

The same phenomenon can be observed in an electric circuit analysis. A circuit response may grow and blow up, rather than decay, with time. This type of response is called an “unbounded response” and typically happens in circuits

containing dependent sources [52]. In those cases, the Thevenin equivalent resistance with respect to the terminals of either an inductor or a capacitor is negative. This negative resistance generates a negative time constant, and the resulting currents and voltages increase in time without limit. In actual circuits, the response eventually reaches a limiting value and goes into a saturation state when a component breaks down prohibiting further increase in voltage or current.

The developed *LTSPICE* circuits undergo a transient analysis to determine the onset characteristics of the system. By sweeping a large domain of $\Delta T / T_a$ values and monitoring the pressure given by the voltage v_c , it is found that the open-ended resonator (Figure 5.3) will become unstable when $\Delta T / T_a$ exceeds 1.62 giving rise to self-sustained acoustic oscillations in the resonator. The resonant frequency of the system is obtained by replacing the current source with an AC source and performing a frequency sweep. It is calculated to be about 164 Hz. Those values are in very close agreement with those obtained by the root locus analysis.

Another validation of these results is obtained by solving equation (5.28) using the Laplace inverse method and a *MATLAB* code. Both *LTSPICE* and *MATLAB* require initial values of the pressure v_c to be inputted. For comparison purposes, the same arbitrary initial values are used for the *LTSPICE* transient analysis and the *MATLAB* program. The time response of v_c for different $\Delta T / T_a$ values is shown in Figure 5.6 while the frequency response is displayed in Figure 5.7.

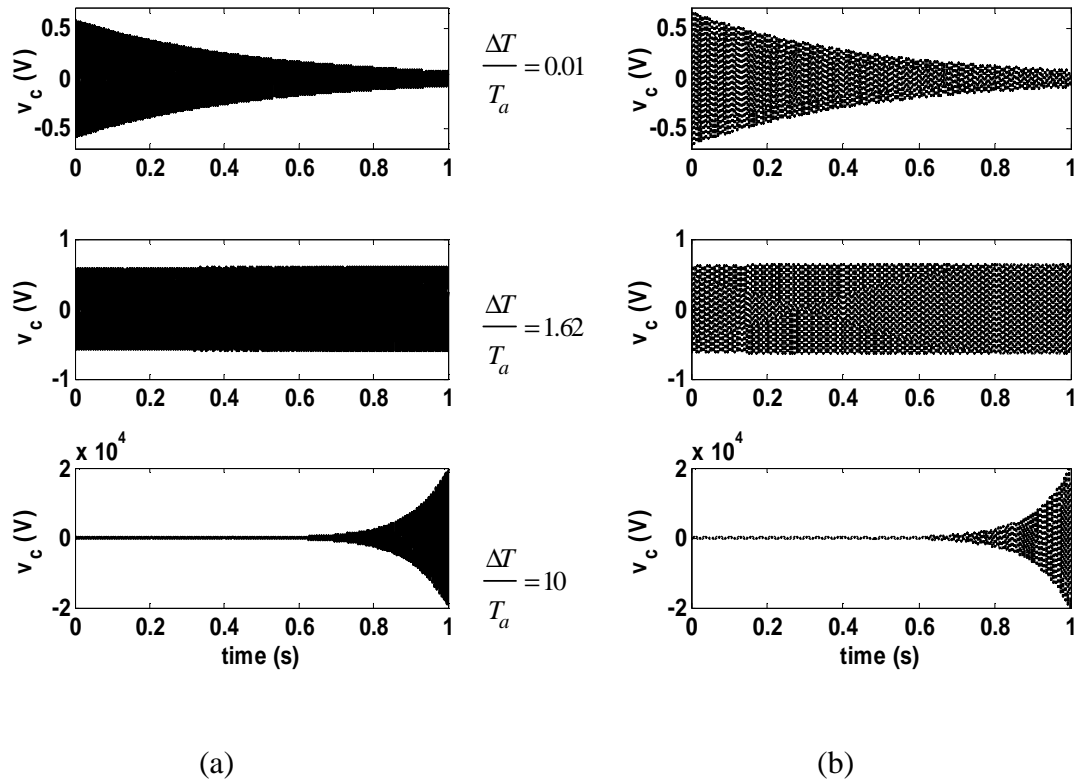


Figure 5.6 Stable, marginally stable and unstable pressure pulsations v_c in the open-ended standing wave resonator obtained by (a) *MATLAB* and (b) *LTSPICE* model

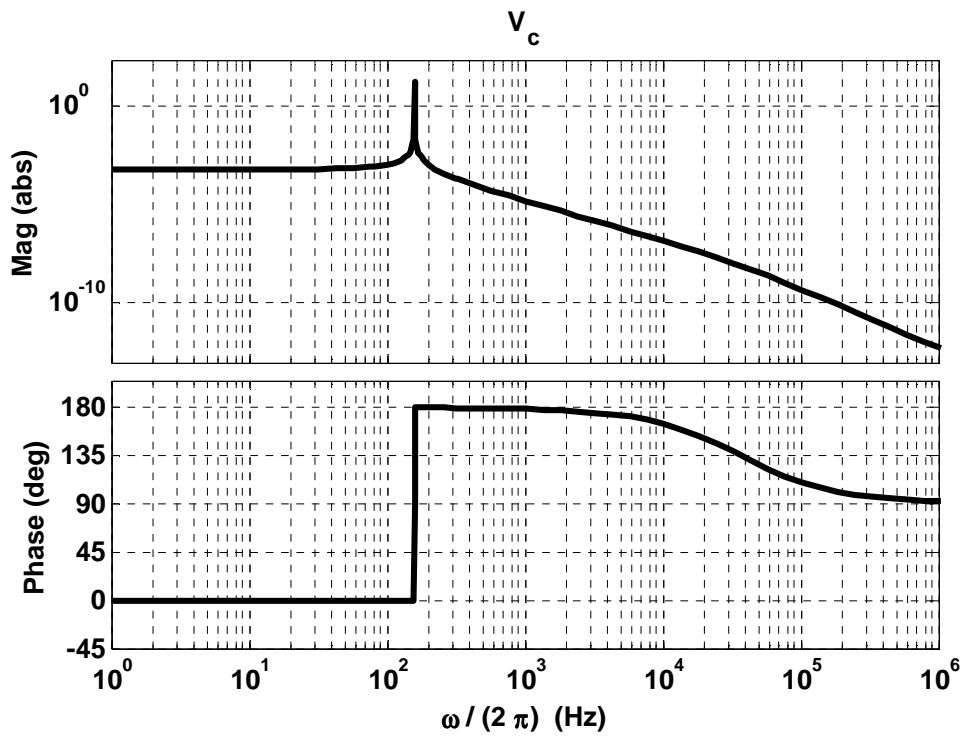


Figure 5.7 Frequency response of open-ended standing wave resonator at $\Delta T/T_a = 1.62$ (resonant frequency ~ 165 Hz)

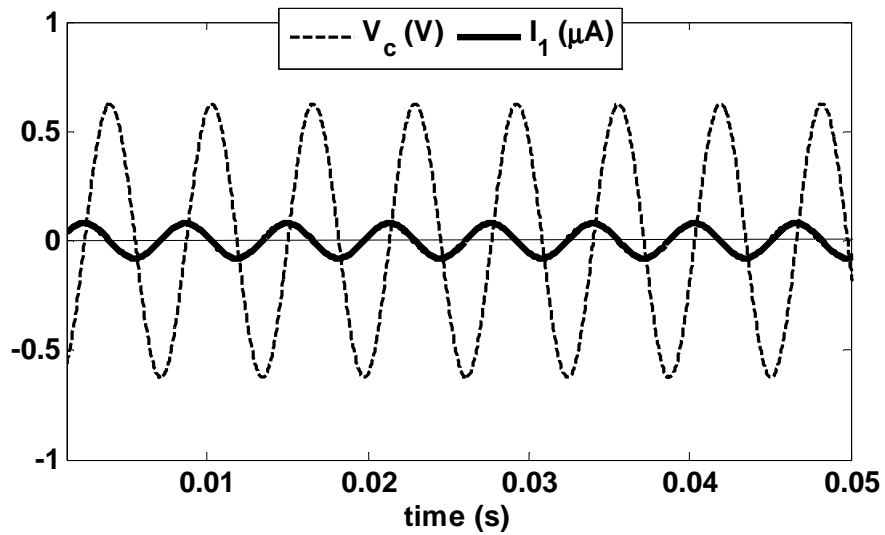


Figure 5.8 Comparison of v_c and I_1 in an open-ended standing wave resonator obtained via *LTSPICE*

Several performance metrics that are characteristic of standing wave thermoacoustic engines can be also inferred from electric circuit analogy modeling. Typically, *standing* wave harvesters are called so, because the time phasing between pressure and velocity of the oscillating working gas is close to that of a standing wave (almost out of phase). To achieve that phasing condition, imperfect thermal contact between the gas particles and the stack solid boundaries is needed, so that the gas can be considerably thermally isolated from the adjacent solid in parts of its cyclic motion but still exchange heat in others [50]. This condition enforces the size of the stack pores to be in the vicinity of the thermal and viscous penetration depths of the gas, and is also responsible for the imaginary component in the term G_{st} in equation (5.11). This is contrast to what happens in the other class of thermoacoustic engines referred to as traveling wave engines. Figure 5.8 shows a comparison between v_c and I_1 obtained from the circuit solution that validates the previous phenomenon.

5.5.4. Performance of TAP with piezo-diaphragm

For the *TAP* harvester with the piezo-cap on, it is found that the system will become unstable when $\Delta T / T_a$ exceeds 1.71 giving rise to self-sustained acoustic oscillations in the resonator, as depicted by Figure 5.9. The developed *LTSPICE* circuit in Figure 5.2 undergoes a transient analysis to determine the onset characteristics of the system. By sweeping a large domain of $\Delta T / T_a$ values and monitoring the pressure given by the voltage v_c , it is found that the system becomes unstable when $\Delta T / T_a$ exceeds 1.71 and the resonant frequency of the system is

calculated to be about 453 Hz. Once again, those values are in very close agreement with those obtained by the root locus analysis. The time response of v_c for different $\Delta T / T_a$ values is shown in Figure 5.10 while the frequency response is displayed in Figure 5.11. In Figure 5.12, time responses of v_c and I_1 , are again shown to be close to the behavior of a standing wave.

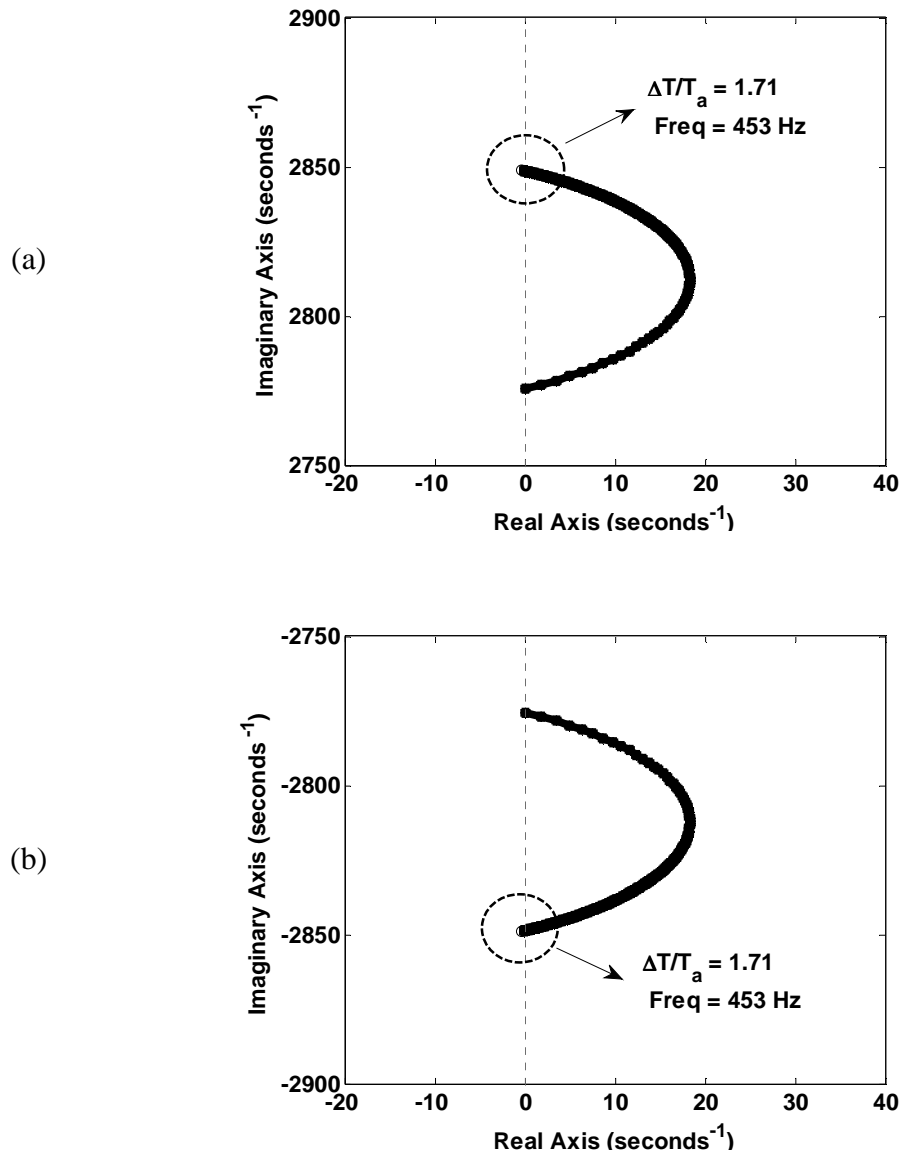


Figure 5.9 Close up on (a) positive and (b) negative sections of the imaginary axis in the root locus plot for TAP harvester

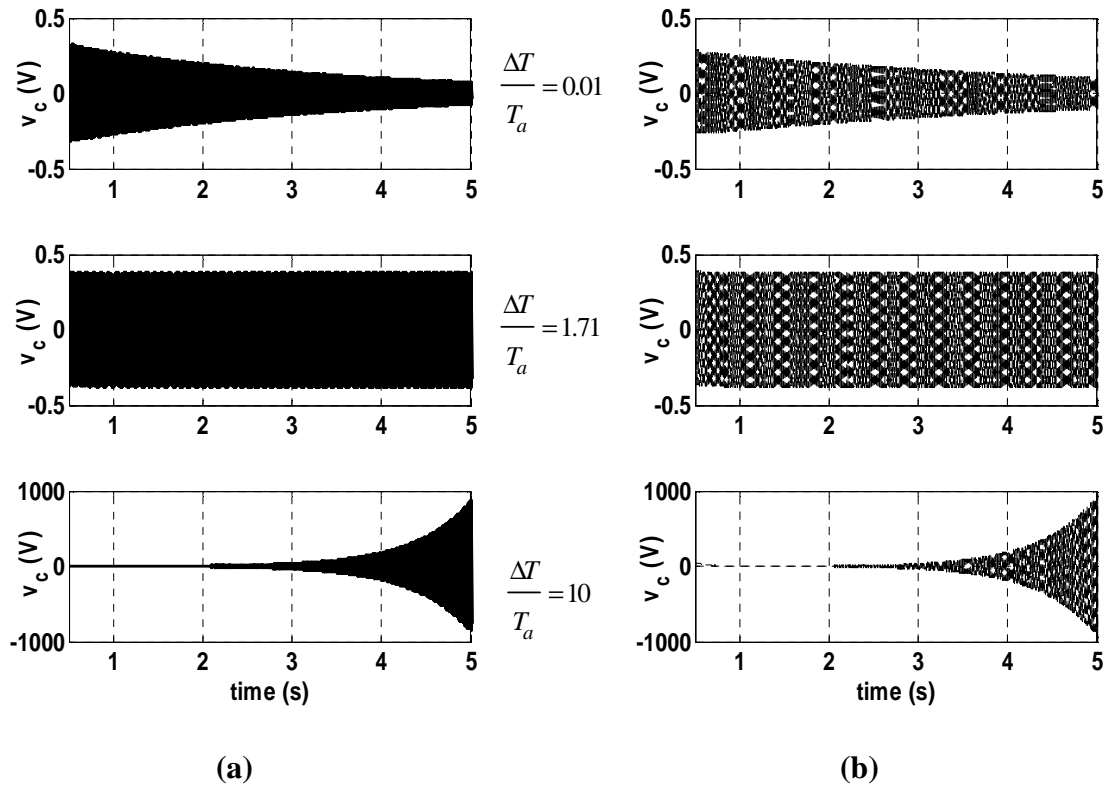


Figure 5.10 Stable, marginally stable and unstable pressure pulsations v_c in the *TAP* harvester obtained by (a) Root locus analysis and (b) *LTSPICE* model

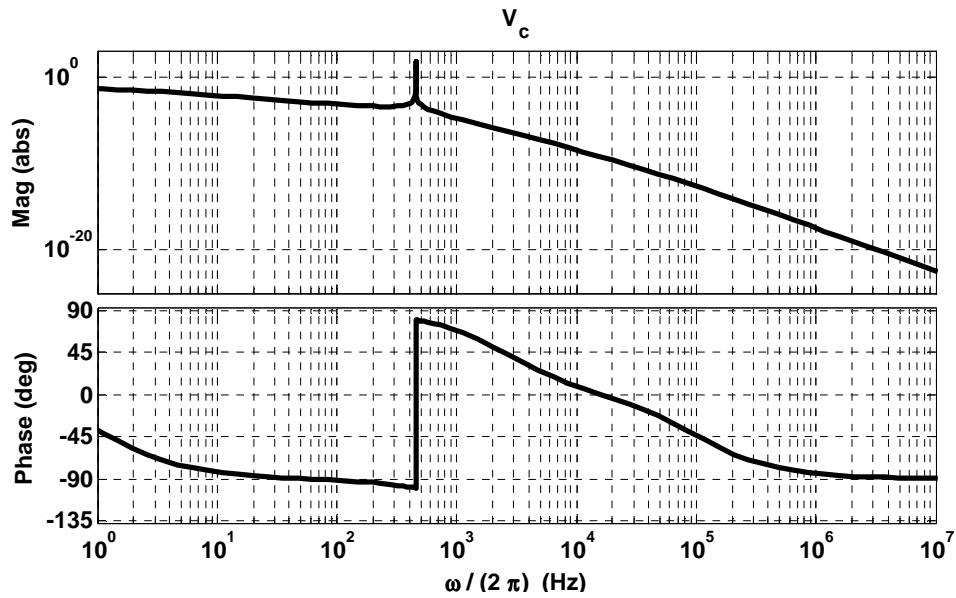


Figure 5.11 Frequency response of the *TAP* system at $\Delta T/T_a = 1.71$ (resonant frequency ~ 453 Hz)

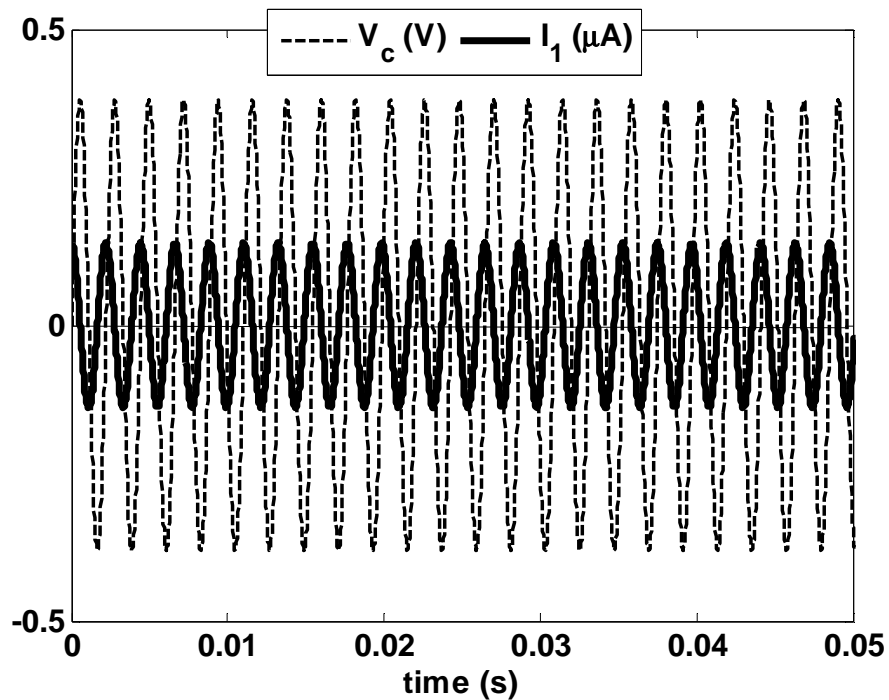


Figure 5.12 Comparison of v_c and I_1 in the TAP harvester obtained via LTSPICE

5.6. Comparison with Experimental Prototype

5.6.1. Frequency of oscillations

The experimental prototype of the standing wave thermoacoustic harvester discussed in Chapter 4 and shown in Figure 4.2 is used here to validate the proposed theory. The frequency of the self-sustained oscillations as well as the onset temperature gradients are compared against theoretical results obtained using circuit analogy and root locus. In addition, a *DeltaEC* [34] model of the harvester is used to further validate the obtained data with regard to steady state performance of the harvester.

As explained earlier, an electrical heater element in the form of a resistance wire is used to simulate the heat input at the hot heat exchanger. The heater provides the input thermal energy necessary to generate the self-sustained thermoacoustic waves. For the system under consideration, such conditions are attained when the heater thermal input power is about 40 W. The frequency of oscillations is measured to be 388 *Hz*, with the piezo-diaphragm on and 187 *Hz* with an open-ended resonator. Table 5.1 shows a comparison between the frequency of oscillations calculated from the electric network using *SPICE*, and numerically using *DeltaEC* and that achieved experimentally, for both cases with and without the piezo-diaphragm. The experimental values appear to be in reasonable agreement with the predications in both cases.

Table 5.1 Comparison between theoretical and experimental oscillation frequencies

	Frequency (<i>Hz</i>)	
	Open-ended	With Piezo-diaphragm
<i>SPICE</i>	165	453
<i>DeltaEC</i>	191	411
Experiment	187	388

5.6.2. Temperature Gradient

A resistance wire powered by a DC power source is used to heat the hot side of the stack and create the temperature difference across its end. Several experiments are carried out with different levels of power inputs to the stack, with the piezo-diaphragm placed at the end of the resonator. For each run, the evolution of the

temperature difference across the stack is measured with time until it reaches a constant value and then input power is tuned off. Acoustic oscillations inside the resonator are only sustained when the power input to the heating element exceeds a certain threshold. For each of the previous experiments, the temperature gradient ∇T is plotted against time. Results are plotted in Figure 5.13. The horizontal dashed line at $\nabla T_{onset} = 14520 \text{ K/m}$ represents the minimum temperature gradient needed to achieve self-sustained oscillations in the harvester. It can be seen that a power input of about 40 W (or higher) is required to achieve that condition.

As calculated earlier, a ratio of $\Delta T / T_a = 1.71$ is predicted by the root locus method and the electric circuit analog to onset sustainable oscillations for a harvester of the same dimensions. Assuming an ambient temperature of around 300 K and using the stack length of 33.75 mm, this is equivalent to $\nabla T_{onset} = 15200 \text{ K/m}$, which is represented in Figure 5.13 by the horizontal dotted line. This value for the temperature gradient is very consistent with the experimental realizations.

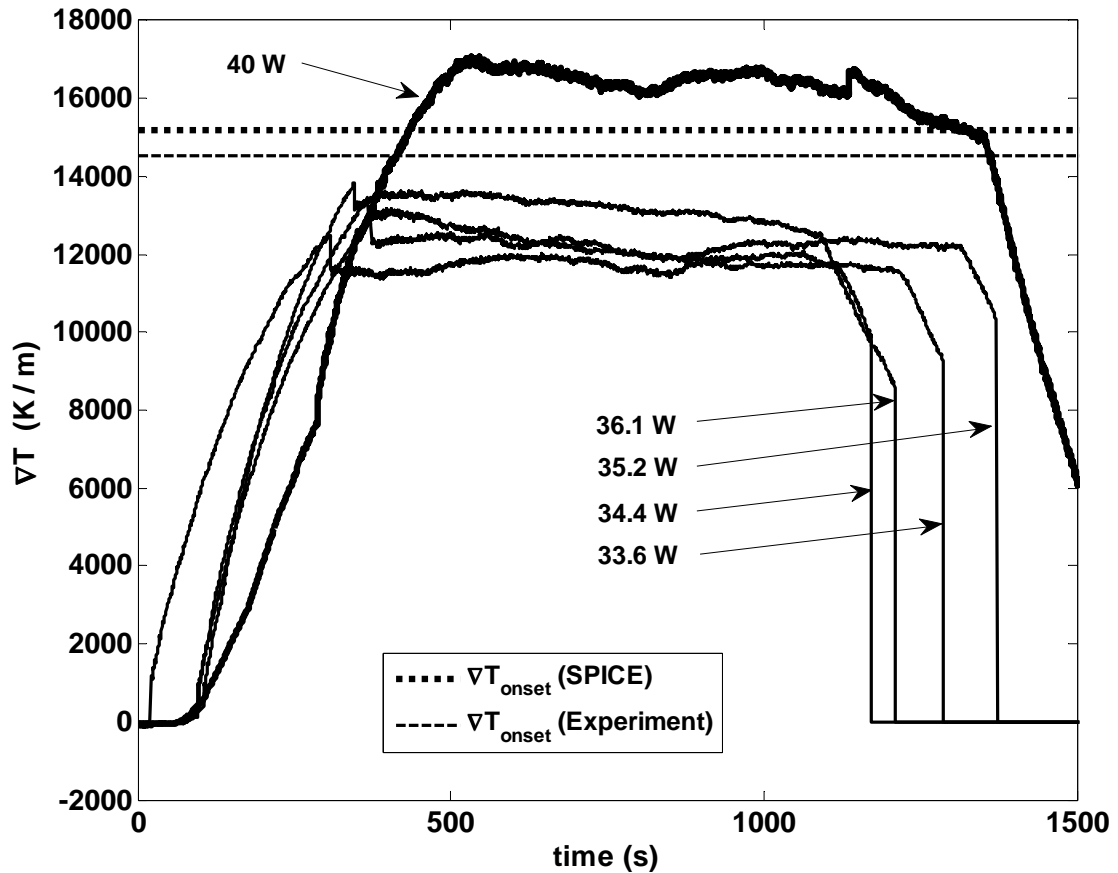


Figure 5.13 Temperature gradient in the stack of the *TAP* harvester at different power inputs. Horizontal lines show the predicted and the actual gradient required to onset oscillations.

Figure 5.14(a) shows the progression of the hot (T_h), mid-point (T_m), and ambient (T_a) temperatures of the stack at heat input of around 40 W, which is sufficient to maintain acoustic oscillations inside the resonator. Heat input is turned off after about 1000 seconds explaining the drop in the temperatures. In Figure 5.14 (b), the temperature variation with the resonator's length x as predicted by *DeltaEC* is shown. Experimentally measured temperatures are coherent with *DeltaEC*'s predictions with some minor discrepancies at the ambient end of the stack. Due to the

lack of a heat sink, the temperature drops to ambient temperature (300 K) about 4 cm outside the stack, with the right side of the stack is observed to be maintained at around 400 K.

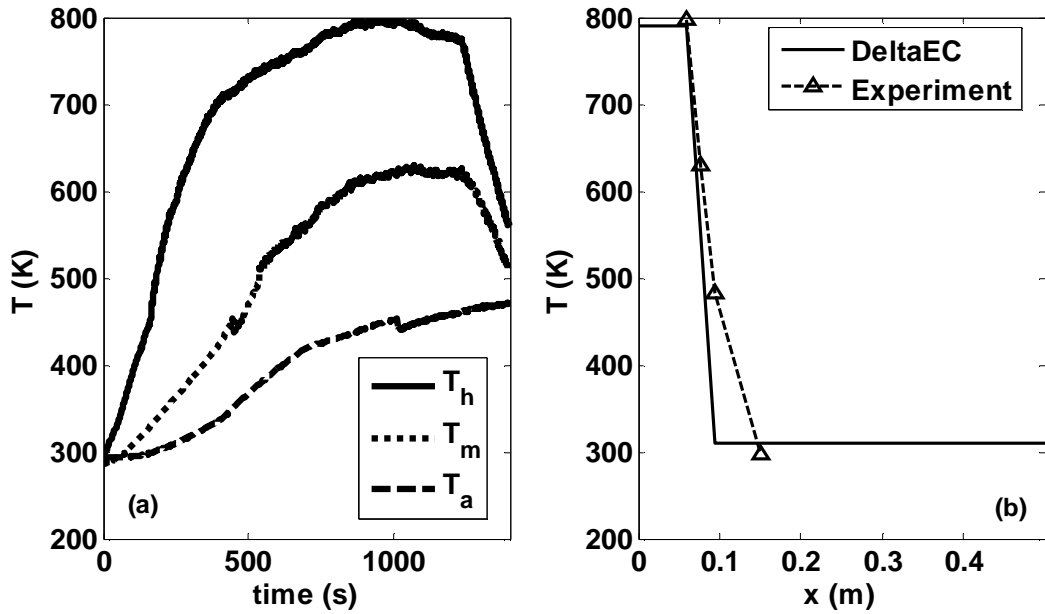


Figure 5.14 (a) Temperature evolution inside the stack of the *TAP* harvester at 40 W of power input, and (b) temperature distribution along the resonator at steady state

5.7. Summary

This chapter has presented an electrical network analogy of standing wave thermoacoustic-piezoelectric (*TAP*) energy harvesters. The developed network is used as a tool to provide a comprehensive analysis of the transient behavior and the onset of self-sustained oscillations in *TAP* resonators as compared to conventional thermoacoustic resonators with open-ended resonators. The electrical circuit analog provides a unifying approach to the multi-field problem which combines the dynamics of the acoustic resonator and stack, with the characteristics of the

piezoelectric harvester. With the help of a *SPICE* code, the developed electric circuit is used to analyze the system's stability with regard to the input heat and hence predict the necessary temperature ratio required to establish the sustainable oscillations inside the harvester's resonator. An alternative root locus technique is presented which is build off of the developed system equations and can be used to predict the required temperature gradients as well.

These approaches provide a very practical approach to the design of *TAP* energy harvesters both in the time and frequency domain. Such capabilities do not exist presently in the well-known design tool *DeltaEC* which is limited to steady-state analysis.

The obtained values for the onset temperature gradients are found to be slightly higher for the piezo-diaphragm equipped harvester as compared to conventional open-ended resonators. The predictions of the developed analysis tools are validated against an experimental prototype and are shown to be in good agreement.

Chapter 6

6. Piezo-driven Thermoacoustic Refrigerators: Modeling and Theoretical Analysis

6.1. Introduction

Contrary to standing wave thermoacoustic harvesters, thermoacoustic refrigerators use a driving acoustic wave as an input energy to stimulate a temperature gradient between the two ends of the stack. This is referred to as the “*reverse thermoacoustic effect*” and the thermoacoustic device serves as a refrigerator or a heat pump.

The general concepts governing acoustic wave propagation in resonator cavities still apply. Hence, slight modifications are applied to the equations governing the pressure and velocity waveforms in order to take into consideration the effect of the different boundary conditions (such as the existence of a driving speaker at one end of the tube). Focus is given here to thermoacoustic refrigerators driven by piezo-speakers, i.e. speakers that rely on piezo-diaphragms in their operation., as opposed to conventional electromagnetic speakers.

The methodologies considered in Chapter 2 are used here as well to model thermoacoustic refrigerators. Even though the effect of the stack on the acoustic waveforms is negligible, its effect on the radiated acoustic power along the tube is

not, as will be seen later. The amount of acoustic power at the location of the stack determines the magnitude of the induced temperature gradient and thus it is a key performance parameter. This calls for some modifications in the equations governing acoustic pressure and velocity to account for the stack location, geometry and porosity.

One goal of this study is to integrate the model developed here with dynamic magnifiers aimed at enhancing the performance in a manner similar to that described in Chapter 2. Details of the implementation of magnifiers in refrigerator systems are discussed at the end of this chapter.

6.2. Piezoelectric Speakers

Thermoacoustic refrigerators discussed here are driven by piezo-speakers. These speakers are mainly constituted of a piezo-diaphragm that exhibits mechanical strain when a voltage is applied across its electrodes, and responds by flexing in proportion to the applied electrical input. The conversion of electrical pulses into mechanical vibrations drive the acoustic pulsations along the resonator which are needed to create the temperature difference across the ends of the stack. We refer to this type of systems as **Piezo-driven Thermoacoustic Refrigerators (PDTARs)**.

The use of piezo-speakers results in a system that is generally advantageous to conventional electromagnetic speakers driven thermoacoustic refrigerators. Piezoelectric speakers are more resistant to overloads that would normally destroy

most drivers and can operate more efficiently at high frequencies. A more detailed comparison between the performances of thermoacoustic refrigerators driven by different speaker types is discussed by Chinn 2010 [53].

The speaker used here is a commercially available PZ-94 piezoelectric speaker from ISL products [44] and shown in Figure 6.1 (a). The speaker consists of a piezo-diaphragm sitting on a shunting material and sandwiched between a couple of flexible screen meshes which are used as electrodes and mounting structures. A plastic diaphragm is then mounted on top and glued to the top mesh at the center point as illustrated in Figure 6.1 (b). When a voltage is applied across the top and bottom screens, the piezo-element expands or contracts (depending on the voltage direction) while the shunting layer remains the same causing a moment to be created between the two and the whole diaphragm to deflect. When excited by an AC signal, the disk deflects back and forth and displaces the adjacent air particles. This generates the acoustic power output that drives the acoustic oscillations along the resonator. The dimensions of the speaker are as shown in Figure 6.1 (c).

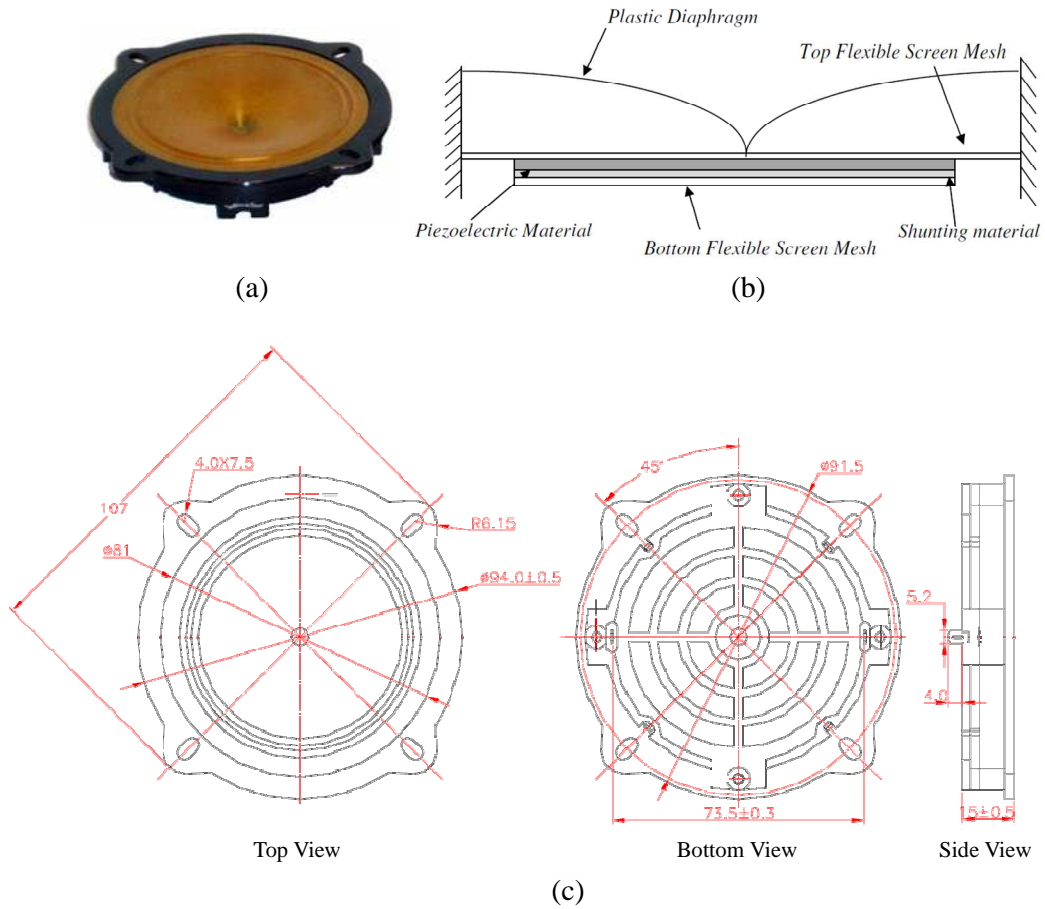


Figure 6.1 (a) PZ-94 Piezo-speaker from ISL Products, (b) Schematic diagram of speaker's operation, and (c) Dimensions of the speaker (units in mm ± 0.5)

6.3. Constant Area PDTAR

6.3.1. Pressure and Velocity Waveforms

Based on the mathematical model suggested by [39], the variation of the spatial component of oscillating pressure $P(x)$ and velocity $U(x)$ for a one-dimensional plane wave propagation along the x -direction is governed by,

$$\partial_{xx}^2 P(x) + \kappa^2 P(x) = 0 \quad (6.1)$$

and,

$$U(x) = \frac{i}{\rho\omega} (1 - f_v) \partial_x P(x) \quad (6.2)$$

where κ and f_v are functions of the working gas thermo-physical properties, thermal and viscous boundary thicknesses [40]. A constant area *PDTAR*'s resonator, as shown in Figure 6.2, consists mainly of 3 segments: a cold part of the tube from $x = 0$ to $x = x_1$, a hot tube from $x = x_2$ to $x = L$, and a stack in between.

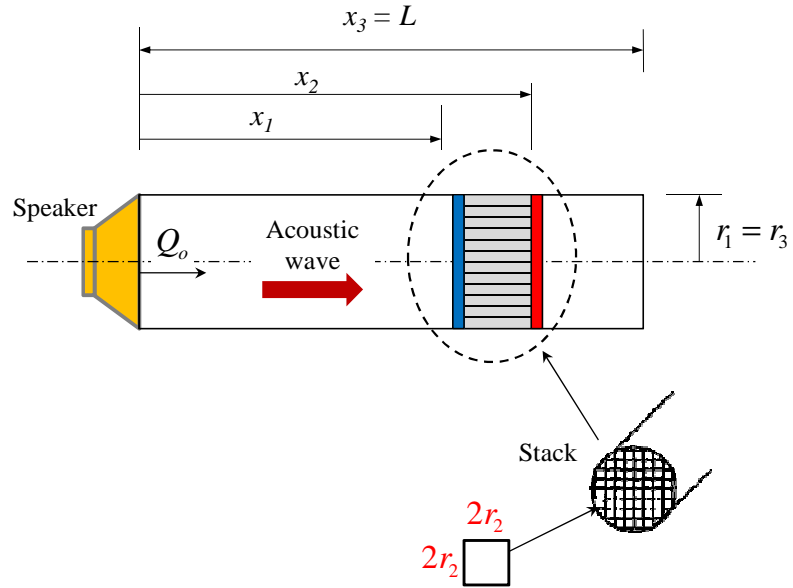


Figure 6.2 Schematic drawing of a constant area *PDTAR*

For this simple model equation (6.1) can be more specifically rewritten as,

$$\partial_{xx}^2 P_{1,2,3}(x) + \kappa_{1,2,3}^2 P_{1,2,3}(x) = 0 \quad (6.3)$$

with,

$$\kappa_{1,3}^2 = \kappa_o^2 \left[1 + f_{v,1,3} + (\gamma - 1) f_{k_{1,3}} \right] \quad (6.4)$$

$$\kappa_2^2 = \kappa_o^2 \left[\frac{1 + (\gamma - 1) f_{k_2}}{1 - f_{v_2}} \right] \quad (6.5)$$

where,

$$f_{v,k_{1,3}} = (1 - i) \frac{\delta_{v,k}}{r_{1,3}} \quad (6.6)$$

$$f_{v,k_2} = \frac{\tanh \left[(1 + i) r_2 / \delta_{v,k} \right]}{\left[(1 + i) r_2 / \delta_{v,k} \right]} \quad (6.7)$$

where f_k is a function of the working gas thermal boundary thickness and,

$$\kappa_o = \omega / c + \alpha i \quad (6.8)$$

As defined in Chapter 2, $\delta_{v,k}$ denotes the viscous and thermal boundary thicknesses (also referred to as penetration depths), γ is the ratio of isobaric to isochoric specific heats of the working gas, ρ is the gas density, c is the adiabatic sound speed in that gas and α is the wave attenuation (loss) factor. The expressions with the 1 and 3 indices are for the first and last segments of the resonator. Since the resonator has a uniform area (i.e. $r_1 = r_3$), therefore $f_{v,k_1} = f_{v,k_3}$ and $\kappa_1 = \kappa_3$. For the stack, the expressions given with the index 2 are for a stack with the given cross section in Figure 6.2. For convenience, general expressions for arbitrarily shaped stacks are given by [41].

The solution of equation (6.3) takes the following form,

$$P_{1,2,3}(x) = C_{1,2,3} \left(e^{-i\kappa_{1,2,3}x} + R_{1,2,3} e^{i\kappa_{1,2,3}x} \right) \quad (6.9)$$

and thus,

$$U_{1,2,3}(x) = \frac{iC_{1,2,3} \left(1 - f_{v_{1,2,3}} \right)}{\rho\omega} \left(-i\kappa_{1,2,3} e^{-i\kappa_{1,2,3}x} + i\kappa_{1,2,3} R_{1,2,3} e^{i\kappa_{1,2,3}x} \right) \quad (6.10)$$

where the constants $C_{1,2,3}$ and $R_{1,2,3}$ are to be obtained from the system's boundary conditions.

6.3.2. Boundary Conditions

The boundary conditions for this system of equations are simply continuity based such that the pressures are equal at the interface of the 3 segments, *i.e.*

$$P_1(x_1) = P_2(x_1), \quad P_2(x_2) = P_3(x_2) \quad (6.11)$$

The volume flow rate at those points, *i.e.* the velocity-area product, should also satisfy the continuity equation,

$$S_1 U_1(x_1) = S_2 U_2(x_1), \quad S_2 U_2(x_2) = S_3 U_3(x_2) \quad (6.12)$$

where $S_{1,2,3}$ denotes the cross sectional area of the different segments.

Finally, the velocity of the gas particles at the beginning of the tube should match that supplied by the driving speaker, while the rigid end at the other end implies a zero velocity condition,

$$U_1(0) = \frac{Q_o}{S_1}, \quad U_3(L) = 0 \quad (6.13)$$

where Q_o is the volume flow rate provided by the speaker. Substituting the second half of equation (6.13) into equation (6.10) gives,

$$\frac{iC_3(1-f_{v_3})}{\rho\omega}(-i\kappa_3 e^{-i\kappa_3 L} + i\kappa_3 R_3 e^{i\kappa_3 L}) = 0 \quad (6.14)$$

which simplifies to,

$$R_3 = e^{-2i\kappa_3 L} \quad (6.15)$$

while using the first half of equation (6.13) with equation (6.10) gives,

$$\frac{iC_1(1-f_{v_1})}{\rho\omega}(-i\kappa_1 + i\kappa_1 R_1) = \frac{Q_o}{S_1} \quad (6.16)$$

which yields,

$$C_1 = \frac{\rho\omega Q_o}{S_1 \kappa_1 (1-f_{v_1})(1-R_1)} \quad (6.17)$$

Similarly, by using equations (6.11) through (6.13), the rest of the constants can be determined in terms of C_1 and R_3 , yielding

$$C_2 = \frac{2C_1 e^{-i\kappa_1 x_1}}{e^{-i\kappa_2 x_1} \left(1 + \frac{1}{\Delta}\right) + R_2 e^{i\kappa_2 x_1} \left(1 - \frac{1}{\Delta}\right)} \quad (6.18)$$

$$C_3 = \frac{2C_2 e^{-i\kappa_2 x_2}}{e^{-i\kappa_3 x_2} (1 + \Delta) + R_3 e^{i\kappa_3 x_2} (1 - \Delta)} \quad (6.19)$$

$$R_1 = e^{-2i\kappa_1 x_1} \left[\frac{e^{-i\kappa_2 x_1} \left(1 - \frac{1}{\Delta}\right) + R_2 e^{i\kappa_2 x_1} \left(1 + \frac{1}{\Delta}\right)}{e^{-i\kappa_2 x_1} \left(1 + \frac{1}{\Delta}\right) + R_2 e^{i\kappa_2 x_1} \left(1 - \frac{1}{\Delta}\right)} \right] \quad (6.20)$$

$$R_2 = e^{-2i\kappa_2 x_2} \left[\frac{e^{-i\kappa_3 x_2} (1 - \Delta) + R_3 e^{i\kappa_3 x_2} (1 + \Delta)}{e^{-i\kappa_3 x_2} (1 + \Delta) + R_3 e^{i\kappa_3 x_2} (1 - \Delta)} \right] \quad (6.21)$$

where,

$$\Delta = \frac{(1 - f_{v_{1,3}}) \kappa_{1,3} S_{1,3}}{(1 - f_{v_2}) \kappa_2 S_2} \quad (6.22)$$

6.3.3. Acoustic Power

The acoustic power propagating along the thermoacoustic resonator by the loudspeaker can be written as,

$$P_{ac,1,2,3}(x) = \frac{S_{1,2,3}}{2} \operatorname{Re} \left[P_{1,2,3}(x) \operatorname{conj}(U_{1,2,3}(x)) \right] \quad (6.23)$$

Equation (6.23) is similar to equation (2.30) used which is used with thermoacoustic energy harvesters. Note that equation (2.30) gives the acoustic power at the end of the resonator ($x = L$) in order to determine the input power to the piezo-

element, while equation (6.23) provides the acoustic energy flux at any point along the resonator. This is necessary to be able to capture the acoustic power at the stack location which is a key factor in constituting the temperature gradient across the stack ends.

The radiation of acoustic power along a tube with a stack located between x_1 and x_2 typically takes the shape shown in Figure 6.3 [33].

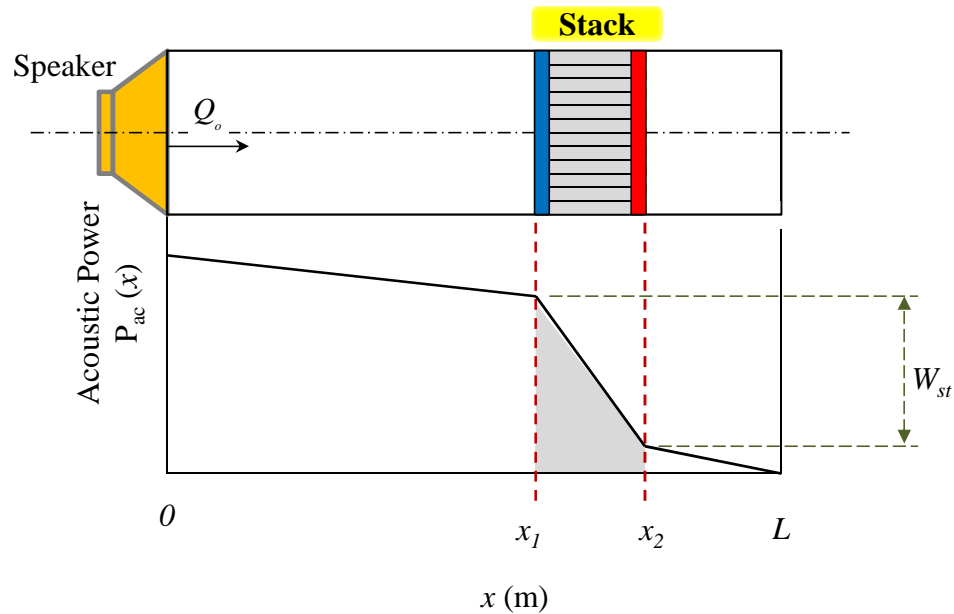


Figure 6.3 Propagation of acoustic power inside a thermoacoustic refrigerator

The amount of power absorbed or produced by the stack \dot{W}_{st} is obtained by evaluating equation (6.23) at the ends of the stack and taking the difference between them to yield,

$$\dot{W}_{st} = P_{ac}(x_2) - P_{ac}(x_1) \quad (6.24)$$

As expected, a negative value is obtained for \dot{W}_{st} for thermoacoustic refrigerators. In thermodynamic convention, this denotes that an energy/work related quantity has been absorbed instead of being produced. Contrary to thermoacoustic engines, whereby an acoustic energy is produced in the stack and is ultimately harvested at the end of the tube by means of a transducer, values obtained for \dot{W}_{st} from equation (2.44) are expectedly positive.

6.4. Variable Area PDTAR

The *PDTAR* built as a prototype for experimental validation consists of two adjacent tubes with two different cross sections. The piezo-speaker is hooked to the first tube, and thus the first part of the resonator has an area equal to that of the speaker face. However, such a tube size will require a considerably large stack. Stacks of a smaller cross section have generally shown to be more effective and have a better resolution for a one-dimensional temperature gradient as heat conduction across the axis perpendicular to the wave propagation is fairly limited. For such purpose, another tube of a smaller diameter is attached to the first tube and represents the major length of the resonator. The stack is placed towards the end of the second tube. A schematic of this design of the *PDTAR* is shown in Figure 6.4.

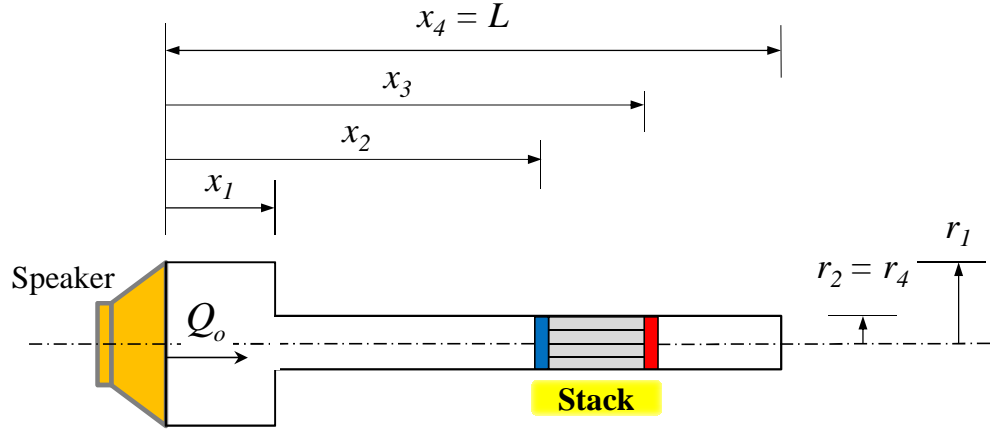


Figure 6.4 Schematic of a variable area PDTAR

To be able to provide a legitimate comparison with the experimental results to follow in the next chapter, the mathematical model described in section 6.3 has to be adjusted to reflect the new design. The new resonator now consists of 4 segments, with an area change at the interface between the 2 tubes at the end of x_1 . Pressure and velocity waveforms as well as acoustic power are now described as,

$$P_j(x) = C_j \left(e^{-i\kappa_j x} + R_j e^{i\kappa_j x} \right) \quad (6.25)$$

and,

$$U_j(x) = \frac{iC_j(1-f_{v_j})}{\rho\omega} \left(-i\kappa_j e^{-i\kappa_j x} + i\kappa_j R_j e^{i\kappa_j x} \right) \quad (6.26)$$

and,

$$P_{ac_j}(x) = \frac{S_j}{2} \text{Re} \left[P_j(x) \text{conj}(U_j(x)) \right] \quad (6.27)$$

where $j = 1, 2, 3$ and 4. Pressure continuity is still maintained, hence:

$$P_1(x_1) = P_2(x_1), P_2(x_2) = P_3(x_2), P_3(x_3) = P_4(x_3) \quad (6.28)$$

The volumetric flow rate, given by the velocity-area product, also has to be equal at x_1 , x_2 , and x_3 giving:

$$S_1 U_1(x_1) = S_2 U_2(x_1), S_2 U_2(x_2) = S_3 U_3(x_2), S_3 U_3(x_3) = S_4 U_4(x_3) \quad (6.29)$$

The boundary condition at $x = 0$ and $x = L$ remain instated as,

$$U_1(0) = \frac{Q_o}{S_1}, U_4(L) = 0 \quad (6.30)$$

Equations (6.28), (6.29) and (6.30) provide 8 linear equations in 8 unknowns. These can be solved simultaneously to obtain values for R_1 through R_4 , and C_1 through C_4 . Once these are obtained, the waveforms of the pressure, velocity and acoustic power can be correspondingly obtained from equations (6.25), (6.26) and (6.27).

6.5. Performance of the PDTAR

Table 6.1 lists some dimensions and geometrical parameters of the resonator and stack of a piezo-driven thermoacoustic refrigerator. These values resemble those of the experimental prototype that is going to be discussed in the subsequent chapter.

Atmospheric air at a mean temperature of 21°C is used as the working medium for the refrigerator.

Table 6.1 Dimensions of a variable area *PDTAR*

Dimension	Value	
r_1	4.6 cm	1.8 "
r_2, r_4	1.1 cm	0.4 "
r_3	~0.4 mm	9.4 "
x_1	5 cm	1.9 "
x_2	23.2 cm	9.1 "
x_3	25.5 cm	10.0 "
$x_4 = L$	30 cm	11.8 "

Using these values and the derivations highlighted above, a *MATLAB* script is used to solve for the acoustic pressure, velocity and acoustic power propagation as functions of both frequency and location along the resonator.

6.5.1. *Speaker Deflection Characteristics*

As highlighted by equation (6.13) and (6.17), the volumetric deflection of the speaker Q_o is required as a starting point for the mathematical model. To provide a coherent comparison with the experimental prototype of the *PDTAR*, a laser vibrometer is used to scan the surface of the PZ-94 speaker (at a constant voltage input) across a frequency span from 0 to 800 *Hz*, and this data is used to plot the frequency response of Q_o and is incorporated in the *MATLAB* code. Due to the

speaker's complex and multi-structural design, a couple of natural frequencies are experimentally observed. The peak speaker deflection is found to take place at around 520 and 625 Hz .

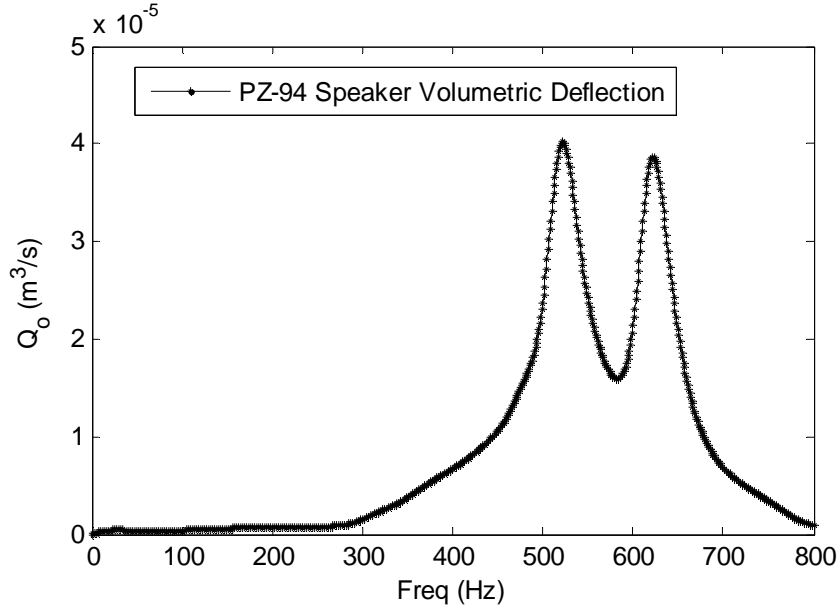


Figure 6.5 Deflection Characteristics for the PZ-94 Piezo-Speaker

Figure 6.6 shows the variation of the pressure, velocity and acoustic power at any location x inside the *PDTAR* resonator over the frequency range from 0 to 800 Hz . This way of compiling the frequency and location dependence of the acoustic waveforms provides a useful design map for a thermoacoustic refrigerator. Such maps give indications about resonance inside the resonator cavity and the first harmonics as well as an idea about the pressure and power distribution along the resonator and the stack effect on both.

The speaker-driven resonator which has a rigid closed end at $x = L$ represents an intermediate stage between a closed-closed tube and an open-closed tube due to

the speaker's deflection. Therefore, as expected, the first resonance mode of the refrigerator happens at about 387 Hz (as shown in Figure 6.6) which lies between the first modes of a closed-closed tube (half-wavelength resonator) and an open-closed tube (quarter wavelength resonator). These happen at 579 Hz ($c/2L$) and 289 Hz ($c/4L$) respectively.

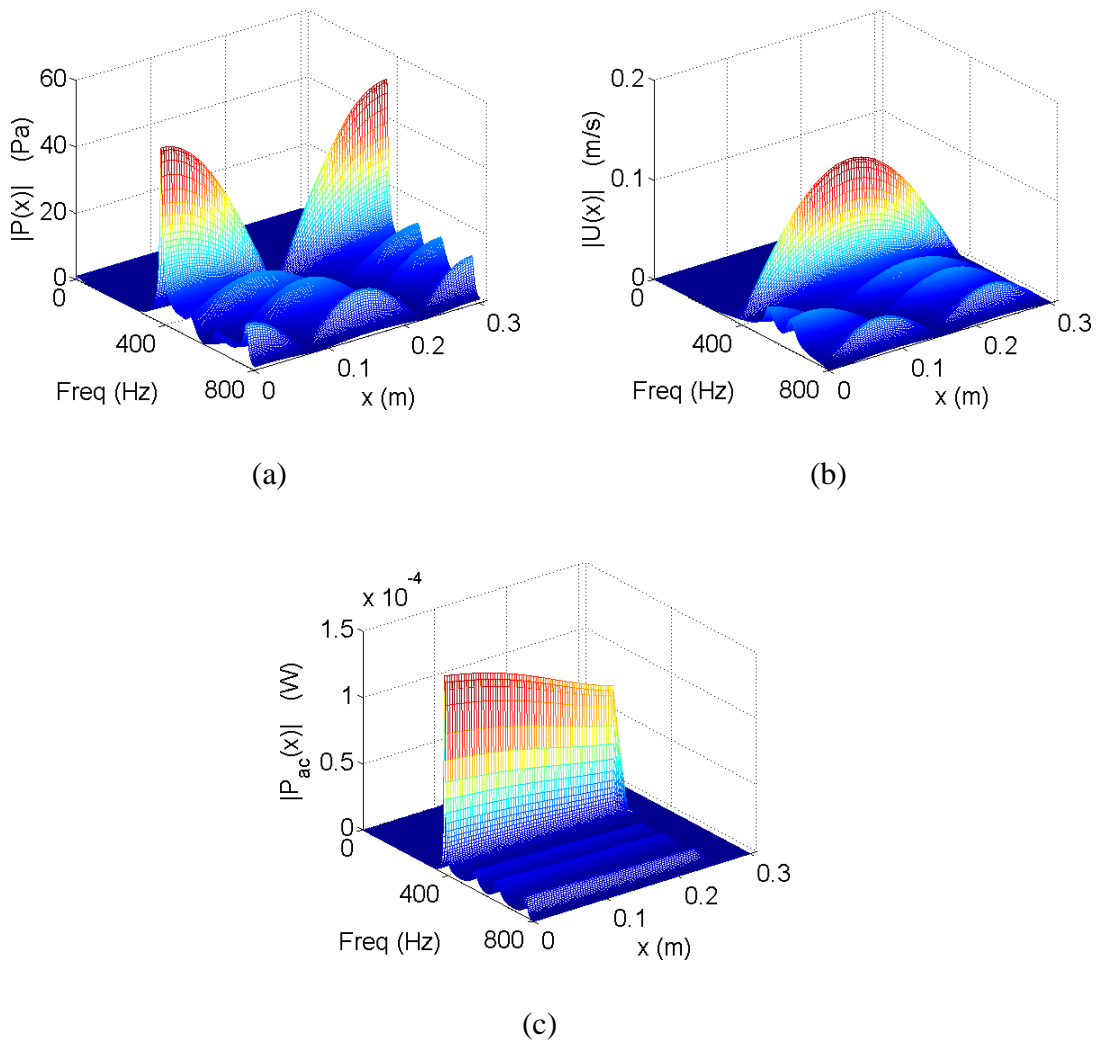


Figure 6.6 Variation of (a) Pressure, (b) velocity and (c) acoustic power with time and frequency for the given PDTAR

6.5.2. Stack Effect

The stack is the most important component in the thermoacoustic refrigerator. The temperature difference across the stack ends represents the output of the refrigerator and maximizing it is the main design goal. This temperature gradient is a function of both the acoustic power absorbed in the stack and the magnitude of the pressure pulsations at the stack's location. It can be observed in Figure 6.6 (c) that the acoustic power flow in the resonator drops drastically at the location of the starting point of the stack. This happens at $x_2 = 23.2$ cm as listed in Table 6.1.

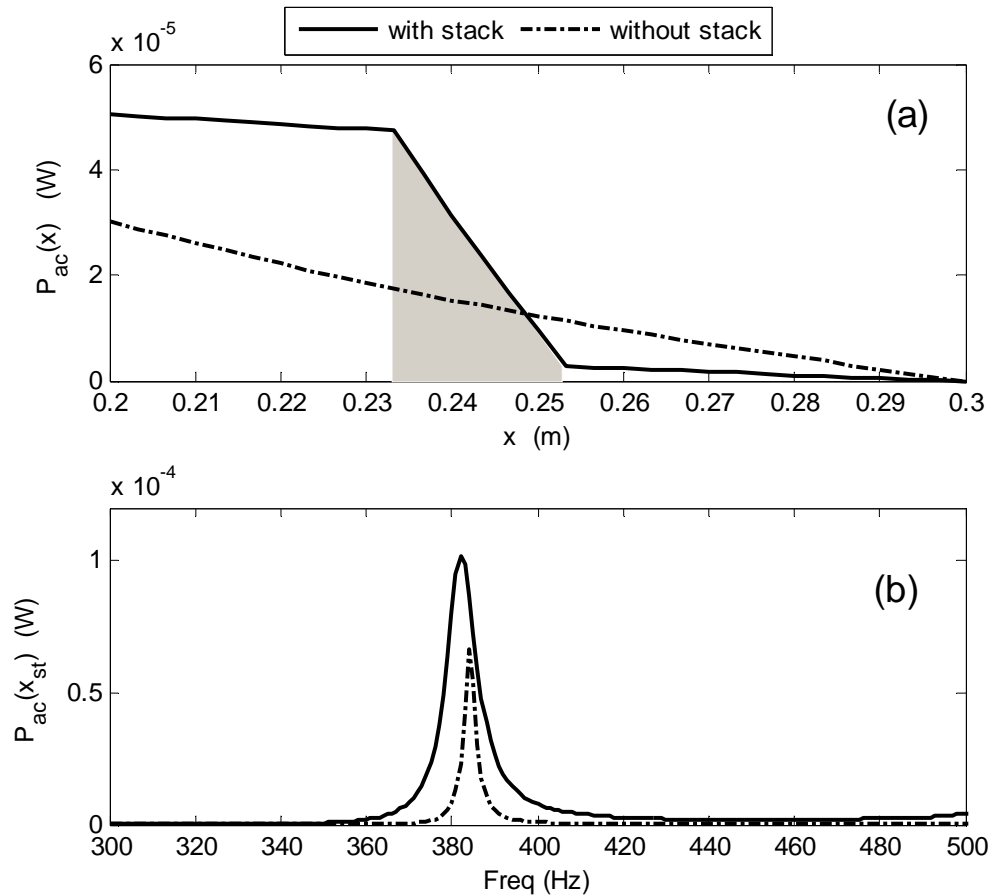


Figure 6.7 (a) Acoustic power in the vicinity of the stack location at resonant freq. of 387 Hz, and (b) frequency response of acoustic power with and without the stack

The power absorbed in the stack, which is directly proportional to the temperature difference induced, is given by equation (6.24), as the difference between the acoustic power across the stack ends. Figure 6.7 (a) shows the propagation of the acoustic power in the resonator before, during and after the stack at 387 Hz. The shaded area denotes the location of the stack and the corresponding drop in the acoustic power reflecting the energy consumption. The dotted line shows the results of stackless *PDTAR* of the same dimensions, and shows the effect of the stack on the power consumption inside the tube. Figure 6.7 (b) shows the frequency response of the acoustic power at $x = x_{st}$ where x_{st} is the stack mid-point location, while the dotted line represents the case without a stack. It can be again seen that more power is available for consumption at the resonant frequency range in the presence of the stack.

6.5.3. Stack Location

In thermoacoustic refrigerators, the general rule of thumb is to position the stack in a region of maximum acoustic power. In *PDTARs*, stacks are typically located in either the first or the last third of the resonator's length [32], as shown in Figure 6.8. This represents a region where the pressure-velocity product is at its peak. Most of the literature contains thermoacoustic refrigerators with stacks placed in one of these 2 locations.

It is worth noting that the direction of the expected temperature gradient depends on the chosen location with the hot end of the stack always closer to the

nearest pressure node. For this study and the experimental prototype, stack location 2 (Figure 6.8) is chosen. Finally, stack locations to be avoided are locations of both pressure and velocity antinodes (zero pressure and velocity points). Acoustic power diminishes and ideally reaches zero at these points, hence no temperature difference will be produced across the stack ends at these locations.

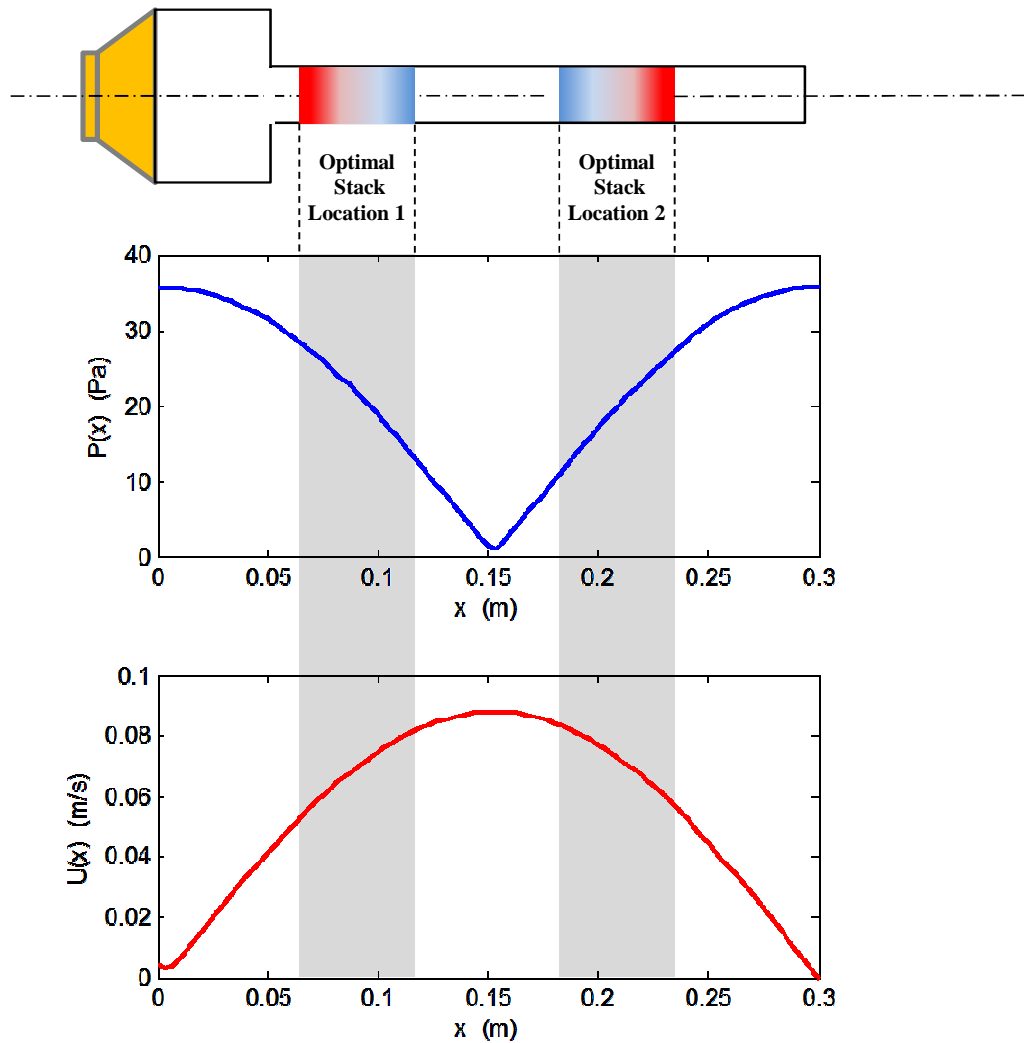


Figure 6.8 Optimal stack locations in a typical *PDTAR*

6.5.4. Attenuation Effect

The frequency dependent wavenumber described by equation (6.8) contains an imaginary part represented by the attenuation or loss factor α , similar to that presented in Chapter 2. For simplicity, α has been set to zero in the previous sections assuming ideal lossless wave propagation along the resonators. However, in reality losses do occur in the form of friction with the walls and possibly leaks and thus a finite value for α is considered and is essential for valid comparison with the experimental data.

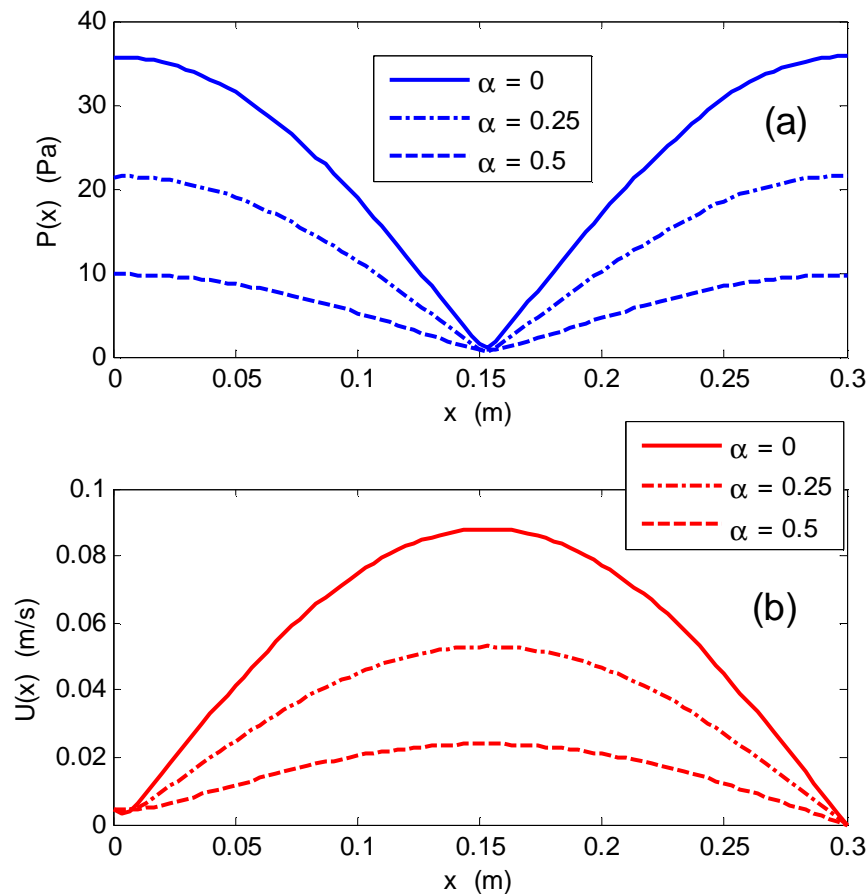


Figure 6.9 (a) Pressure and (b) velocity waveforms at 387 Hz in the *PDTAR* resonator for different wave attenuation factors

In the presence of a non-zero loss factor, the magnitude of pressure and velocity waves is attenuated as shown by Figure 6.9. As a consequence, the resonance of the acoustic tube becomes comparable with the peaks happening due to the speaker's deflection characteristics. This is shown clearly in Figure 6.10 for $\alpha = 0.25$ and $\alpha = 0.5$. This is more similar to what happens experimentally. This will be shown clearly in results in Chapter 7.

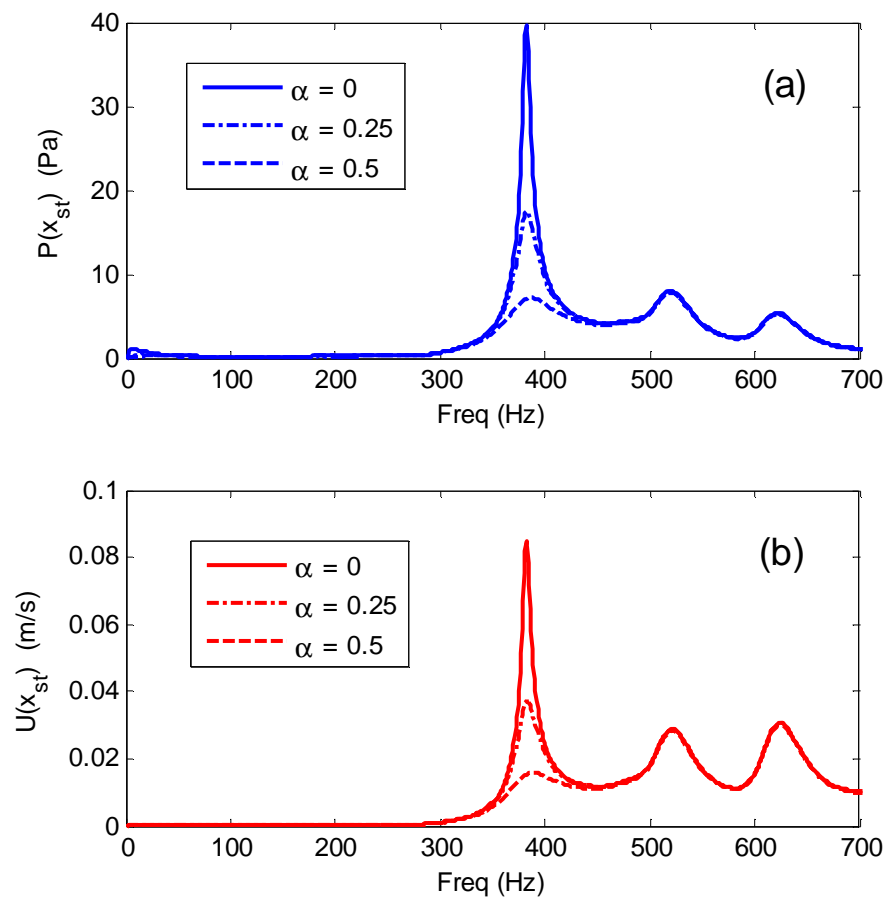


Figure 6.10 Frequency response of (a) Pressure and (b) velocity in the *PDTAR* resonator for different wave attenuation factors

6.5.5. *DeltaEC* Model

As mention earlier in Chapter 4, *DeltaEC* [34] is a computational code developed at the Los Alamos National Laboratory that is used to model thermoacoustic systems. The code integrates the wave and energy equations in one spatial dimension using a low-amplitude acoustic approximation and sinusoidal time dependence in a user defined geometry that is defined as consequent segments.

To model the *PDTAR*, we use the DUCT segments to model the acoustic resonator, a STKSLAB segment for the stack, a HARDEND to simulate the rigid enclosure at the end of the tube and a VEDUCER segment to model the PZ-94 piezo-speaker. To model the piezo-speaker using *DeltaEC*, the matrix coupling the speaker's electrical and mechanical characteristics has to be supplied. Details on how to calculate the electrical and mechanical impedances for the piezo-speaker and how to incorporate that in the *DeltaEC* model using the VEDUCER segment are explained thoroughly in Appendix A.5. Figure 6.11 shows how the *DeltaEC* schematic for the *PDTAR* looks like.

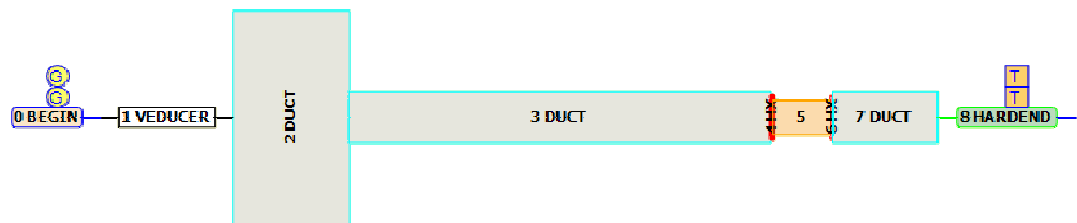


Figure 6.11 *DeltaEC* schematic diagram for the *PDTAR*

48	5 STKSLAB	Stack						
49		3.8795E-04	a Area	m ²		1169.2	A p	Pa
50		0.4400	b GasA/A			-166.42	B Ph(p)	deg
51		2.5000E-02	c Length	m		3.8490E-04	C U	m ³ /s
52		7.0000E-04	d y0	m		-76.968	D Ph(U)	deg
53		1.0000E-04	e Lplate	m		6.5574E-03	E Htot	W
54	Master-Slave Links					2.1385E-03	F Edot	W
55						294.00	G TBeg	K
56						302.36	H TEnd	K

Figure 6.12 Stack Section in the *DeltaEC* model of the *PDTAR*

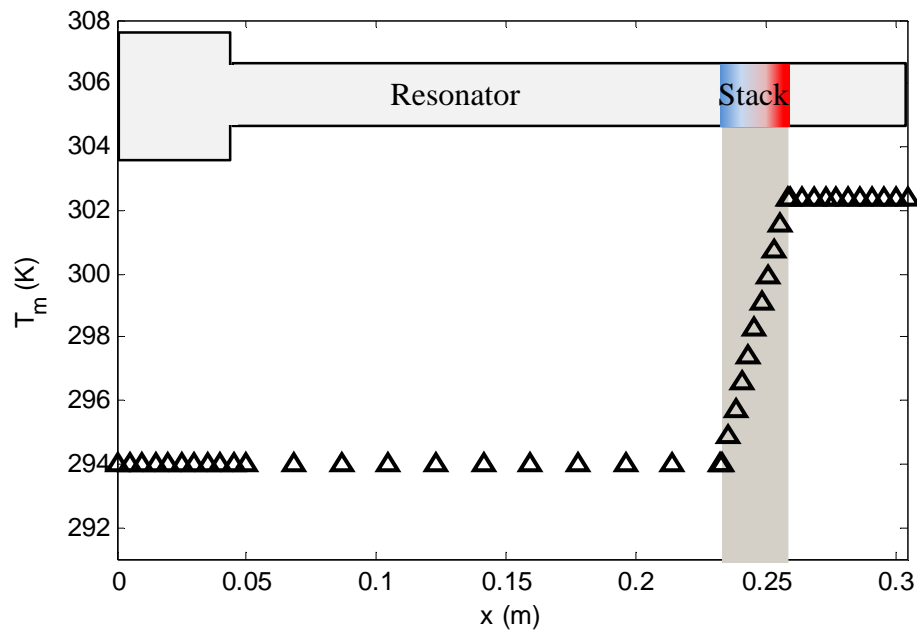


Figure 6.13 *DeltaEC*'s temperature variation along the resonator of the *PDTAR*

DeltaEC is particularly useful in computing design parameters such as the operating resonance frequency and the expected temperature gradients. For a *PDTAR* with dimensions similar to those listed in Table 6.1, *DeltaEC* computes a resonant frequency of 395 Hz for the acoustic cavity, which is in close agreement to that obtained using the mathematical model (387 Hz). A temperature difference of about 8.5 K is expected across the stack, when an ambient temperature of 294 K is used as

the working gas initial temperature. This is also in reasonable agreement with the experimental values to be shown in Chapter 7. Figure 6.12 shows the STKSLAB section representing the stack region in the *PDTAR* and the steady state temperature distribution in the resonator is shown in Figure 6.13. It should be noted here that *DeltaEC* incorporates temperature variation in the equations of the stack segments only, and assumes constant temperature otherwise, which explains the pattern of Figure 6.13.

6.6. *PDTAR with a dynamic magnifier*

Similar to the concept presented in Chapter 2, a *PDTAR* can be equipped with a simple magnifier system in the form of a coupling spring and a mass, and consequently tuned to amplify the initial deflection driving the acoustic wave at the beginning of the resonator. Figure 6.14 shows a schematic diagram for a *PDTAR* with a dynamic magnifier.

The initial boundary condition at $x = 0$ will remain unchanged as,

$$U_1(0) = \frac{Q_o}{S_1} \quad (6.31)$$

but with the difference that Q_o is now the volume velocity of the magnifier mass m_m which has to be first obtained as transfer function of the speaker volume velocity, now defined as Q_{sp} . Again, for simplicity, we assume that both the speaker and the magnifier mass move back and forth with one *DOF* equal to Q_{sp} / S_1 for the speaker

and Q_o / S_1 for the mass. The following equation can then be depicted in a manner similar to that discussed in Chapter 2,

$$\left(i\omega m_m + \frac{k_c}{i\omega} \right) \frac{Q_o}{S_1} - \frac{k_m Q_{sp}}{i\omega S_1} = S_1 P_1(0) \quad (6.32)$$

where k_c is the stiffness of the spring connecting the speaker and the mass m_m , and $P_1(0)$ is the pressure at the beginning of the resonator tube (i.e. $x = 0$). $P_1(0)$ can be expressed, using equation (6.25), as,

$$P_1(0) = C_1 (1 + R_1) \quad (6.33)$$

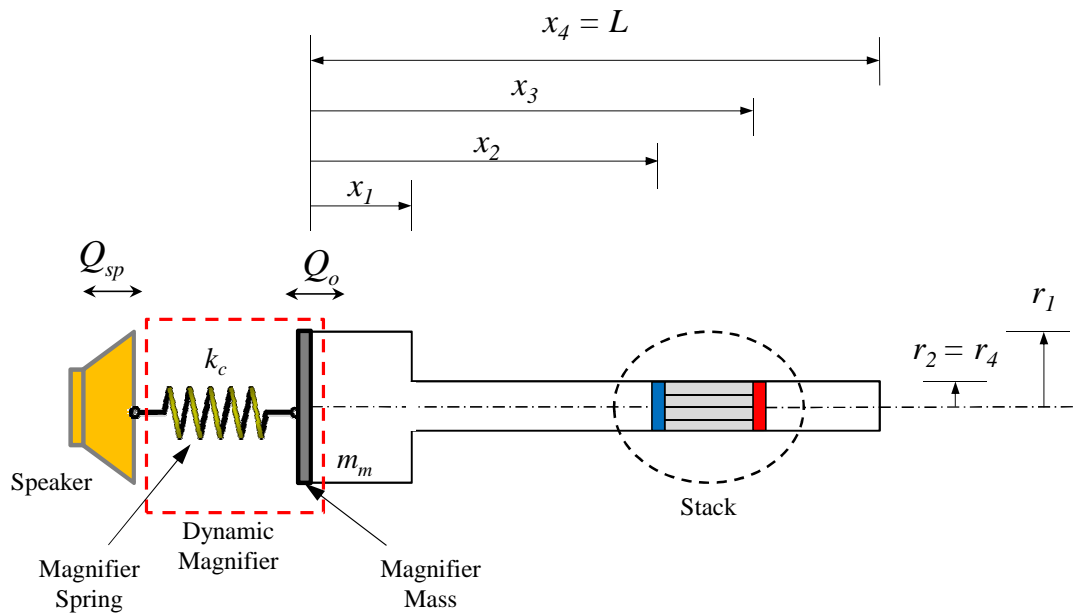


Figure 6.14 Schematic of a PDTAR with a dynamic magnifier (DMPDTAR)

Substituting equations (6.17) and (6.33) in (6.32) yields,

$$\left(i\omega m_m + \frac{k_c}{i\omega} \right) \frac{Q_o}{S_1} - \frac{k_m}{i\omega} \frac{Q_{sp}}{S_1} = \frac{\rho\omega Q_o (1+R_1)}{\kappa_1 (1-f_{v_1})(1-R_1)} \quad (6.34)$$

which can be rearranged to give,

$$Q_o = \frac{k_m}{i\omega} \left(i\omega m_m + \frac{k_c}{i\omega} - \frac{S_1 \rho\omega (1+R_1)}{\kappa_1 (1-f_{v_1})(1-R_1)} \right)^{-1} Q_{sp} \quad (6.35)$$

Equation (6.35) is a frequency dependent transfer function that can be used to indicate whether the volume flow rate of the magnifier mass (input) will be higher or lower than that of the speaker (input). Magnification of the speaker deflection will be expected to result in higher acoustic power consumption across the stack ends and should yield a higher temperature difference.

Substituting (6.35) in (6.31) gives,

$$U_1(0) = \frac{k_m}{i\omega S_1} \left(i\omega m_m + \frac{k_c}{i\omega} - \frac{S_1 \rho\omega (1+R_1)}{\kappa_1 (1-f_{v_1})(1-R_1)} \right)^{-1} Q_{sp} \quad (6.36)$$

Equation (6.36) constitutes the new boundary condition at the beginning of the tube, while,

$$U_4(L) = 0 \quad (6.37)$$

constitutes the boundary condition at the other end. Finally, equations (6.36) and (6.37) along with (6.28) and (6.29) form 8 linear equations which can be solved simultaneously for R_1 through R_4 and C_1 through C_4 . Afterwards, equations (6.25), (6.26) and (6.27) can be used to obtain the pressure, velocity and acoustic power variations along the resonator and reveal the peak frequencies.

Finally, as with the energy harvesters discussed in Chapter 2, proper selection of the magnifier parameters is critical to ensure Q_o is amplified over Q_{sp} . Results of a *PDTAR* with a dynamic magnifier with several combinations of m_m and k_c are presented in details in Chapter 7, along with comparison with experimental findings.

6.7. Summary

This chapter has provided a comprehensive mathematical model that can be used to assess the pressure, velocity and acoustic power flow in the resonators of piezo-driven thermoacoustic refrigerators (*PDTARs*). The model was also appended to include *PDTARs* augmented with dynamic magnifiers.

More results for a *PDTAR* prototype, with and without a dynamic magnifier, are presented thoroughly in Chapter 7, along with experimental validation.

Chapter 7

7. Experimental Investigation of Piezo-driven Thermoacoustic Refrigerators

7.1. Introduction

This chapter presents a detailed presentation of an experimental prototype of a *PDTAR* that has similar dimensions to the one discussed in Chapter 6. Details are given of the experimental setup and instrumentation used to measure the different performance metrics of the refrigerator such as pressure and temperature difference across the stack ends. Comparisons are made throughout between data from the carried out tests and theoretical predictions computed using the equations discussed earlier.

Finally, *PDTARs* augmented with dynamic magnifiers are presented and eventually shown to enhance the performance of the refrigerator. Higher pressure is observed to build up inside the resonator, and a larger temperature difference is noticed across the stack ends when the magnifier parameters are suitably chosen.

7.2. PDTAR Experimental Prototype

A prototype of a piezo-driven thermoacoustic refrigerator (*PDTAR*) similar to the design displayed in Figure 6.4, and with the dimensions listed in Table 6.1 is developed.

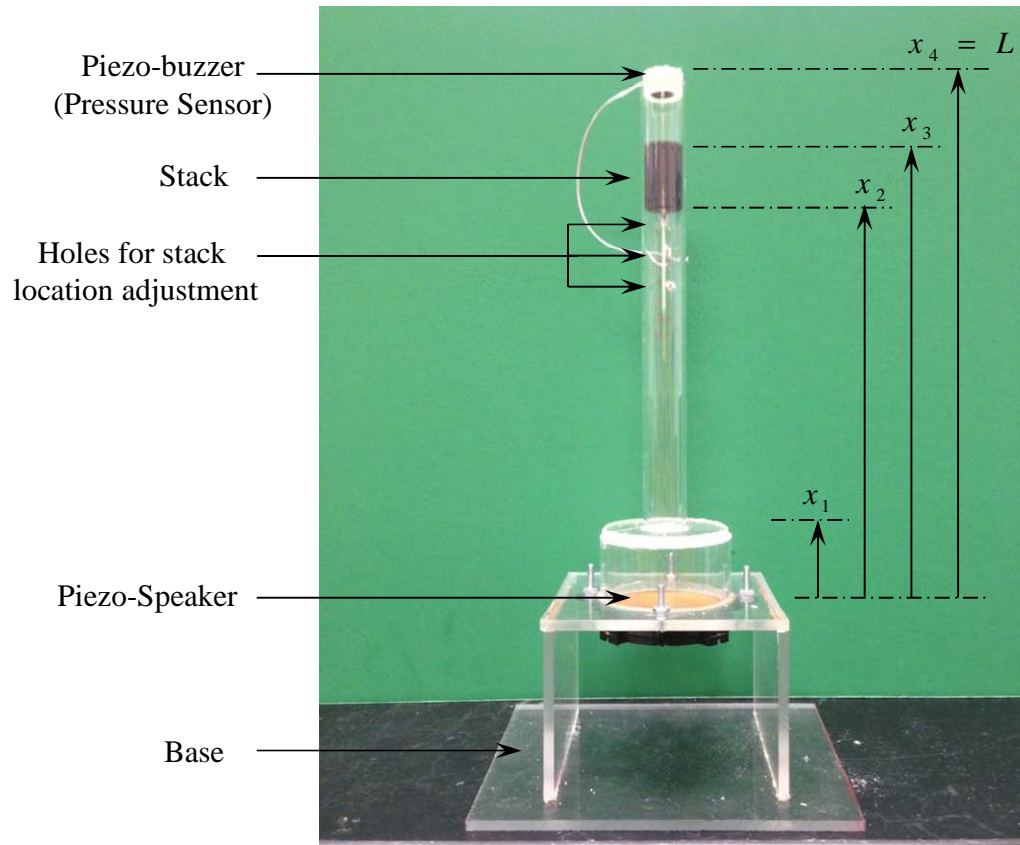


Figure 7.1 Experimental prototype of a *PDTAR*

The *PDTAR* experimental prototype, shown in Figure 7.1, consists of an acrylic base on which the *PZ-94* piezo-speaker is mounted. The resonator consists of two adjacent tubes, the first has an area that fits the speaker face, and the second is small enough to fit the stack. The stack is fashioned out of a spiral 35 mm camera film. A nylon fishing line is glued across the film as shown in Figure 7.2, and the film is rolled up and glued at the ends to form the stack porous body. The resonator is closed at the top with a rigid plug and a PC-board 12 VDC piezo-buzzer, to be used as a pressure transducer, is mounted on the plug facing the inside of the acoustic tube.

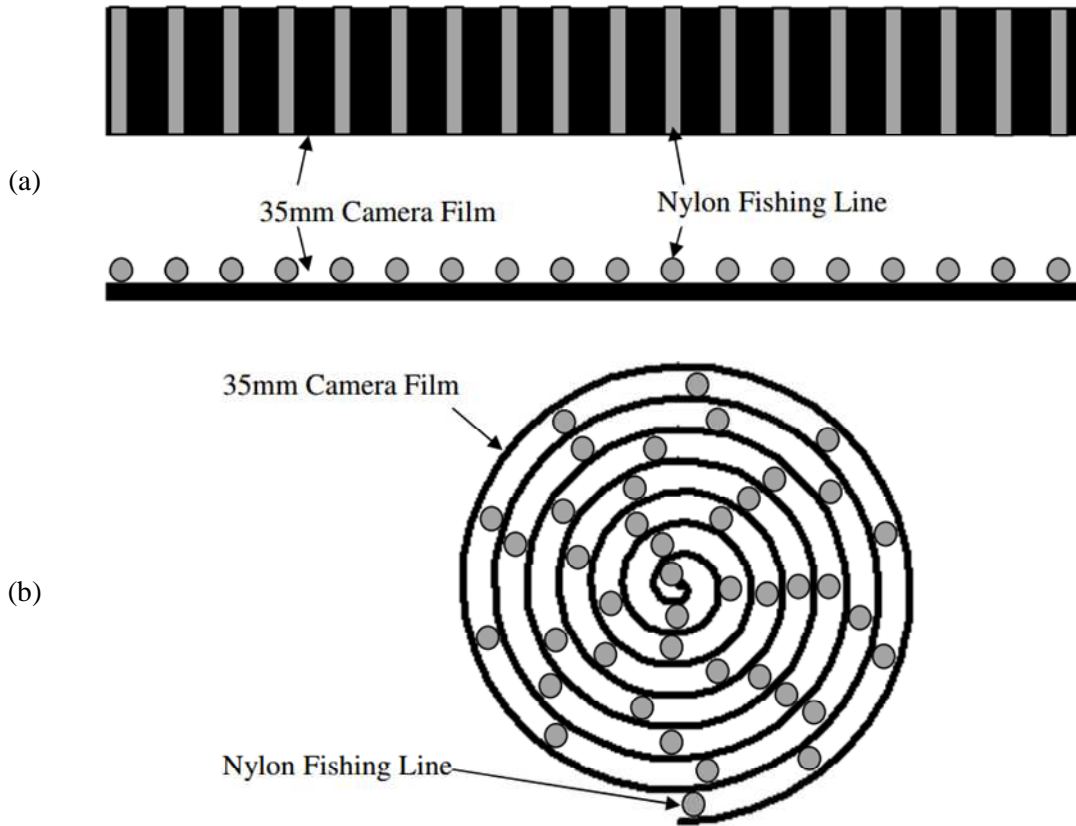


Figure 7.2 (a) View of the stack before it is rolled up, and (b) top cross sectional view of the assembled stack

7.3. Experimental Setup

The *PZ-94* speaker is driven by an amplifier that receives the input voltage signal from a function generator. During operation, the piezo-buzzer at the top enclosure is used to evaluate the pressure at what is expected to be a pressure node. The magnitude of the pressure $P(L)$ is proportional to the pressure at the stack center point location $P(x_{st})$, as can be seen in Figure 6.9, and can be used as an initial indication of the expected temperature gradient across the stack ends.

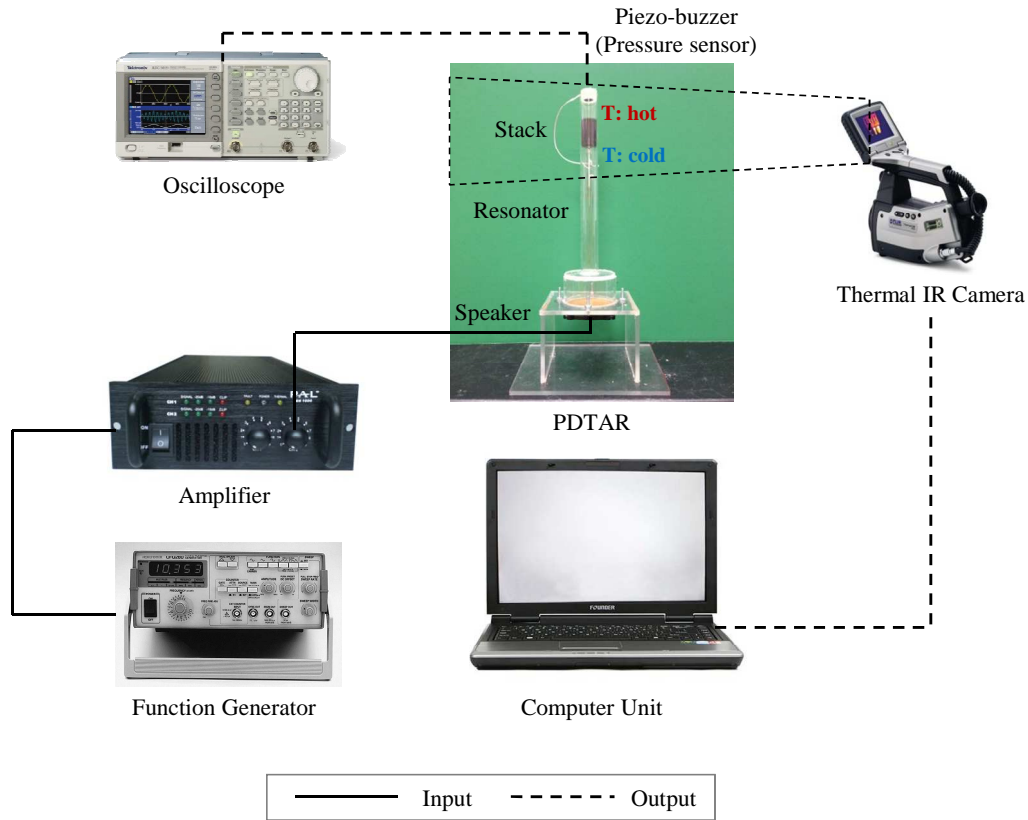


Figure 7.3 Experimental setup used to analyze the *PDTAR* performance

An infrared thermal camera (model ThermoCAM® SC3000, from FLIR Systems, Boston, MA) is used to measure the evolution of the temperature difference across the stack ends with time. Because of the thin and transparent walls, the camera was able to gain relatively accurate visual information of the actual temperatures inside the refrigerator. A couple of thermocouples were hooked to the top and bottom ends of the stack in a control experiment to test the temperatures against the camera data, and the difference between the two never exceeded ± 1 K, which can be attributed to conduction in the resonator walls. A schematic diagram showing the entire experimental setup is shown in Figure 7.3.

7.4. Performance of the PDTAR

7.4.1. Pressure $P(L)$

The pressure sensor placed at the top of the resonator at $x = L$ is first used to measure the frequency response of the pressure $P(L)$. The speaker is driven by a low-voltage signal (about 5V peak) and the function generator is used to sweep the frequencies in the range from 0 to 700 Hz, where the first fundamental modes of the cavity and the speaker are expected to be seen. It should be noted here that this experiment is similar to the one used to measure Q_o of the speaker, and hence $U(0)$, the results of which are shown in Figure 6.5. The later experiment was explained earlier as the results of Figure 6.5 were included in the mathematical model explained in Chapter 6.

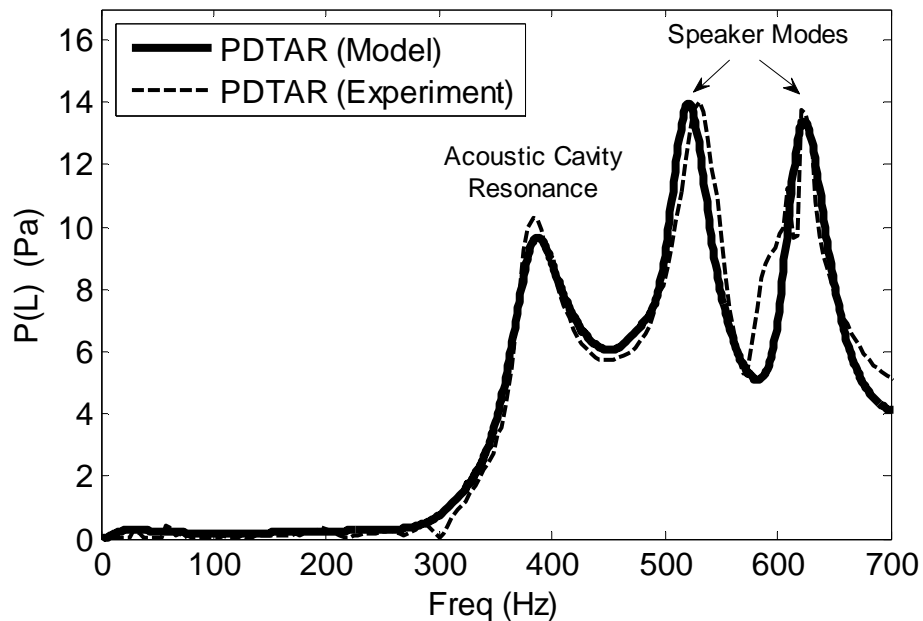


Figure 7.4 Comparison between theoretical and experimental data of the pressure at the end of the resonator $P(L)$ for the given PDTAR prototype

Figure 7.4 shows a comparison between the data obtained from the pressure sensor and the theoretical predictions of $P(L)$ obtained using the model described in Chapter 6 using an attenuation factor $\alpha = 0.5$. The sine sweep shows a peak at about 387 Hz representing the first mode of the acoustic cavity. This, as explained before, lies between the first modes of a closed-closed tube (half-wavelength resonator) and an open-closed tube (quarter wavelength resonator) which are theoretically predicted to be at 579 Hz and 289 Hz respectively. Two other peaks are observed at about 50 and 625 Hz which are a result of the speaker's characteristics shown earlier in Figure 6.5. The resonance from the acoustic cavity results in a node pressure $P(L)$ of about 11 Pa, while the 2 other peaks result in 14 and 13.5 Pa respectively. A very close agreement is noticed here between the experimental data from the pressure transducer and the mathematical model described in Chapter 6.

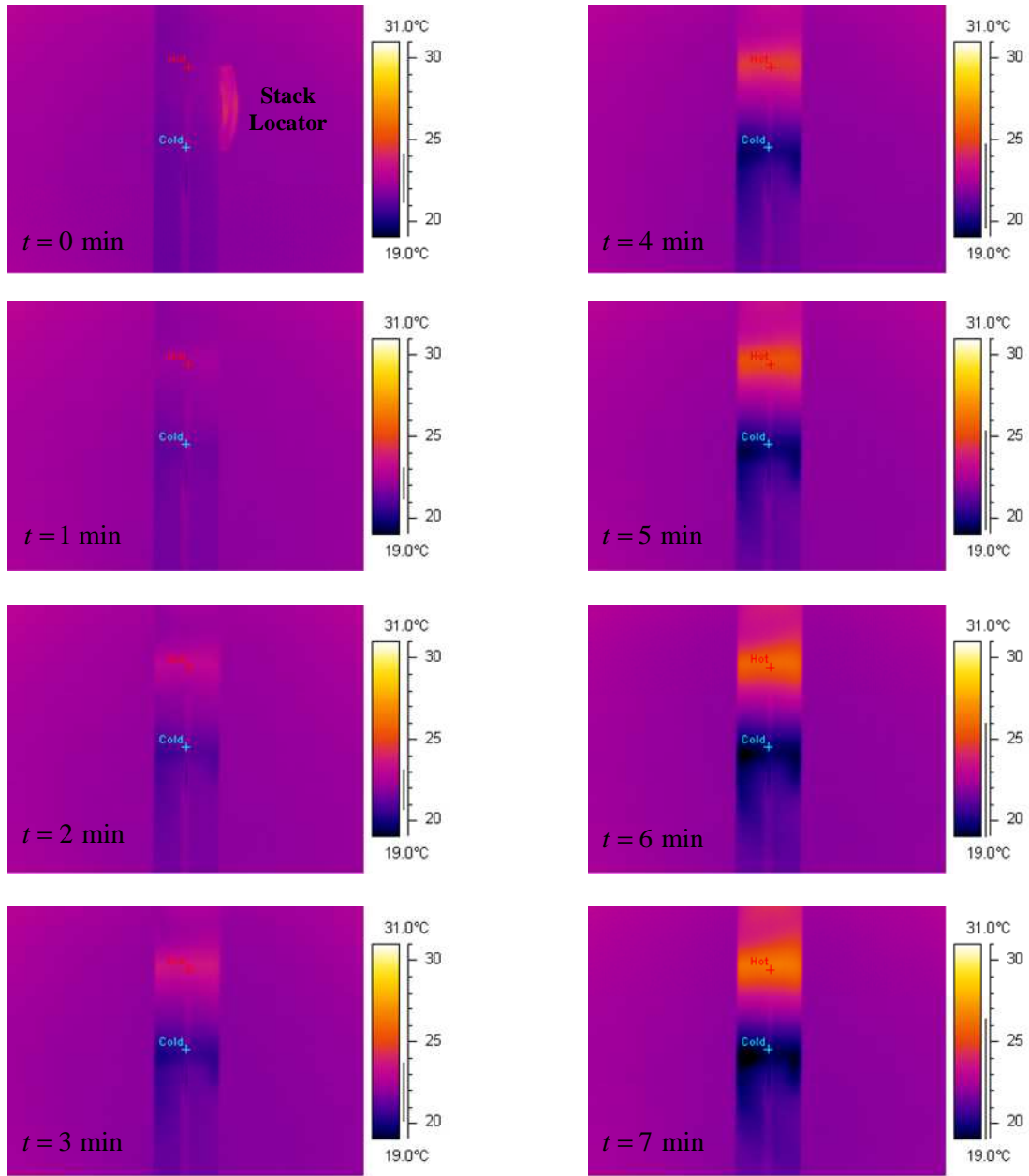


Figure 7.5 Evolution of the temperature difference across the stack ends during the *PDTAR* operation (ΔT at 7 minutes is almost 7 K)

7.4.2. Temperature Difference (ΔT)

Next, the temperature difference across the stack ends is measured at the peak pressure frequency using the thermal camera. The refrigerator is now driven using a peak voltage input of about 30 V from the signal amplifier, and a power input of about 6 Watts. The development of the temperature difference with time is shown in Figure 7.5 for 7 minutes of the *PDTAR* operation, after which the temperature difference almost reaches a steady value. A thick piece of adhesive tape with the same length as the stack is attached to resonator at the stack location, as shown in the first image of Figure 7.5 at the beginning of the experiment to help locate the locations of the cold end and the hot end on the thermal camera software interface. For the given *PDTAR* prototype, the starting ambient temperature is about 21°C, the cold end eventually cools down to slightly less than 19°C, and the hot end heats up to about 26°C, giving a difference of about 7 degrees.

7.5. *PDTAR* with a dynamic magnifier

7.5.1. Experimental Prototype

The *PZ-94* speaker used in the *PDTAR* experiment has a curved plastic-diaphragm that makes connecting the magnifier spring to its surface futile. So in an attempt to experimentally investigate a piezo-driven thermoacoustic refrigerator with a dynamic magnifier, the plastic-diaphragm is taken off the speaker so that a mechanical spring can be attached to the flat screen mesh as displayed in Figure 7.6. However when tested, with the same input voltage as in Figure 7.4, the speaker

without the plastic-diaphragm results in a much lower pressure $P(L)$ across almost the entire frequency domain. A dynamic magnifier connected to this configuration of the speaker would not be in a fair comparison with the *PDTAR*.

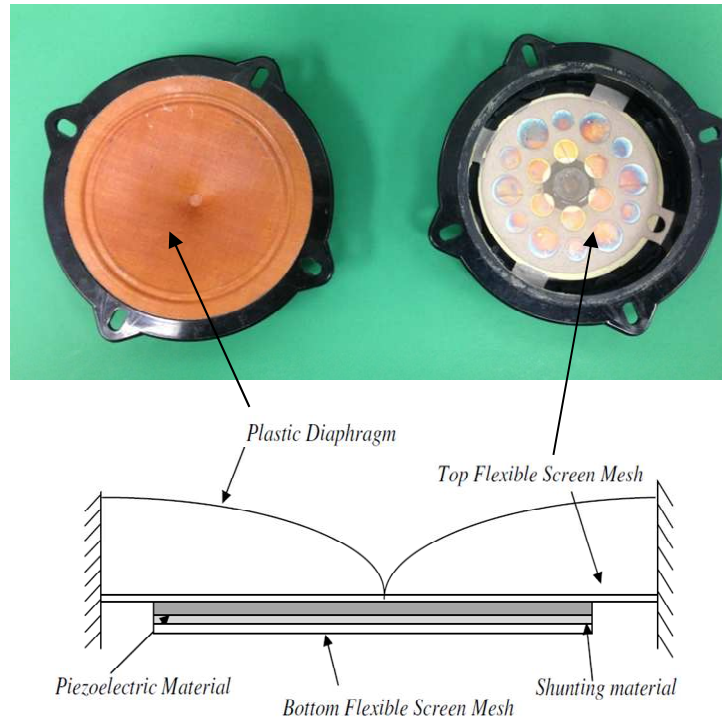


Figure 7.6 PZ-94 Piezo-speaker with and without the plastic-diaphragm

In order to provide a flat surface to attach the magnifier spring to, a circular aluminum plate (0.008" thick) is placed on top of the *PZ-94* speaker's plastic diaphragm. A different assortment of springs can then be glued to the aluminum plate and to the magnifier mass from the other end to form the magnifier system. Figure 7.7 through Figure 7.9 show the response of $P(L)$ to the different speaker configurations discussed. It can be noticed from Figure 7.8 that adding the aluminum plate reduces the speaker peak frequency slightly due to the added mass but does not significantly change the pressure response. Adding the glue dampens the peak from 14 *Pa* to about

11 Pa, as shown in Figure 7.9, but is, nonetheless, the most convenient mechanism to connect the dynamic magnifier. Finally, the prototype of the *PDTAR* equipped with the magnifier can be seen in Figure 7.10.

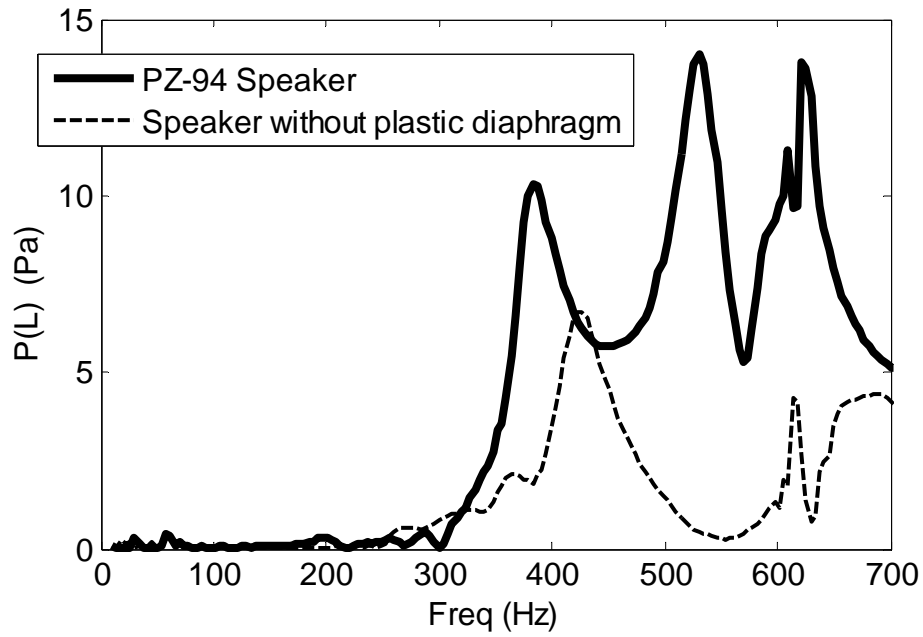


Figure 7.7 End pressure $P(L)$ for a *PDTAR* with a PZ-94 speaker and a *PDTAR* with the speaker without the plastic diaphragm

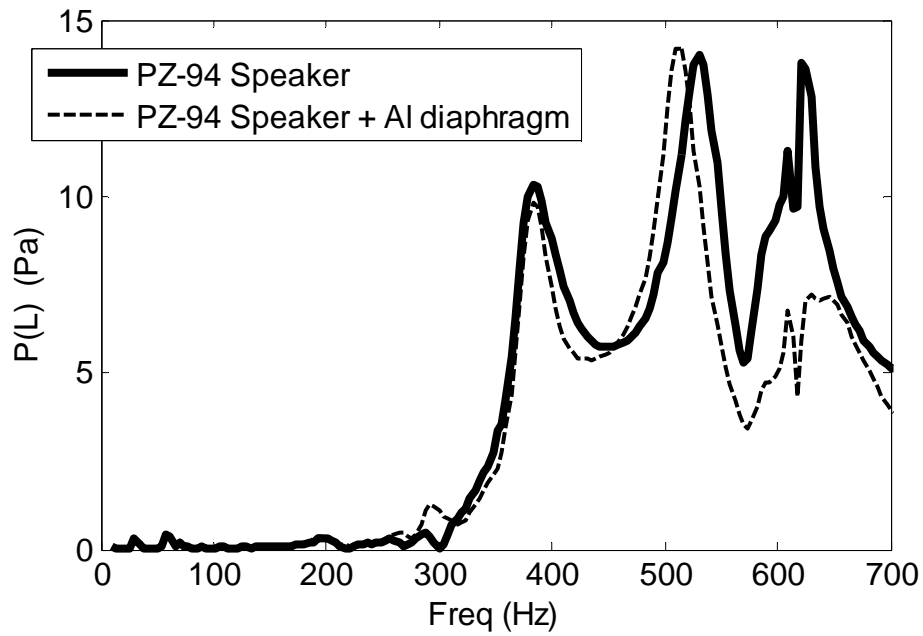


Figure 7.8 End pressure $P(L)$ for a *PDTAR* with a PZ-94 speaker and a *PDTAR* with a PZ-94 speaker with an aluminum plate on top

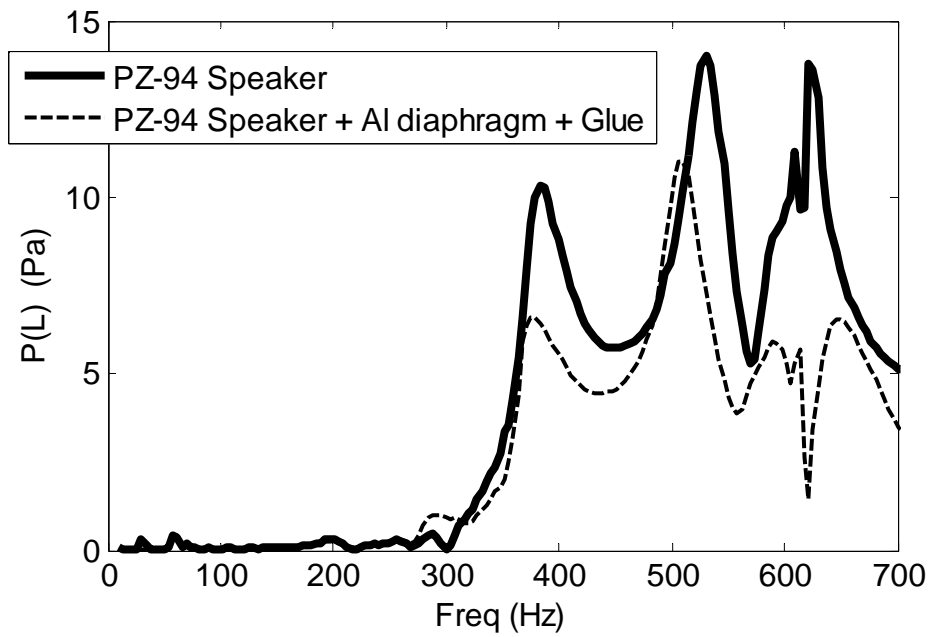


Figure 7.9 End pressure $P(L)$ for a *PDTAR* with a PZ-94 speaker and a *PDTAR* with a PZ-94 speaker with an aluminum plate on top with glue in the center to attach the magnifier spring to it

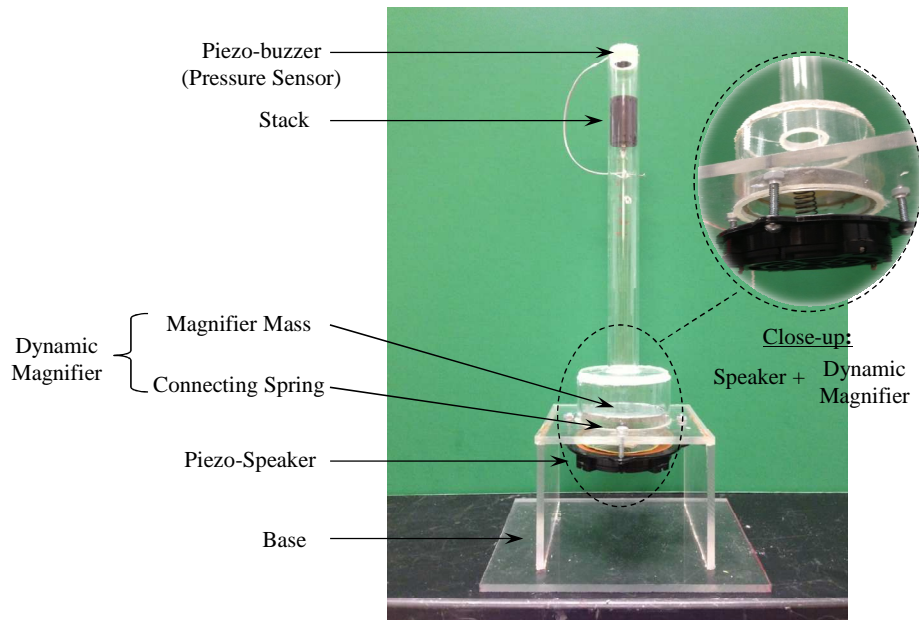


Figure 7.10 Experimental prototype of a *PDTAR* with a dynamic magnifier

7.5.2. Performance of the *PDTAR* with a dynamic magnifier

As with the thermoacoustic-piezoelectric harvester, several combinations of k_c and m_m are attempted. The pressure at the end of the tube and the temperature difference across the stack ends are measured experimentally for each combination. The magnifier mass is in the form of another aluminum circular plate (0.008" thick) placed on a plastic ring that has the same diameter of the speaker face. In this form m_m is about 8 grams. Additional mass can be attached to the back of the aluminum plate in the form of small steel nuts placed in symmetrical location as shown previously in Figure 4.28. Figure 7.1 summarizes some of the experiments carried out with a *PDTAR* with a dynamic magnifier.

Table 7.1 Experiments done with a *PDTAR* with a dynamic magnifier

Magnifier #	k_c (lb/in)	m_m (grams)	$P(L)_{magnifier} / P(L)_{PDTAR}$
1	474	8	1.58
2	25	8	0.68
3	25	12	0.85
4	474	12	1.21
5	474	16	1.15
6	901	12	0.75
7	200	8	0.67
8	901	8	0.063

The dynamic magnifiers highlighted in gray in Table 7.1 are the ones with pressure magnification and an improved temperature difference across the stack over the conventional *PDTAR*. Magnifier #1 uses a spring of a 474 *lb/in* stiffness and no added mass on the aluminum plate representing the magnifier mass. It is observed to have the highest pressure magnification ratio. As an example for an effective magnifier and a non-effective one, Figure 7.11 and Figure 7.12 show the variation of $P(L)$ for magnifiers #1 and #2 respectively, and how they compare to the conventional *PDTAR*.

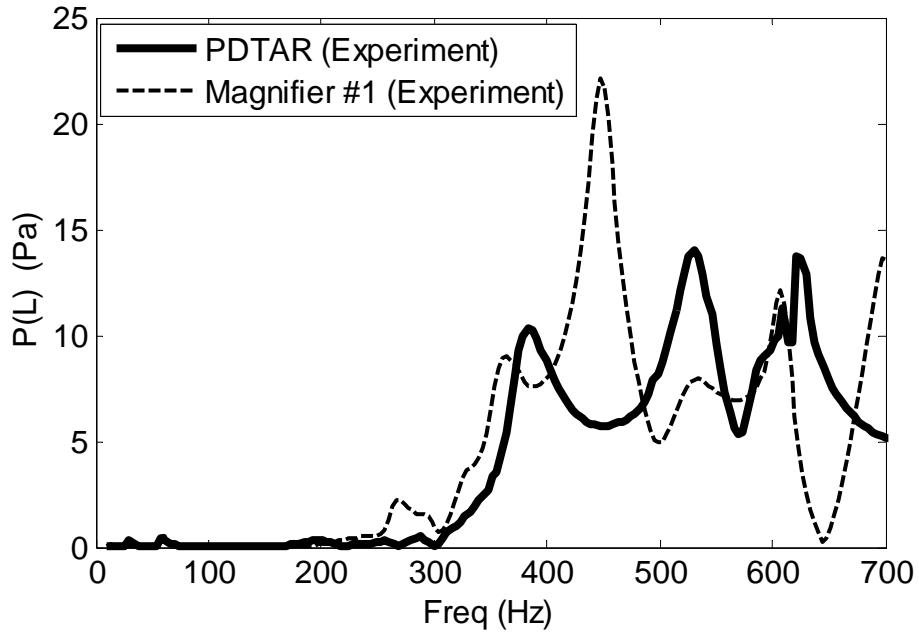


Figure 7.11 End pressure $P(L)$ for the conventional *PDTAR* and a *PDTAR* with Magnifier #1

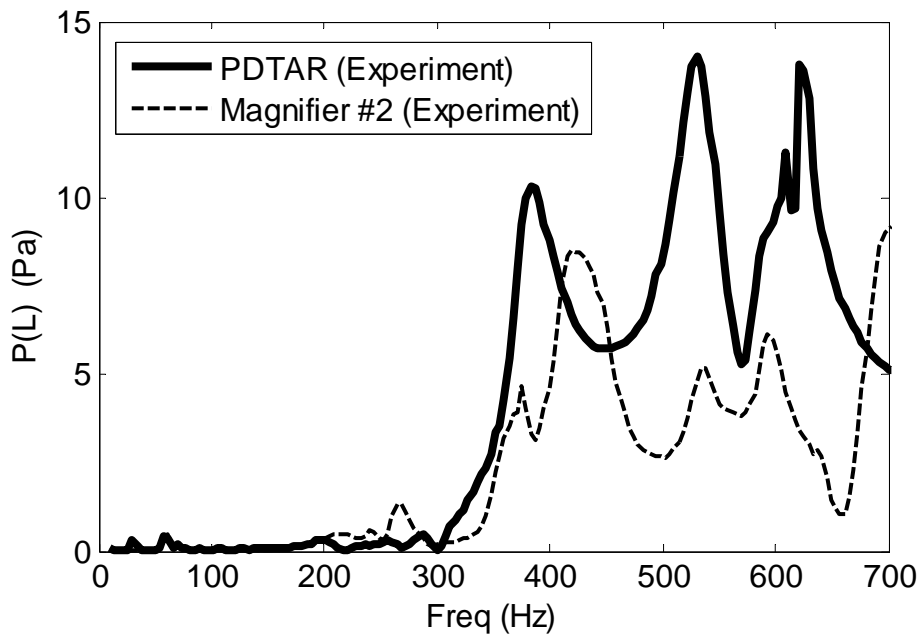


Figure 7.12 End pressure $P(L)$ for the conventional *PDTAR* and a *PDTAR* with Magnifier #1

Figure 7.13 shows the steady state temperature difference across the stack for the *PDTAR* prototype with magnifier #1, while Figure 7.14 shows the temperature evolution with time in comparison with the conventional *PDTAR*. The final difference between the hot and cold ends reached is 10 K which is about 1.4 times that reached by the conventional *PDTAR* prototype. This amounts to almost the same magnification ratio indicated by the end pressure data (~ 1.58), which was mentioned earlier to be an indication of expected temperature difference. Finally, Figure 7.15 shows the improvements in the temperature difference starting from a *PDTAR* without a stack (negligible thermoacoustic effect), to a conventional *PDTAR*, to a *PDTAR* with an effective dynamic magnifier.

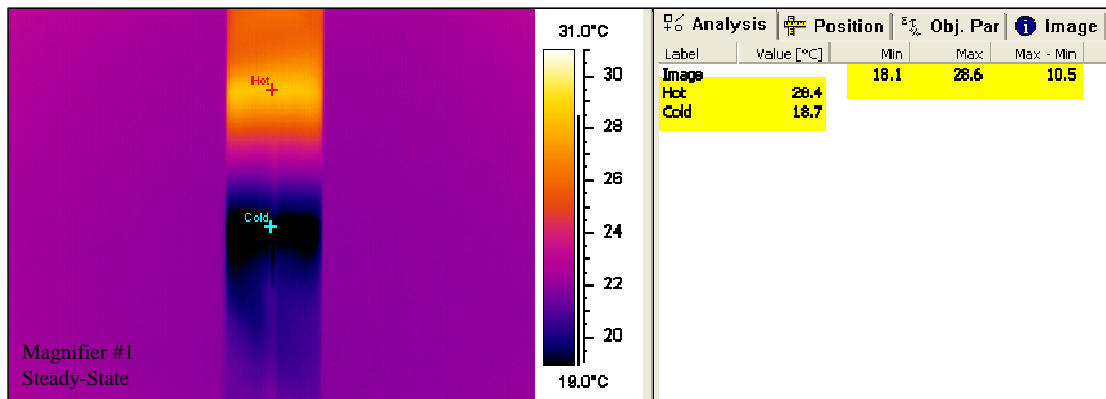


Figure 7.13 Steady-state temperature difference of *PDTAR* with Magnifier#1 (ΔT is about 10 K)

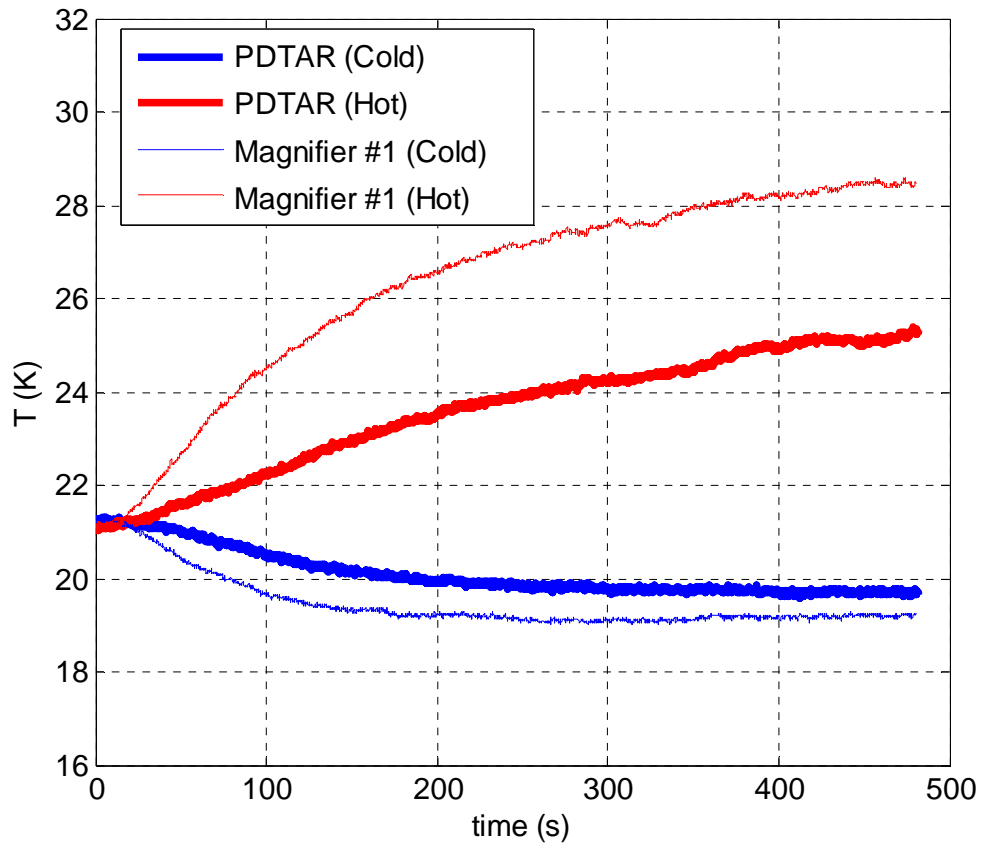


Figure 7.14 Temperature development of hot and cold stack ends for the *PDTAR* and a *PDTAR* with Magnifier #1

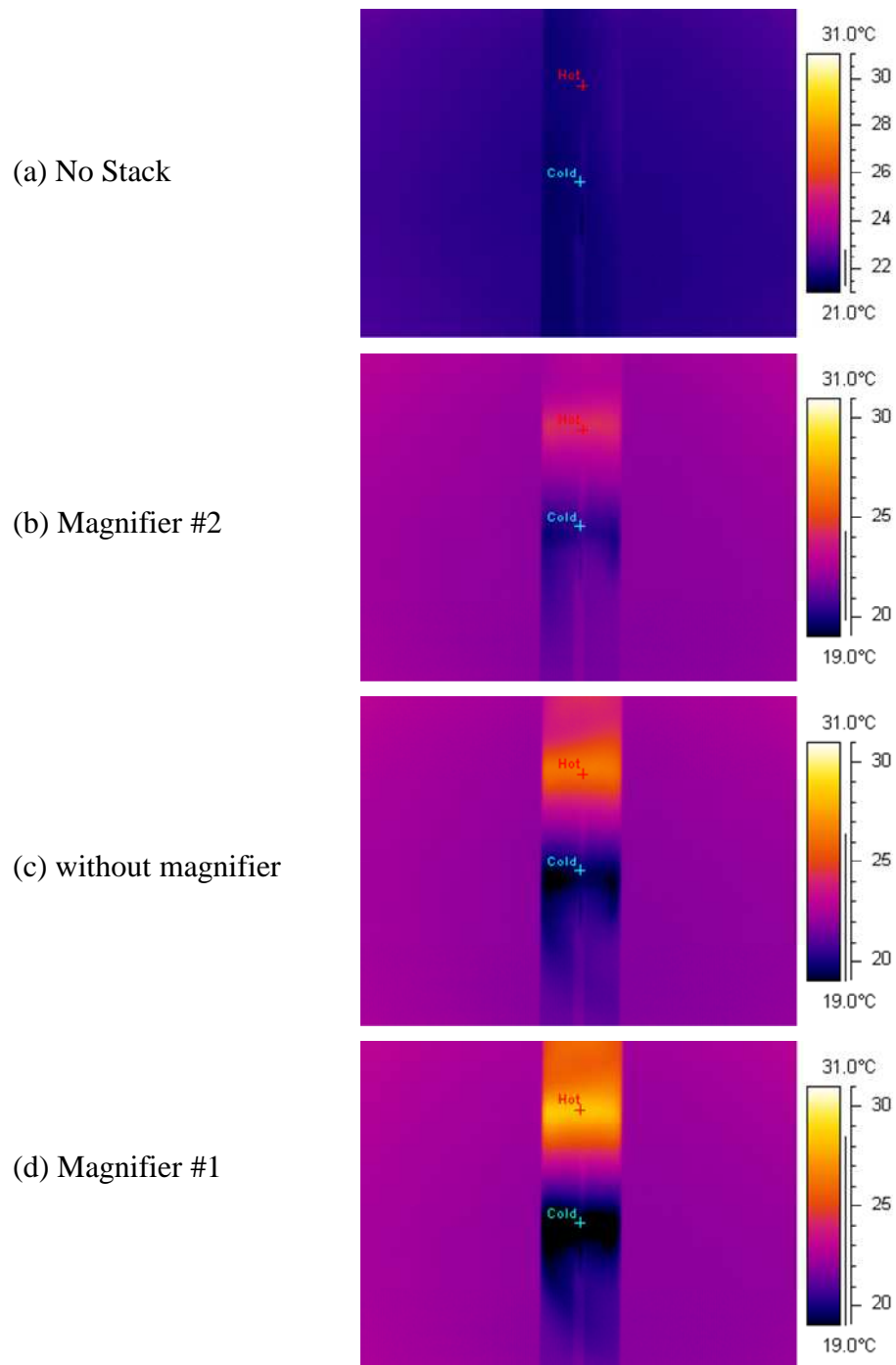


Figure 7.15 Steady state temperature difference of a PDTRAR with (a) no stack (0 K), (b) Magnifier#2 (4 K), (c) no magnifier (7 K) and (d) Magnifier #1 (10 K)

7.5.3. Comparison with the mathematical model

A mathematical model is developed for the *PDTAR* with the dynamic magnifier using the procedure highlighted in section 6.6, and is used to compare with the experimental data obtained from the first case (Magnifier #1) in Table 7.1. Shown in Figure 7.16 is a comparison between the volume velocities at the beginning of the resonator ($x = 0$) for the conventional *PDTAR* (i.e. volume flow rate of speaker) and for a *PDTAR* with Magnifier #1 (i.e. volume flow rate of magnifier mass) as predicted by the model. The plot shows about 3 times amplification of the volume velocity as a result of using the dynamic magnifier. Also notable, is the added frequency peak in the plot due to the added magnifier system.

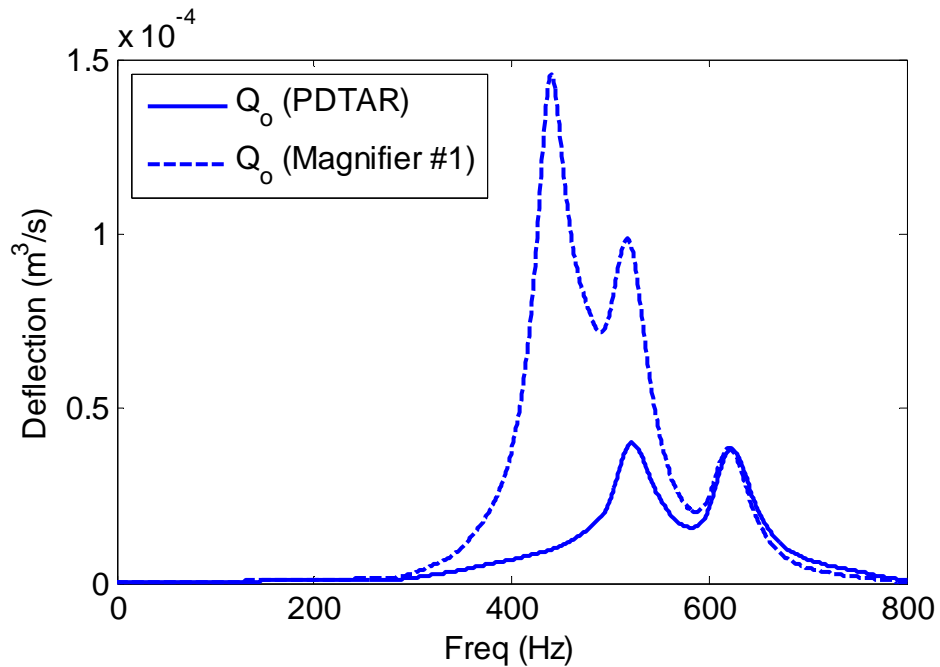


Figure 7.16 Volume velocity at the beginning of the resonator ($x = 0$) for the *PDTAR* and a *PDTAR* with Magnifier #1 as computed by the mathematical model

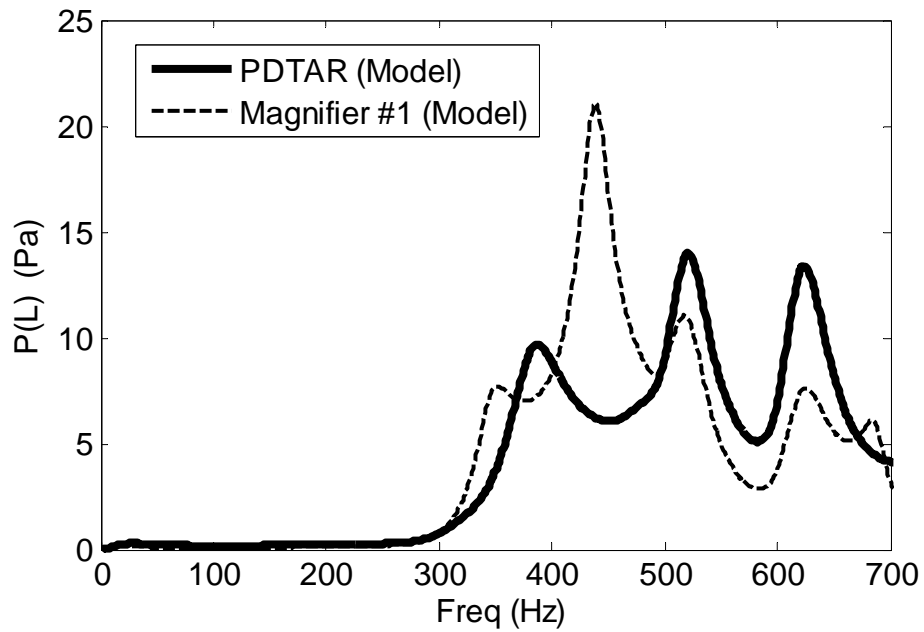


Figure 7.17 End pressure $P(L)$ for the conventional *PDTAR* and a *PDTAR* with Magnifier #1 as computed by the mathematical model

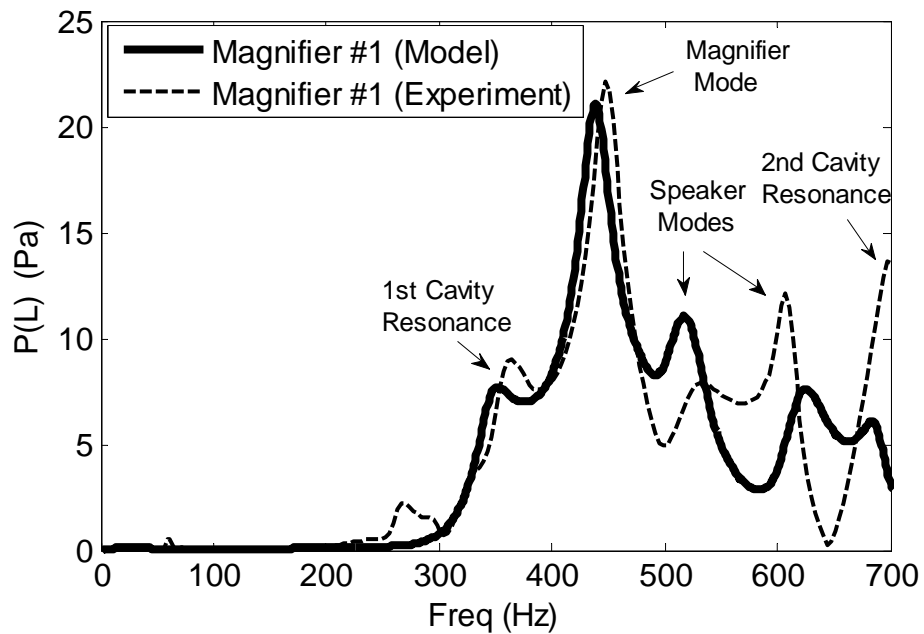


Figure 7.18 Comparison between experimental and theoretical data for the end pressure $P(L)$ for the conventional *PDTAR* and a *PDTAR* with Magnifier #1

Figure 7.17 shows the model prediction for the end pressure $P(L)$ for the prototype with and without the magnifier. This figure is in coherent agreement with Figure 7.11 which represents the experimental version of the same data. Finally, Figure 7.18 shows a comparison between theory and experimental results for the *PDTAR* with the magnifier. As expected, the plot shows frequency peaks at the resonator's first and second modes, at the speaker's modes and at the magnifier's added mode.

7.6. Possible improvements to the PDTAR experimental setup

This section discusses some modifications that can be applied to the experimental prototype that should potentially improve its performance with and without the dynamic magnifier in the future.

7.6.1. Resonator matching

One modification to improve the refrigerator's performance would be to ensure perfect matching between the resonances of the acoustic resonator in the *PDTAR*, with and without a magnifier, and one of the speaker's natural modes. This can be done by slightly varying the resonator's length. This tuning has been shown to enhance the outcome of thermoacoustic devices, as illustrated earlier in Chapter 4.

7.6.2. Air tight Resonators

In order to make the *PDTAR* experimental prototype as flexible as possible for several experiments that can examine and investigate different operating parameters, one of the design objectives was to not make the prototype sealed in one permanent

setting. For example, in the conjunction between the speaker and the resonator, the speaker is mounted on the acrylic base, as shown in Figure 7.1 using four bolts. This way, the speaker could be taken off and replaced as frequently as possible. This was a key design factor to enable the use of different speakers and magnifier settings to be able to carry out the different experiments presented in this chapter. On another note, several holes were drilled in the resonator tube and plugged with screws to enable the movement of the stack from one location to the other. Finally, the plug that represents the rigid enclosure at the top of the resonator was not sealed permanently to facilitate opening and closing the tube in order to displace or replace the stack.

All these considerations mentioned above, although enable easy and time effective experimentation, but represent multiple sources of pressure leak in the resonator. This contributes in the pressure losses that lead the pressure waveform to lose a portion of its magnitude before radiating to the end of the tube as shown in Figure 6.10. Pressure build up that happens inside an air tight resonator is very important to induce a higher temperature difference. It is worth noting here that a *PDTAR* prototype of similar dimensions was made for the sole purpose of temperature tests with one stack location and one speaker. The resonator was hole free, was sealed properly and a rigid aluminum cap was fitted at the end of the tube and silicon paste was applied around it. Using the same speaker with the same input power, a temperature difference of about 18 *K* was obtained across the stack ends. The prototype however was not available for reuse with different configurations or enhancements such as a dynamic magnifier. Therefore, it was the aim of this study to

compare the performance of a *PDTAR* with a magnifier relative a conventional one using the same prototype. The results shown should be projected and applicable to any *PDTAR*.

7.7. Summary

This chapter illustrated the experiments carried out with piezo-driven thermoacoustic-piezoelectric refrigerators, with and without dynamic magnifiers. Experimental results included measurements of the resonator end pressure as well as temperature difference across the stack. Comparisons have been made between the theoretical predictions and the experimental data.

Furthermore, an experiment to show the potential of experimental *PDTARs* with dynamic magnifiers has also been presented showing again the superiority of the magnified devices in terms of the developed temperature difference, and hence the device's cooling effect. Equations developed in Chapter 6 have been employed to verify these results and close agreement was observable.

Chapter 8

8. Conclusions and Future Work

This chapter summarizes the conclusions arrived at during the course of the study. Presented also here are some ideas that can be pursued as a natural extension of the current dissertation. Finally, some concluding remarks outlining the major contributions of this work to the general body of the state-of-the-art of the field of thermoacoustics.

8.1. Conclusions

This dissertation has presented comprehensive theoretical and experimental investigations of thermoacoustic engines integrated with piezoelectric membranes to create a new class of energy harvesters. This class of harvesters converts the thermoacoustic energy directly into electrical power output. The feasibility of coupling the thermoacoustic-piezoelectric (*TAP*) harvester with dynamic magnifier system as a means for improving the electric power output and the conversion efficiency is demonstrated theoretically and experimentally. Novel approaches based on the analysis of the electrical analogies of the dynamically magnified *TAP* (*DMTAP*) and application of the root locus analysis are developed and presented in order to gain better understanding of the dynamics and transient behavior of this class of multi-field harvesters. With these approaches, it has been possible to compute and accurately predict critical temperature gradients that onset the acoustic waves in the harvesters. Such approaches open new dimensions to the analysis, design, and optimization of *DMTAP* which are currently unavailable in the literature.

The dissertation has presented also a novel class of piezo-driven thermoacoustic refrigerators (*PDTARs*) which rely in their operation on the inverse thermoacoustic effect. With high amplitude pressure oscillations, introduced by controlled vibrations of a piezoelectric diaphragm in a working medium, a temperature gradient is created across the ends of a porous body located in an acoustic resonator. The concept of *PDTARs* with dynamic magnifiers is introduced and its feasibility is demonstrated theoretically and experimentally. It is shown that dynamically magnified *PDTARs* are capable of generating higher cooling effect than plain *PDTARs*. This enhanced performance will definitely contribute to a higher coefficient of performance (*COP*) of the thermoacoustic refrigerator.

8.2. Future Work

8.2.1. Miniature Thermoacoustic-Piezoelectric Harvesters

Small size thermoacoustic-piezoelectric harvesters can be very effective in scavenging energy for small, wireless autonomous devices and sensor networks, wherever a source of heating is feasible and easily accessible. The low amount of power provided by *TAP* harvesters is ideal to drive these low-energy systems and electronics. Harvested energy can be stored in capacitors or batteries and to be used when needed by the application. Some efforts have been in place to build miniature thermoacoustic engines as shown in Figure 8.1, but none have been reported of a small-scale *TAP* harvester device.

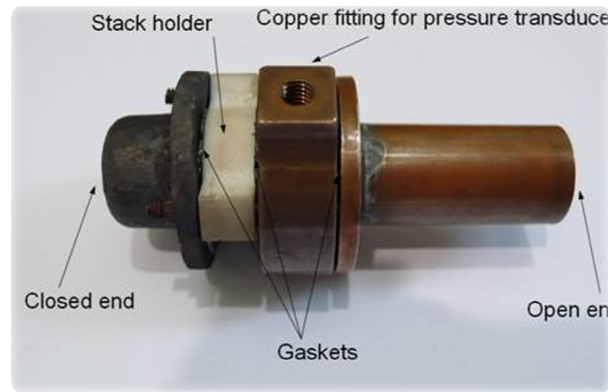


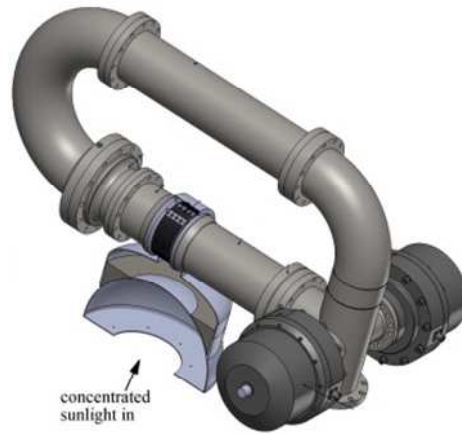
Figure 8.1 Open-ended small-scale experimental thermoacoustic engine without an energy harvesting element [54]

8.2.2. Solar and Waste-heat Driven Thermoacoustic-Piezoelectric Energy Harvesting

TAP energy harvesters can appealingly be driven by any source of heat. One of the possible extensions of this work would be to incorporate the current design of *TAP* and *DMTAP* harvesters in combustion-based systems and cycles, whereas the waste heat from the combustion processes would be used to generate the temperature gradient required across the stack to onset the acoustic oscillations and drive the *TAP* harvester. Another extension possibility is to use solar concentrators in areas of adequate solar power intensity to onset acoustic oscillations in the resonators. Some efforts have been reported in operating thermoacoustic resonators with these different heating sources as shown, for example, in Figure 8.2. Applying these ideas to thermoacoustic-piezoelectric harvesters with and without dynamic magnifiers can be very effective.



(a)



(b)

Figure 8.2 (a) A solar-driven standing wave thermoacoustic engine courtesy of Penn State University [55] and (b) a schematic of a solar-powered traveling wave thermoacoustic engine courtesy of the Chinese Academy of Science [56]

8.2.3. *Effect of Varying Area Resonators*

For the *TAP* prototype illustrated in this study (Figure 4.2), a Helmholtz-like resonator of a greater cross sectional area than the tube carrying the stack and the heating element was used. This is a common practice with standing wave thermoacoustic harvesters aimed at amplifying the power flow from the system. Literature suggests that resonator geometry optimization is a key factor in deciding the shape and magnitude of the pressure waveform. Examples of that include a detailed study to model standing waves in acoustic cavities with arbitrary complex geometries, where higher pressure ratios have been reported, for example, by El-Sabbagh [57] at certain variations of the resonator's area as shown in Figure (8.3). Another example is a study where “*anharmonic*” thermoacoustic-resonators with

varying area are used to improve the resonance's quality factor and magnify the fundamental mode [58].

Modifying the system of equations developed to take into effect a cross sectional area that varies in the wave propagation direction should be attempted. After initiating the new equations as a function of any general area variation pattern, attempts to optimize the resonator geometry should be feasible.

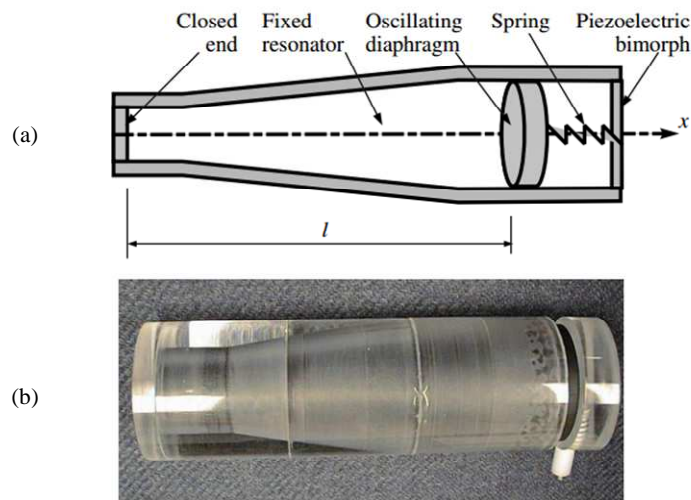


Figure 8.3 (a) A Schematic of a diaphragm driven resonator excited by a piezoelectric bimorph and (b) a photo of the experimental prototype of the resonator in a study of gas-filled axisymmetric acoustic area-varying resonators by El-Sabbagh [57]

8.3. Original Contributions

This dissertation is aimed at providing a comprehensive theoretical and experimental analysis of thermoacoustic devices integrated with piezoelectricity and dynamic magnification for the purpose of energy harvesting and refrigeration. The

theoretical analysis and modeling as well as the experimental demonstrations presented here are considered as original contributions to the state-of-the-art of the thermoacoustic field. No thermoacoustic engine or refrigerator with dynamic magnification capabilities has been reported in the literature.

In this regard, this study introduces a new approach towards optimizing the performance of thermoacoustic-piezoelectric devices. The novelty of the proposed idea relies on the fact that it is independent of the efforts being spent in attempts to optimize the stack parameters (such as spacing, porosity and location) or the heat transfer efficiency (such boundary thickness, gas type and thermo-physical properties). This approach takes a step outside the box of current thermoacoustic research focus and makes use of techniques adopted elsewhere in the field of energy harvesting of coupled structures, in this case namely the concept of dynamic magnification.

Dynamically-magnified thermoacoustic-piezoelectric harvesters have been shown to significantly improve the electrical energy production of the harvester when tuned optimally. On the other hand, dynamic magnification of piezo-driven thermoacoustic refrigerators was shown to enhance the cooling capability of the refrigerator by generating a larger temperature difference across the stack ends.

Furthermore, the analyses of electrical analogs of thermoacoustic systems using *SPICE* and root locus techniques are also among the major contributions of this

dissertation. With these tools, it is possible to predict the transient behavior and the onset of self-sustained oscillations of thermoacoustic systems. Such capabilities are currently unavailable in the most widely used code *DeltaEC* of *LANL* which is limited only to steady state analysis and design of thermoacoustic systems.

Last but not least, ways to optimize the developed systems are numerous and are only limited by our imagination.

Appendices

Appendix A: Numerical Modeling of Thermoacoustic-Piezoelectric Systems using *DeltaEC*

A.1. Introduction

This appendix presents an overview of numerical modeling of different thermoacoustic devices. One of the familiar utilities used in thermoacoustic modeling is the *DeltaEC* software. *DeltaEC* stands for “Design Environment for Low-amplitude Thermoacoustic Energy Conversion”. The software is used to simulate and optimize the design of thermoacoustic engines and refrigerators by solving the one-dimensional wave equation in gas or liquid, based on the low amplitude acoustic approximation in user defined geometries [34]. A Runge-Kutta based numerical integration of the momentum, continuity and energy equations of the fluid flow is carried out in one dimension across sections referred to as segments. The model is made up of several segments placed adjacent to each other and the integration is carried out across the built network of segments. These segments include the resonator geometry, the appropriate stack material and geometry, the cold (or ambient) and hot heat exchangers, the boundary conditions and many other specific design parameters.

A.2. *DeltaEC*

The *DeltaEC* solver assumes a sinusoidal time dependence of all the oscillating variables. Based on this assumption, the temporal part of the governing equations is transformed from differential equations in time to algebraic equations of time. The remaining part of the governing differential equations now becomes function of space only making the solution processing faster and much simpler.

```
2 O BEGIN
3 1.0000E+05 a Mean P Pa
4 Gues 388.05 b Freq Hz
5 800.00 c TBeg K
6 500.00 d |p| Pa
7 0.0000 e Ph(p) deg
8 0.0000 f |U| m^3/s
9 0.0000 g Ph(U) deg
10 Optional Parameters
11 air Gas type
```

Figure A.1.0.1 Screenshot of *DeltaEC* interface of the beginning segment of a *TAP* model

The model starts with the *BEGIN* segment which possesses information on the type of working gas or gas mixture used, the frequency of operation, the mean pressure and temperature and the driving pressure or velocity amplitude if any (depending on whether the modeled system is an engine or a refrigerator) as outlined in Figure A.1.0.1. The segments following the *BEGIN* section usually include segments for the resonator tube (*DUCT*), the stack (*STK*) and both heat exchangers (*HX*) as indicated in Figure A.1.0.2. For thermoacoustic-piezoelectric models, a piezo-element is placed at the end of the model as a transducer segment (*DUCER*). In the case of refrigerators, a speaker (*SPEAKER*) is placed at the beginning which can

be piezo or electromagnetic. The other end is defined by the boundary condition as either a rigid end (HARDEND) with infinite acoustic impedance or an open end with zero acoustic impedance (SOFTEND). The *DeltaEC* model for a typical *TAP* system is displayed in Figure A.1.0.3.

Row	Label	Value	Unit
26	3 HX		
27	Same 1a	2.9865E-04	a Area m ²
28		0.7500	b GasA/A
29		7.5000E-03	c Length m
30		6.8250E-05	d y0 m
31	Gues	0.51343	e HeatIn W
32	Master-Slave Links	-1.2077E-02	F Edot W
33	Possible targets	800.00	G GasT K
34	ideal	800.32	H SolidT K
35	4 STKCIRC		
36	Same 1a	2.9865E-04	a Area m ²
37		0.7500	b GasA/A
38		3.3750E-02	c Length m
39		3.8225E-04	d radius m
40		2.2750E-05	e Lplate m
41	Master-Slave Links	8.9559E-04	F Edot W
42		800.00	G TBeg K
43		295.20	H TEnd K

Figure A.1.0.2 Screenshot of *DeltaEC* interface of the stack and hot heat exchanger of a *TAP* model

The system runs by choosing some parameters under study as guesses (GUESS) to solve for and setting values for others as targets to try to reach (TARGET). The number of guesses and targets must match, and the program solves for the complex pressure, velocity, temperature, acoustic heat flux and acoustic power at the end of each segment. In the transducer segments, the program also solves for the potential difference or the current across the piezo load.

State plots of any variable at the end of any segment can be obtained, which are referred to as state plots. Finally, it's also possible to study the effect of changing one variable in any segment on another one using the incremental plots feature.

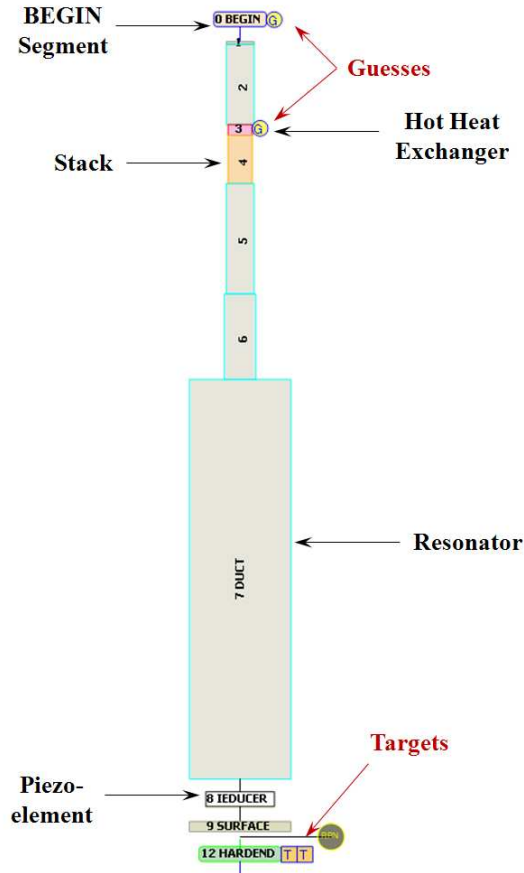


Figure A.1.0.3 Schematic of the developed *DeltaEC* model for a TAP

A.3. Piezo-elements in *DeltaEC*

In thermoacoustic-piezoelectric harvesters, it is essential that the piezo-element at the end of the resonator tube is incorporated correctly in the *DeltaEC* model. This is done using the transducer segment available in the *DeltaEC* library. In this segment, the pressure difference across the element ΔP_p and the voltage V are related to the volume velocity Q of the interfacing working gas and the electric current I by this relation,

$$\begin{Bmatrix} \Delta P_p(i\omega) \\ V(i\omega) \end{Bmatrix} = T_{DE}(i\omega) \begin{Bmatrix} Q(i\omega) \\ I(i\omega) \end{Bmatrix} \quad (\text{A.1.1})$$

where $T_{DE}(i\omega)$ is a 2x2 matrix that couples the acoustic and electrical domains of the piezo-element and is required by *DeltaEC* as an input when using the transducer segment. This matrix is built up from 4 constituent transfer functions as follow,

$$T_{DE}(i\omega) = \begin{bmatrix} T_{11,DE}(i\omega) & T_{12,DE}(i\omega) \\ T_{21,DE}(i\omega) & T_{22,DE}(i\omega) \end{bmatrix} \quad (\text{A.1.2})$$

These transfer functions represent the mechanical and acoustic impedances as well as the coupling electro-acoustical functions of the piezo-element. These impedances depend on the type and geometry of the piezo-element used. For a *TAP* that has a piezoelectric diaphragm anchored at the end, the oscillation of the piezo-element in its first mode should resemble the pattern shown in Figure 2.2 (a). The experimental setup for the *TAP* (discussed in details in Chapter 4) includes a *PZT-5A* piezoelectric diaphragm at the end of the resonator. In the subsequent section, a guided procedure will be presented to help obtain the 4 transfer functions required as inputs for *DeltaEC* for this piezo diaphragm.

A.4. Transfer Functions for the Piezo-diaphragm Coupling Matrix

(a) Finite Element Model

The piezo-element under study is a Lead-Zirconate-Titanate (*PZT-5A*) diaphragm that has a 63.5 mm diameter and is 1.91 mm thick as shown in Figure A.1.0.4. Measured experimentally, the piezo diaphragm resonates at a first natural frequency of about 300 *Hz*. The diaphragm is tuned, by supporting it on an aluminum

substrate (0.1 mm thick and 71 mm diameter) and adding a weight of 2.81 g at its center, to have a modified first natural frequency at around 388 Hz to be in resonance with the acoustic cavity. Figure A.1.0.5 shows a schematic drawing of the *PZT-5A* Piezo diaphragm supported on the aluminum backing.

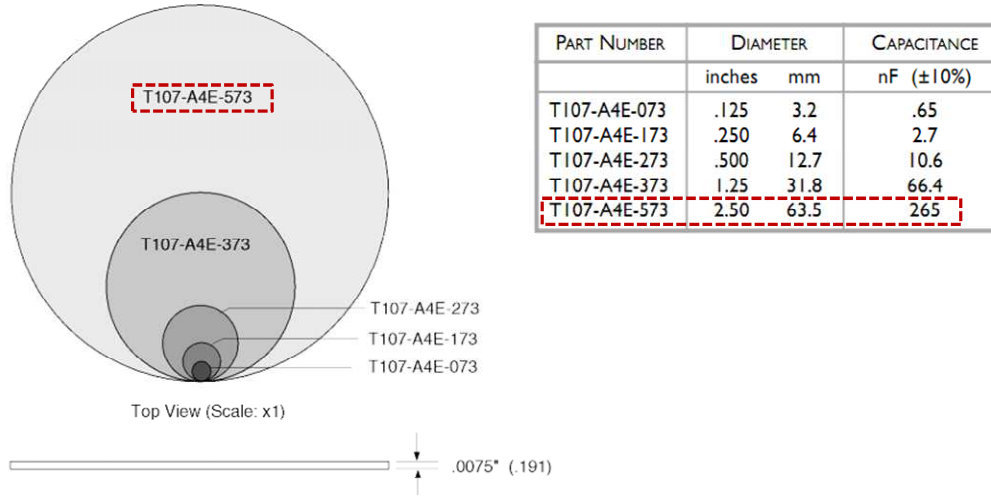


Figure A.1.0.4 *PZT-5A* Piezo diaphragm (63 mm, .191 mm thick) from Piezo Systems, Inc.

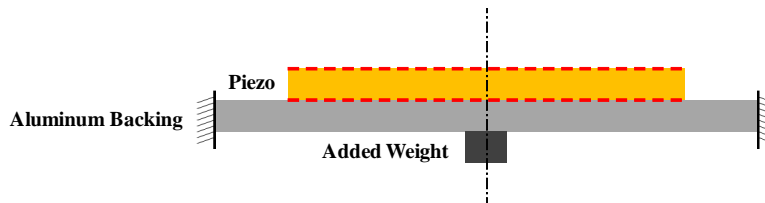


Figure A.1.0.5 Schematic of the *PZT-5A* Piezo diaphragm supported on aluminum backing

A finite element model (FEM) of this disk pre and after tuning is performed on ANSYS (Figure A.1.0.6) and the natural frequencies obtained coherently match the experimental values as shown in Figure A.1.0.7 and Figure A.1.0.8 respectively.

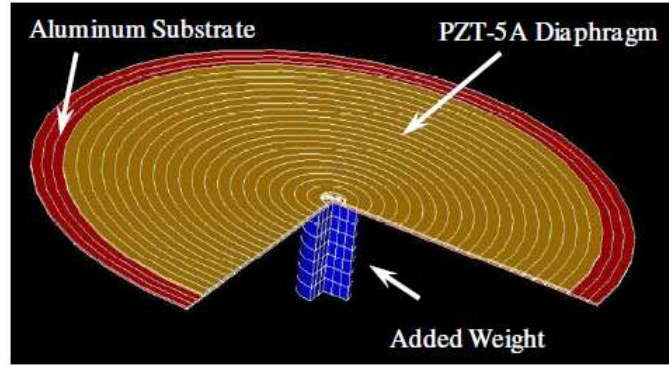


Figure A.1.0.6 ANSYS Finite element model of the piezo diaphragm tuning configuration

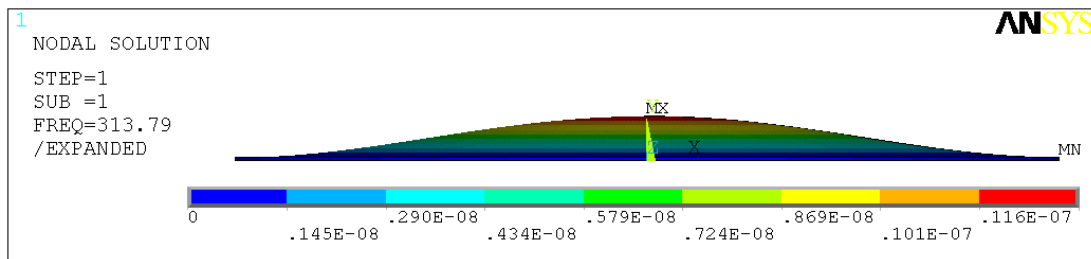


Figure A.1.0.7 ANSYS FEM model: First mode of Piezo diaphragm before tuning – 313.8 Hz

The model for the diaphragm before adding the aluminum backing and the center weights contains 167 elements while that including them has 1208 elements. Both analyses were done using the PLANE223 axi-symmetric piezoelectric element available in the ANSYS library. The piezoelectric strain coefficients, compliance coefficients and the relative permittivity at constant stress used in the model are obtained from IEEE standard on piezoelectricity and listed in the ANSYS verification manuals.

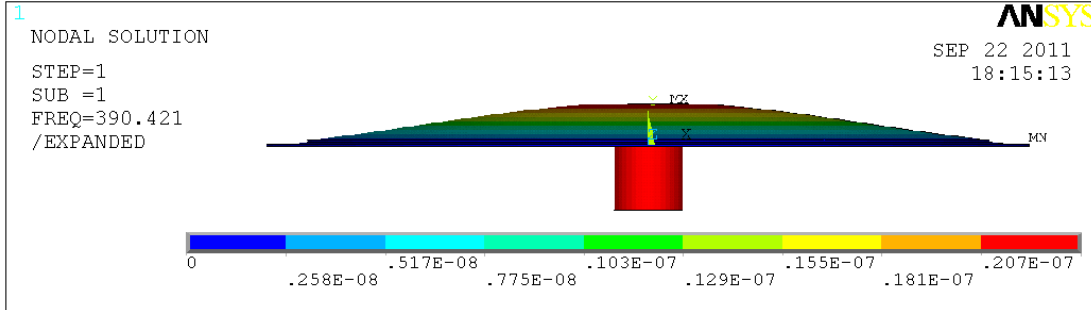


Figure A.1.0.8 ANSYS FEM model: First mode of Piezo diaphragm after tuning (supported on aluminum backing with added center weight) – 390.4 Hz

(b) Eigensystem Realization Algorithm (ERA)

The Eigensystem Realization Algorithm (ERA) is an algorithm used to identify the parameters of structures subjected to a unit pulse or any general type input excitation. A brief emphasis here is placed on the identification of system characteristics from the system’s time domain response to an impulse excitation [42].

For a feed through free oscillating structure/actuator system, the state matrix A_c , the input matrix B_c and the output matrix C_c can be used to describe the system in the continuous-time domain. While the eigenvalues and Markov parameters are unique to a system, these 3 matrices are not. Another set of matrices A_d , B_d and C_d can describe the same system possessing the same characteristics in the discrete-time domain [43]. The Hankel matrix $H_{ab}(0)$ of a system is defined as,

$$H_{ab}(0) = \overline{O}\overline{C} \tag{A.1.3}$$

where \bar{O} and \bar{C} are the observability and controllability matrices of the system. This Hankel matrix $H_{ab}(0)$ can be factored out using singular value decomposition such that,

$$H_{ab}(0) = R\Lambda S^T \quad (\text{A.1.4})$$

where R and S are orthonormal unitary matrices. S^T represents the transpose of the matrix S while Λ takes the form,

$$\Lambda = \begin{bmatrix} [\Lambda_n] & \vdots & [0] \\ \dots & \vdots & \dots \\ [0] & \vdots & [0] \end{bmatrix} \quad (\text{A.1.5})$$

with Λ_n being a diagonal matrix containing the n singular values of $H_{ab}(0)$.

The B_d and C_d matrices of the identified system can be obtained from,

$$B_d = \Lambda_n^{1/2} S_n^T E_m \quad (\text{A.1.6})$$

and,

$$C_d = E_s R_n \Lambda_n^{1/2} \quad (\text{A.1.7})$$

where E_m is given by,

$$E_m = [\mathbf{I}_{m \times m} \quad 0 \quad 0 \quad 0 \quad \dots \quad 0]^T \quad (\text{A.1.8})$$

and,

$$E_s = [\mathbf{I}_{s \times s} \quad 0 \quad 0 \quad 0 \quad \dots \quad 0] \quad (\text{A.1.9})$$

with m and s being the number of actuators and sensors respectively, S_n^T and R_n being the first n rows and n columns of S^T and R respectively. As for the A_d matrix, it can be extracted from the Hankel matrix $H_{ab}(1)$ which is given by,

$$H_{ab}(1) = \bar{O}A_c\bar{C} \quad (\text{A.1.10})$$

and A_d is equal to,

$$A_d = \Lambda_n^{-1/2} R_n^T H_{ab}(1) R_n \Lambda_n^{-1/2} \quad (\text{A.1.11})$$

Finally, the matrices of the identified system can be used to obtain the system's corresponding transfer function.

The Hankel matrices $H_{ab}(0)$ and $H_{ab}(1)$ can be formed from the system's impulse response to start off this procedure. Figure A.1.0.9 shows a flow chart summarizing the above procedure.

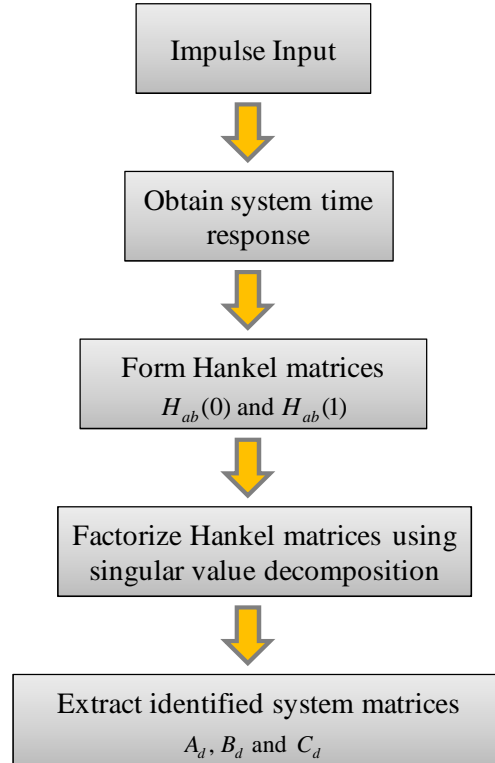


Figure A.1.0.9 Flow chart of the ERA procedure

(c) Identification of the Piezo-diaphragm transfer functions

The procedure adopted here is aimed at obtaining a good approximation of the transfer function matrix $T_{DE}(i\omega)$ required by *DeltaEC* to be able to model the piezo-element in the *TAP* and hence fully model the system. This procedure is based on solving the inverse problem which relies on using the response of a system to a user specified input to extract the system characteristics. The developed mathematical model used here is referred to as the Element Realization Algorithm (ERA). Using *ANSYS*, the time response of the piezo diaphragm to a simulated impulse input is obtained. The ERA is then used to identify the system characteristics and thus the required transfer functions.

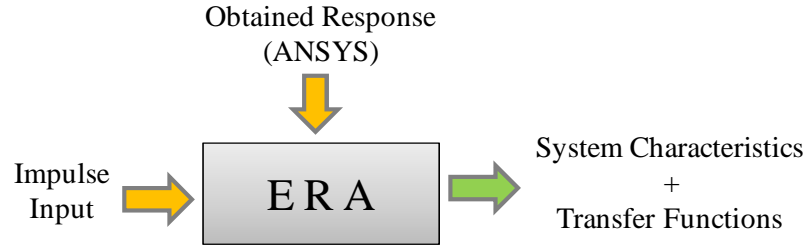


Figure A.1.0.10 Using ERA to solve the Inverse Problem

Consider the following relationship used to describe coupling between the acoustic and electrical domains of the element type used to model the piezo diaphragm,

$$\begin{Bmatrix} u_{center}(i\omega) \\ q(i\omega) \end{Bmatrix} = \begin{bmatrix} T_{11}(i\omega) & T_{12}(i\omega) \\ T_{21}(i\omega) & T_{22}(i\omega) \end{bmatrix} \begin{Bmatrix} \Delta P_p(i\omega) \\ V(i\omega) \end{Bmatrix} \quad (\text{A.1.12})$$

where $u_{center}(i\omega)$ and $q(i\omega)$ are the diaphragm center point deflection and charge respectively.

Using the FEM to simulate an impulse voltage input while keeping a zero pressure input, as indicated in Figure A.1.0.11 (a), the response obtained should be of a system that is described by,

$$u_{center}(i\omega) = T_{12}(i\omega)V(i\omega) \quad (\text{A.1.13})$$

and,

$$q(i\omega) = T_{22}(i\omega)V(i\omega) \quad (\text{A.1.14})$$

Using the obtained time responses $u_{center}(t)$ and $q(t)$ to the impulse voltage input from the FEM, the systems governed by the transfer functions $T_{12}(i\omega)$ and $T_{22}(i\omega)$ can be identified. If identified correctly, the realized system should have the same time response as that obtained from the FEM.

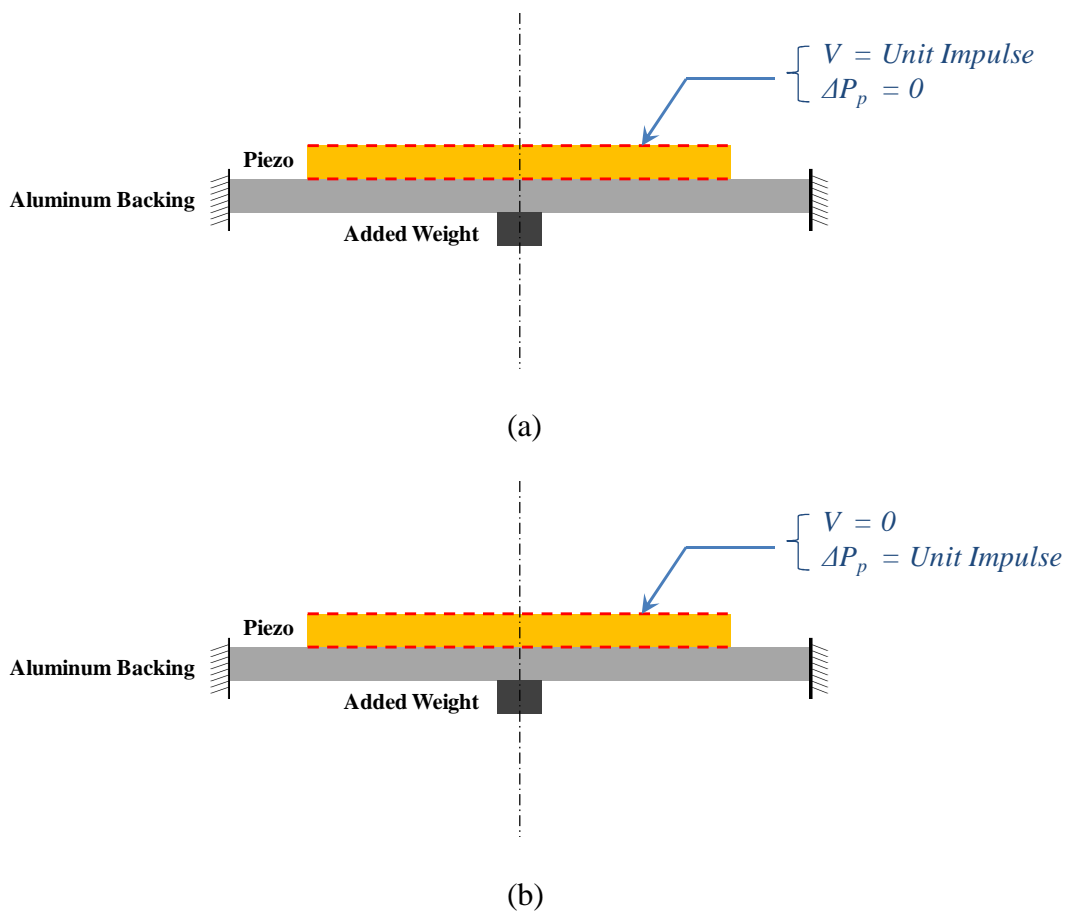


Figure A.1.0.11 Unit impulse inputs applied to the piezo diaphragm in the FEM to obtain the transfer functions (a) $T_{12}(i\omega)$, $T_{22}(i\omega)$ and (b) $T_{11}(i\omega)$, $T_{21}(i\omega)$

Similarly, simulating an impulse pressure input while maintaining zero voltage, as indicated in Figure A.1.0.11 (b), the response obtained should be of a system that is described by,

$$u_{center}(i\omega) = T_{11}(i\omega)\Delta P_p(i\omega) \quad (\text{A.1.15})$$

and,

$$q(i\omega) = T_{21}(i\omega)\Delta P_p(i\omega) \quad (\text{A.1.16})$$

Using the obtained time responses $u_{center}(t)$ and $q(t)$ to the impulse pressure input, the systems governed by the transfer functions $T_{11}(i\omega)$ and $T_{21}(i\omega)$ can be identified. If identified correctly, the realized system should have the same time response as that obtained from the FEM as can be seen from Figure A.1.0.12 and Figure A.1.0.13.

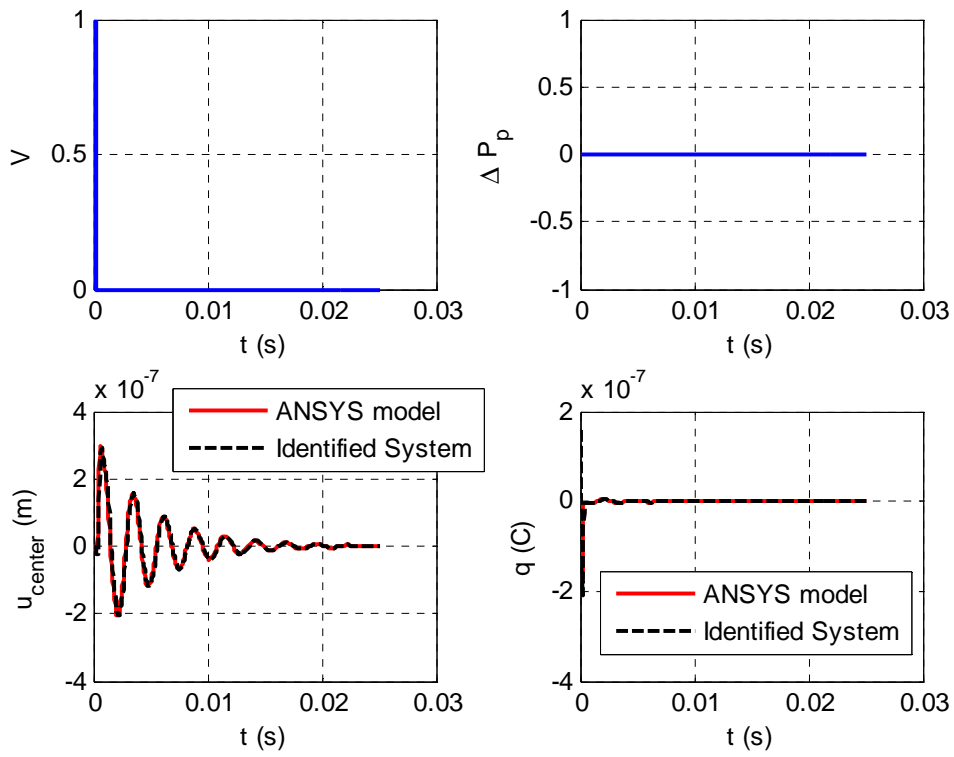


Figure A.1.0.12 Time response of the diaphragm center point deflection $u_{center}(t)$ and charge $q(t)$ to a unit voltage impulse while maintaining a zero differential pressure

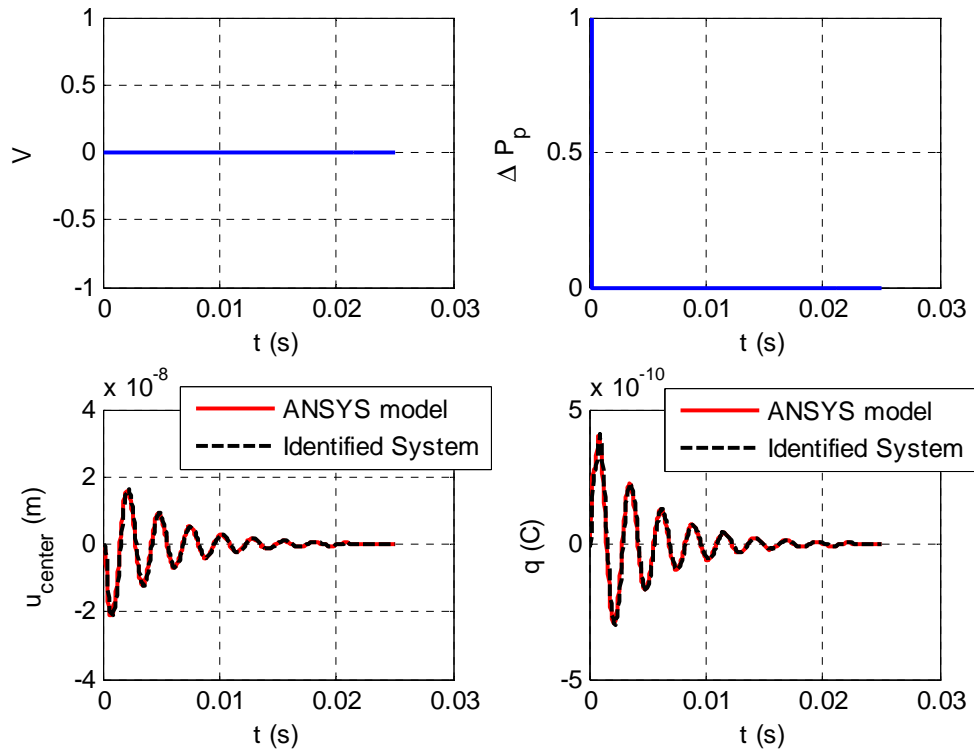


Figure A.1.0.13 Time response of the diaphragm center point deflection $u_{center}(t)$ and charge $q(t)$ to a unit pressure impulse while maintaining a zero voltage

The time response of both modeled and identified systems are shown in Figure A.1.0.12 and Figure A.1.0.13 for both the center point deflection and the electric charge. It can be noticed that the identified system has an identical response as the original system, thus making the obtained transfer functions from the ERA procedure fully descriptive of the diaphragm characteristics.

Table A.1.0.1 lists numerical values for the obtained transfer function coefficients for $T_{11}(i\omega)$, $T_{12}(i\omega)$, $T_{21}(i\omega)$ and $T_{22}(i\omega)$. Figure A.1.0.14 shows the frequency response of the magnitudes of these transfer functions in the domain

starting from 100 Hz up till 10⁵ Hz. The plot shows the structural resonance $T_{11}(i\omega)$ of the diaphragm at about 390 Hz, while the electric characteristics $T_{22}(i\omega)$ appear to be relatively flat in the plotted domain. The plots for $T_{12}(i\omega)$ and $T_{21}(i\omega)$ show the response of the coupled electrical and structural piezo characteristics.

Table A.1.0.1 Values of the transfer functions coefficients governing the PZT-5A diaphragm

$$T_{ij}(i\omega) = \frac{a_{10}(i\omega)^{10} + a_9(i\omega)^9 + \dots + a_2(i\omega)^2 + a_1(i\omega) + a_0}{b_{10}(i\omega)^{10} + b_9(i\omega)^9 + \dots + b_2(i\omega)^2 + b_1(i\omega) + b_0}$$

n	$T_{11}(i\omega)$		$T_{12}(i\omega)$		$T_{21}(i\omega)$		$T_{22}(i\omega)$	
	a_n	b_n	a_n	b_n	a_n	b_n	a_n	b_n
10	-1.5e-12	1	2e-10	1	6.5e-13	1	1.6e-7	1
9	6.2e-7	8.3e4	-4.6e-5	9.43e4	-2.5e-7	1.1e5	5.804	3.7e7
8	-0.043	5.95e9	5.622	5.44e9	0.02357	8e9	-6.6e5	7.5e12
7	3006	2.16e14	-4.76e5	1.91e14	-1811	3e14	5.2e10	6.32e17
6	-1.62e8	6.08e18	2.82e10	4.61e18	1.11e8	8.7e18	-3.5e15	2.8e22
5	5.81e11	1.05e23	-1.04e15	7.5e22	-3.54e12	1.6e23	1.2e20	6.8e26
4	1.14e17	1.2e27	1.85e19	7.9e26	7.08e16	1.9e27	-1.5e24	9.5e30
3	-6.3e20	9.21e30	1.9e22	5.9e30	-2.08e21	1.5e31	7.2e27	8.5e34
2	6.1e25	4.3e34	-4.4e27	2.5e34	3.7e25	8.5e34	-2.4e32	5.3e38
1	-1.7e30	5.9e37	1.6e31	3.7e37	-1.3e28	1.1e38	-5.2e34	6.15e41
0	-3.7e34	1.84e41	2.48e35	1.06e41	1.6e33	3.8e41	-1.4e39	2.5e45

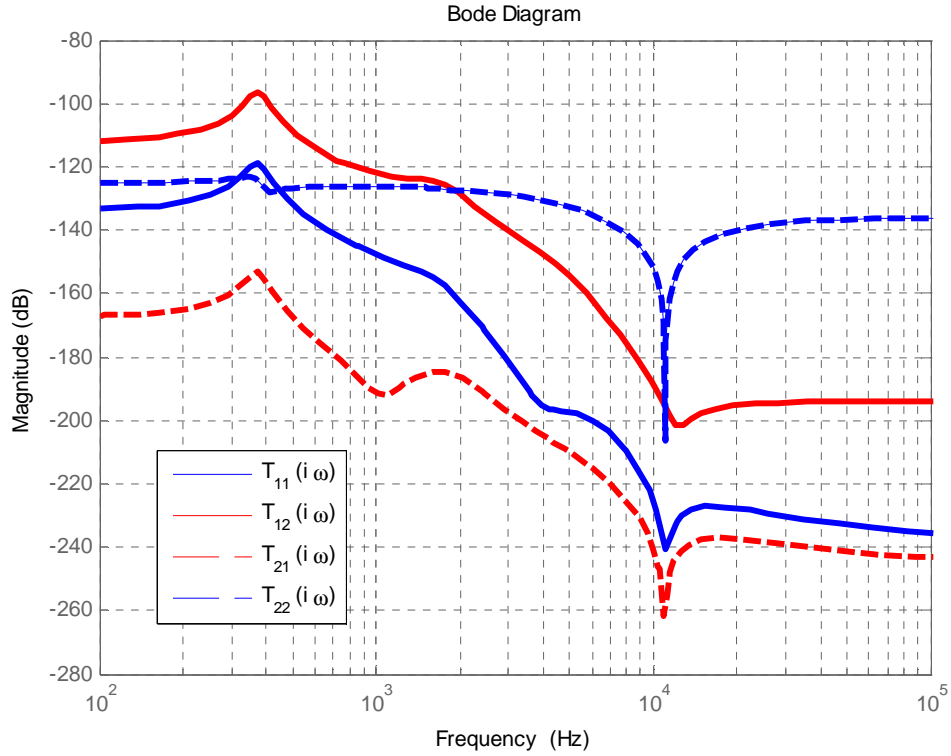


Figure A.1.0.14 Frequency response of the magnitude of the transfer functions $T_{11}(i\omega), T_{12}(i\omega), T_{21}(i\omega)$ and $T_{22}(i\omega)$

(d) Integration with DeltaEC

As discussed earlier in equations (A.1.1) and (A.1.2), the *DeltaEC* model uses the following relationship to model a transducer segment in a thermoacoustic harvester,

$$\begin{Bmatrix} \Delta P_p(i\omega) \\ V(i\omega) \end{Bmatrix} = \begin{bmatrix} T_{11,DE}(i\omega) & T_{12,DE}(i\omega) \\ T_{21,DE}(i\omega) & T_{22,DE}(i\omega) \end{bmatrix} \begin{Bmatrix} Q(i\omega) \\ I(i\omega) \end{Bmatrix} \quad (\text{A.1.17})$$

with the 2x2 matrix $T_{DE}(i\omega)$ being the user-specified input to *DeltaEC*. On the other hand, the piezo diaphragm transfer functions obtained in the previous section are for the following system of equations,

$$\begin{Bmatrix} u_{center}(i\omega) \\ q(i\omega) \end{Bmatrix} = \begin{bmatrix} T_{11}(i\omega) & T_{12}(i\omega) \\ T_{21}(i\omega) & T_{22}(i\omega) \end{bmatrix} \begin{Bmatrix} \Delta P_p(i\omega) \\ V(i\omega) \end{Bmatrix} \quad (\text{A.1.18})$$

Equation (A.1.18) can be written as,

$$\begin{Bmatrix} \Delta Vol(i\omega) \\ q(i\omega) \end{Bmatrix} = \begin{bmatrix} T'_{11}(i\omega) & T'_{12}(i\omega) \\ T_{21}(i\omega) & T_{22}(i\omega) \end{bmatrix} \begin{Bmatrix} \Delta P_p(i\omega) \\ V(i\omega) \end{Bmatrix} \quad (\text{A.1.19})$$

whereby the center point displacement u_{center} is transformed into an approximate change in volume ΔVol using the diaphragm deflection pattern obtained from the finite element model. $T'_{11}(i\omega)$ and $T'_{12}(i\omega)$ represent the adjusted transfer functions of the first row to match the new equation. Differentiating both rows of equation (A.1.19) once with respect to time, the change in volume and electric charge become a volume velocity and an electric current respectively yielding,

$$\begin{Bmatrix} Q(i\omega) \\ I(i\omega) \end{Bmatrix} = \begin{bmatrix} i\omega T'_{11}(i\omega) & i\omega T'_{12}(i\omega) \\ i\omega T_{21}(i\omega) & i\omega T_{22}(i\omega) \end{bmatrix} \begin{Bmatrix} \Delta P_p(i\omega) \\ V(i\omega) \end{Bmatrix} \quad (\text{A.1.20})$$

Rearranging (A.1.20) we obtain,

$$\begin{Bmatrix} \Delta P_p(i\omega) \\ V(i\omega) \end{Bmatrix} = \begin{bmatrix} i\omega T'_{11}(i\omega) & i\omega T'_{12}(i\omega) \\ i\omega T_{21}(i\omega) & i\omega T_{22}(i\omega) \end{bmatrix}^{-1} \begin{Bmatrix} Q(i\omega) \\ I(i\omega) \end{Bmatrix} \quad (\text{A.1.21})$$

Equating (A.1.17) and (A.1.21) we conclude that,

$$\begin{bmatrix} T_{11,DE}(i\omega) & T_{12,DE}(i\omega) \\ T_{21,DE}(i\omega) & T_{22,DE}(i\omega) \end{bmatrix} = \begin{bmatrix} i\omega T'_{11}(i\omega) & i\omega T'_{12}(i\omega) \\ i\omega T_{21}(i\omega) & i\omega T_{22}(i\omega) \end{bmatrix}^{-1} \quad (\text{A.1.22})$$

and thus the input parameters to the *DeltaEC* transducer segment can be obtained from the already calculated transfer functions.

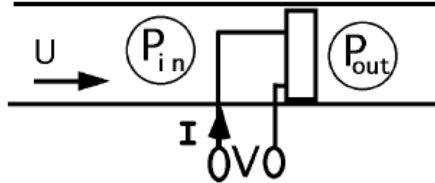


Figure A.1.0.15 Schematic of the DUCER segment used to model the piezo-element in *DeltaEC*

The final step needed would be to obtain the values of these transfer functions by evaluating them at the operating frequency of operation of the *TAP* ($\sim 390 \text{ Hz}$). Figure A.1.0.16 summarizes the complete procedure used to model a *TAP* using *DeltaEC*. A detailed look at the *DeltaEC* results is available in comparison to the obtained experimental results in Chapter 5.

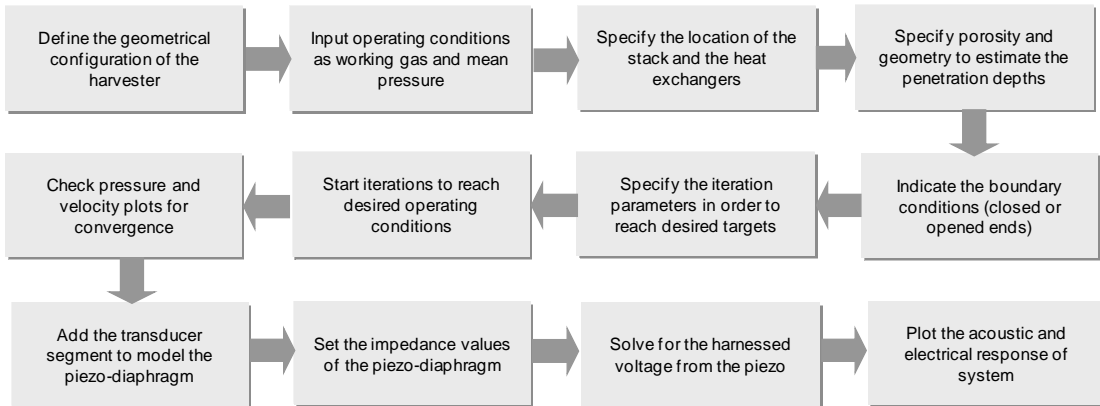


Figure A.1.0.16 Modeling a thermoacoustic-piezoelectric harvester (*TAP*) using *DeltaEC*

A.5. Numerical Modeling of Piezo-driven Thermoacoustic Refrigerators

Unlike the modeling of thermoacoustic-piezoelectric harvesters, using *DeltaEC* to model piezo-driven thermoacoustic refrigerators is actually simpler. The piezo speaker is again modeled using a transducer segment VEDUCER which describes the piezo speaker by the following governing relationship,

$$\begin{Bmatrix} V(i\omega) \\ \Delta P_p(i\omega) \end{Bmatrix} = \begin{bmatrix} Z_e(i\omega) & -\tau(i\omega) \\ \tau'(i\omega) & -Z_m(i\omega) \end{bmatrix} \begin{Bmatrix} I(i\omega) \\ Q_o(i\omega) \end{Bmatrix} \quad (\text{A.1.23})$$

Equation (A.1.23) is similar to equation (A.1.17) used in modeling thermoacoustic-piezoelectric harvesters. Q_o is the flow rate provided by the speaker. As stated earlier, Z_e , Z_m , τ and τ' are frequency dependent functions that correlate the effort variables to the flow ones, and are characteristic of the speaker itself.

The experimental setup for the piezo-driven thermoacoustic refrigerator (discussed in Chapter 7) includes a PZ-94 Harsh Environment Speaker from ISL products [44] as shown in Figure A.1.0.17. The piezo speaker has a diameter of 91.5 mm and operates optimally in the frequency range from 400 Hz to 20 kHz.

By removing the piezoelectric disk from the speaker and clamping it between two electrically non-conductive surfaces, the real and imaginary parts of the electric impedance Z_e could be obtained. This is done by connecting the two electrodes to an impedance analyzer which reads out the impedance values.



Figure A.1.0.17 Piezo-speaker (ISL Products PZ-94 Harsh Environment Speaker) [44]

The coupling variables τ and τ' were found by measuring the volumetric flow rate that corresponds to driving the piezo speaker at a given voltage keeping the other parameters at zero to obtain τ . In the *DeltaEC* VEDUCER segment, it is assumed that the coupling variables follow the relationship $\tau' = -\tau$, and hence the value of τ' could be obtained as well.

Finally, the mechanical impedance Z_m was obtained by applying a dynamic force on the speaker's back while measuring the volumetric flow rate (volume velocity) on the front end using a PSV200 scanning Laser Doppler Vibrometer (LDV) as shown in Figure A.1.0.18. Upon obtaining the equivalent pressure of the applied force and by knowing the corresponding volumetric deflection rate, the mechanical impedance could be found using equation(A.1.23). It should be noted here that since the four variables Z_e , Z_m , τ and τ' are frequency dependent, the values obtained here are only applicable at the operating frequency of the refrigerator and should be re-obtained if the operating frequency is to change.

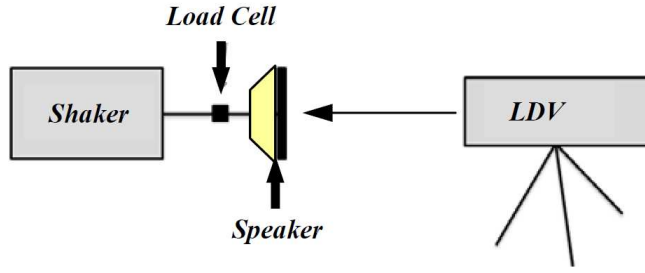


Figure A.1.0.18 Setup used to measure Z_m and τ of the piezo speaker

Table A.1.0.2 lists the values of Z_e , Z_m , τ and τ' for the piezo-driven thermoacoustic refrigerator under study while Figure A.1.0.19 displays a schematic of the developed *DeltaEC* model.

Table A.1.0.2 Impedance values inputted to *DeltaEC* for the thermoacoustic refrigerator speaker

Z_e (Ω)		τ (Vs / m^3)		τ' (Pa / A)		Z_m ($\text{Pa s} / \text{m}^3$)	
Re	Im	Re	Im	Re	Im	Re	Im
14.64	-372.7	8023.0	5.547e4	-8023	-5.547e4	1.357e6	-2.66e6

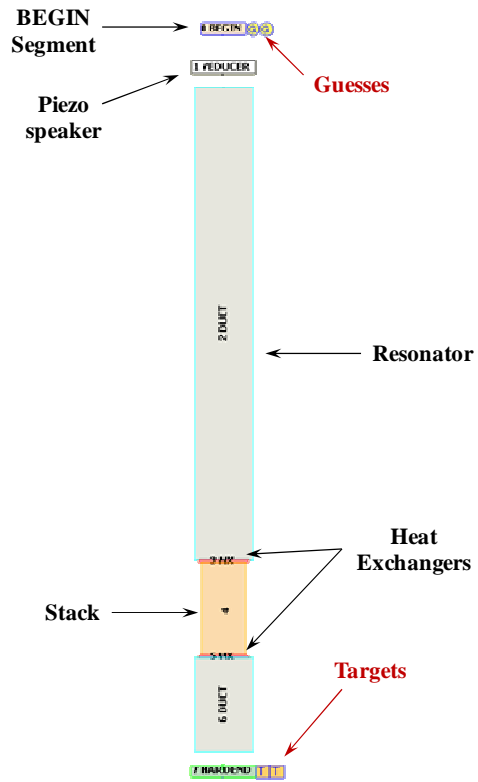


Figure A.1.0.19 Schematic of the developed *DeltaEC* model for a piezo-driven thermoacoustic refrigerator

Bibliography

- [1] D. L. Gardner, and C. Q. Howard, 2009, “Waste-Heat-Driven Thermoacoustic Engine and Refrigerator”, *Proceedings of ACOUSTICS2009*, Adelaide, Australia.
- [2] B. Arman, J. Wollan, V. Kotsubo, S. Backhaus, and G. Swift, 2004, “Engine Driven Large Multiple Pulse Tube Refrigerators”, *Proceedings of the 13th Int’l Cryocooler Conference*, New Orleans, LA.
- [3] J. A. Adeff and T. J. Hofler, 2000, “Design and construction of a solar-powered, thermoacoustically driven, thermoacoustic refrigerator”, *J. Acoust. Soc. Am.*, 107(6), pp. 37-42.
- [4] C. Shen, Y. He, Y. Li, H. Ke, D. Zhang, and Y. Liu, 2009, “Performance of solar powered thermoacoustic engine at different tilted angles”, *Applied Thermal Engineering*, 29, pp. 2745-2756.
- [5] A. Wekin, C. D. Richards, N. Shafrei-Tehrany, and K. I. Matveev, 2007, “On the coupling between standing-wave thermoacoustic engine and piezoelectric transducer”, *Proceedings of IMECE2007*, Seattle, WA.
- [6] C. Jensen and R. Raspet, 2010, “Thermoacoustic power conversion using a piezoelectric transducer”, *J. Acoust. Soc. Am.*, 128(1), pp. 98-103.
- [7] R.V.L. Hartley, 1951, “Electric Power Source”, *US Patent No. 2,549,464*.
- [8] W. A. Marrison, 1953, “Heat-Controlled Acoustic Wave System”, *US Patent No. 2,836,033*.
- [9] P. H. Ceperley, 1979, “A pistonless Stirling engine – The traveling wave heat

- engine”, *J. Acoust. Soc. Am.*, 66(5), pp. 1508-1513.
- [10] K.T. Feldman Jr., 1966, “A Study of Heat Generated Oscillations in a Closed End Pipe”, *Ph.D. Dissertation*, University of Missouri.
- [11] P. H. Ceperley, 1980, “Resonant Traveling Wave Heat Engine”, *US Patent No.* 4,355,517.
- [12] C.D. West, 1983, “Liquid Piston Stirling Engines”, Van Nostrand Reinhold, NY.
- [13] T. Yazaki, A. Iwata, T. Maekawa, and A. Tominaga, 1997, “Traveling Wave Thermoacoustic Engine in a Looped Tube”, *Physical Review Letters*, 81(15), pp. 3128-3131.
- [14] S. Backhaus and G. Swift, 2000, “A thermoacoustic-Stirling heat engine: Detailed study”, *J. Acoust. Soc. Am.*, 107(6), pp. 3148-3166.
- [15] M. Petach, E. Tward, and S. Backhaus, 2004, “Design of a High Efficiency Power Source (HEPS) Based on Thermoacoustic Technology”, *Final report*, NASA contract no. NAS3-01103, CDRL 3f.
- [16] S. Backhaus and G. Swift, 2002, “New Varieties of Thermoacoustic Engines”, *Proceedings of the 9th ICSV*, Orlando, FL.
- [17] T. J. Hofler, 1986, “Thermoacoustic Refrigerator Design and Performance”, *Ph.D. Dissertation*, University of California.
- [18] G. Swift, 1988, “Thermoacoustic Engines”, *J. Acoust. Soc. Am.*, 84(4), pp. 1145-1180.
- [19] S.L. Garrett, J.A. Adeff, and T.J. Hofler, 1993, “Thermoacoustic Refrigerator for Space Applications”, *Journal of Thermophysics and Heat Transfer*, 7(4),

pp. 595.

- [20] D.J. McKelvey and S.C. Ballister, 1995, “Shipboard electronic thermoacoustic cooler”, *M.S. in Engineering Acoustics and M.S. in Applied Physics*, DTIC Report No. AD A300-514.
- [21] Pennsylvania State University, Graduate Program in Acoustics, Thermoacoustic Refrigeration Research Group’s webpage, “<http://www.acs.psu.edu/thermoacoustics/refrigeration>”
- [22] M.E.H. Tijani, J.C.H. Zeegers, and A.T.A.M. de Waele, 2002, “Construction and performance of a thermoacoustic refrigerator”, *Cryogenics* 42, pp. 59-66.
- [23] M.E.H. Tijani, J.C.H. Zeegers, and A.T.A.M. de Waele, 2002, “Design of thermoacoustic refrigerators”, *Cryogenics* 42, pp. 49-57.
- [24] D. A. Russell and P. Weibull, 2002, “Tabletop thermoacoustic refrigerator for demonstrations”, *Am. J. Phys.* 70(12), pp. 1231-1233.
- [25] W. R. Martini, R. P. Johnston, and Maurice A. White, 1974, “Stirling Engine Power System and Coupler”, *US Patent No.* 3,822,388.
- [26] R. M. Keolian and K. J. Bastyr, 2006, “Thermoacoustic Piezoelectric Generator, *US Patent No.* 7,081,699 B2.
- [27] O.G. Symko, E. Abdel-Rahman, Y.S. Kwon, M. Emmi, R. Behunin, 2004, “Design and development of high-frequency thermoacoustic engines for thermal management in microelectronics”, *Microelectronics Journal* 35, pp. 185-191.
- [28] O.G. Symko, E. Abdel-Rahman, D. Zheng, and T. Klein, 2004, “High Frequency Thermoacoustic Refrigerator”, *US Patent No.* 2004/0000150 A1.

- [29] B. J. Andersen and O. G. Symko, 2009, “Helmholtz-like resonators for thermoacoustic prime movers”, *J. Acoust. Soc. Am.*, 125(2), pp. 787-792.
- [30] D. Sun, L. Qiu, B. Wang, Y. Xiao, 2009, “Novel Helmholtz resonator used to focus acoustic energy of thermoacoustic engine”, *Applied Thermal Engineering* 29, pp. 945-949.
- [31] S. Direk, 2001, “Design of a Mini Thermo-Acoustic Refrigerator”, *M.S. Thesis*, Naval Postgraduate School, Monterey, CA.
- [32] H. Babaei and K. Siddiqui, 2008, “Design and optimization of thermoacoustic devices”, *Energy Conversion and Management* 49, pp. 3585-3598.
- [33] G. Swift, 2002, “Thermoacoustics: A unifying perspective for some engines and refrigerators”, *Acoustical Society of America*, American Institute of Physics Press, NY.
- [34] B. Ward, J. Clark, and G. Swift, 2008, “Design Environment for Low-amplitude Thermoacoustic Energy Conversion: *DeltaEC* - Version 6.2”, *Users Guide*, Los Alamos National Laboratory, LA-CC-01-13 (www.lanl.gov/thermoacoustics).
- [35] M. Damianakis, J. Goethals, J. Kowtko, and P. Cornwell, 2005, “Enhancing Power Harvesting Using a Tuned Auxiliary Structure”, *Journal of Intelligent Material System Structures* 16, pp. 825-834.
- [36] P.S. Ma, J.E. Kim, and Y.Y. Kim, 2010, “Power-Amplifying Strategy in Vibration-Powered Energy Harvesters”, *Active and Passive Smart Structures and Intelligent Systems*, *Proceedings of SPIE Conference*, Paper#7643-23, San Diego, CA.

- [37] O. Aldraihem and A. Baz, 2011, “Energy Harvester with a Dynamic Magnifier”, *Journal of Intelligent Material Systems and Structures* 22, pp. 521-530.
- [38] C. D. Richards, M. J. Anderson, D. F. Bahr, and R. F. Richards, 2004, “Efficiency of energy conversion for devices containing a piezoelectric component”, *J. Micromech. Microeng.* 14, pp. 717-721.
- [39] N. Rott, 1980, “Thermoacoustics”, *Advances in Applied Mechanics* 20, pp. 135-174.
- [40] H. Bailliet, P. Lotton, M. Bruneau, and V. Gusev, 2000, “Coupling Between Electrodynamic Loudspeakers and Thermoacoustic Cavities”, *ACUSTICA* 86, pp. 363-373.
- [41] W. P. Arnott, H. E. Bass, and R. Raspet, 1991, “General formulation of thermoacoustics for stacks having arbitrarily shaped pore cross sections”, *J. Acoust. Soc. Am.*, 90(6), pp. 3228-3237.
- [42] J.N. Juang, 1994, “Applied System Identification”, Prentice Hall.
- [43] G. Franklin, J. Powell and A.E. Naeini, 1994, “Feedback Control of Dynamic Systems”, Third Edition, Addison-Wesley Pub. Co.
- [44] ISL Products Piezo Speaker, PZ-94 Harsh Environment Loudspeaker System, “<http://www.islproducts.com/Products/PiezoSpeaker/PZ-94/PZ-94.pdf>”.
- [45] R. J. Adrian and J. Westerweel, 2011, “Particle Image Velocimetry”, Cambridge University Press.
- [46] E. L. Worthington, 2010, “Piezoelectric Energy Harvesting: Enhancing Power Output by Device Optimization and Circuit Techniques”, *Ph.D. Dissertation*,

Cranfield University, UK.

- [47] F. Yildiz, 2009, “Potential ambient energy-harvesting sources and techniques”, *J. of Tech. Stud.*, Vol. 35, No. 1, pp. 40-48.
- [48] D. Shen, 2009, “Piezoelectric Energy Harvesting Devices for Low Frequency Vibration Applications”, *Ph.D. Dissertation*, Auburn University, Auburn, Alabama.
- [49] J. Blauert and N. Xiang, 2009, “Acoustics for Engineers, 2nd Edition”, Troy Lectures, Springer.
- [50] G. Swift, 2007, “Thermoacoustic Energy Conversion”, Chapter 7 of the Springer Handbook of Acoustics, edited by Thomas Rossing, Springer.
- [51] O. Aldraihem and A. Baz, 2012, “Onset of Self-Excited Oscillations of Traveling Wave Thermo-acoustic-piezoelectric Energy Harvester using Root-Locus Analysis”, *J. Vib. Acoustics* 134, 011003.
- [52] J. Nilsson and S. Riedel, 2000, “Electric Circuits, 6th Edition”, Prentice Hall, New Jersey.
- [53] D. Chinn, 2010, “Piezoelectrically-driven Thermoacoustic Refrigerator”, *M.S. Thesis*, University of Maryland, College Park, Maryland.
- [54] S. Jung and K. Matveev, 2010, “Study of Small-Scale Standing-Wave Thermoacoustic Engine”, *J. Mech. Eng. Sc.* 224(1), pp. 133-141.
- [55] Pennsylvania State University, Engineering, Energy & Environmental Institute webpage, “http://www.engr.psu.edu/e3i/a_acoustics.htm”
- [56] Z. Wu, W. Dai, M. Man and E. Luo, 2012, “A Solar-powered Traveling-wave Thermoacoustic Electricity Generator”, *Solar Energy* 86(9), pp. 2376-2382.

- [57] A. El-Sabbagh, 2005, “Gas-filled Axisymmetric Acoustic Resonators”, *Ph.D. Dissertation*, University of Maryland, College Park, Maryland.
- [58] M. Nouh, N. Arafa and E. Abdel-Rahman, 2009, “Stack Parameters Effect on the Performance of Anharmonic Resonator Thermoacoustic Heat Engine”, *Proceedings of the 3rd IRF*, Porto, Portugal.